Comenius University in Bratislava
Faculty of Mathematics, Physics and Informatics

Beta-decay study of neutron-deficient isotope ^{182}Au

Dissertation Thesis

2025 Mgr. Jozef Mišt

Comenius University in Bratislava
Faculty of Mathematics, Physics and Informatics

Beta-decay study of neutron-deficient isotope ^{182}Au

Dissertation Thesis

Study Program:	Nuclear and Subnuclear Physics
Field of Study:	Nuclear and Subnuclear Physics
Department:	Department of Nuclear Physics and Biophysics
Supervisor:	Mgr. Boris Andel, PhD.
Consultant:	doc. Mgr. Stanislav Antalic, PhD.

Bratislava, 2025 Mgr. Jozef Mišt

28977468

Comenius University Bratislava
Faculty of Mathematics, Physics and Informatics

THESIS ASSIGNMENT

Name and Surname:	Mgr. Jozef Mišt
Study programme:	Nuclear and Subnuclear Physics (Single degree study, Ph.D. III. deg., full time form)
Field of Study:	Physics
Type of Thesis:	Dissertation thesis
Language of Thesis:	English
Secondary language:	Slovak

Title: Beta-decay study of neutron-deficient isotope 182Au

Annotation: The topic of the project belongs to important research field of current nuclear physics – decay spectroscopy. Decay-spectroscopy methods make it possible to obtain valuable information on properties and structure of nuclei. One of the approaches is to measure beta-decaying isotopes, which often populate excited states in daughter nuclei. By detecting gamma rays from subsequent deexcitations of these states it is possible to study beta-decay properties of the mother nucleus and the structure of the daughter nucleus. Depending on the region of the nuclear chart, or specific isotope, it may be possible to gain new information on nuclear deformation, shape coexistence, nuclear isomers, or to test predictions of the shell model alongside obtaining basic information on excited levels.

Presently, we have new high statistics data available on beta decay of 182Au, which were obtained at the detection system ISOLDE Decay Station (IDS). In this measurement, four Germanium Clover detectors were a part of IDS, which in combination with the high statistics enables the use of an effective method of gamma-gamma coincidences to study excited states in the daughter nucleus. During the work on this PhD project, the main task will be to build a detailed level scheme for 182Pt, determine feeding intensities to these levels in beta decay of 182Au and to consider the influence of the pandemonium effect. Additional task will be to examine the possibility to obtain new information on the shape coexistence or presence of isomers.

Aim: The PhD project is aimed at analysis of experimental data obtained at experimental facility ISOLDE (CERN, Switzerland), and physical interpretation of the results. The goal will be analysis and interpretation of data on beta decay of 182Au and populated states in 182Pt.

Participation in ongoing research projects of our group, which are carried out within international collaboration, is foreseen during the PhD study. Student is expected to take an active part in the experimental measurements at nuclear research facilities abroad and to present results at international conferences.

Literature:
W. D. Loveland, D. J. Morrissey and G. T. Seaborg, Modern Nuclear Chemistry, John Wiley & Sons, 2005.

C. Wagemans, The Nuclear Fission Process, CRC Press, 1991.

K. Heyde, Basic Ideas and Concepts in Nuclear Physics, Institute of Physics Publishing, 3rd edition 2004.

K. S. Krane, Introductory Nuclear Physics, John Wiley & Sons, 1988.

28977468

Comenius University Bratislava
Faculty of Mathematics, Physics and Informatics

R. Julin, Gamma-Ray and Conversion-Electron Spectroscopy of Exotic Heavy Nuclei. In: The Euroschool on Exotic Beams - Vol. I. Lecture Notes in Physics, vol 651. Springer, 2004.
B. Rubio and W. Gelletly, Beta Decay of Exotic Nuclei. In: The Euroschool on Exotic Beams - Vol. III. Lecture Notes in Physics, vol 764. Springer, 2009.
Papers published in peer-reviewed journals.

Comment: Because of international collaboration and expected participation in measurements abroad, flexibility, good knowledge of English and ability to work both independently and within a team are required. Basic knowledge of C++ and ROOT is required as well.
Collaboration: CERN (Switzerland), University of York (UK), KU Leuven (Belgium), GSI Darmstadt (Germany)

Keywords: beta decay, gamma ray, excited states, decay properties

Tutor: Mgr. Boris Andel, PhD.
Consultant: doc. Mgr. Stanislav Antalic, PhD.
Department: FMFI.KJFB - Department of Nuclear Physics and Biophysics
Head of department: prof. RNDr. Jozef Masarik, DrSc.

Assigned: 27.01.2021

Approved: 08.02.2021 prof. RNDr. Jozef Masarik, DrSc.
Guarantor of Study Programme

Student

Tutor

28977468

Univerzita Komenského v Bratislave
Fakulta matematiky, fyziky a informatiky

ZADANIE ZÁVEREČNEJ PRÁCE

Meno a priezvisko študenta:	Mgr. Jozef Mišt
Študijný program:	jadrová a subjadrová fyzika (Jednoodborové štúdium, doktorandské III. st., denná forma)
Študijný odbor:	fyzika
Typ záverečnej práce:	dizertačná
Jazyk záverečnej práce:	anglický
Sekundárny jazyk:	slovenský

Názov: Beta-decay study of neutron-deficient isotope 182Au
Štúdium beta premeny neutrónovo deficitného izotopu 182Au

Anotácia: Téma projektu spadá pod dôležitú oblasť súčasnej jadrovej fyziky – rozpadovú spektroskopiu. Metódy jadrovej sprekroskopie umožňujú získavanie cenných poznatkov o vlastnostiach a štruktúre jadier. Jedným z prístupov je štúdium izotopov podliehajúcich beta premene, ktorá často obsadzuje vzbudené stavy v dcérskom jadre. Detekciou gama kvánt z následných deexcitácií týchto stavov je možné študovať vlastnosti beta premeny materského jadra a štruktúru dcérskeho jadra. V závislosti od oblasti v tabuľke izotopov, alebo konkrétneho izotopu, je často možné získať popri základných informáciách o vzbudených hladinách aj nové informácie o deformácii jadra, tvarovej koexistencii, jadrových izoméroch, prípadne testovať predpovede vrstvového modelu.
V súčasnosti máme k dispozícii nové dáta s vysokou štatistikou pre beta premenu 182Au, získané na detekčnom systéme ISOLDE Decay Station (IDS). Súčasťou IDS v danom meraní boli štyri Germániové Clover detektory, čo v kombinácii s vysokou štatistikou umožňuje študovať vzbudené hladiny v dcérskom produkte účinnou metódou gama-gama koincidencií. Vrámci riešeného PhD projektu bude hlavnou úlohou zostaviť detailnú schému stavov v 182Pt, vyhodnotiť intenzity ich obsadzovania v beta premene 182Au a zaoberať sa vplyvom pandemonium efektu. Zároveň bude úlohou overiť možnosť získať dodatočné informácie o tvarovej koexistencií alebo prítomnosti izomérov.

Cieľ: PhD projekt je zameraný na analýzu experimentálnych dát zo zariadenia ISOLDE (CERN, Švajčiarsko) a fyzikálnu interpretáciu výsledkov. Cieľom bude spracovanie a interpretácia dát pre beta premenu 182Au a obsadzované stavy v 182Pt.
Počas štúdia sa predpokladá účasť na prebiehajúcich výskumných projektoch našej skupiny, realizovaných vrámci medzinárodnej spolupráce. Od študenta sa očakáva aktívna spolupráca na experimentálnych meraniach v jadrových výskumných zariadeniach v zahraničí a prezentácia výsledkov na medzinárodných konferenciách.

Literatúra:
W. D. Loveland, D. J. Morrissey and G. T. Seaborg, Modern Nuclear Chemistry, John Wiley & Sons, 2005.
C. Wagemans, The Nuclear Fission Process, CRC Press, 1991.
K. Heyde, Basic Ideas and Concepts in Nuclear Physics, Institute of Physics Publishing, 3rd edition 2004.

28977468

Univerzita Komenského v Bratislave
Fakulta matematiky, fyziky a informatiky

K. S. Krane, Introductory Nuclear Physics, John Wiley & Sons, 1988.
R. Julin, Gamma-Ray and Conversion-Electron Spectroscopy of Exotic Heavy Nuclei. In: The Euroschool on Exotic Beams - Vol. I. Lecture Notes in Physics, vol 651. Springer, 2004.
B. Rubio and W. Gelletly, Beta Decay of Exotic Nuclei. In: The Euroschool on Exotic Beams - Vol. III. Lecture Notes in Physics, vol 764. Springer, 2009.
Články publikované v karentovaných časopisoch.

Poznámka: Vzhľadom na medzinárodnú spoluprácu a očakávanú účasť na meraniach v zahraničí je vyžadovaná flexibilita, dobrá znalosť angličtiny a schopnosť samostatnej práce ako aj spolupráce v rámci tímu. Ďalej je vyžadovaná znalosť základov C++ a ROOT.
Spolupráca: CERN (Switzerland), University of York (UK), KU Leuven (Belgium), GSI Darmstadt (Germany)

Kľúčové slová: beta premena, gama žiarenie, vzbudené stavy, rozpadové vlastnosti

Školiteľ: Mgr. Boris Andel, PhD.
Konzultant: doc. Mgr. Stanislav Antalic, PhD.
Katedra: FMFI.KJFB - Katedra jadrovej fyziky a biofyziky
Vedúci katedry: prof. RNDr. Jozef Masarik, DrSc.

Spôsob sprístupnenia elektronickej verzie práce:
bez obmedzenia

Dátum zadania: 27.01.2021

Dátum schválenia: 08.02.2021

prof. RNDr. Jozef Masarik, DrSc.
garant študijného programu

....

študent

....

školiteľ

Declaration of authorship

I declare, I am the sole author of the Dissertation Thesis titled *Beta-decay study of neutron-deficient isotope* ^{182}Au. The presented work was carried out with the guidance of my supervisor and with the use of the listed literature and sources.

Bratislava, 2025 ....

Jozef Mišt

Abstract

The investigation of exotic isotopes is one of the main topics in nuclear research. Neutron-deficient isotopes in the lead region (Z=82) manifest various interesting phenomena of nuclear structure and radioactive decay, such as shape coexistence, isomeric states and β-delayed fission. The main topic of this Dissertation Thesis is the γ-ray spectroscopy of ^{182}Pt after β decay of ^{182}Au (Z=79, N=103), and α-decay spectroscopy of ^{182}Au. The parent isotope was studied during the IS665 experiment performed at the radioactive ion beam facility ISOLDE at CERN in Switzerland. The nuclei were produced in spallation of a thick uranium target by proton beam, and their decays were measured at the detection system ISOLDE Decay Station. The analysis of γ rays emitted after electron capture/β^+ decay of ^{182}Au was performed, and the level scheme of isotope ^{182}Pt was established based on γ-γ coincidences. Transitions known from previous β-decay studies were confirmed, and 125 new levels and 336 new γ-ray transitions were placed in the level scheme of ^{182}Pt, expanding it up to ~ 3.7 MeV in the excitation energy. Internal conversion coefficients for three transitions were determined from measurements of conversion electrons. Moreover, γ rays from the 455-keV transition previously observed only via conversion electrons were detected for the first time. Unusually high β-decay feeding intensity of 4^+ levels was observed, considering the decay of the currently known (2^+) ground state in ^{182}Au into such states corresponds to the second forbidden non-unique β decays, which are typically highly suppressed. Several possible explanations are discussed, namely the 3^+ assignment for the ^{182}Au ground state, a new 5^+ isomeric state in this nucleus, and the pandemonium effect. The α-decay scheme of ^{182}Au was extended by two new fine structure α decays and branching ratio of $b_\alpha(^{182}\mathrm{Au}) = 0.129(11)\%$ was derived. Relative intensities were determined, and hindrance factors for α-decay branches were calculated relative to unhindered decays in neighbouring isotopes. The $I^\pi = (1^+, 2^+, 3^+)$ assignment was proposed for the ground state of ^{178}Ir based on the conversion coefficient of the 55-keV transition.

Key words: beta decay, alpha decay, gamma ray, excited states, decay properties

Abstrakt

Výskum exotických izotopov je jednou z hlavných tém jadrového výskumu. Neutrónovo chudobné izotopy z oblasti olova (Z=82) prejavujú viaceré zaujímavé javy jadrovej štruktúry, ako je tvarová koexistencia, izomérne stavy a oneskorené štiepenie po β premene. Hlavnou témou tejto dizertačnej práce je γ spektroskopia ^{182}Pt po β premene ^{182}Au (Z=79, N=103) a rozpadová α spektroskopia ^{182}Au. Materský izotop sa študoval počas experimentu IS665 uskutočneného v zariadení na produkciu rádioaktívnych iónových zväzkov ISOLDE v CERNe vo Švajčiarsku. Jadrá boli produkované spaláciou hrubého uránového terča protónovým zväzkom a ich rádioaktívne premeny boli merané na detekčnom systéme ISOLDE Decay Station. Vykonala sa analýza γ žiarenia emitovaného po elektrónovom záchyte a β^+ premene ^{182}Au a schéma vzbudených hladín izotopu ^{182}Pt bola zostavená na základe γ-γ koincidencií. Prechody známe z predchádzajúcich štúdií β premeny boli potvrdené a 125 nových levelov a 336 nových γ prechodov sa umiestnilo do schémy hladín ^{182}Pt, čím bola rozšírená do excitačnej energie ~ 3.7 MeV. Vyhodnotili sa konverzné koeficienty pre tri prechody na základe merania konverzných elektrónov. Navyše bolo prvýkrát detegované γ žiarenie z prechodu s energiou 455 keV, ktorý bol pozorovaný len prostredníctvom konverzných elektrónov. Pozorovala sa nezvyčajne vysoká intenzita obsadzovania β premenou pre 4^+ stavy vzhľadom na to, že rozpad súčasne známeho (2^+) základného stavu v ^{182}Au na takéto hladiny zodpovedá druhej zakázanej non-unique β premene, ktorá je zvyčajne značne potlačená. Je diskutovaných niekoľko možných vysvetlení, konkrétne priradenie spinu a parity 3^+ pre základný stav ^{182}Au, nový 5^+ izomérny stav v tomto jadre a pandemonium efekt. Rozpadová schéma α premeny ^{182}Au bola rozšírená o dva nové prechody a určil sa vetviaci pomer $b_\alpha(^{182}\mathrm{Au}) = 0.129(11)\%$. Určili sa relatívne intenzity α prechodov a príslušné faktory potlačenia boli vypočítané vzhľadom na nepotlačené α premeny v susedných izotopoch. Na základe zmeraného konverzného koeficientu prechodu s energiou 55 keV sa priradila hodnota spinu a parity $I^\pi = (1^+, 2^+, 3^+)$ pre základný stav ^{178}Ir.

Kľúčové slová: beta premena, alfa premena, gama žiarenie, vzbudené stavy, rozpadové vlastnosti

Preface and Acknowledgements

Since the discovery of the atomic nucleus by E. Rutherford in 1911 [Rut11], our understanding of nuclei has greatly evolved. Over the years, the focus of nuclear physics shifted from natural radioactivity to, among other things, the nuclear structure of exotic nuclei far away from the stability line. These studies were allowed by the development of advanced experimental facilities and sophisticated detection systems. One such facility is ISOLDE [Kug00; Bor17b], the largest producer of radioactive ion beams, which has been in operation for over 55 years. It provides a unique opportunity to explore properties of exotic nuclei through various techniques, such as decay, laser, and mass spectroscopy or Coulomb excitation studies. The presented Thesis focuses on the first of these methods — decay spectroscopy. Particles and radiation emitted in the radioactive decay of atomic nuclei carry invaluable information about the studied isotopes, from which details on their structure can be extracted by the analysis of decay data.

The presented Thesis is a result of my analysis of the data on ^{182}Au β and α decay, which were collected during the IS665 experiment at IDS at the ISOLDE facility. While I was not directly involved in the data collection for this specific experiment, I participated in other experimental campaigns at ISOLDE during my study, which helped me become more familiar with this facility and gain a deeper understanding of the experimental techniques. I believe this Thesis will be a small step towards shedding more light on atomic nuclei.

Here, I would like to thank my supervisor, Mgr. Boris Andel, PhD., for his valuable support, guidance, patience, and help with the data analysis. My sincere gratitude also goes to doc. Mgr. Stanislav Antalic, PhD., for fruitful discussions and providing the opportunity to participate in experiments at various facilities.

Moreover, I would like to thank Prof. Andrei N. Andreyev for valuable discussions about data analysis and interpretation of the results.

I am grateful to my colleagues at the department, Mgr. Adam Broniš, PhD., Mgr. Adam Sitarčík, PhD. and M.Sc. Mohammed Alem Sultani for many valuable discussions regarding physics and technical support, and for a great work environment.

Finally, I would like to thank my parents, brother and friends, whose support was crucial to keep me motivated in my studies.

Contents

List of Figures

List of Tables

List of Abbreviations

CE Conversion electron

CERN European Organization for Nuclear Research

EC Electron capture

FWHM Full Width at Half Maximum

g.s. Ground state

GPS General Purpose Separator

HF Hindrance factor

HPGe High-Purity Germanium

HRS High Resolution Separator

ICC Internal conversion coefficient

IDS ISOLDE Decay Station

ISOLDE Isotope Separation On-Line Device

PSB Proton-Synchrotron Booster

RILIS Resonance Ionization Laser Ion Source

TAS Total Absorption Spectroscopy

Introduction

Nuclei around the closed proton shell $Z = 82$ manifest various phenomena of nuclear structure and radioactive decay, such as isomeric states, β-delayed fission and shape coexistence. Nuclear isomers are excited levels with hindered decays to the ground state, giving rise to their relatively long half-life. Such decays indicate a large difference in the underlying structure between the two states [Wal20]. The β-delayed fission is a rare decay mode of nuclei far from the stability line. If β decay populates a high-lying excited state in the daughter nucleus, close to its fission-barrier height, fission can compete with γ-ray de-excitation and provide a unique insight into the low-energy fission. [And13; And18]. Thanks to the low-energy nature of β-delayed fission, it is sensitive to microscopic shell effects. Recently, an unexpected asymmetric fission-fragment mass distribution of β-delayed fission of ^{178,180}Tl was observed, discovering a new region of asymmetric fission [And10; Els13; Lib13].

Shape coexistence appears when the nucleus occupies a low-lying excited state with the same spin and parity as the ground state but with a different deformation [Woo92; Hey11]. An excellent example of this phenomenon is the triple shape coexistence of the spherical, prolate, and oblate states in ^{186}Pb [And00; Oja22]. A simple explanation is based on the so-called intruder states created by an excitation of a proton pair above the $Z = 82$ closed shell, and with its excitation energy reduced by the residual proton-neutron interaction.

Shape coexistence is also a prominent feature of neutron-deficient gold ($Z = 79$) and platinum ($Z = 78$) nuclei and has been extensively studied by several in-beam and decay spectroscopy studies [Mue99; Ven17; Ven20; Sed20; Ven22; Bal22; Kon00; De 90; Pop97; Car90; Heb90]. Ground states (g.s.) of gold isotopes down to ^{187}Au are nearly spherical. However, a sudden shift in their mean-squared charged radii and a change to prolate deformation was observed for $^{183-186}$Au ($N = 104-107$) situated near the $N = 104$ midshell [Wal87; Krö88; Wal89; Le 97]. Recent laser spectroscopy studies [Cub18; Har20; Cub20; Har21; Cub23b] showed that $^{180-182}$Au continue with the trend of strong deformation, while ^{176,177,179}Au return back to spherical shapes. A similar situation also occurs in platinum isotopes with two coexisting configurations, weakly oblate g.s. and prolate excited states. The energy of the prolate configuration in $^{178-186}$Pt is lowered below the oblate one, making it the g.s. of these nuclei [Gar22].

This Thesis focuses on the analysis of data on the electron capture (EC)/β^{+}-decay and α-decay of ^{182}Au ($N = 103$) measured during the IS665 experiment [And20a] at the ISOLDE facility [Kug00; Cat17; Bor17b] in CERN. Nuclei are produced at ISOLDE in spallation, fragmentation or fission of a thick target by a high-energy primary beam, they diffuse out of the target, are ionised in the ion source and separated according to their mass in a magnetic field. Selective ionisation methods can be employed, resulting in a high-purity radioactive ion beam.

The β decay is sensitive to the change of spin and parity of the initial and final state, and the change of nuclear structure overall, via the log ft values. For this reason, emitted γ quanta and conversion electrons carry information about the structure and properties of the daughter and parent nucleus. We aimed for an extension of the currently known level scheme of ^{182}Pt, the first evaluation of log ft values in this decay, and an investigation of the structure of both parent and daughter isotopes in this β decay. Additionally, an α-decay spectroscopy coupled with hindrance factors gives important information about nuclear structure, and will be used to address structural changes in ^{182}Au α decay.

The presented work is divided into five chapters. In Chapter 1, the objectives of this Thesis are summarised. Afterwards, Chapter 2, presents the physical background related to the analysis. Details on decay modes of exotic nuclei are given, followed by an introduction to the nuclear models. Additionally, nuclear shape coexistence and various types of nuclear isomers are briefly described. Information on the ISOLDE facility and detection setup IDS (ISOLDE Decay Station) in general and specifically concerning the IS665 experiment, respectively, is given in Chapter 3. The energy and efficiency calibrations of HPGe and silicon detectors of IDS are also described in this chapter. In Chapter 4, we present previous studies concerning the studied isotopes and we present our results on the β and α decay of ^{182}Au. The final Chapter contains the summary of the obtained results. Additional coincidence spectra, the full level scheme of ^{182}Pt deduced in this work, and the full lists of transitions and levels are given in Appendix A, B and C, respectively.

Chapter 1

Objectives of the Dissertation Thesis

The main goal of the Thesis is the study of decay properties of ^{182}Au and the structure of its decay products. This task can be divided into two parts.

The primary objective is the study of excited levels in ^{182}Pt populated in electron capture (EC)/β^{+} of ^{182}Au. Currently known information on excited levels in ^{182}Pt fed by β decay (up to ~1.9 MeV) [Dav99] is limited with respect to the high Q_{EC} = 7864(23) keV [Wan21] of the decay. High statistics and relatively high detection efficiency for high-energy γ-rays will allow us to extend the currently known level scheme of ^{182}Pt using γ-γ coincidences. Additionally, the analysis of conversion electrons will be performed to search for $E0$ transitions, which are often indicators of shape coexistence. The β-decay feeding intensities will be determined, and log ft values for this β decay will be calculated for the first time in order to investigate changes between the mother nucleus and the populated state. Moreover, the presence of isomeric states in ^{182}Au will be investigated.

The secondary objective of the Thesis is the study of ^{178}Ir as the α-decay daughter isotope of ^{182}Au. We aim for the confirmation and extension of the α-decay scheme of ^{182}Au employing α-γ coincidences. Hindrance factors will be calculated and used for the determination of spin and parity for levels in ^{178}Ir.

Chapter 2

Theoretical background

2.1 Nuclear decay

The majority of known nuclei are unstable and decay into other nuclei, reaching a more stable state. The number of nuclei that decayed during the unit of time (its activity A) is proportional to the decay constant λ of this isotope, which can be expressed as [Kra88]

$$\lambda = -\frac{1}{N}\frac{dN}{dt} = \frac{A}{N}. \tag{2.1}$$

Integration of this formula results in the law of nuclear decay:

$$N(t) = N_0 e^{-\lambda t}, \tag{2.2}$$

where N_0 is the number of nuclei at $t = 0$.

The half-life $T_{1/2}$ of an isotope is defined as the time in which half of the initial amount of nuclei decays. Considering $N(T_{1/2}) = N_0/2$, the Eq. (2.2) gives

$$T_{1/2} = \frac{ln2}{\lambda}. \tag{2.3}$$

If the nucleus undergoes more than one type of radioactive decay, partial decay constants λ_i for each decay can be defined as

$$\lambda_i = \lambda b_i, \tag{2.4}$$

where b_i is the branching ratio for a specific decay. The sum of all partial decay constants of a nucleus gives the total decay constant. Similarly, the partial half-life of the decay $T_{1/2,i}$ is given as follows:

$$T_{1/2,i} = \frac{ln2}{\lambda_i} = \frac{T_{1/2}}{b_i}. \tag{2.5}$$

In this section, we will describe the most common types of nuclear decay, namely the α and β decays and internal transitions.

2.1.1 Alpha decay

Alpha decay is a process of α particle (^4_2He nucleus) emission. This process can be expressed in the following way [Hod97]:

$$^A_ZX_N \rightarrow {}^{A-4}_{Z-2}Y_{N-2} + \alpha. \tag{2.6}$$

Alpha decay can spontaneously occur only when its energy balance Q_α is positive, which can be given in terms of binding energies B:

$$Q_\alpha = B(^{A-4}_{Z-2}Y) + B(^4_2He) - B(^A_ZX). \tag{2.7}$$

Because of its high binding energy ($B(^4_2He) = 28.3\,\mathrm{MeV}$), the emission of α particle is preferred over other light particles. Alpha decay is energetically allowed for nuclei with $A \gtrsim 150$, but it can also be observed for neutron-deficient nuclei in the vicinity of ^{100}Sn [Van18].

Under the assumption of the parent nucleus being at rest, the released energy can be derived from the energy conservation law using the nuclear masses of involved nuclei m_X, m_Y, and m_α as follows:

$$Q_\alpha = (m_X - m_Y - m_\alpha)c^2 = E_Y + E_\alpha. \tag{2.8}$$

The released energy is distributed between the daughter nucleus and α particle as their respective kinetic energies E_Y and E_α. The Q value of α decay can be expressed in the same way in terms of atomic masses; a small difference in electron binding energies for each atom can be neglected.

Alpha decay is a two-body process, therefore, according to the momentum conservation law, the momenta of both — daughter nucleus and the α particle — are equal, but of opposite directions:

$$p_Y = p_\alpha. \tag{2.9}$$

Considering low energies of α particles ($\sim 4-12\,\mathrm{MeV}$), non-relativistic formula for kinetic energy $E = \frac{p^2}{2m}$ can be used. Equations (2.8) and (2.9) then give the following for the energy of released α particle:

$$E_\alpha = \frac{Q_\alpha}{1 + \frac{m_\alpha}{m_Y}} \approx Q\frac{A-4}{A}, \tag{2.10}$$

where A is the mass number of the mother nucleus. The remaining part of the Q value is the recoil of the daughter nucleus.

$$E_Y = Q_\alpha \frac{m_\alpha}{m_Y + m_\alpha} \approx Q_\alpha \frac{4}{A}. \tag{2.11}$$

In general, the α particle carries away about 98% of the energy released in the decay [Kra88].

Both the α particle and daughter nucleus are charged particles, therefore, α particle needs to overcome a Coulomb barrier $V_C(r)$:

$$V_C(r) = \frac{1}{4\pi\varepsilon_0} \frac{2Z_Y e^2}{r} \tag{2.12}$$

where r is distance between the α particle and center of daughter nucleus with proton number Z_Y. The height of the Coulomb barrier is greater than the energy of α particle (for example, 28 MeV and 4.2 MeV, respectively, for the decay of ^{238}U), therefore, the α particle is emitted from the nucleus in the process of quantum tunnelling [Lov06]. This process is illustrated in Fig. 2.1.

According to the theory of α decay [Gam28; Gur28], the pre-formed α particle repeatedly hits the potential barrier with the frequency f and with a probability P to penetrate this barrier at each hit:

$$\lambda_\alpha = fP. \tag{2.13}$$

Corresponding frequency can be estimated from its velocity and nuclear radius R [Lov06]:

$$f = \frac{v}{2R} = \frac{1}{2R}\sqrt{\frac{2V_0 + Q_\alpha}{\mu}}, \tag{2.14}$$

where V_0 is the depth of a nuclear potential well and μ is the reduced mass of α particle and the daughter nucleus :

$$\mu = \frac{m_\alpha m_Y}{m_\alpha + m_Y}. \tag{2.15}$$

The probability of penetrating the barrier can be expressed using the Gamow factor G:

$$P = e^{-2G}, \tag{2.16}$$

which is given as:

$$G = \frac{\sqrt{2\mu}}{\hbar} \int_R^b \sqrt{V(r) - Q_\alpha}\, dr. \tag{2.17}$$

The upper integration bound b is the distance at which the barrier height $V(r)$ equals the energy of the α particle (see Fig. 2.1) [Kra88; Hod97].

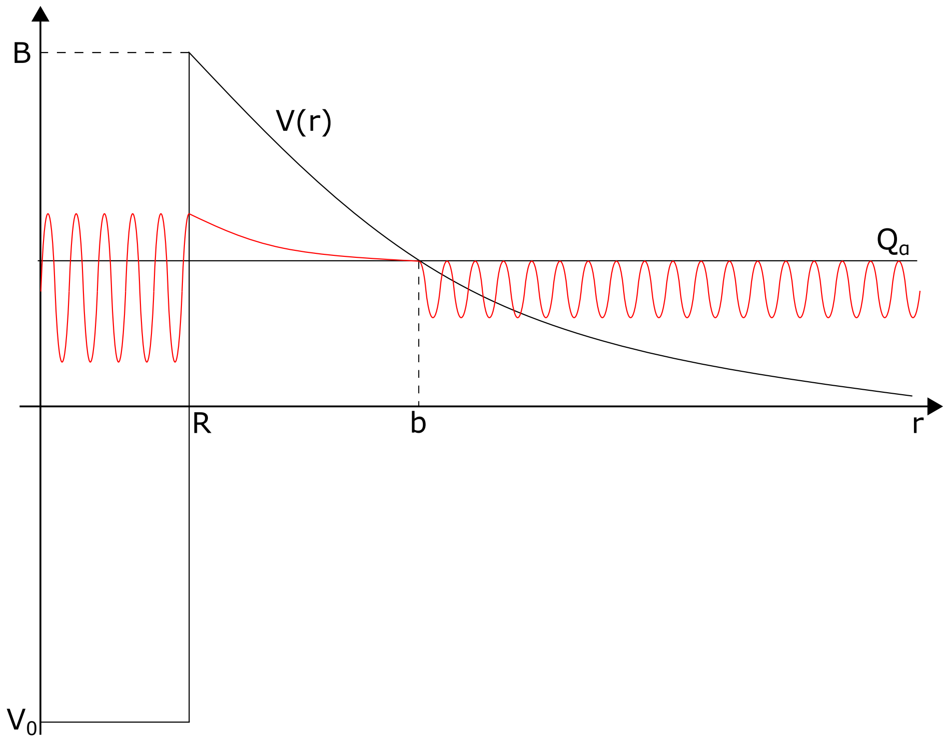

Figure 2.1: A schematic representation of α particle tunnelling through the Coulomb barrier of height B. The depth of nuclear potential is denoted as V_0. The effective width of this barrier (distance from the nuclear radius R to the α-particle separation point b) greatly depends on the energy of the decay Q_α, influencing the half-life of α decay.

Previous equations result in the following formula:

$$logT_{1/2} = a(Z) + \frac{b(Z)}{\sqrt{Q_\alpha}}, \tag{2.18}$$

where $a(Z)$ and $b(Z)$ are constants for each element. This formula, known as the Geiger-Nuttall law [Gei11], shows the extreme sensitivity of the α-decay half-life on the Q_α value.

Another important factor is the change in angular momentum between the initial (J_i) and final (J_f) states. If these values are not equal, the α particle carries away angular momentum l_α. In this case, the α particle needs to overcome an additional centrifugal potential:

$$V_l(r) = \frac{l_\alpha(l_\alpha + 1)\hbar^2}{2\mu r^2}. \tag{2.19}$$

The amount of angular momentum the α particle can carry is limited in the following way:

$$|J_i - J_f| \leq l_\alpha \leq J_i + J_f. \tag{2.20}$$

The spin of the α particle is 0, therefore, this angular momentum is purely orbital. The change of angular momentum is associated with the change of parity between the initial and final state of $\Delta\pi = (-1)^{l_\alpha}$. Thus, decays with even l_α result in the same parity of the initial and final state, while odd l_α changes parity [Lov06].

The α decay can populate several different final states in the daughter nucleus. The effective Q value for the decay to excited state Q_{ex} is lowered by the excitation energy of the state E_{ex}:

$$Q_{ex} = Q_{gs} - E_{ex}, \tag{2.21}$$

where Q_{gs} is Q_α for the decay to the ground state. For this reason, the energy spectrum of α decay often consists of several distinct peaks known as the fine structure of α decay. Because of the lower decay energy, Eq. (2.18) predicts a longer half-life and lower branching ratio for decay to the excited state. However, decay to an excited state may be favoured if its structure is similar to that of the mother nucleus. Thus, α decay can be effectively used to study nuclear structure [Kra88].

For this purpose, the hindrance factor HF of an α transition can be defined as the ratio of the measured partial half-life and its theoretical prediction:

$$\mathrm{HF} = \frac{T_{1/2,exp}}{T_{1/2,theo}}. \tag{2.22}$$

Transitions can be classified into the following categories based on their HF [Lov06]:

- HF = 1 − 4 for favoured decays between states with the same spin and parity. In the case of odd-A nuclei, the α particle is formed from nucleons occupying lower-lying orbits. Since the unpaired nucleon remains in its original orbit, the daughter nucleus is created in the excited state.

- HF = 4 − 10 suggests a favourable overlap or a mixing between the states involved in the transition.

- HF = 10−100 indicates an unfavourable overlap of wave functions with the parallel spin projections of the initial and final state.

- HF = 100 − 1000 for α decays changing parity, but still with parallel spin projections.

- HF > 1000 means a parity-changing transition with antiparallel spin projections.

The half-life of α decay is heavily dependent on its Q_α value. This dependence is removed when considering the reduced α-decay width δ_α^2. It is defined using the decay constant λ and barrier penetration factor P:

$$\delta_\alpha^2 = \frac{\lambda_\alpha h}{P}. \tag{2.23}$$

Reduced α-decay widths can be calculated using the method derived by Rasmussen [Ras59], involving the numerical calculation of the barrier penetration factor P given in Eqs. (2.16) and (2.17). The α particle needs to penetrate potential $V(r)$, which is a sum of the Coulomb potential $V_C(r)$, centrifugal potential $V_l(r)$, and nuclear potential $V_N(r)$ given as

$$V_N(r) = -1100 exp\left(-\frac{r - 1.17A^{1/3}}{0.574} \right) \text{MeV}. \tag{2.24}$$

The hindrance factor of the α decay can also be calculated using reduced widths

$$\text{HF} = \frac{\delta_{\alpha,ref}^2}{\delta_\alpha^2}, \tag{2.25}$$

where $\delta_{\alpha,ref}^2$ is the average value of the reduced widths of unhindered decays in the neighbouring nuclei.

2.1.2 Beta decay

During the β decay, a neutron in the nucleus is transformed into a proton or vice versa, increasing or decreasing its atomic number Z by 1. The mass number A is not changed in this decay. There are three types of decay referred to as β decay [Hod97]:

- β^- decay occurs in neutron-rich isotopes in which a neutron n is converted to a proton p, electron e^-, and electron antineutrino $\bar{\nu}_e$ while the latter two are emitted from the nucleus:

$$^A_Z X_N \rightarrow {}^{A}_{Z+1}Y_{N-1} + e^- + \bar{\nu}_e. \tag{2.26}$$

- β^+ decay occurs in neutron-deficient isotopes in which a proton p is converted to a neutron n, positron e^+, and electron neutrino ν_e while the latter two are emitted from the nucleus:

$$^A_Z X_N \rightarrow {}^{A}_{Z-1}Y_{N+1} + e^+ + \nu_e. \tag{2.27}$$

- Electron Capture (EC) occurs in neutron-deficient isotopes in which the nucleus captures an electron e^- from an atomic shell and a proton p is converted to a neutron n while only an electron neutrino ν_e is emitted from the nucleus:

$$ {}^{A}_{Z}X_N + e^- \rightarrow {}_{Z-1}^{\ A}Y_{N+1} + \nu_e. \tag{2.28} $$

The released energy Q_β can be expressed in terms of atomic masses of parent and daughter nucleus (m_X and m_Y respectively) and mass of electron m_e in the following way for each type of β decay [Kra88]:

$$ Q_{\beta^-} = [m_X - m_Y]c^2, \tag{2.29} $$

$$ Q_{\beta^+} = [m_X - m_Y - 2m_e]c^2, \tag{2.30} $$

$$ Q_{EC} = [m_X - m_Y]c^2 - B_n. \tag{2.31} $$

The difference in binding energies of electrons in the atomic shell between the parent and the daughter atom was neglected. In the case of EC, the atom is left in an excited state with an excitation energy equal to the binding energy of the captured electron B_n. The created vacancy in the atomic shell is filled by an electron from a higher orbital, which is accompanied by the emission of characteristic X rays. Alternatively, Auger or Coster-Krönig electron can be emitted.

Both β^+ decay and EC lead to the same daughter nucleus, however, as can be seen from Eqs. (2.30) and (2.31), there is a difference in Q value of $2m_ec^2 - B_n$ in favour of EC. Term $2m_ec^2 \cong 1.022\,\text{MeV}$ is much greater than B_n, thus, there are nuclei for which EC is energetically allowed ($Q_{EC} > 0$) while the β^+ decay is not ($Q_{\beta^+} < 0$).

In the case of β^- and β^+ decays, the decay energy (Q) and momentum are distributed among the daughter nucleus and two emitted particles. Because of this, the energy spectrum of the electron, respectively positron, is continuous with the endpoint at Q_β, as opposed to the α decay. For the endpoint energy consideration, the recoil energy of the daughter nucleus can be neglected because of its significantly higher mass in comparison to the electron and neutrino. In the case of EC, a neutrino with kinetic energy equal to Q_{EC} is always emitted due to the two-body nature of this decay.

Previous Eqs. (2.29) - (2.31) are valid for decay between the ground states of the nuclei. In the case of β decay to the excited state of the daughter nucleus, the effective Q value Q_{ex} is lower than that for decay to the ground state Q_{gs} [Kra88]:

$$ Q_{ex} = Q_{gs} - E_{ex}. \tag{2.32} $$

where E_{ex} is the excitation energy of this excited state. The excitation energy is usually emitted in the form of γ radiation (see section 2.1.3). Measurement of these γ quanta allows us to obtain information about the structure and properties of both decaying and populated states, since β decay is sensitive to changes in nuclear structure, as will be discussed later in this section.

Besides energy conservation, angular momentum is conserved in β decay. The change of total angular momentum between parent and daughter nucleus (J_i and J_f, respectively) can be expressed in the following way:

$$\Delta\vec{J} = \vec{J}_i - \vec{J}_f = \vec{L} + \vec{S}. \tag{2.33}$$

where $\vec{L}$ is the orbital angular momentum carried away by the emitted electron and neutrino, and $\vec{S}$ is the sum of their spins [Lil01].

In the allowed approximation of the theory of β decay, emitted leptons do not carry away any orbital angular momentum, thus, $L = 0$ (the so-called allowed decay). In this case, the change of the total angular momentum is only caused by S. Intrinsic spin of both electron and neutrino is $s = 1/2$, therefore, their sum can be either $S = 0$, in case they are antiparallel, or $S = 1$ for spins in parallel. Decays with $S = 0$ are called Fermi decays, and those with $S = 1$ are Gamow-Teller decays. This means that for allowed decay, the total angular momentum of the daughter nucleus can be either the same as the one of the parent nucleus, or it can differ by 1. In the case of orbital angular momentum being carried away, the parity of the initial and final state changes in the following way:

$$\pi_f = (-1)^L \pi_i. \tag{2.34}$$

which means that parity is not changed in the allowed decay. This results in the following selection rules for allowed decay:

$$\Delta J = 0, 1 \qquad \Delta\pi = +1. \tag{2.35}$$

Specifically, β decays between two 0^+ states ($\Delta J = 0, L = 0, S = 0$) are referred to as superallowed decays.

Decays not following selection rules for allowed decays are the so-called forbidden decays, which, although not strictly forbidden, occur with lower probability. For these decays, both the change of parity and non-zero change of orbital angular momentum are possible. In the case of the first forbidden decay, the electron and neutrino carry away orbital angular momentum $L = 1$. Coupling with the spin of the lepton pair allows a change of total angular momentum of $\Delta J = 0, 1, 2$, therefore, the selection rules for this decay are:

$$\Delta J = 0, 1, 2 \qquad \Delta\pi = -1. \tag{2.36}$$

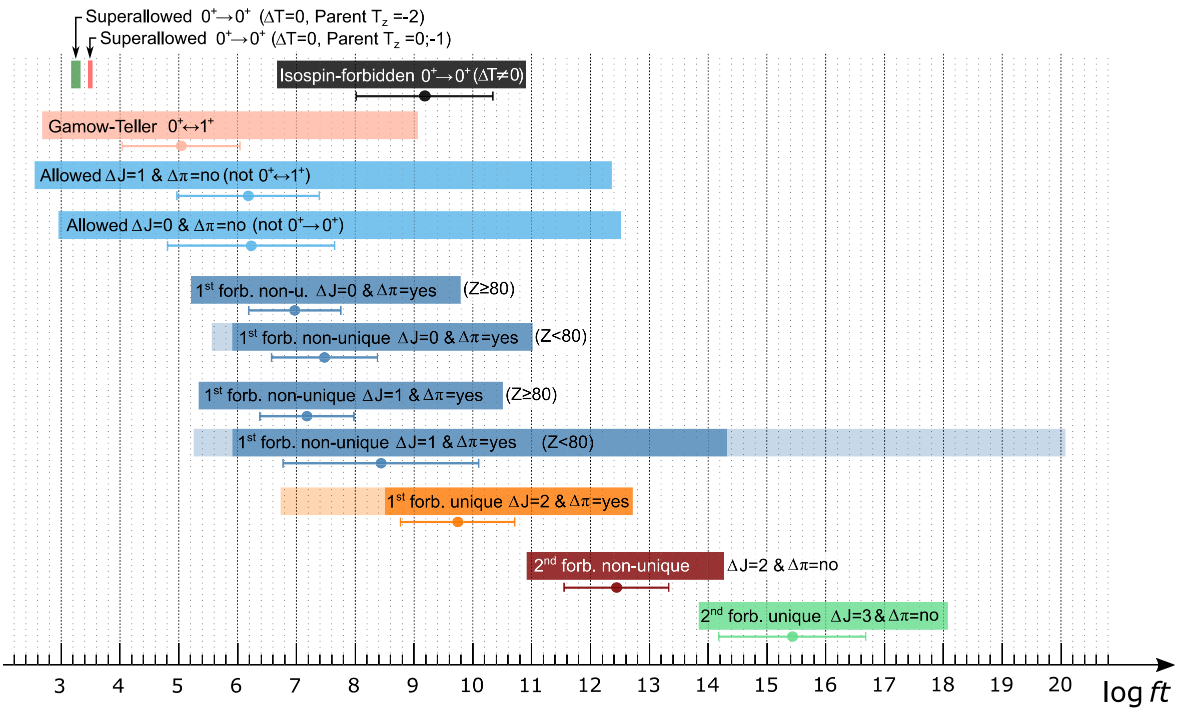

Figure 2.2: A systematics of log ft values in β decay. The figure was taken from Ref. [Tur23].

The second forbidden decay happens when $L = 2$ and the selection rules:

$$\Delta J = 2, 3 \qquad \Delta\pi = +1. \tag{2.37}$$

Similarly, third, fourth and higher degrees of forbidden decays are possible. Forbidden decays with the highest ΔJ possible for a given forbiddenness are referred to as unique decays, such as first forbidden unique decay with $\Delta J = 2$ and $\Delta\pi = -1$ or second forbidden unique decay with $\Delta J = 3$ and $\Delta\pi = +1$ [Kra88].

To compare β decays of different nuclei, the comparative half-life, or the so-called ft value, is used. It is a product of the partial half-life of the decay t and the Fermi integral f. Using the Fermi integral for allowed and first forbidden non-unique decays, the f_0t value can be expressed as:

$$f_0t = ln2\frac{2\pi^3\hbar^7}{G_F^2(B_F + B_{GT})m_e^5c^4}, \tag{2.38}$$

where G_F is the strength constant of the weak interaction, and B_F and B_{GT} are the Fermi and Gamow-Teller reduced transition probabilities, respectively. They are given as:

$$B_F = \frac{g_V^2}{2J_i + 1}|M_F|, \qquad B_{GT} = \frac{g_A^2}{2J_i + 1}|M_{GT}|, \tag{2.39}$$

where g_V^2 and g_A^2 are vector and axial-vector coupling constants of the weak interaction, and matrix elements $|M_F|$, $|M_{GT}|$ express similarity in wave functions of the initial and final state of the decay. The Fermi integral needs to be modified for other types of β decays. For the first forbidden unique decay, the corresponding $f_1 t$ value is given as follows:

$$f_1 t = 12 \times ln2 \frac{2\pi^3 \hbar^7}{G_F^2 B_{1u} m_e^5 c^4}, \tag{2.40}$$

where B_{1u} is the reduced transition probability for the first forbidden decay with corresponding matrix element [Suh07].

Since the half-lives of β decays span several orders of magnitude, the logarithm of the ft value is more commonly used. The ranges of experimental log ft values are different for allowed and forbidden β decays, as can be seen in Fig. 2.2. Therefore, systematics of log ft values, compiled for example in Ref. [Sin98], or the more recent one in Ref. [Tur23], can be used to assign spins and parities in nuclei if the assignment for either the initial or final state is known. However, intervals of log ft values for different types of transitions are overlapping, therefore, a log ft value of a particular unknown decay may be within the range of several different transition types. As can be seen in Fig. 2.2, each decay type has a lower limit in log ft values. If a new transition has a log ft value lower than the reliably established lower limit for a certain decay type, it can be assigned a forbiddenness category of a lower order. In this way, the maximal change of angular momentum in an unknown transition can be deduced [Ram73].

2.1.3 Internal transitions

Nuclei created in radioactive decay are often in excited states. The most common ways to lower their excitation energy and reach the ground state are the emission of γ quanta and internal conversion.

Gamma decay

When a nucleus transitions from a state with energy E_i to a state with energy E_f, the energy difference $\Delta E = E_i - E_f$ is released and distributed between the emitted γ ray and the recoiling nucleus according to the momentum and energy conservation laws:

$$\Delta E = E_\gamma + T_N = E_\gamma + \frac{E_\gamma^2}{2Mc^2}, \tag{2.41}$$

where M is the mass of the nucleus. Using approximation $(\Delta E)^2 \approx E_\gamma^2$, since $E_\gamma \ll Mc^2$, we get

$$E_\gamma \approx \Delta E - \frac{(\Delta E)^2}{2Mc^2}. \tag{2.42}$$

The energy recoiling nucleus receives is very small (~ 12 eV for nucleus with mass $A = 182$ and $E_\gamma = 2$ MeV) compared to the typical precision of γ-ray spectroscopy measurements (~100 eV), therefore, it can be neglected and $E_\gamma \approx \Delta E$ is standardly used [Hod97].

Electromagnetic radiation, including γ radiation, can be of either electric (E) or magnetic (M) character. The multipolarity of a photon is defined by the angular momentum it carries. A photon with $L = 1$ is called a dipole, $L = 2$ is a quadrupole and so on, in general, a photon with angular momentum L is called 2^L-pole. Because of this, electromagnetic transitions are denoted by their type and angular momentum as EL or ML, for example, $E2$ refers to an electric quadrupole. Due to the angular momentum conservation law, when a nucleus with angular momentum J_i transitions to a state with angular momentum J_f, the angular momentum of the emitted photon is restricted by this selection rule:

$$|J_i - J_f| \leq L \leq J_i + J_f. \tag{2.43}$$

The lowest possible value of L is $L = 1$, since there are no photons with zero angular momentum. Therefore, for transitions between two 0^+ states ($E0$ transitions), emission of γ ray is not possible. These states decay via internal conversion, which will be discussed later in this section. In rare cases, emission of two γ quanta is possible. Additionally, in the case the energy difference ΔE is larger than $2m_ec^2 \cong 1022$ keV, an electron-positron pair can be created and emitted [Hod97].

The parity of the photon depends on both its angular momentum and character. The same multipoles of different characters have opposite parity. The change of parity for a given multipole and character of the transition is given in the following way [Lov06]:

$$\text{Electric transition:} \qquad \pi_f = (-1)^L \pi_i, \tag{2.44}$$

$$\text{Magnetic transition:} \qquad \pi_f = (-1)^{L+1} \pi_i, \tag{2.45}$$

where π_i and π_f are parities of the initial and final state, respectively.

The probability of γ ray emission varies with regard to transition character, energy and carried angular momentum. Decay constants for both electric $\lambda(EL)$ and magnetic $\lambda(ML)$ transitions can be expressed by the following Weisskopf single-particle estimates:

$$\lambda(EL) \cong \frac{4.4(L+1)}{L[(2L+1)!!]^2}\left(\frac{3}{L+3}\right)^2\left(\frac{E_\gamma}{197}\right)^{2L+1} R^{2L} \times 10^{21}, \tag{2.46}$$

$$\lambda(ML) \cong \frac{1.9(L+1)}{L[(2L+1)!!]^2}\left(\frac{3}{L+3}\right)^2\left(\frac{E_\gamma}{197}\right)^{2L+1} R^{2L-2} \times 10^{21}. \tag{2.47}$$

For γ-ray energy E_γ in MeV and for nuclear radius $R = 1.2A^{1/3}$ in fm, resulting decay constants are in s^{-1} [Wei51].

Based on these estimates, we can expect higher emission probability for lower multipoles and higher transition energy, an increase of L by 1 decreases transition probability by about 5 orders of magnitude. The ratio between the electric and magnetic decay constant for a given multipolarity and energy is

$$\frac{\lambda(E)}{\lambda(M)} \approx 2.3R^2 \approx 2.9A^{2/3}, \tag{2.48}$$

thus, electric transitions are more probable in comparison to magnetic ones by approximately an order of 100. Therefore, we can deduce that the lowest permitted multipole usually dominates for a given transition, but in case this multipole is of magnetic character, an admixture of a higher electric multipole may be present. This gives rise to transitions with mixed multipolarity, for example, $M1+E2$ [Kra88].

Internal conversion

Internal conversion is an alternative way for a nucleus to decrease its excitation energy. This process occurs when the nucleus transfers its excitation energy directly (without photon emission) to an orbital electron, which is ejected. Kinetic energy T_e of this conversion electron (CE) is given by

$$T_e = \Delta E - B_e, \tag{2.49}$$

where ΔE is energy of transition and B_e is binding energy of emitted CE. Electrons from different atomic shells can be emitted, resulting in several distinct lines in the electron energy spectrum. Each of these lines is referred to according to the principal quantum number n of the ejected electron, K for $n = 1$, L for $n = 2$, M for $n = 3$, and so on. Binding energies of electrons from individual orbitals of a given shell are different, thus, for example, L_1, L_2, and L_3 electrons can be emitted from the second shell with slightly different energies. The electron binding energy of each shell is a lower threshold energy for internal conversion, therefore, for low-energy transitions, only electrons from higher shells can be emitted.

Emitted CE leaves a vacancy in the atomic shell, which is filled by an electron from the higher shell. The energy difference between the binding energies of these two electrons is released in the form of a characteristic X-ray. Alternatively, Auger or Coster-Krönig electron is emitted [May79].

The internal conversion coefficient (ICC) α characterises the competition between the internal conversion and γ-ray emission. It is defined in the following way:

$$\alpha = \frac{N_{IC}}{N_\gamma} = \frac{\lambda_{IC}}{\lambda_\gamma}, \tag{2.50}$$

where N_{IC} and N_γ are measured numbers of transitions via internal conversion (emitted CEs) and γ-ray emission, respectively, and λ_{IC} and λ_γ are respective partial decay constants. Similarly, the internal conversion coefficient can be defined individually for CEs from each shell. The total internal conversion coefficient can be written as a sum of coefficients for all shells:

$$\alpha = \alpha_K + \alpha_L + \alpha_M + \ldots \tag{2.51}$$

The total decay constant of the internal transition process can then be written as

$$\lambda = \lambda_\gamma(1 + \alpha). \tag{2.52}$$

The internal conversion coefficient can be approximately calculated for given multipole L of electric and magnetic transitions using these formulae:

$$\alpha(EL) \cong \frac{Z^3}{n^3}\left(\frac{L}{L+1}\right)\left(\frac{e^2}{4\pi\varepsilon_0\hbar c}\right)^4\left(\frac{2m_ec^2}{\Delta E}\right)^{L+5/2} \tag{2.53}$$

$$\alpha(ML) \cong \frac{Z^3}{n^3}\left(\frac{e^2}{4\pi\varepsilon_0\hbar c}\right)^4\left(\frac{2m_ec^2}{\Delta E}\right)^{L+3/2} \tag{2.54}$$

where Z is the atomic number, n is principal quantum number of ejected CE and $e^2/4\pi\varepsilon_0\hbar c \approx 1/137$ is the fine structure constant [Lov06].

Previous equations show the great significance of the internal conversion process for heavy nuclei, as ICC increases with Z^3. The internal conversion coefficient decreases with the increase of transition energy, which is the opposite behaviour to that for γ-ray emission. Internal conversion gets more important for higher multipoles, in these cases, it can even become the dominant process of deexcitation. Furthermore, it is crucial for transitions between two 0^+ states, for which γ-ray emission is forbidden [Kra88].

$E0$ transitions

Electric monopole transitions ($E0$) connect two states with the same spin and parity. As was already mentioned, in the case of two 0^+ levels, the emission of γ rays is forbidden. Other $I^\pi \to I^\pi$, $I \neq 0$ transitions usually proceed via a mixed $E0 + M1 + E2$ transition and both γ rays and CEs are emitted. The internal conversion coefficient for a given shell in such a case can be written using the intensity of conversion electrons (e.g. I_K) and γ rays I_γ for each multipolarity [Dow20]:

$$\alpha_K(E0 + M1 + E2) = \frac{I_K(M1) + I_K(E2) + I_K(E0)}{I_\gamma(M1) + I_\gamma(E2)}. \tag{2.55}$$

This equation can be written as

$$\alpha_K(E0 + M1 + E2) = \frac{\alpha_k(M1) + \delta^2(E2/M1)[1 + q_K^2(E0/E2)]\alpha_K(E2)}{1 + \delta^2(E2/M1)} \tag{2.56}$$

using the ICCs for pure $M1$ and $E2$ transitions. Mixing ratios $\delta^2(E2/M1)$ and $q_K^2(E0/E2)$ are defined as [Chu58; Lan82]

$$\delta^2(E2/M1) = \frac{I_\gamma(E2)}{I_\gamma(M1)} \tag{2.57}$$

and

$$q_K^2(E0/E2) = \frac{I_K(E0)}{I_K(E2)}. \tag{2.58}$$

The $\delta^2(E2/M1)$ mixing ratio can be experimentally extracted from the measurement of γ-γ angular correlations or the angular distribution of γ rays from oriented nuclei. The definition of $q_K^2(E0/E2)$ can be extended also for pure $E0$ ($0^+ \to 0^+$) transitions without an $E2$ component using $I_K(E2)$ from the $E2$ ($0^+ \to 2^+$) transition deexciting the same initial level [Kib22].

The $E0$ transitions are an important indication of changes in nuclear shape. Such transitions are a good probe of shape coexistence (see Chapter 2.4) and mixing between two states of different deformation. This is expressed in monopole transition strength $\rho^2(E0)$ [Woo99; Kib22]

$$\rho^2(E0) = \alpha^2\beta^2(\Delta\langle r^2\rangle)^2\frac{Z^2}{R^4}, \tag{2.59}$$

where α^2 and β^2 ($\alpha^2 + \beta^2 = 1$) are mixing amplitudes of two configurations, $R = 1.2A^{1/3}$ fm is the nuclear radius, and $\Delta\langle r^2\rangle$ is the difference in the mean-square charge radii of the initial and final state.

Monopole strength $\rho^2(E0)$ can also be obtained experimentally as

$$\rho^2(E0) = q_K^2(E0/E2)\frac{\alpha_K(E2)}{\Omega_K(E0)}W_\gamma(E2) = \frac{I_K(E0)}{I_K(E2)}\frac{\alpha_K(E2)}{\Omega_K(E0)}\frac{b(E2)ln2}{T_{1/2}}. \tag{2.60}$$

The $E2$ transition rate $W_\gamma(E2)$ was expressed using the branching ratio of this transition $b(E2)$ and half-life $T_{1/2}$ of the initial excited state. The quantity $\Omega_K(E0)$ is electronic factor of $E0$ transition, which can be calculated using BrIcc [Kib08; Dow20]. Values of monopole strength usually lie in the range 10^{-3} to 10^{-1}, therefore, $10^3 \cdot \rho^2(E0)$ is usually reported [Kib22].

2.1.4 γ-ray spectroscopy after β decay

As was mentioned in Chapter 2.1.2, β decay is sensitive to changes in nuclear structure, which is commonly displayed via log ft values that can be used to estimate the magnitude of spin change in the decay. Their experimental determination requires the knowledge of a partial half-life of β decay to a particular level in the daughter nucleus, which can be obtained from the β decay branching ratio of the mother nucleus b_β and direct β-decay feeding intensity I_β into this state (see Eq. (2.5)). Because of the continuous nature of the β-particle energy spectrum, I_β cannot be extracted from the measurement of the emitted electrons or positrons. Instead, γ-ray spectroscopy is employed and transitions deexciting the populated states are measured. Once the level scheme of the daughter isotope is built using, for example, the γ-γ coincidence method, the β-decay feeding intensities can be calculated as the difference in transition intensities feeding and depopulating each level [Rub09]. Log ft values determined using γ-ray spectroscopy have been successfully used to estimate spins and parities of excited levels in many nuclei, for example, in ^{180}Tl [Els11], ^{66}Mn and its decay products [Str18], ^{207}Tl [Ber20] and ^{216}Bi [And24].

Gamma-ray spectroscopy usually uses germanium detectors, such as HPGe (high-purity germanium), thanks to their high energy resolution. Their drawback is the significant decrease in detection efficiency with an increasing γ-ray energy. Therefore, such measurements are influenced by the so-called pandemonium effect [Har77]. This occurs when low-intensity and high-energy transitions are not observed because of the low experimental sensitivity. The pandemonium effect is the most prominent for relatively low-lying levels in decays with high Q_β values. Unobserved feeding by γ-ray transitions from higher-lying levels in the daughter nucleus causes an artificial increase of the apparent β-decay feeding intensity calculated as the difference in the intensity of transitions populating and depopulating the level, see Fig. 2.3.

An alternative method is the total absorption spectroscopy (TAS). Instead of germanium detectors, large-volume scintillators with 4π solid angle coverage are used, offering excellent detection efficiency. Rather than individual γ rays, the full emitted cascade is detected, directly giving information on the β-decay feeding intensity. However, because of the poor energy resolution, TAS measurements cannot, in general,

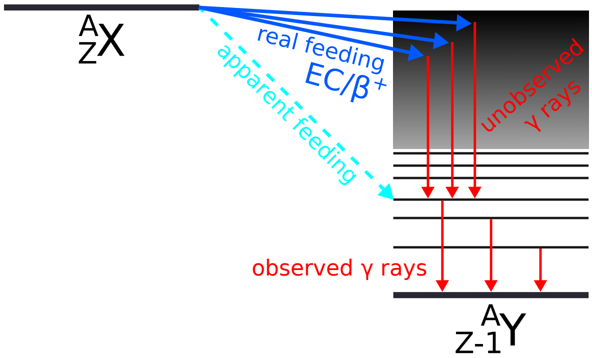

Figure 2.3: A schematic representation of the pandemonium effect. High-energy and low-intensity transitions may not be detected, increasing apparent β-decay feeding intensity for low-lying levels in the daughter isotope.

determine feeding intensity into individual levels, only its global distribution [Alg18; Alg21].

2.2 Nuclear shape

The shape of the nucleus can be expressed by its radius R as follows:

$$R(\theta,\phi) = R_0\left(1 + \sum_{l=2}^{\infty}\sum_{\mu=-\lambda}^{\lambda} a_{\lambda\mu} Y_{\lambda\mu}(\theta,\phi)\right), \tag{2.61}$$

where R_0 is the average nuclear radius, θ and ϕ are spherical coordinates and $a_{\lambda\mu}$ are amplitudes of corresponding spherical harmonic functions $Y_{\lambda\mu}$ of degree λ (multipole) and order of μ [Hod97].

Note that summing starts from the value $\lambda = 2$. For $\lambda = 0$, we get a spherical nucleus, which is expressed by the term R_0. The dipole term ($\lambda = 1$) is not a true deformation, it represents a periodical shift in the centre of mass of the nucleus, which can happen only under the effect of an external force. The simplest deformation of the nucleus is, therefore, a quadrupole deformation with $\lambda = 2$. This deformation gives the nucleus an ellipsoidal shape. Octupole deformation ($\lambda = 3$) leads to pear-shaped nuclei [Lil01].

Spherical harmonics amplitudes for the quadrupole deformation can be expressed in terms of β and γ parameters:

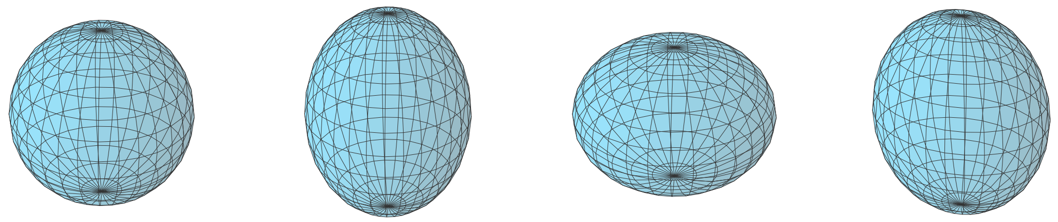

Figure 2.4: A schematic representation of the spherical and quadrupole (prolate, oblate and triaxial) shapes of nuclei.

$$a_{20} = \beta cos(\gamma), \tag{2.62}$$

$$a_{21} = a_{2-1} = 0, \tag{2.63}$$

$$a_{22} = a_{2-2} = \frac{1}{\sqrt{2}}\beta sin(\gamma). \tag{2.64}$$

Values $\gamma = n\pi/3$ lead to axially symmetric nuclei. In this case, the deformation parameter β_2 can be defined, expressing the magnitude of deformation along the major axis. It is given in the following way [Kra88]:

$$\beta_2 = \frac{4}{3}\sqrt{\frac{\pi}{5}}\frac{\Delta R}{R_{av}} \approx 1.06\frac{\Delta R}{R_{av}}, \tag{2.65}$$

where ΔR is the difference between the semimajor and semiminor axes of the ellipse and R_{av} is the average radius of the nucleus. Based on the value of this parameter, the nucleus can have one of two distinct shapes. The first one is the prolate shape with one axis longer than the remaining two for $\gamma = 0°$ (also $\gamma = 120°$ and $\gamma = 240°$), giving $\beta_2 > 0$. The second one is the oblate shape with one axis shorter than the remaining two for $\gamma = 60°$ ($\gamma = 180°$, $\gamma = 300°$) and $\beta_2 < 0$. Other values of the γ parameter lead to triaxially deformed nuclei. These shapes are compared to the spherical one in Fig. 2.4.

2.3 Nuclear models

2.3.1 Liquid drop model

The liquid drop model was the first nuclear model to explain some of the nuclear properties successfully. This model describes the nucleus as a sphere of incompressible charged liquid. Such a concept led to the development of the semi-empirical Bethe-Weizsäcker formula for the binding energy of the nucleus [Wei35]:

$$B(A,N) = a_V A - a_S A^{2/3} - A_C \frac{Z(Z-1)}{A^{1/3}} - a_{Sym} \frac{(A-2Z)^2}{A} \pm a_P A^{-3/4} \qquad (2.66)$$

with parameters a_V, a_S, a_C, a_{Sym} and a_P. Their values $a_V = 15.5$ MeV, $a_S = 16.8$ MeV, $a_C = 0.72$ MeV, $a_{Sym} = 23$ MeV and $a_P = 34$ MeV [Kra88] were empirically obtained by fitting the experimental data, see Fig. 2.5. The first term is the volume term, which is the contribution to the binding energy from each nucleon. The nuclear force is a short-range interaction, therefore, each nucleon interacts only with its closest neighbours, giving linear dependence on A. The second term, known as the surface term, is a correction to the volume term. Nucleons on the surface are less bound as other nucleons do not fully surround them, decreasing the binding energy of the whole nucleus. The third term expresses Coulomb repulsion between positively charged protons. The range of this interaction is infinite, and each proton therefore interacts with all of the others, giving $Z(Z-1)$ dependence. The symmetry term expresses increased instability of the nuclei with an excess of either protons or neutrons. The last term is the pairing term, accounting for the tendency of nucleons to form spin-coupled pairs. This term is positive for even-even nuclei, negative for odd-odd nuclei and zero for odd-mass nuclei [Lov06].

2.3.2 Spherical Shell model

Several nuclear properties, such as abundance in nature, binding energies per nucleon or two-proton and two-neutron separation energies, show sudden changes at specific proton Z and neutron N numbers, which cannot be described by the liquid drop model. These numbers are 2, 8, 20, 28, 50, 82, and 126, and are known as the so-called magic numbers. They are equivalent to the closed atomic shells of noble gases, and their existence indicates the shell properties of the atomic nucleus.

The shell model was independently developed by Mayer [May48; May49] and Haxel, Jensen and Suess [Hax49]. Similar to the atomic shell, the nuclear shell model describes the nucleus as independent nucleons occupying orbitals in a central potential. However, contrary to an atom, no central particle generates this potential. Instead, this mean-field potential results from an average of all nucleon-nucleon interactions. It is often described by the Woods-Saxon potential [Woo54]

$$V(r) = \frac{-V_0}{1 + e^{\frac{r-R}{a}}}, \qquad (2.67)$$

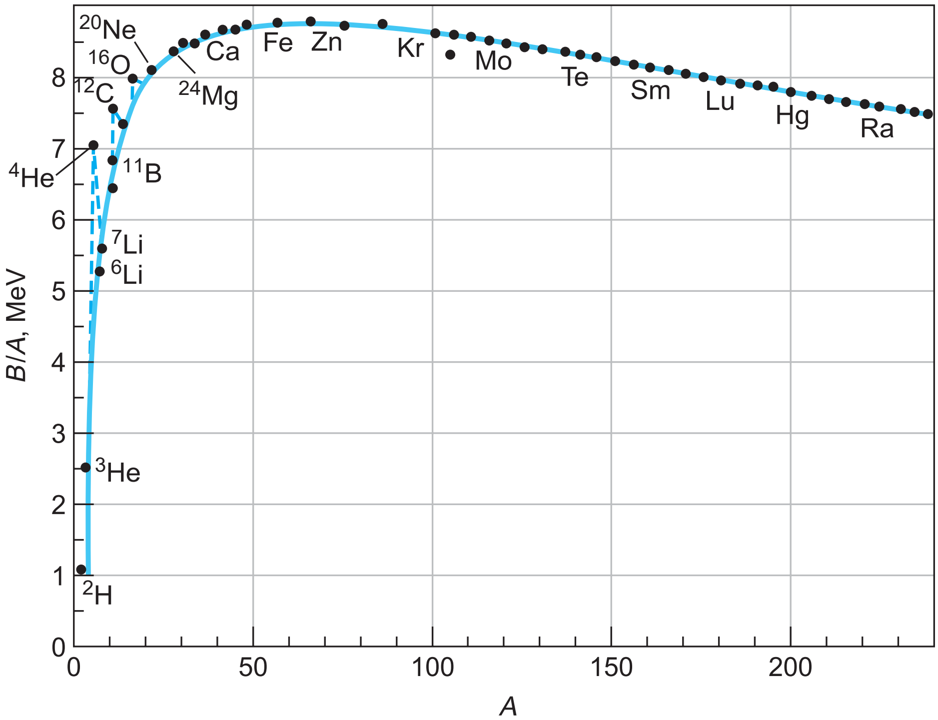

Figure 2.5: A plot of experimental values of binding energy per nucleon B/A. The solid blue line represents the Bethe-Weizsäcker formula. The figure was taken from Ref. [Tip08].

where V_0 (typically $\approx 50\,\mathrm{MeV}$) is the depth of the potential, R is the nuclear radius and $a \approx 0.5\,\mathrm{fm}$ is the surface thickness parameter [Eis70].

Solving the three-dimensional Schrödinger equation for this potential results in energy levels with specific values of orbital momentum l. Levels are labelled by their order for given l and by the l itself (s for $l = 0$, p for $l = 1$, d for $l = 2$, etc.). Since there are two possible values of intrinsic spin $s = \pm\frac{1}{2}$ and $2l + 1$ possible projections of l, the Pauli exclusion principle allows $2(2l+1)$ protons or neutrons to occupy the same level. In this way, the first three magic numbers can be reproduced.

An important term that needs to be added to the total potential is the spin-orbital interaction $V_{SO}(r)\vec{l}\cdot\vec{s}$. The total angular momentum of a nucleon $\vec{j} = \vec{l} + \vec{s}$ has two possible values, $j = l + \frac{1}{2}$ and $j = l - \frac{1}{2}$. Note that $j > 0$, therefore, only one possible value $j = \frac{1}{2}$ exists for the $l = 0$ case. Using $\vec{j}^2 = (\vec{l}+\vec{s})^2 = \vec{l}^2 + \vec{l}\cdot\vec{s} + \vec{s}^2$, the term $\vec{l}\cdot\vec{s}$ can be expressed in the following way:

$$\vec{l}\cdot\vec{s} = \frac{1}{2}(\vec{j}^2 - \vec{l}^2 - \vec{s}^2). \tag{2.68}$$

The expected value of this term is

$$\langle \vec{l} \cdot \vec{s} \rangle = \frac{1}{2}[j(j+1) - l(l+1) - s(s+1)]\hbar^2. \tag{2.69}$$

This causes the splitting of a single level into two based on the j value, with the $j = l + \frac{1}{2}$ state being pushed down and the $j = l - \frac{1}{2}$ orbital up in energy. The degeneracy of each level is $2j + 1$. The energy difference between levels is proportional to their l:

$$\langle \vec{l} \cdot \vec{s} \rangle_{j=l+1/2} - \langle \vec{l} \cdot \vec{s} \rangle_{j=l-1/2} = \frac{1}{2}(2l + 1)\hbar^2. \tag{2.70}$$

The shell model using the Woods-Saxon potential and spin-orbital interaction successfully explains all known magic numbers and predicts a new one for neutrons at 184 [Kra88; Lil01].

The shell model can effectively explain the spins and parities of nuclear ground states for spherical nuclei. Nucleons within the same shell form a $j = 0$ pair, therefore, even-even nuclei have $I = 0^+$ ground states. In the case of odd-even nuclei, the one unpaired proton or neutron defines the spin and parity of the whole nucleus [Kra88].

2.3.3 Deformed Shell model

The shell model assumes a spherically symmetric nucleus and nuclear potential. However, this is usually true only for nuclei near closed shells. Minimising energy often leads to a deformed shape of nuclei with partially filled shells. This is addressed in the deformed shell model (also known as the Nilsson model), introducing a quadrupole deformation perturbation to the nuclear potential [Nil55].

$$V = \frac{m}{2}(\omega_x^2 x^2 + \omega_y^2 y^2 + \omega_z^2 z^2) + Cls + Dl^2 \tag{2.71}$$

The constants C and D are selected to reproduce the shell model levels in the spherical limit. Oscillator frequencies ω_x^2, ω_y^2 and ω_z^2 for cylindrically symmetric potential are given as

$$\omega_x^2 = \omega_y^2 = \omega_0^2\left(1 + \frac{2}{3}\delta\right), \tag{2.72}$$

$$\omega_z^2 = \omega_0^2\left(1 - \frac{4}{3}\delta\right), \tag{2.73}$$

where ω_0^2 is the frequency of a spherical harmonic oscillator and δ is the Nilsson deformation parameter.

The angular momentum of a nucleon is no longer a good quantum number, therefore, Nilsson orbitals are labelled by new asymptotic quantum numbers $\Omega^{\pi}[Nn_z\Lambda]$. These quantum numbers are shown in Fig. 2.6. The quantum number Ω is the projection of a nucleon's total angular momentum j along the symmetry axis. This can be split into two parts, Λ - the projection of angular momentum l, and Σ - the projection of the intrinsic spin s. It is defined as $\Omega = \Lambda + \Sigma = \Lambda \pm 1/2$. N is the principal quantum number of the oscillator. It determines the parity of a Nilsson state as $\pi = (-1)^N$. The last quantum number is n_z, denoting the number of oscillator quanta along the symmetry axis. It relates to the main quantum number N such that $0 \leq n_z \leq N$.

Unlike in the shell model, individual particles experience different potentials depending on the orientation of their orbit relative to the symmetry axis. Because of this, the shell model levels with degeneracy $2j+1$ split into $(j+1/2)$ levels, each with the degeneracy of 2. A plot of the evolution of nucleon energy levels as a function of deformation is called a Nilsson diagram. The energy shift of Nilsson levels depends on the strength of their interaction with the deformed core. For prolate nuclei, this strength is the highest for the state with the lowest projection $\Omega = \frac{1}{2}$. The energy of this state is lowered with increasing deformation. On the other hand, the interaction of the $\Omega = j$ state with the core is the weakest, raising its energy. This trend is reversed for the oblate deformation [Cas90].

2.3.4 Collective models

In the nuclear shell model, a few valence nucleons are responsible for the properties of the whole nucleus. This approach successfully describes low-lying excited states in odd-odd and odd-even nuclei. However, some nuclear properties, such as rotational and vibrational spectra, cannot be described in such a way since they result from a collective motion of multiple nucleons.

Nuclear rotation

In quantum mechanics, the rotation of a spherical object is forbidden. However, in the case of the deformed nucleus, an axis of rotation can be defined, and the nucleus can rotate. In such nuclei, rotational angular momentum vector R is coupled with the intrinsic angular momentum of the nucleus J into its total angular momentum I (see Fig. 2.6):

$$I = R + J. \tag{2.74}$$

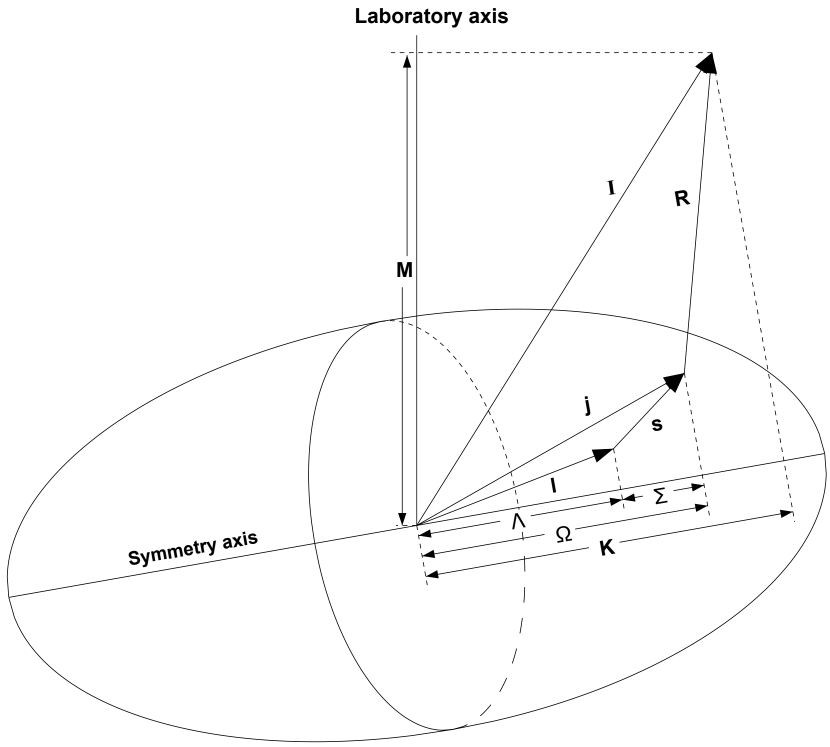

Figure 2.6: Asymptotic quantum numbers of the Nilsson model. Projections of angular momentum l, spin s and total angular momentum j of a nucleon along the symmetry axis are labelled as Λ, Σ and Ω, respectively. The total angular momentum of a nucleus I includes collective rotation R. Its projections into the symmetry axis and rotational axis are K and M, respectively. The figure was taken from Ref. [Fir96].

The rotational energy of a nucleus in a ground state with an angular momentum I is given in the following way:

$$E = \frac{\hbar^2}{2\mathcal{J}}[I(I+1) - K(K+1)], \tag{2.75}$$

where $\mathcal{J}$ is the nuclear moment of inertia and K is the projection of the nuclear angular momentum, as shown in Fig. 2.6. An increase in the angular momentum leads to a band of states built on top of a bandhead with increasing excitation energy. The angular momentum of each band member increases by $1\hbar$, and the parity of the bandhead gives their parity [Cas90].

In the rigid rotor approximation, the moment of inertia of the ellipsoid is

$$\mathcal{J}_{rig} = \frac{2}{5}MR_{av}^2(1 + 0.31\beta_2), \tag{2.76}$$

where M and R_{av} are the nuclear mass and average radius, respectively, and β_2 is the quadrupole deformation parameter defined in Eq. (2.65). The atomic nucleus is not a rigid system, and some degree of fluidity is present, decreasing the nuclear moment of inertia. Experimental values of $\mathcal{J}$ vary from 0.2 to 0.5 of the value for the rigid rotor [Hod97].

Collective rotation can also be observed for excited states, for example, originating from single-particle excitation. In such a case, the excitation energy of this state needs to be added to the energy of each rotational state. Because of this, several rotational bands can be observed in a given nucleus, each built on top of a different intrinsic excited state [Cas90].

The Eq. (2.75) can be simplified for ground states of even-even nuclei with $J = K = 0$:

$$E = \frac{\hbar^2 I(I+1)}{2\mathcal{J}}. \tag{2.77}$$

Mirror symmetry of the nucleus in this case allows only rotational states with even values of I [Kra88].

For higher values of I, a deviation between the predicted and observed energies emerges. This is explained as the effect of the centrifugal force stretching the nucleus and increasing its moment of inertia. Therefore, the previous equation needs to be modified as follows:

$$E = \frac{\hbar^2}{2\mathcal{J}}[I(I+1) - \alpha, I^2(I+1)^2]. \tag{2.78}$$

where α is an empirical parameter used to fit experimental energies [Hod97].

Nuclear vibration

Vibration is a periodic change in nuclear shape around an equilibrium state. This can be expressed by modifying the Eq. (2.61) and adding time dependence to the amplitudes of spherical harmonics $a_{\lambda\mu}(t)$:

$$R(\theta,\phi,t) = R_0\left(1 + \sum_{l=2}^{\infty}\sum_{\mu=-\lambda}^{\lambda} a_{\lambda\mu}(t)Y_{\lambda\mu}(\theta,\phi)\right). \tag{2.79}$$

Similar to the static deformation, quadrupole, octupole or hexadecupole nuclear vibrations (or higher modes) for $\lambda = 2$, 3, and 4, respectively, are possible [Hod97], see Fig. 2.7(a).

The most common type of vibration in nuclei is the quadrupole vibration. A quantum unit of vibrational energy is a phonon. In the case of spherical even-even nuclei, one-phonon vibration produces the 2^+ excited state with energy E. Higher-energy vibrational states can be reached by coupling more phonons together. A two-phonon excitation produces a triplet of 0^+, 2^+, 4^+ states at double the energy of one phonon.

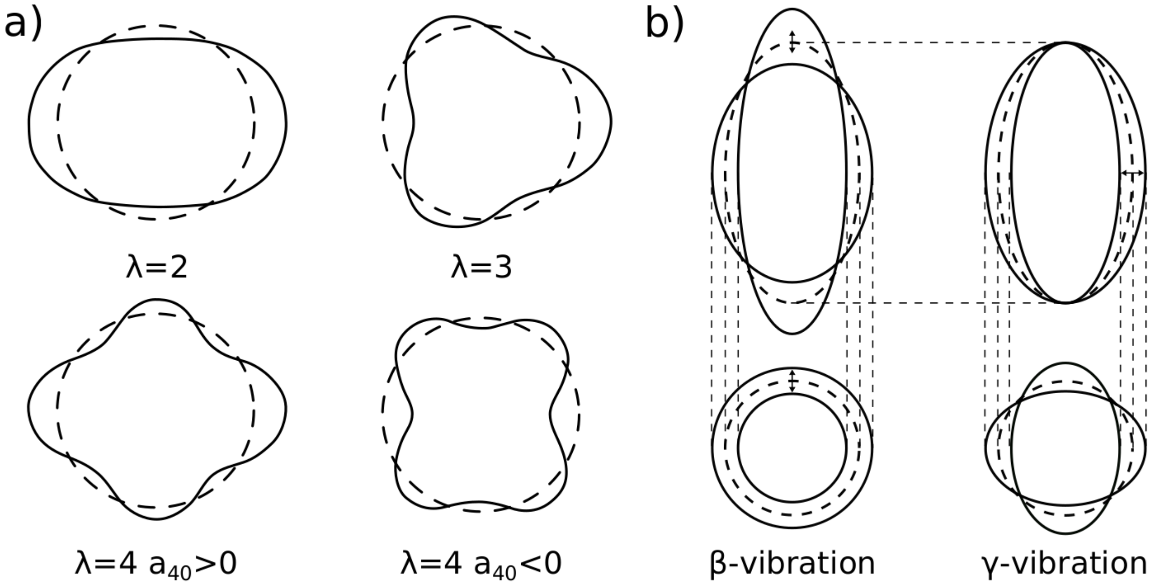

Figure 2.7: Schematic representation of nuclear vibrations. a) Quadrupole, octupole and hexadecapole vibration of a spherical nucleus. b) The β and γ modes of quadrupole vibrations of a prolate nucleus. Top: a cut through the plane of the symmetry axis, bottom: a cut through the plane perpendicular to the symmetry axis. The figure was taken from Ref. [Rin80] and modified.

Similarly, three-phonon vibration leads to $J^{\pi} = 0^{+}, 2^{+}, 3^{+}, 4^{+}, 6^{+}$ multiplet with the energy of $3E$.

Two types of vibrations are possible for deformed nuclei, β and γ vibrations, associated with periodic changes in corresponding parameters of quadrupole deformation. The β vibrations with $K = 0$ are aligned along the symmetry axis, preserving axial symmetry. On the other hand, γ vibrations with $K = 2$ break axial symmetry, and the nucleus oscillates at right angles to the symmetry axis. These modes are visualised in Fig. 2.7(b). Both β and γ vibrational states can become rotational bandheads, giving rise to the β (2^{+}, 4^{+}, 6^{+} ...) and γ (2^{+}, 3^{+}, 4^{+} ...) bands [Cas90].

2.4 Shape coexistence

Nuclear shape coexistence occurs when the nucleus exhibits excited states with a different shape than the ground state at relatively low excitation energy. It has been observed for many nuclei, usually located in regions of isotopes near closed shells of one nucleon type (either proton or neutron) and between closed shells of the other

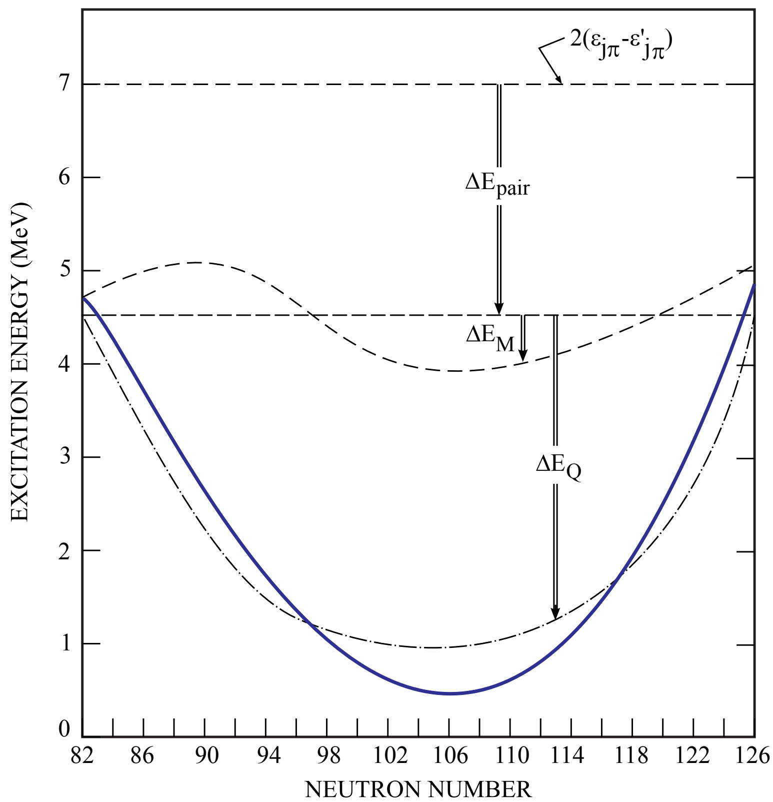

Figure 2.8: A contribution of different energy terms to the excitation energy of the lowest proton 2p-2h intruder state for heavy nuclei as a function of the neutron number. The unperturbed energy of the excited state $2(\varepsilon_{j_\pi} - \varepsilon_{j'_\pi})$ is lowered by the pairing energy ΔE_{pair}, monopole correction ΔE_M and quadrupole interaction ΔE_Q. The solid blue line represents the resulting energy. The figure was taken from Ref. [Hey11].

one (the so-called mid-shell). The most extensive manifestation of shape coexistence is observed in the neutron-deficient lead region [Woo92; Hey00; Hey11].

One of the best-known cases of shape coexistence is a triple shape coexistence of low-energy states in the neutron-deficient isotope ^{186}Pb. Two of these states are excited states of prolate and oblate quadrupole deformation, respectively, while the ground state of this nucleus is spherical [And00; Oja22]. The phenomenon of shape coexistence is also well-known for neutron-deficient mercury isotopes, such as ^{180,182,184}Hg [Els11; Rap17; Str23]. In these isotopes, as well as other even-even nuclei, an excited 0^+ state with a different deformation compared to the g.s. is present. The energy spacing of rotational levels in bands built on top of the two 0^+ states is different, caused by the different shapes of these two bandheads, resulting in different moments of inertia. Since both the ground and excited states have spin and parity 0^+, deexcitation of this excited state requires an $E0$ transition for which emission of a γ quantum is forbidden. Therefore, as was mentioned in section 2.1.3, deexcitation of these coexisting states proceeds mainly via internal conversion (emission of two γ rays and creation of an electron-positron pair if the excitation energy is above 1022 keV are also possible).

Shape coexistence can be explained using the shell model via the so-called intruder states. These states are created by the excitation of two nucleons above the closed shell, leaving two so-called holes below this closed shell. In the neutron-deficient lead region, it is the closed proton shell $1h_{11/2}$ at $Z = 82$. Excitation of a proton pair to the higher shell $2f_{7/2}$ creates np-mh state, for example, 2p-2h for lead isotopes or 2p-4h for mercury isotopes. The excitation energy of the lowest 0^+ intruder state in the case of 2p-2h excitation can be derived as

$$E_{intr}(0^+) = 2(\varepsilon_{j_\pi} - \varepsilon_{j'_\pi}) - \Delta E_{pair} + \Delta E_M + \Delta E_Q. \tag{2.80}$$

The first term $2(\varepsilon_{j_\pi} - \varepsilon_{j'_\pi})$ represents the unperturbed energy required to excite a proton pair across the shell gap. The remaining terms represent the pairing energy gain ΔE_{pair}, monopole correction ΔE_M and proton-neutron quadrupole interaction ΔE_Q. Contributions of these terms are shown in Fig. 2.8. As a result, the energy of such excitation is lowered, creating the intruder state of prolate deformation, in contrast to the spherical or weakly oblate ground state. The excitation energy of intruder states shows quadratic dependence on neutron number, with the minimum for neutron mid-shell at $N = 104$, as can be seen for mercury isotopes in Fig. 2.9 [Hey00; Hey11].

2.5 Nuclear isomers

Nuclear isomers are meta-stable excited states of nuclei. For an excited state to be considered isomeric, its half-life must be long compared to other excited states. In practice, the key point in defining an isomer is the experimental sensitivity to differentiate between prompt radiation accompanying the creation of the nucleus and delayed decay radiation of a meta-stable state. This usually means that the half-life of the isomeric state should be longer than 1 ns [Wal99; Wal20]. Currently, there are about 2600 known isomers with half-lives over 10 ns [Gar23].

A crucial part of isomer formation is the secondary energetic minimum in the nuclear potential (additional to the primary minimum of the ground state). A small change in a specific nuclear parameter leads only to an increase in excitation energy, therefore,

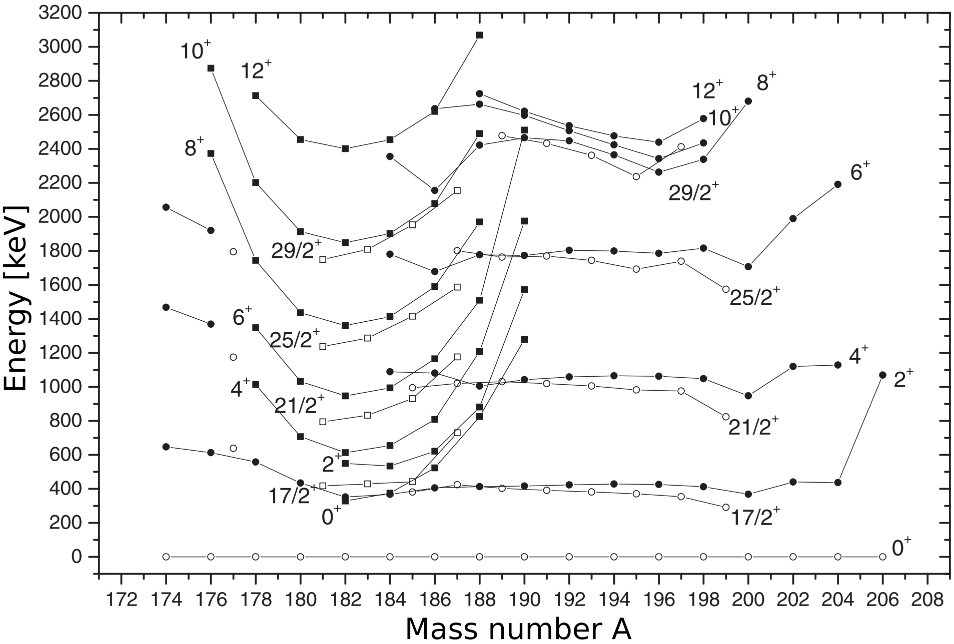

Figure 2.9: Level systematics for the isotopes of mercury. The excitation energy of intruder states and their rotational bands (full squares) show quadratic dependence on the neutron number of the isotope. The figure was taken from Ref. [Jul01].

a large change is required to lower the excitation energy of the nucleus, see Fig. 2.10. However, such large changes lead to hindered transitions. We can differentiate several types of nuclear isomers based on the cause of the secondary minimum and long half-life of the excited state [Wal20].

2.5.1 Shape isomers

Shape isomers can be formed in nuclei, which have a secondary potential minimum at large deformation. Deexcitation of these isomers by γ-ray transition is hindered by the required large deformation change. These isomers can be found mainly in nuclei with $A \approx 80$, $A \approx 100$ and in the neutron-deficient lead region [Möl09]. An example of a shape isomer is the prolate 0^+ excited state in ^{72}Kr with a half-life of 26 ns [Clé05].

A specific case of shape isomers are fission isomers in the trans-actinide region, where hindered γ-ray deexcitation to states in the primary potential minimum competes with fission. Since fission isomers are located in the secondary minimum of the fission barrier, their half-lives are short (up to 14 ms in the case of ^{242}Am [Gar23]) compared to the fission from the ground state, because fission from the isomeric state has to overcome smaller fission barrier [Hal92].

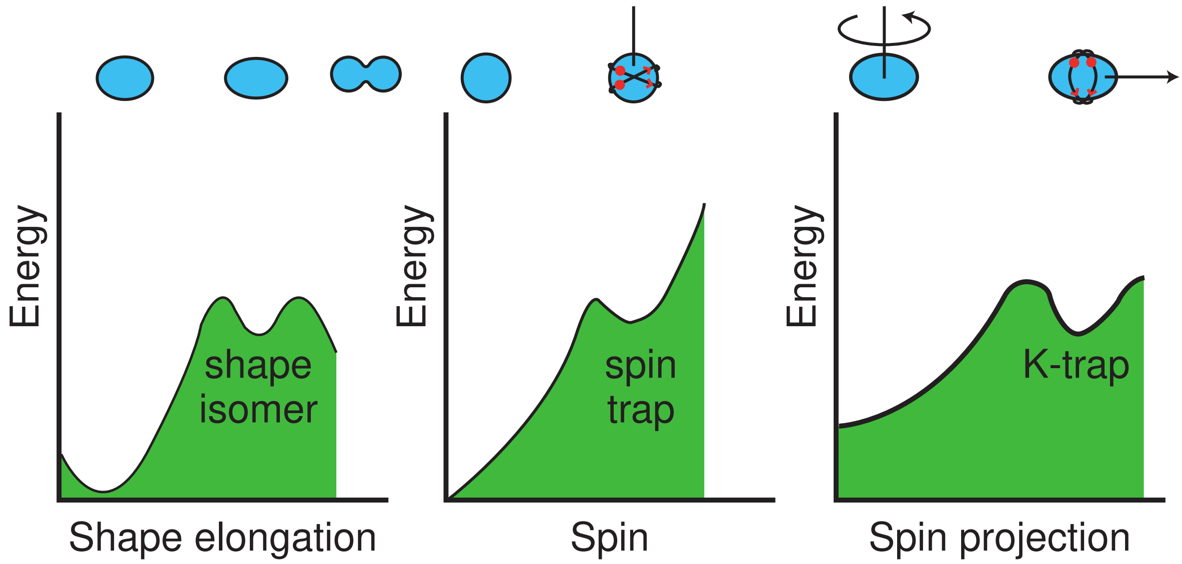

Figure 2.10: Schematic representation of the isomer creation. If the excitation energy of a nucleus with respect to a certain parameter exhibits a secondary minimum, large changes in this parameter are required for the nucleus to deexcite. The specific parameter defines the kind of isomer, elongation for shape isomers, spin for spin isomers and spin projection (quantum number K) for K isomers. The figure was taken from Ref. [Wal99].

2.5.2 Spin isomers

Spin isomers are created when decay to a lower-energy state requires a large change in nuclear spin. The emission of a high multipolarity transition is required for such decay, which is suppressed, as can be seen from Weisskopf estimates (see Eqs. (2.46) and (2.47)). Spin isomers decay mostly via emission of γ quantum or internal conversion, but there are known cases of α decay, proton emission or β decay of such isomeric states [Wal99].

Spin isomers are common in odd-A nuclei in the vicinity of either proton or neutron closed shells. They originate from the excitation of the unpaired nucleon to a high-spin state, such as $1g_{9/2}$, $1h_{11/2}$ and $1i13/2$ which are due to spin-orbital splitting brought down with energy close to low-spin states [May79].

An extreme example of a spin isomer is the 9^- isomeric state in ^{180m}Ta with the excitation energy of $E = 75\,\mathrm{keV}$. Deexcitation from the isomeric to the 1^+ ground state requires a change of spin $\Delta I = 8$, leading to an extremely long half-life of $T_{1/2} > 4.5 \times 10^{16}$ years. Because of such a long half-life, ^{180m}Ta can be found in nature as the only primordial isomeric state [Leh17].

2.5.3 K isomers

The quantum number K is defined as a projection of the total nuclear spin along the symmetry axis in axially deformed nuclei, found away from the closed shells. A large change in K is tied to a change in nuclear spin orientation and may lead to isomer formation [Wal24].

According to selection rules, multipolarity L of γ radiation deexciting K isomer has to be at least as large as the change of K in this transition. Transitions that do not meet this rule are not strictly forbidden but are hindered. The degree of forbiddenness of these transitions can be expressed as [Wal99]:

$$\nu = \Delta K - L. \tag{2.81}$$

A hindrance factor of a K isomer deexcitation can be calculated as a ratio of the experimental and theoretical (Weisskopf estimates from Eq. (2.46) and (2.47)) half-life of a transition as follows:

$$F_W = \frac{T_{1/2,exp}}{T_{1/2,Wei}} \tag{2.82}$$

The hindrance factor increases by a factor of f_ν (called reduced hindrance) per degree of forbiddenness ν, $f_\nu = F_W^{1/\nu}$ [Jai21]. These values for known K isomers vary in a broad range (~30-200 for most cases) and can be obtained from experimental systematics found in Ref. [Kon15].

An example of a K isomer is the 8^-, $K = 8$ isomer in ^{180}Hf. It decays with a half-life of 5.5 hours to the 8^+ rotational state based on the $K = 0$ ground state. The multipolarity of emitted γ ray is $L = 1$, leading to a high degree of forbiddenness $\nu = 7$ [Gar23].

A large change in quantum number K also plays an important role in the β decay. High-K isomers preferentially decay to states in the daughter isotope with similar values of K. Similarly to γ decay, the hindrance factor can be defined using the ft values:

$$F_\beta^{\Delta K} = \frac{ft^{\Delta K}}{ft^{\Delta K=0}}. \tag{2.83}$$

Systematics show that for each unit of ΔK, β decay transitions are suppressed by the factor of ≈ 80 [Wal24]. An example of β decaying K isomer is the 7^- ^{176}Lu with $K = 7$, decaying into 6^+ and 8^+ rotational states of the $K = 0$ g.s. bandhead of ^{176}Hf. While such decays are classified as the first forbidden non-unique, large change of $\Delta K = 7$ leads to a half-life of 3.7×10^{10} years and to log ft values of 19.2 and 20.0, respectively [Hul14].

2.5.4 Seniority isomers

A quantum number seniority v is defined as the number of nucleons in a shell not coupled into $I = 0$ pairs. Seniority isomers can generally be observed in semi-magic nuclei with either proton or neutron shell closure. A typical example of seniority isomers can be found in $N = 50$ isotones ^{92}Mo, ^{94}Ru, ^{96}Pd, and ^{98}Cd. As for all even-even nuclei, the g.s. seniority of these nuclei is zero. Breaking of a proton pair occupying the $g_{9/2}$ orbital results in a series of $I^{\pi} = 2^{+}$, 4^{+}, 6^{+}, and 8^{+} excited states with $v = 2$. In contrast to other types of isomers, seniority isomers do not involve a change in seniority. The hindrance of $E2$ transitions between the $v = 2$ states and the low energy of the $8^{+} \rightarrow 6^{+}$ transition causes the 8^{+} states in these isotopes to be isomeric [Isa11; Wal20].

Chapter 3

Experimental background

3.1 ISOLDE facility

The ISOLDE facility (Isotope Separation On-line DEvice) is one of the world-leading laboratories for radioactive ion beam production and nuclear structure studies. It is located at the European Organisation for Nuclear Research (CERN) near Geneva in Switzerland. Currently, over 1300 isotopically pure beams of 75 elements with intensities ranging from 1 to more than 10^{10} ions/s can be produced at ISOLDE and delivered to various experimental setups [Bor17a].

3.1.1 Production of nuclei

The ISOLDE facility is located at Proton-Synchrotron Booster (PSB), which produces a proton beam with the energy of 1.4 GeV in the form of 2.4 μs long pulses with a repetition time of 1.2 s. Each pulse contains approximately $3{\times}10^{13}$ protons and the average current of up to 2 μA is delivered to the ISOLDE target. These pulses from PSB are grouped in a so-called supercycle with variable length (usually between 20 and 50 pulses) and are distributed to several CERN facilities, one of which is ISOLDE [Kug00; Cat17].

Nuclei of interest are produced in proton-induced spallation, fission or fragmentation of target material (Fig. 3.1). In fission, two similar mass neutron-rich fragments are produced, and several neutrons are released. In spallation, many nucleons are ablated from the target nucleus, creating various, mostly neutron-deficient, nuclei. Fragmentation reactions produce nuclei close to the initial target as well as very light nuclei.

Several different target materials are used to maximise the production of the desired isotope. The most commonly used target material at ISOLDE is the uranium carbide

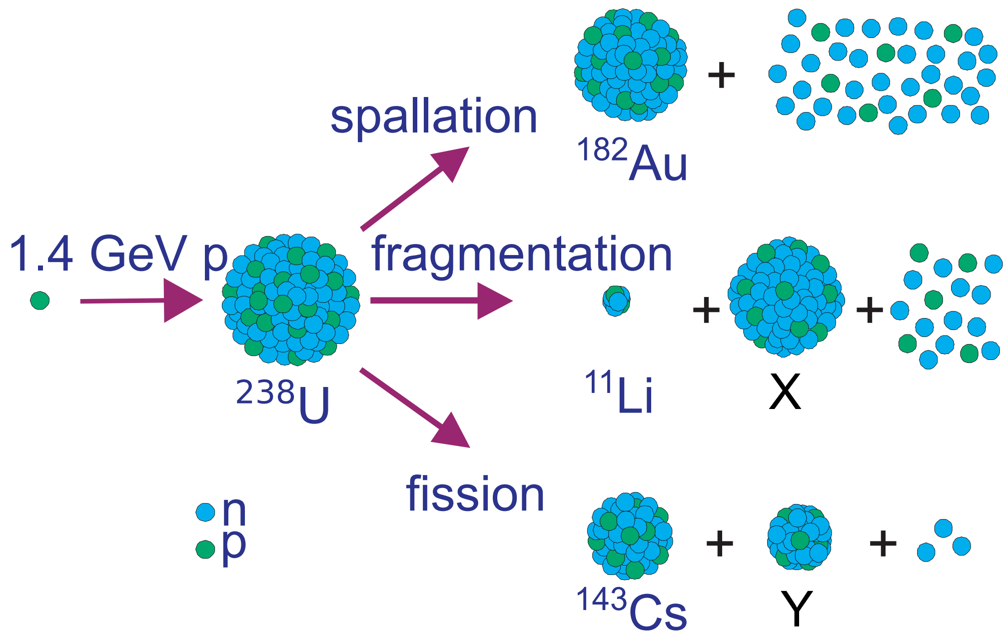

Figure 3.1: Schematic drawing of main reaction channels for production of radioactive ion beams at ISOLDE. Spallation, fragmentation or fission of heavy target nuclei, such as uranium, are used to produce isotopes of interest. The figure was taken from Ref. [Lin04] and modified.

UC_x target with a thickness of 50 g/cm^2, but other materials, such as lead or tantalum, can also be used. Produced nuclei diffuse from the target and effuse through the transfer line towards the ion source. An important characteristic of the target is the release time of the produced isotopes. Both the target and transfer line are heated to a temperature of over 2000 °C to decrease the diffusion and effusion times. Release time of several tenths of a second can be achieved for certain target and produced element combinations [ISO; Got16].

3.1.2 Ionisation

There are three ionisation methods commonly used at ISOLDE: surface ionisation, plasma ionisation and laser ionisation. Many different isotopes of various elements are produced in the target, therefore, selective ionisation is needed. Surface ionisation is performed in a hot tungsten or tantalum cavity, and nuclei are ionised in collisions with the surface of this cavity. This ionisation method is used for elements with low ionisation potentials, such as alkali metals. In a plasma ion source, nuclei are bombarded by accelerated electrons, creating a low-pressure plasma. Together with the cooled transfer line to suppress the transport of non-volatile elements, it is used to ionise noble gases [Van06].

The third method is the resonant laser ionisation performed by RILIS (Resonance Ionization Laser Ion Source). This ion source uses step-wise resonant excitation of atomic transitions by laser radiation in a hot cavity. A schematic view of RILIS can be seen in Fig. 3.2. The laser system of RILIS consists of several Titanium:Saphire and dye lasers pumped by a system of Nd:YAG and Nd:YVO_4 lasers. Wavelengths of these lasers can be tuned in the range of 210 − 950 nm, including frequency multiplying up to the fourth harmonics. The average time before atoms diffuse out of the hot cavity of an ion source is 0.1 ms, therefore, the lasers work with a repetition frequency of 10 kHz. This ensures that each atom is exposed to at least one pulse of laser light [Fed17].

Atomic transitions are unique for each element, therefore, a pure ion beam of a particular element can be produced using a suitable excitation scheme. It has to be noted that although this ionisation method is element selective, contamination by surface ionised elements, such as francium or thallium in the lead region, may still be present. Currently, about 40 elements can be ionised by RILIS with efficiencies of up to 27%. Two- or three-step ionisation schemes are usually used. The first laser (respectively the first two lasers) excites the valence electron from the ground state to a high-lying energy level. The last laser removes this electron from the atomic shell, thus creating a 1^+ ion. This can be done via a non-resonant transition to a continuum or a resonant transition to either auto-ionising (above ionisation potential) or a Rydberg state (below ionisation potential). In the latter case, ionisation is achieved by collisions with other atoms [Fed17].

When the nucleus has a non-zero spin, as it is usually the case for odd N and/or odd Z nuclei, energy levels in the atomic shell split because of the interaction of the nuclear spin with the intrinsic spin of an electron. This effect causes the hyperfine structure of atomic transitions. An isomeric state in the nucleus with a different spin than that of the g.s. has a different hyperfine structure. This difference can be used to selectively ionise only the isomeric or ground state by tuning the laser frequency to a particular hyperfine transition. It has to be noted that because of the Doppler broadening of transition width and spectral bandwidth of the used laser, the hyperfine structure differences are not always sufficiently large to be resolved [Fed03; Fed17; Cam16]. This method was successfully used to selectively study isomeric states with different spins, for example, in ^{188}Bi or ^{184}Hg [And20b; Rap17].

Ionised atoms are extracted from the ion source by an electrostatic potential of

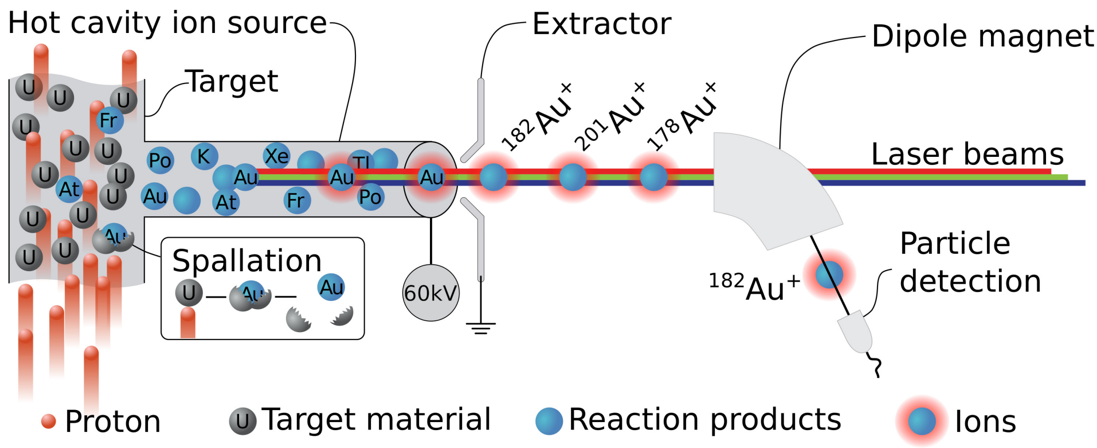

Figure 3.2: Schematic view of RILIS at ISOLDE. Step-wise excitation and ionisation of atomic electron by laser radiation in a hot cavity is an element-selective ionisation method used for the production of high-purity ion beams. Ionised isotopes are extracted from the ion source by an electric field, and the isotope of interest is separated using a magnetic field. The figure was taken from Ref. [Rot13] and modified.

30 – 60 kV and are mass separated before delivery to the detection system [Cat17].

3.1.3 Mass separation

There are two mass separators at ISOLDE, the GPS (General Purpose Separator) and the HRS (High Resolution Separator), each with its own target and ion source unit. These separators use the magnetic field to bend the trajectory of an ion beam. For a given bending radius r and beam energy E, isotope separation is performed by setting the magnetic field B for a mass of a desired isotope M:

$$B = \frac{\sqrt{2ME}}{rq} \tag{3.1}$$

The GPS consists of one double-focusing magnet with a bending angle of 70° and a bending radius of 1.5 m. This separator contains an electrostatic switchyard, which allows the simultaneous separation of three beams, the main (central) one and two additional ones with masses within the range of ±15% from the central mass. The central beam is transported down the main GPS beamline, while the other two beams are transported down the GLM (lower-mass beam) and GHM (higher-mass beam) beamlines and can be used by small-sized experimental setups. For a separator, we define its resolution, or mass resolving power, as

$$R = \frac{M}{\Delta M}, \tag{3.2}$$

where M is a set mass of a beam and ΔM is the full width at half the maximum of mass distribution of this beam. For the GPS, it reaches the value of approximately $R = 800$ [Kug00; Cat17].

The second separator at ISOLDE, HRS consists of two magnets with a bending radius of 1 m and bending angles of 90° and 60°. Unlike the GPS, the HRS can separate only one beam with a set mass, however, a higher mass resolving power of about $R = 6000$ can be reached.

Both the GPS and HRS beamlines join up into one central beamline via a merging switchyard. This beamline splits up and distributes the beam to one of several experimental setups at ISOLDE.

3.2 ISOLDE Decay Station

Decay measurement of ^{182}Au was performed at the IDS (ISOLDE Decay Station), which is one of the permanent detection setups at the ISOLDE [IDS]. The mass-separated beam from one of the separators passes through a collimator with a variable aperture width of 2 − 10 mm. After that, the beam is implanted on an aluminised Mylar tape inside a vacuum chamber, positioned above the dedicated tape station. Moving this tape can remove long-lived decay products from the implantation position. The tape movement can be either manual or automatic in response to a certain number of proton pulses or supercycles from the accelerator.

Many different detectors of various types can be installed at IDS. The core part of this detection setup was a set of four Canberra EUROBALL HPGe Clover detectors [Mir] for the detection of emitted γ and X-rays, which are mounted around the vacuum chamber. Each Clover detector consists of four individual crystals with a diameter of 50 mm and a length of 70 mm, each working as an individual detector.

The versatile design of IDS allows the installation of different types of additional detectors around the implantation point to serve the needs of a specific experiment. Several different setups have already been used in the past, for example:

- High efficiency β-γ setup consisted of additional HPGe detectors, which could be placed at a specific angle to perform angular correlation studies, and a 3-cm-thick rectangular NE102 plastic scintillator as β trigger covering ~95% solid angle around the implantation point [Ber20].

- Fast-timing setup employed two $LaBr_3(Ce)$ γ detectors for half-life measurements in the sub-nanosecond range and three plastic scintillators [Fra17].

- Neutron detection setup used INDIE (IDS Neutron Detector) based on the VANDLE detector. It consists of 26 3×6×120 cm^3 scintillating bars placed further away from the vacuum chamber, serving also as a time-of-flight detector [Pet16].

- Particle spectroscopy setup consisted of the MAGISOL Si-plugin chamber, which contained an array of five double-sided silicon strip detectors (DSSD) backed with four unsegmented silicon-pad detectors (PAD), in the shape of a box. The size of these detectors was 50×50 mm^2, and each DSSD was divided into 256 3×3 mm^2 pixels [Fyn17].

- Conversion electron spectroscopy setup employed two silicon detectors placed inside the vacuum chamber. The first one was a 0.5-mm-thick 900-mm^2 PIPS detector placed behind the tape. The second one was the SPEDE spectrometer, which utilised a 24-fold-segmented, 1-mm-thick annular silicon detector cooled by circulating ethanol to -20°C. The 24 segments of this detector were arranged in three concentric rings around the aperture in the centre, with 8 segments each [Str20].

Over the years after the ^{182}Au measurement presented in this Thesis, the IDS setup received several upgrades. A secondary measurement position was added between the implantation position and the tape station for studying long-lived decays. A detector support structure was also considerably upgraded, allowing for the mounting of up to 15 HPGe detectors around both measurement points [IDS; Cub23a].

3.3 Experiment IS665

The ^{182}Au nuclei studied as a part of the IS665 experiment were produced using a standard uranium carbide UC_x target. The production rate was much higher than the detection system could handle, therefore, the intensity of the ^{182}Au ion beam was limited in several ways. Only two evenly spaced (~ 15 s apart) proton pulses with decreased intensity out of a 25-pulse-long supercycle were delivered to ISOLDE, resulting in the average current of approximately 0.17 μA. Moreover, the beam gate was opened after a delay of 0.4 s following the impact of each proton pulse for the duration of 2 s, after which it was closed until the next pulse arrived. The implantation tape of

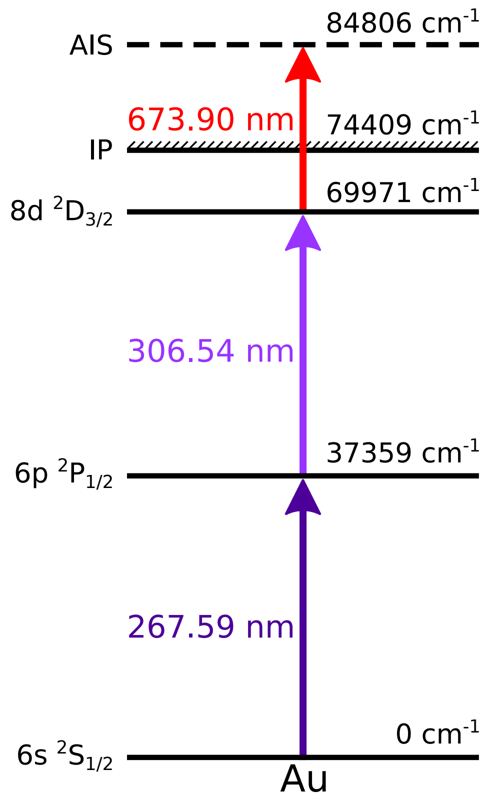

Figure 3.3: Ionisation scheme for gold isotopes used by RILIS. The first two lasers are used to excite the valence electron, while the third one ionises the atom via excitation to an autoionising state (AIS) above the ionisation potential (IP) [Mar06].

IDS was moved once per supercycle, 10 s after every second proton pulse delivered to ISOLDE.

Gold atoms were selectively ionised by RILIS using the excitation scheme developed in Ref. [Mar06]. It consisted of three lasers with wavelengths of 267.59, 306.54, and 673.90 nm, see Fig. 3.3. The ionisation efficiency of this scheme was estimated to be over 3% [Mar06]. Extraction potential of 30 kV was used and the ^{182}Au ion beam was mass-separated using the GPS and subsequently delivered to the IDS.

During the IS665 experiment, a new vacuum chamber was used at the IDS, designed specifically for this measurement [Cub22]. The chamber had a box-shaped design with dimensions of $134 \times 134 \times 257$ mm with ≈1-mm-thick aluminium windows, allowing the detection of X-rays and low-energy γ quanta.

The box geometry of this chamber allowed the cubic arrangement of four previously mentioned HPGe Clover detectors, providing an efficient solid angle coverage. One was placed above the chamber, the second was behind the tape and the remaining two were

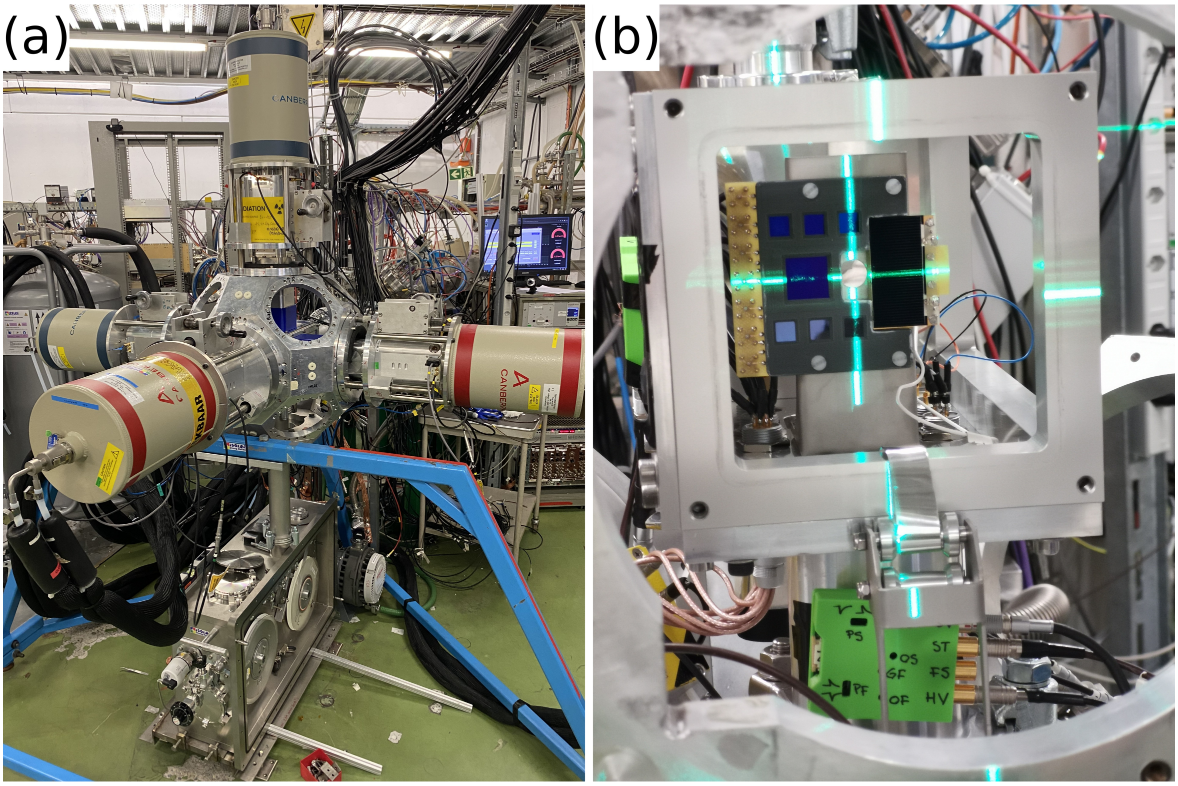

Figure 3.4: Detection system IDS. (a) The core part of IDS was a set of four HPGe Clover detectors. They were mounted in a frame around the vacuum chamber, which was placed above the tape station [IDSa]. (b) An array of seven silicon detectors and a solar cell placed inside the vacuum chamber of IDS. Courtesy of R. Lică.

mounted horizontally on the left and right sides of the chamber, as seen in Fig. 3.4. Two of the used detectors had end caps consisting of thin carbon windows, giving them higher low-energy detection efficiency in comparison to the other two detectors with regular aluminium end caps.

Inside the chamber, an array of 7 Hamamatsu silicon PIN diodes with a thickness of 300 μm was placed, which were able to detect α particles, conversion electrons and fission fragments. The array was placed in front of the tape, with the hole allowing the beam to pass. It consisted of one larger detector (S3204-09 [Hama]) and six smaller detectors (S3590-09 [Hamb]) placed above and below (three detectors each) the large one (see Fig. 3.4). They were partially covered with a plastic mask, resulting in the effective dimensions of $15{\times}15\,\mathrm{mm}^2$ and $7{\times}7\,\mathrm{mm}^2$ for the large and small detectors, respectively. One solar cell sensitive only to fission fragments was also placed inside the chamber.

The data acquisition employed the XIA DGF Pixie-16 [Pix] modules. The frequency of the internal clocks of these modules was 250 MHz, which allowed a timestamp recording for each event with a precision of 4 ns. This allows off-line software correlation of coincident signals. Additionally, module and channel numbers were recorded for every signal besides energy information, identifying the detector in which each event originated.

3.4 Detector calibration

3.4.1 Germanium detectors

Energy calibration of HPGe detectors was made individually for each of the 16 crystals using radioactive sources of ^{152}Eu [Mar13], ^{241}Am [Bas06], ^{137}Cs [Bro07] and ^{60}Co [Bro13]. Because of the shift of energy calibration over time, this calibration was insufficient for the ^{182}Au decay data. Therefore, it was corrected using known γ lines emitted after β decay of ^{182}Au [Str21], see Table 3.1. These values were extracted from the data set from the ^{182}Tl decay study performed also at IDS [Str23], where ^{182}Au was present as a member of the ^{182}Tl β-decay chain. The energy calibration in this study was performed using the ^{152}Eu source and a ^{138}Cs sample produced on-line. Several intense transitions from ^{182}Au decay products ^{182}Pt and ^{182}Ir were also used for the calibration [Sin15]. The calibration correction was performed four times during the whole duration of ^{182}Au decay measurement.

The quadratic function was used for the calibration. This was sufficient to describe the energy response of two Clover detectors (8 crystals). However, a misalignment in the case of the remaining crystals was observed for energies above ~1.6 MeV. Because of this, the whole energy range was divided into four regions, each with a separate calibration curve. The curve obtained using the entire energy range was used for the first region. For the remaining three regions (1.4 – 2.1 MeV, 2.1 – 2.6 MeV and above 2.6 MeV), calibration curves fitted through the points within these energy intervals were used. We also determined the energy of several intense peaks in the energy spectrum of the first eight crystals and used them as additional points for the calibration. Specific energy intervals were chosen separately for each crystal as intersecting points between individual functions. Figure 3.5 shows the energy calibration of crystals 3 (using one quadratic function) and 9 (using four quadratic functions).

A part of γ rays deposit their energy in multiple crystals of one Clover detector through Compton scattering and photoeffect. In such cases, the full energy of these γ rays can be reconstructed using the so-called add-back method by summing the

Table 3.1: A list of γ-ray energies from the ^{182}Au β decay used for calibration of Clover detectors [Str21].

Energy (keV)			
155.0(1)	787.2(1)	1810.7(2)	3093.8(1)
264.6(1)	855.5(1)	1845.2(2)	3241.1(1)
344.6(2)	1026.5(1)	2021.7(4)	3414.4(1)
436.3(1)	1084.5(1)	2563.8(1)	3422.2(1)
614.0(1)	1790.4(2)	2845.6(2)	3577.1(1)

deposited energies in coincidence in all crystals of this detector. Add-back was used for all γ-ray analysis presented in this Thesis.

The resulting energy resolution after summing of add-back energy spectra of all 4 Clover detectors was 2.4 keV and 3.7 keV FWHM (Full Width at Half Maximum) for energies of 1085 keV and 3094 keV, respectively. We tested the energy calibration using several natural background peaks and ^{182}Au daughter products. Energy differences between measured and tabulated values are in Table 3.2. The calibration uncertainty of 0.2 keV below 1600 keV and 0.3 keV for higher energies is combined with the uncertainty of all γ-ray transitions in this work.

Radioactive sources of known activities stated in Table 3.3 were used for the efficiency calibration of Clover detectors. The energies and intensities of γ quanta emitted from these sources were taken from [Mar13] and [Bas06]. Add-back was used for the calibration data, and the resulting spectra of all four HPGe detectors were summed together. The efficiency of the detectors ε_γ for energy E_γ can be expressed as a fraction of the number of observed transitions N_γ in a peak with this energy and the number of corresponding γ rays emitted from the source, expressed by an activity of the source A, measurement time t and absolute intensity of a given transition I_γ:

$$\varepsilon_\gamma = \frac{N_\gamma}{AtI_\gamma}. \tag{3.3}$$

In the case of a sequence of three levels with appropriate spins, a nucleus can deexcite between the initial and final state directly (crossover transition) or via an intermediate level. In the first case, a single γ ray with energy E_C is emitted, while a cascade of γ rays with energies E_1 and E_2 ($E_C = E_1 + E_2$) is emitted in the latter case. With a certain probability, γ rays from the cascade can be detected in the same detector and summed together. This reduces the number of detected cascade γ quanta and

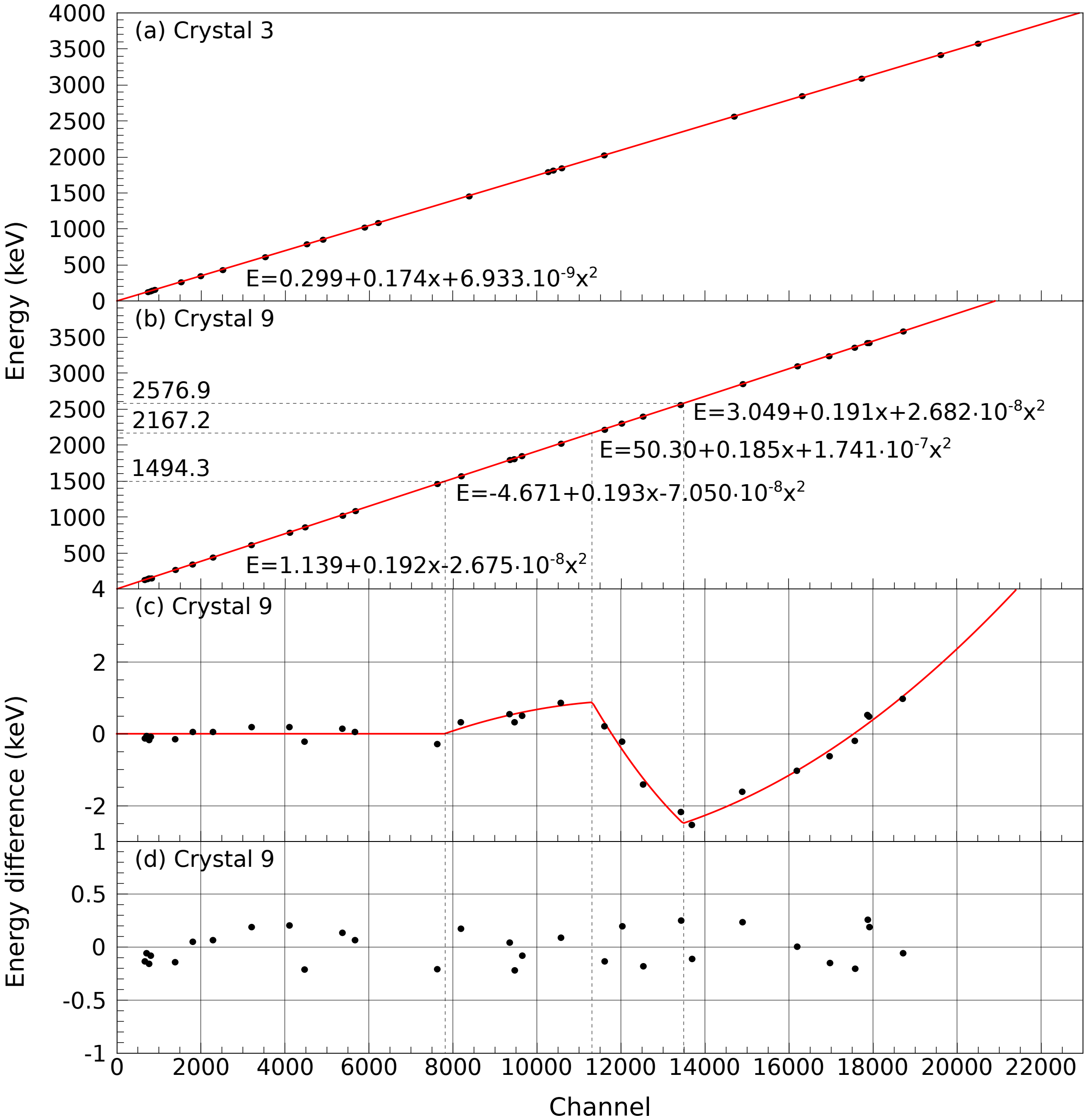

Figure 3.5: Calibration functions of HPGe detectors. Energy calibration was performed individually for each of the 16 crystals of the Clover detectors. (a) Calibration of crystal number 3 using one quadratic function. (b) Calibration of crystal number 9 using four quadratic functions. The exact energy intervals used are marked. (c) Differences between the four calibration curves for this crystal from part (b) and the curve obtained from the whole energy range. (d) Residuals for the calibration curve of the crystal 9.

increases the counts of the crossover transition, resulting in altered detection efficiency of all three transitions. The amount of summed cascade pairs N_{sum} can be expressed

Table 3.2: Differences in measured and tabulated energy of several transitions from the natural background (^{208}Tl [Mar07], ^{214}Bi [Zhu21], ^{228}Ac [Abu14]) and ^{182}Ir [Sin15]. These differences were used to estimate the uncertainty of energy calibration.

Isotope	E_γ^{ref} [keV]	E_γ [keV]	Difference [keV]
^{182}Ir	273.5(1)	273.713(1)	0.21(10)
^{214}Bi	609.321(7)	609.335(17)	0.014(18)
^{182}Ir	790.0(1)	790.175(4)	0.18(10)
^{182}Ir	890.6(1)	890.796(4)	0.20(10)
^{182}Ir	912.1(1)	912.217(4)	0.12(10)
^{228}Ac	968.971(17)	968.817(33)	-0.154(37)
^{182}Ir	1063.4(1)	1063.63(1)	0.23(10)
^{182}Ir	1549.7(2)	1549.88(7)	0.18(21)
^{214}Bi	1764.491(14)	1764.81(5)	0.32(5)
^{214}Bi	2447.69(3)	2447.58(16)	-0.11(16)
^{208}Tl	2614.511(10)	2614.76(5)	0.249(55)

Table 3.3: Radioactive sources used for efficiency calibration of HPGe detectors. Nominal activities and activities on the measurement day are listed, together with measurement times for each radioactive source.

Source	Activity on 01/04/2016 [kBq]	Activity on 06/09/2021 [kBq]	Measurement time [h]
^{241}Am	39.65	39.31	4.49
^{152}Eu	15.57	11.78	17.92

in the following way:

$$N_{sum} = AtI_{cas}\varepsilon_{sum} \cong \frac{1}{4}AtI_{cas}\varepsilon_1\varepsilon_2, \tag{3.4}$$

where I_{cas} is the intensity of a cascade, which is the intensity of a less intense member of the cascade (usually a higher placed transition in a decay scheme) and ε_{sum} is the efficiency with which both γ rays are detected in the same detector. Factor 1/4 arises from the fact that once one member of the cascade is detected (with efficiency ε_1), the second one must be detected in the same detector, which effectively lowers its detection efficiency to one fourth of the original value ε_2. Since the detection efficiency of each particular detector is not exactly the same because of slight differences in geometric efficiencies, differences between carbon-window and aluminium-cap detectors, and a possible influence of the angular correlations, this factor is only approximate.

Table 3.4: Data points used for efficiency calibration of HPGe detectors. Radioactive sources, transition energies and corresponding detection efficiency values are listed. Correction for coincidence summing was performed for these values using Eq. (3.4).

Source	Energy [keV]	Absolute efficiency [%]
^{241}Am	26.3	7.15(17)
	59.5	15.4(4)
^{152}Eu	121.8	15.03(8)
	244.7	10.64(6)
	344.3	9.18(7)
	411.1	7.59(3)
	444.4	7.41(3)
	488.7	6.90(6)
	678.6	5.37(5)
	778.9	5.24(3)
	810.5	4.69(6)
	841.6	5.07(12)
	867.4	4.53(3)
	919.3	4.20(6)
	964.1	4.64(2)
	1085.8	4.21(2)
	1112.1	4.08(2)
	1212.9	3.69(2)
	1299.1	3.52(2)
	1408.0	3.50(2)

To obtain correct values of detection efficiency using ^{152}Eu source, we used modified Eq. (3.3), instead of N_γ we used $N_\gamma + N_{sum}$ for members of cascades and $N_\gamma - N_{sum}$ for crossover transitions parallel to these cascades. The resulting values used for efficiency calibration are in Table 3.4. Several additional γ transitions were considered in the calculation of summing correction, such as the 719.3 keV transition (in coincidence with 244.7 keV summing to 964.1 keV), even if the transitions themselves were not used

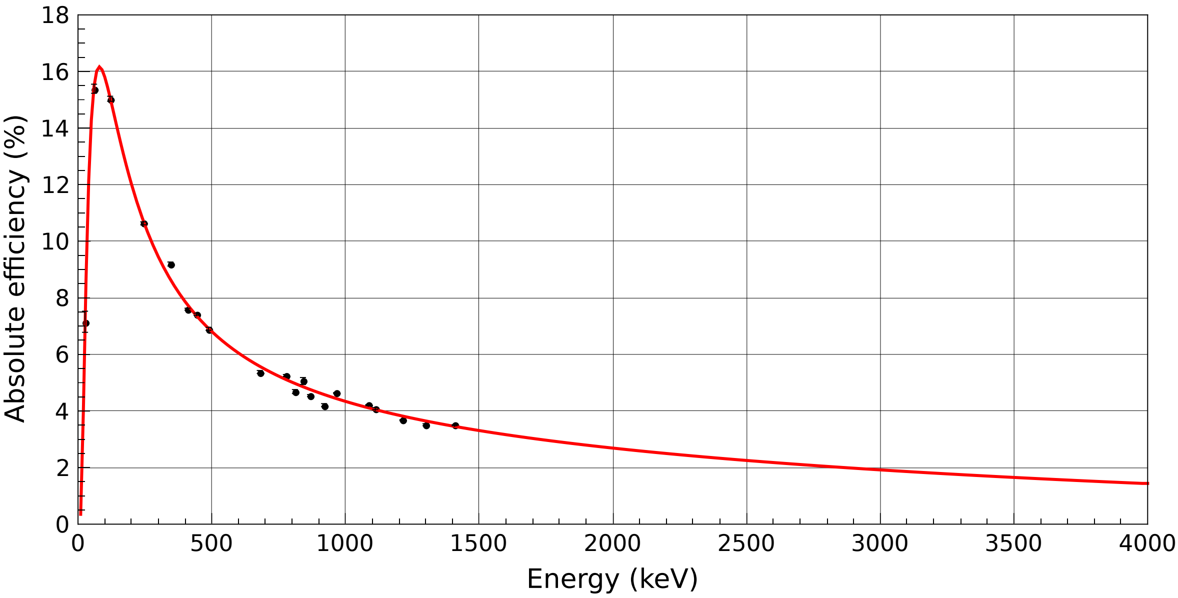

Figure 3.6: Absolute efficiency calibration of HPGe detectors after correction for the coincidence summing. For fitting of data points listed in Table 3.4, Eq. (3.5) was used (red line). The obtained coefficients are $a_0 = -26.577(12)$, $a_1 = 19.592(3)$, $a_2 = -4.7185(4)$, $a_3 = 0.4884(1)$ and $a_4 = -0.01895(1)$.

for calibration due to peak contamination. To obtain the efficiency curve of HPGe detectors, we fitted these data points with the following function:

$$\varepsilon_\gamma = exp[a_0 + a_1 ln(E_\gamma) + a_2 ln^2(E_\gamma) + a_3 ln^3(E_\gamma) + a_4 ln^4(E_\gamma)] \quad (3.5)$$

with a_0 to a_4 being the efficiency calibration parameters. Efficiency calibration was performed in two steps. The calculation of summing correction requires the efficiencies ε_1 and ε_2 to be known, therefore, the efficiency curve without the summing correction was constructed in the first step. After that, the data points were corrected for coincidence summing using Eq. (3.4) and the final efficiency curve in Fig. 3.6 was obtained. Since the uncertainties in the activity of used sources are unknown, an additional uncertainty term of 3% was added to the efficiency values. All calibration points had energies up to ~1.4 MeV, therefore, we increased this value to 5% and 7%, for transitions with energy greater than 1700 and 3500 keV, respectively, to account for the extrapolation of the efficiency curve.

3.4.2 Silicon detectors

For the purpose of energy and efficiency calibrations of silicon detectors, measurement using the 4α source (^{148}Gd, ^{239}Pu, ^{241}Am and ^{244}Cm with activity 1 kBq each) was performed. We used this data only for preliminary calibrations because we observed the same shift over time in the energy calibration as in the case of germanium detectors. In the case of efficiency calibration, it could not be placed directly in the implantation position because of its large size, thus having a different geometric efficiency.

The ^{182}Au decay data were used for the energy calibration of silicon detectors. Two separate calibrations were made, a low-energy calibration for conversion electrons and a high-energy calibration for α particles. We identified three known CE transitions (455.4, 499.5 and 512.5 keV [Dav99]) based on the e^{-}-γ coincidences and used them for energy calibration. This is further explained in Chapter 4.2.4.

Energy calibration for α particles was done in two steps. At first, the low-energy calibration was extrapolated, which allowed us to identify α peaks in the measured spectrum. Then, known transitions originating from the α decay of ^{182}Au (5403(5), 5352(5) and 5283(5) keV), ^{182}Pt (4843(5) keV) and ^{182}Hg (5867(5) keV, coming from the ^{182}Tl beam contamination) [Ach09] were used for the final α-particle energy calibration of silicon detectors. Energy resolution of 11 and 24 keV (FWHM) was achieved for CEs (at 377 keV) and α particles (at 5870 keV), respectively

The efficiency calibration of silicon detectors was performed using the data from ^{181}Au α decay measured during the same experiment, right after the ^{182}Au data collection. The singles α spectrum of this decay is shown in Fig. 3.7(a). This isotope has two main α lines with energies of 5625(5) and 5479(5) keV, with the latter one being followed by the 148-keV γ ray [Bin95]. The total number of 148-keV transitions $N(148)$ can be calculated from the number of counts in the singles γ-ray spectrum S_γ (see Fig. 3.7(c)) and the spectrum gated on the 5479-keV α peak $S_{\alpha\gamma}$ (see Fig. 3.7(b)):

$$N(148) = \frac{S_\gamma(148)(1+\alpha)}{\varepsilon_\gamma}, \tag{3.6}$$

$$N(148) = \frac{S_{\alpha\gamma}(148)(1+\alpha)}{\varepsilon_\gamma \varepsilon_\alpha}, \tag{3.7}$$

where α is the total conversion coefficient of the 148-keV transition and ε_γ and ε_α are respective γ and α detection efficiencies. Using these two equations, detection efficiency for the α particles can be calculated by comparing the detected counts in singles and coincidence spectra:

$$\varepsilon_\alpha = \frac{S_{\alpha\gamma}(148)}{S_\gamma(148)}. \tag{3.8}$$

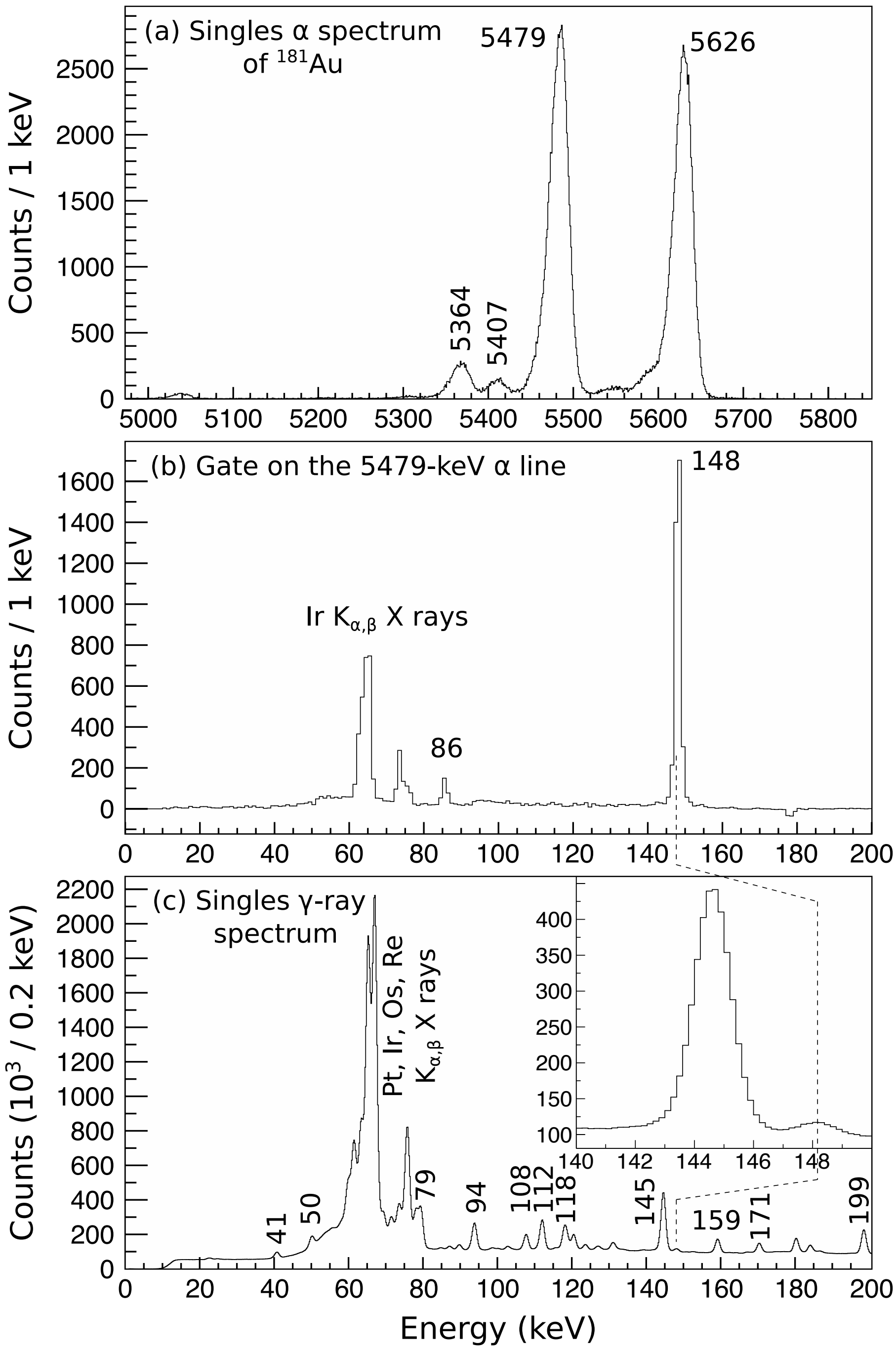

Figure 3.7: The data from the ^{181}Au α decay used for the efficiency calibration of the silicon array. (a) Singles α spectrum. (b) γ-ray spectrum gated on the 5479-keV α peak. (c) Singles γ-ray spectrum. Peaks originating from the β decay of ^{181}Au and its products are labelled [Wu05]. The inset shows the part of the spectrum around the 148-keV transition following the 5479-keV α decay. Detection efficiency can be calculated by comparing the counts of this transition in singles and gated spectra.

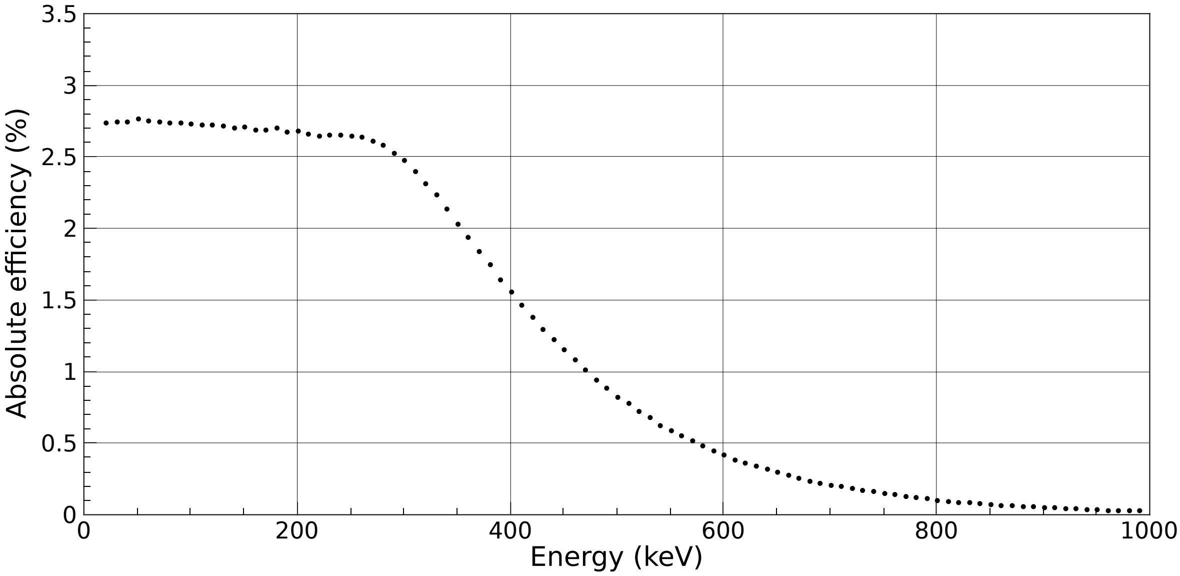

Figure 3.8: Absolute efficiency calibration of silicon detectors for conversion electrons. The efficiency curve was obtained by the Monte-Carlo simulation using the GEANT4.

This result is independent of the multipolarity of the 148-keV transition and its detection efficiency, but it requires that all of the 148-keV singles γ rays originate from the 5479-keV α decay feeding the level at 148 keV in ^{177}Ir. We used the γ-γ coincidences to check for contamination from the ^{181}Au β decay, but no such transitions were found. The only possible contamination could come from the 5407-keV α transition feeding the 223-keV level in ^{177}Ir, which can deexcite by the cascade of 75- and 148-keV γ rays [Bin95]. Relative γ-ray intensities in the ^{181}Au α decay are unknown, but the maximum possible contamination can be determined as the 5479- and 5407-keV α transition intensities ratio, see decay scheme in Ref. [Bin95], reaching 6%. Because of this, we increased the efficiency by 3% of its value and increased its relative uncertainty by 3%. The final efficiency value is $\varepsilon_\alpha = 3.8(4)\%$.

Detection efficiency for CEs is lower than for the α particles because of the electron backscatter. Moreover, it changes with CE energy, because high-energy electrons can pass through the detector without depositing their whole energy, causing a decrease in the efficiency for higher energies. Therefore, we obtained the efficiency curve for conversion electrons from the Monte-Carlo simulation using the GEANT4 [Ago03]. The model of the silicon array with appropriate detector dimensions and distances between them was used [Cub24]. However, the exact distance of the silicon array from the implantation point during the measurement is unknown. We chose the distance of

17.5 mm as it yields approximately the same detection efficiency ($\varepsilon_{\alpha,sim} = 3.77\%$) for the α particles as determined from α-γ coincidences. Values obtained from the simulation were corrected for the difference between the $\varepsilon_{\alpha,sim} = 3.77\%$ and $\varepsilon_{\alpha} = 3.8\%$. The efficiency curve for conversion electrons is shown in Fig. 3.8. The same relative uncertainty as for α-particle detection efficiency ($\sigma_{\varepsilon_\alpha}/\varepsilon_\alpha = 10.5\%$) was applied to the curve in this work.

Chapter 4

Results and Discussion

In this chapter, we present results from the data analysis of ^{182}Au decay measurement and their interpretation. Data were obtained during the experiment IS665 [And20a] in August and September 2021, carried out at IDS at ISOLDE, which were described in chapters 3.1 and 3.2, respectively. Measured data were processed using the xia4ids code [Lic], which was modified to suit the needs of energy calibration as described in Chapter 3.4. Data analysis and visualisation were performed using an object-oriented analysis framework ROOT [Bru97]. Preliminary results from this analysis discussing β-decay feeding intensities were published in Acta Physica Polonica B Proceedings Supplement [Miš24]. Main results from Chapters 4.2 and 4.3 were submitted for publication in Physical Review C [Miš25].

4.1 Previous studies of ^{182}Au and ^{182}Pt

Isotope ^{182}Au lies in the neutron-deficient lead region and undergoes predominantly EC and β^{+} decay to ^{182}Pt with Q_{EC} = 7864(23) keV (resp. $Q_{\beta^{+}}$ = 6842(23) keV) [Wan21] and with branching ratio of b_{β} = 99.87(5)% [Bin95]. The evaluated value half-life of ^{182}Au is $T_{1/2}$ = 15.5(4) s [Sin15].

This nucleus was studied for the first time in 1970 at ISOLDE (CERN). It was observed as the β-decay daughter product of ^{182}Hg produced in spallation of a molten lead target using a 600-MeV proton beam [Han70]. A half-life of $T_{1/2}$ = 19(2) s was reported for the observed α-decay. The first EC/β^{+} decay study of ^{182}Au used the same production method, and two transitions in the ground state band of ^{182}Pt were reported (154.9 and 263.8 keV), together with the half-life of $T_{1/2}$ = 22.1(13) s [Fin72]. The following β-decay studies at ISOLDE [Cai74; Hus76] extended the level scheme of

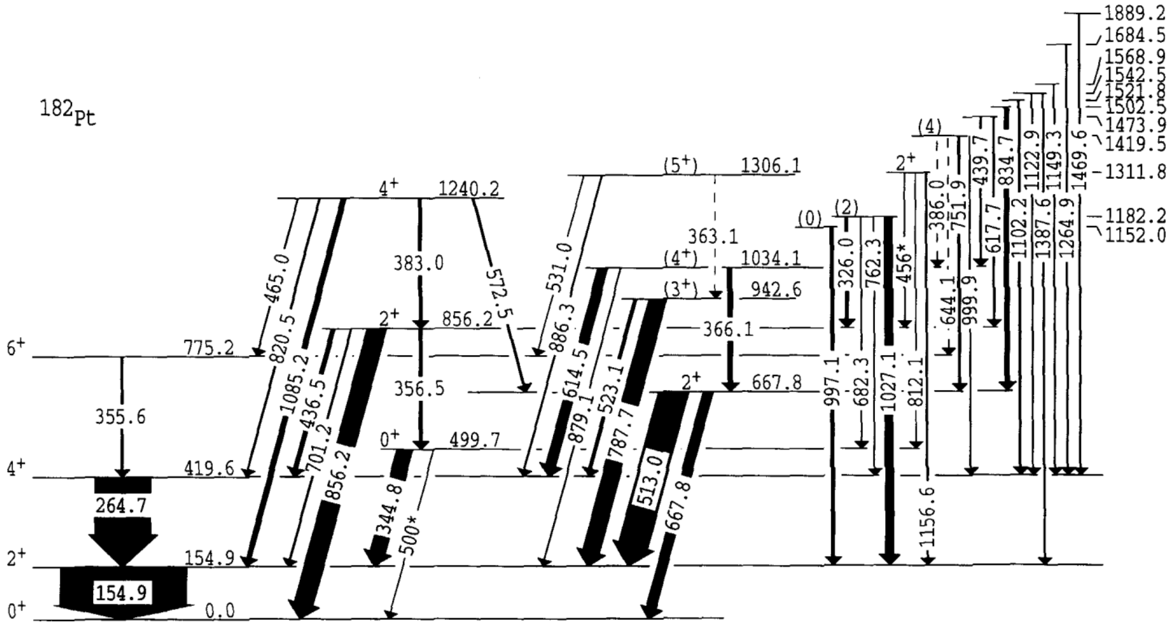

Figure 4.1: Level scheme of ^{182}Pt deduced in Ref. [Dav99].

^{182}Pt, including the coexisting 0_2^+ state and a 2_2^+ level as the bandhead of a γ-vibrational band.

The latest β-decay study of ^{182}Au was performed at the Australian National University [Dav99]. In this study, ^{182}Au was produced in the $4n$ channel of fusion-evaporation reaction of ^{144}Sm target with projectile ^{37}Cl. Several low-spin excited states in ^{182}Pt were identified, and its level scheme was established up to the excitation energy of about 1.9 MeV, which can be seen in Fig. 4.1. The authors of this study note that the maximum energy recorded was limited to 2 MeV. Spins and parities for some levels were determined based on internal conversion coefficient measurements and γ-γ angular correlations.

The isotope ^{182}Au has also been the subject of α-decay studies, investigating its decay to ^{178}Ir with $Q_\alpha = 5525(4)$ keV [Wan21]. It was produced in β decay of ^{182}Hg at ISOLDE and a 5353-keV α transition followed by the 55-keV γ ray was reported. The branching ratio for this transition was deduced to be $b_\alpha = 0.038(8)\%$ with the half-life of $T_{1/2} = 20(2)$ s [Hag79]. Nuclide ^{182}Au has also been studied at Oak Ridge, where it was directly produced in a complete fusion reaction of ^{19}F with an ytterbium target [Bin95]. The previously reported α-γ coincidence was observed, along with two more α decays with energies of 5283 and 5403 keV. The latter was interpreted as the direct decay to the ^{178}Ir g.s. Based on the low hindrance factor HF = 3 of the 5352-keV α decay, the same spin and parity was proposed for the 55-keV level in ^{178}Ir as for ^{182}Au

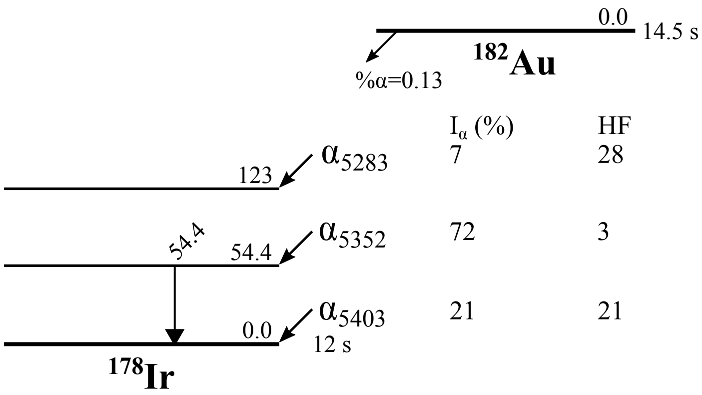

Figure 4.2: Previously-known α-decay scheme of ^{182}Au. The figure was taken from Ref. [Bin95] and modified.

g.s. The branching ratio was determined to be $b_\alpha(^{182}\mathrm{Au}) = 0.13(5)\%$ and a lower half-life value of $T_{1/2} = 14.5(13)$ s compared to the previous studies was reported. A similar value of $T_{1/2} = 15.3(10)$ s was obtained in the same study from the EC/β^+ decay using the 155-keV transition in ^{182}Pt.

The spin of ^{182}Au was at first deduced to be $I = 2-4$ based on the low-temperature nuclear orientation measurement of the g-factor, with the best agreement for $I = 3$ [Rom92]. However, a later ^{182}Hg β-decay study observed $M1$ transitions connecting 1^+ states (543 and 363 keV) directly to the ^{182}Au g.s., excluding spin $I = 3$ and proposing the value of $I^\pi = (2^+)$ [Ibr01]. The same assignment was also given by the in-source laser spectroscopy measurements of the hyperfine structure in atomic transitions [Har20]. A recent similar experiment at CRIS [CRI] with better laser resolution also confirmed the $I^\pi = (2^+)$ assignment [Yan24].

The isotope ^{182}Pt was discovered in 1963 via its α decay [Gra63; Amo11]. It decays dominantly into ^{182}Ir via EC/β^+ decay with branching ratio of 99.962(2)% [Bin95] and $Q_{EC} = 2883(25)$ keV [Wan21]. In the remaining 0.038(2)% [Bin95] of cases it α decays into ^{174}Os ($Q_\alpha = 4951(5)$ keV [Wan21]). The evaluated value half-life of ^{182}Pt is $T_{1/2} = 2.67(12)$ min [Sin15].

Besides previously mentioned β-decay studies of ^{182}Au, excited states in ^{182}Pt were also studied in in-beam measurements. Bands built on top of the 0^+_1, 0^+_2, and 2^+_2 known from β-decay studies were extended, and several new structures were identified in Ref. [Pop97]. Lifetime measurements for the excited states in ^{182}Pt were also performed using the recoil-distance Doppler-shift method, and half-lives for yrast levels up to 10^+ [Gla12] and 14^+ [Wal12] were determined.

Isotope ^{182}Pt, as well as other neutron-deficient even-even platinum isotopes, man-

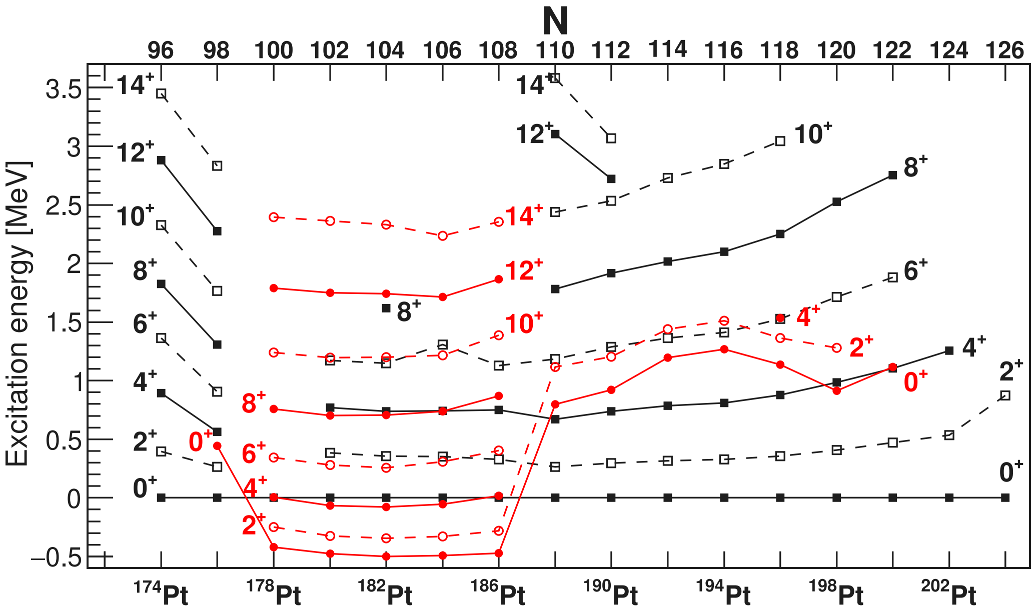

Figure 4.3: Energy systematics of rotational states in even-even platinum isotopes. Intruder states with 2p-6h configuration are marked in red, while states with normal order 0p-4h configuration are marked in black. The figure was taken from Ref. [Gar22].

ifests shape coexistence. The energy of the prolate 2p-6h intruder state ($\beta_2 \approx 0.25$) is lowered below the energy of the weakly deformed 0p-4h oblate configuration ($\beta_2 \approx -0.15$, [Ben87]) for isotopes $^{178-186}$Pt. This makes it the ground state for these isotopes, as can be seen in Fig. 4.3 [Hey00; Gar22]. In ^{182}Pt, the coexisting 0^+ state is located at an excitation energy of 500 keV. A phenomenological mixing model was used on the g.s. and excited levels of this isotope in Ref. [Dav99]. They showed a mixing of three unperturbed bands, two of them built on a more and a less deformed state with $K = 0$, respectively, and a γ-vibration band built with $K = 2$. While the more deformed state contributes dominantly to the 0^+_1 g.s. and the yrast states, the less deformed one forms predominantly the excited 0^+_2 state. Non-yrast states also contain a significant contribution of the γ band [Dav99].

4.2 Results for β decay of ^{182}Au

4.2.1 Introduction to γ-ray analysis

In total, the ^{182}Au decay measurement lasted for $t_M = 6.1$ h. A part of the time distribution of the detected events is in Fig. 4.4. Detector rates significantly increased

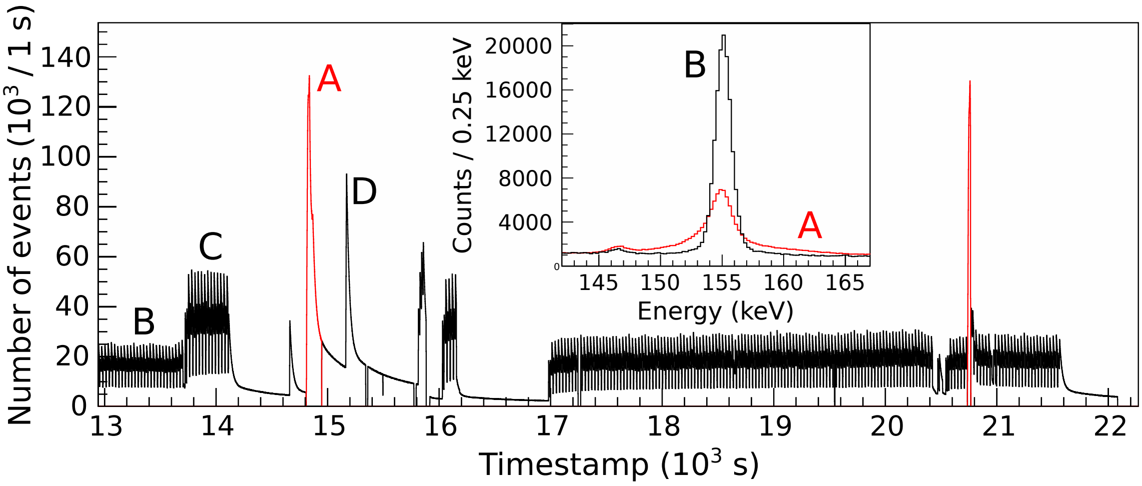

Figure 4.4: A part of the time distribution of all detected events. Labels A, B, C and D denote parts of the measurement with different event rates. Parts highlighted in red were left out of the analysis because the high rate of events caused deterioration of energy resolution. The inset compares the energy resolution of part A (3.3 keV, in red) and part B (1.6 keV in black) for the 154.9-keV line. The same time window of 140 s was used. Total counts in part A were higher than in part B, therefore, this spectrum was scaled down by a factor of 0.24 to match the background around the peak.

twice during the measurement as shown in Fig. 4.4, which caused deterioration of energy resolution of HPGe detectors compared to regular conditions (see inset in Fig. 4.4) approximately by a factor of 2 (from 1.6 keV FWHM in part B to 3.3 keV in part A for the 154.9-keV line). Therefore, the highlighted parts, 140 s and 30 s long, respectively, were left out of our γ-ray analysis. We also observed worsened resolution in two other parts of the measurement, denoted as C (1.8 keV) and D (2.1 keV) in Fig. 4.4, although not as drastically as for part A, therefore, they were included in the analysis.

The singles spectrum of all four Clover detectors using add-back measured during the remaining time of the experiment is shown in Fig. 4.5. The majority of observed γ rays originate from the β decay of ^{182}Au and its daughter products (^{182}Pt, ^{182}Ir and ^{182}Os). The total statistics collected during the measurement was 1.98×10^7 counts of the most intense 155-keV $2^+_1 \to 0^+_1$ γ-rays in ^{182}Pt. When corrected for detection efficiency and absolute transition intensity per 100 decays of 43.8(9) (determined in Chapter 4.2.5), this gives about $3.3(1){\times}10^8$ decays of ^{182}Au in the chamber. We also observed a small contamination of surface-ionised ^{182}Tl in the singles spectrum and determined its amount to be $\sim 1.7 \times 10^5$ decays in the same way as for ^{182}Au, using the

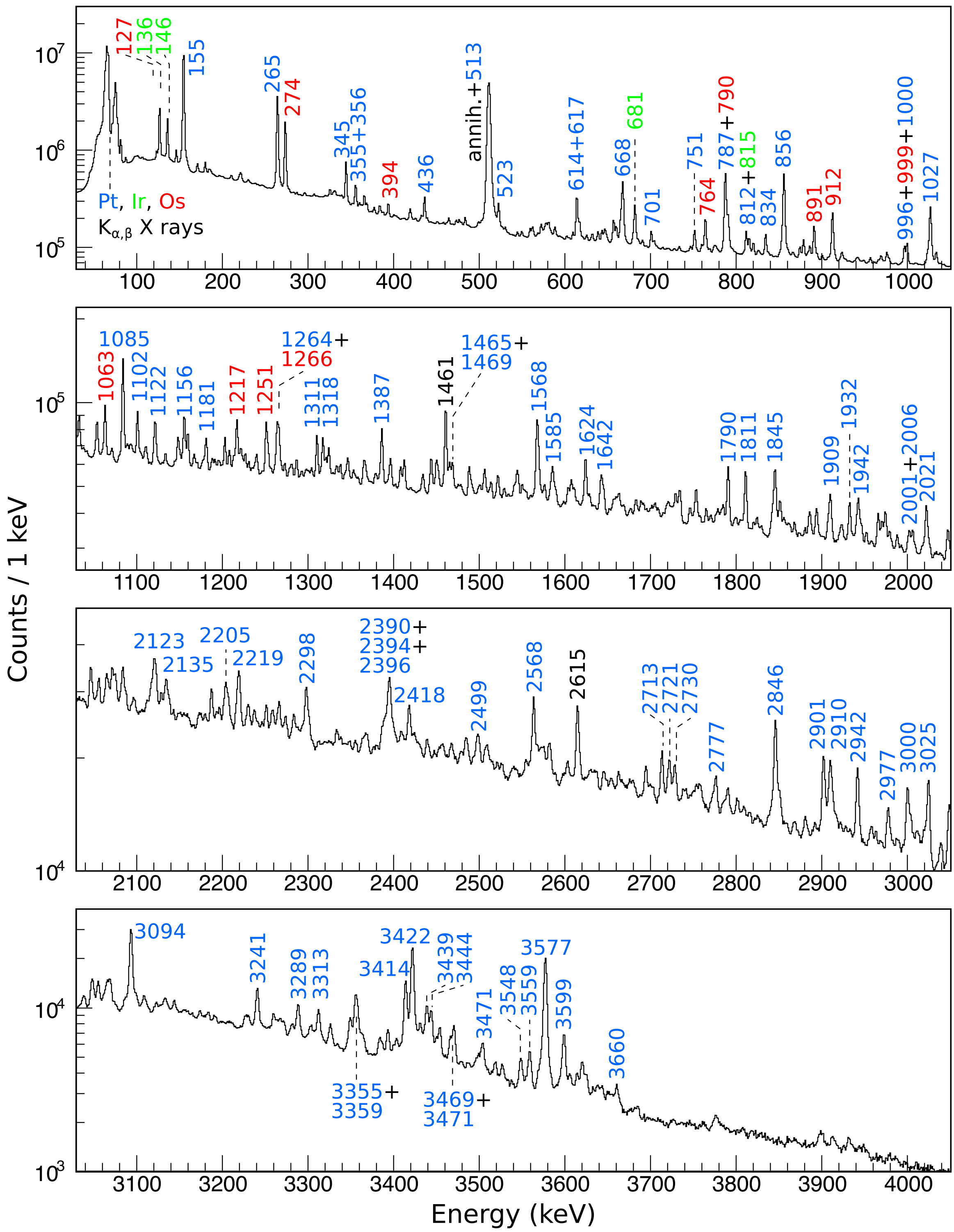

Figure 4.5: Singles γ ray spectrum from the measurement of ^{182}Au. Transitions following the β decay of ^{182}Au, ^{182}Pt and ^{182}Ir are labelled in blue, green, and red, respectively. Energies of natural background peaks are given in black.

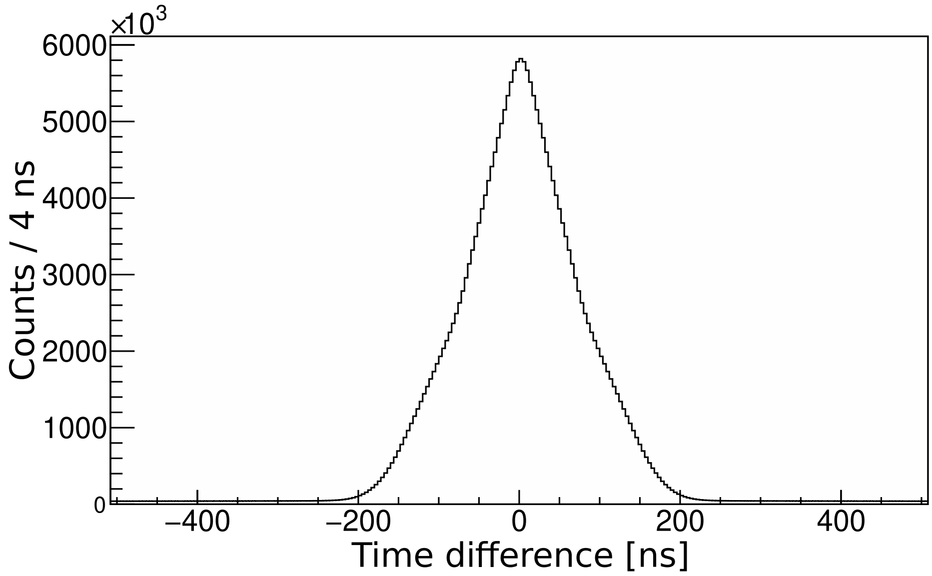

Figure 4.6: Time differences between detection times of two coincident γ quanta.

351-keV transition in ^{182}Hg. Its absolute intensity of ~ 76 per 100 decays was estimated from published transition intensities in Ref. [Rap17].

We used the method of prompt γ-γ coincidences between pairs of HPGe detectors in our analysis. This method requires defining a time window for prompt coincidences to keep the number of true coincident pairs as high as possible and, at the same time, to limit the number of random coincidences. The spectrum of time differences of coincident γ quanta is plotted in Fig. 4.6. Based on the width of the prompt peak, we used the time window of t_{pw} = 200 ns in the analysis of γ-γ coincidences. We also used the time window of 400 < t_{rw} < 600 ns to estimate the time-random coincidences present in the prompt window. To evaluate the effect of time-random coincidences in our data, we gated on the time-random coincidence matrix for several intense transitions and subtracted the obtained random coincidences from the coincidence spectra. Negligible differences were observed, therefore, subtraction of time-random coincidences was not applied to all γ-γ coincidences in general.

When gating on a certain transition, both the true coincidences and coincidences with the background under the peak are present in the spectrum. This background comes from Compton scattering of higher-energy γ rays and may introduce additional peaks to the spectrum, which belong to γ rays in true coincidence with the Compton scattered transition. Thus, background subtraction was performed for all γ-γ coincidence spectra. Background coincidences were estimated by gating on the background regions on both sides of the peak of interest. The background spectrum was appropri-

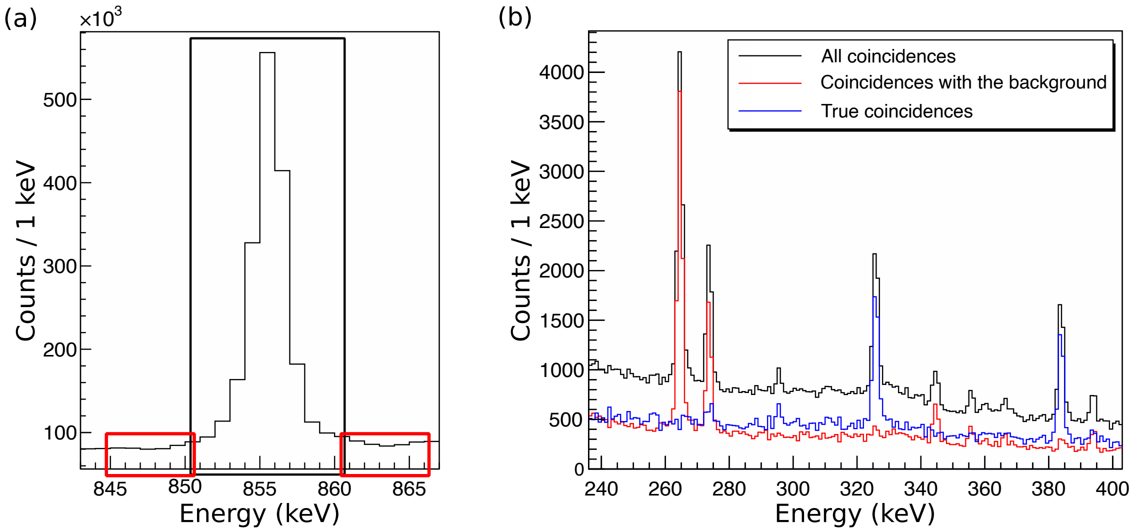

Figure 4.7: An example of background subtraction process for γ-γ coincidence spectra. Panel (a) shows the 856-keV transition in the singles spectrum. Black and red rectangles represent used gates for peak and background, respectively. Panel (b) shows a part of the γ-ray coincidences for the 856-keV transition. Coincidences with the whole peak are given in black and coincidences with the background in red. True coincidences obtained as their difference are given in the blue line. While the line at 856 keV is in coincidence with four strong transitions, only two of them are in true coincidence with this transition.

ately scaled to the gate width used for the peak. We note that the background region left of the peak of interest contains multiple Compton-scattered γ rays from the corresponding transition, and their subtraction could lower the statistics in the coincidence spectrum. However, this effect is very small as no statistically significant differences were observed when gating on background on both sides compared to the right side only. An example of a background subtraction process for a coincidence spectrum can be seen in Fig. 4.7.

The method of γ-γ coincidences can lead to the appearance of artificial peaks in the spectrum caused by the Compton scattering, as can be seen in Fig. 4.8. In the Compton scattering process, γ rays deposit part of their energy in one detector, and the scattered quantum can be detected in another detector with a certain probability. This creates an artificial peak in the gated spectrum with energy $E_C = E_\gamma - E_G$, where E_γ is the initial energy of the scattered γ ray and E_G is the energy of the gated transition. The same artificial peaks appear in both background spectra with shifted energy (E_G is different), therefore, background subtraction creates regions of negative counts above

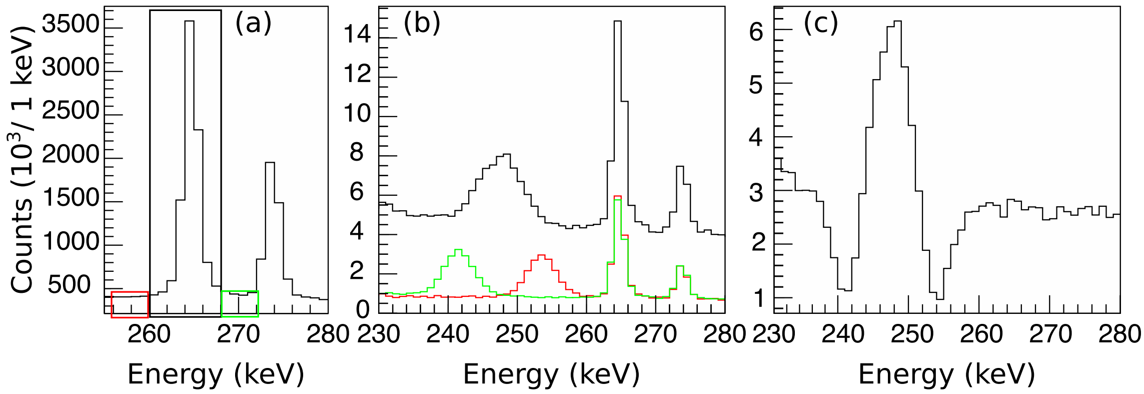

Figure 4.8: An origin of artificial peaks in γ-γ coincidences. (a) The 265-keV transition in singles γ-ray spectrum. (b) Coincidences gated on the 265-keV transition (black line) and background below (red line) and above (green line) this peak. Artificial peak caused by Compton scattering of the 511-keV γ ray is wider than regular peaks, and its position is shifted for each gated region. (c) The resulting artificial peak ($E_C = 511 - 265\,\text{keV} = 246\,\text{keV}$) in background-subtracted coincidences of the 265-keV transition.

and below the artificial peak.

The identification of γ rays emitted from excited states of ^{182}Pt was performed using coincidences with previously known transitions in ^{182}Pt and with platinum X-rays. Coincidence spectra of the two most intense transitions in ^{182}Pt, namely the 155-keV $2_1^+ \rightarrow 0_1^+$ and the 265-keV $4_1^+ \rightarrow 2_1^+$ transitions, are shown in Fig. 4.9. Similar spectra were constructed for all previously reported transitions, except the one at 762 keV, which could not be resolved from the 763-keV transition following the β decay of ^{182}Ir. Coincidences for several intense transitions in ^{182}Pt are shown in Figs. A.1-A.6 in Appendix A. Additionally, newly observed transitions were also gated on to confirm their placement. Such coincidence spectra were used to build the level scheme of ^{182}Pt. This process is shown in Fig. 4.10.

The intensity of γ-ray transitions was determined whenever possible from the singles γ-ray spectrum (see Fig. 4.5). In this case, the total number of γ quanta emitted can be simply obtained using the area of the peak S and detection efficiency for the corresponding energy ε_γ:

$$N_\gamma = \frac{S}{\varepsilon_\gamma} \tag{4.1}$$

The intensity was determined from γ-γ coincidence spectra in the remaining cases. The

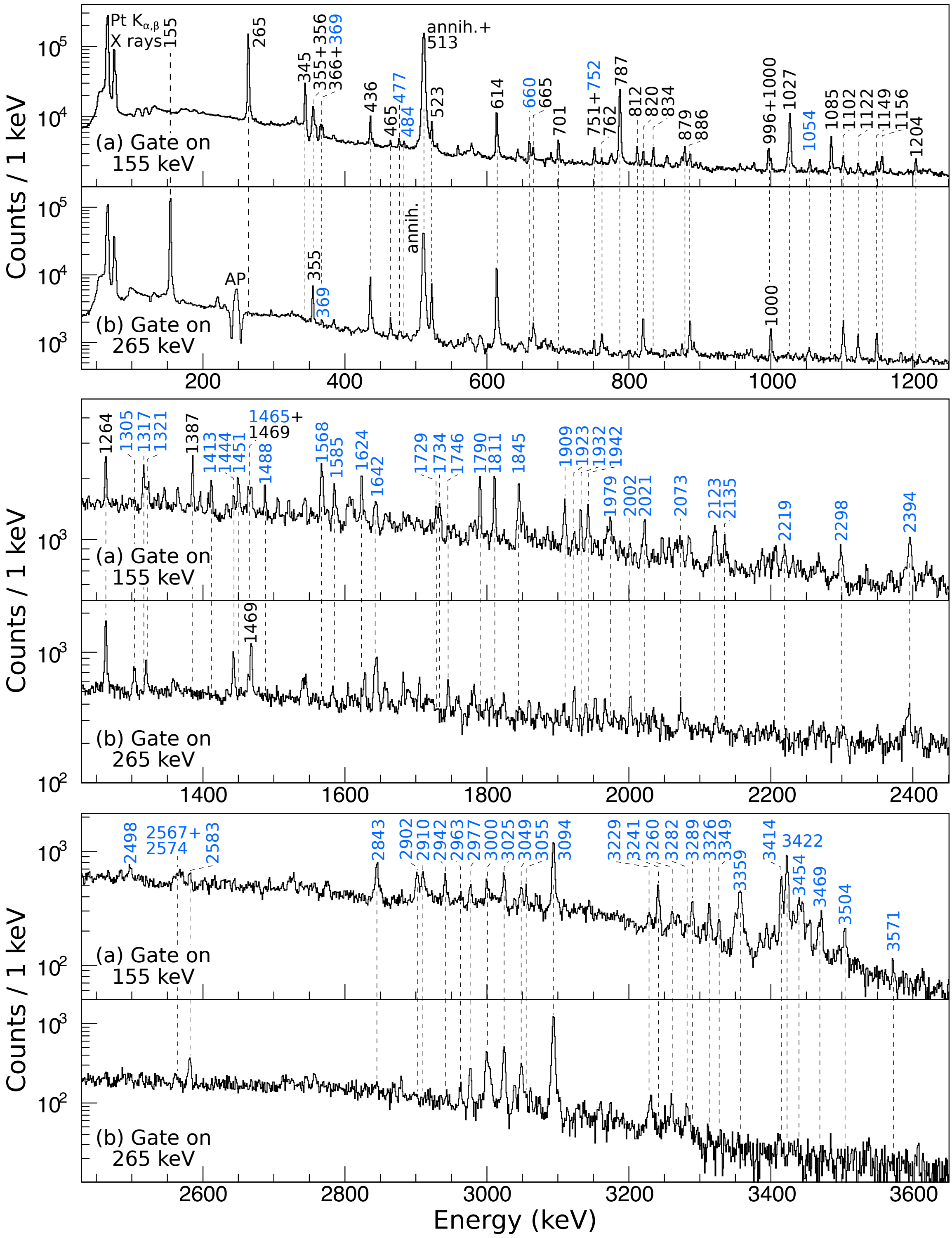

Figure 4.9: γ-ray coincidence spectra with the gate on (a) the 155-keV $2_1^+ \rightarrow 0_1^+$ transition, (b) the 265-keV $4_1^+ \rightarrow 2_1^+$ transition. AP stands for the artificial peak from Compton scattering. New transitions are highlighted in blue.

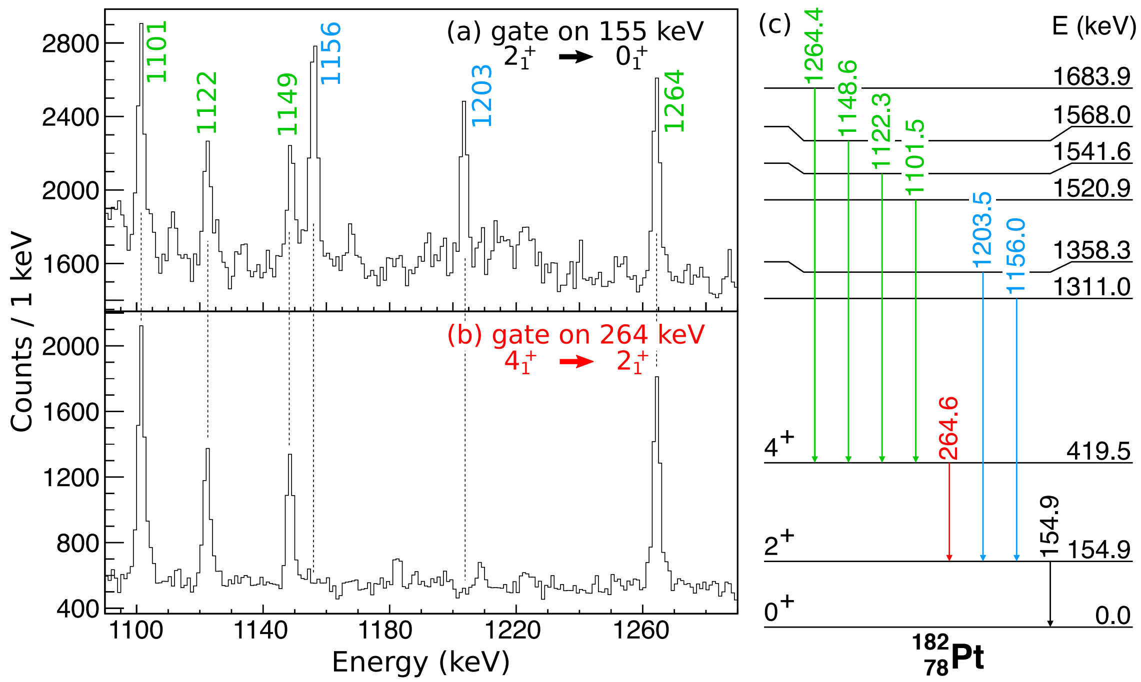

Figure 4.10: An example of level scheme construction based on coincidence spectra. Parts (a) and (b) show coincidence spectra gated on the 155-keV $2_1^+ \rightarrow 0_1^+$ and the 265-keV $4_1^+ \rightarrow 2_1^+$ transitions, respectively. Part (c) shows the partial level scheme deduced from these coincidences. Transitions used as gates are known to be in coincidence [Dav99], therefore, γ rays observed in both spectra (labelled in green) could be placed as feeding the 420-keV level. Transitions coincident only with the 155-keV line (labelled in blue) were placed as feeding the level with the same energy. Note that other coincidence gates were investigated to rule out the possibility of these transitions to feed even higher-lying levels, and confirm their assignment.

equation 4.1 needs to be modified for such transitions in the following way:

$$N_\gamma = \frac{S}{0.75\varepsilon_\gamma \varepsilon_G}(1 + \alpha_G) \tag{4.2}$$

where ε_G and α_G are efficiency and total conversion coefficient for the gated γ line respectively. The second γ ray in coincidence must be detected in a different HPGe detector than the first one, therefore, its detection efficiency is lowered, giving rise to the approximate factor of 0.75.

All γ-ray intensities I_γ were normalised to the intensity of the 155-keV transition:

$$I_\gamma = \frac{N_\gamma}{N_{155}} \times 100\% \tag{4.3}$$

If transition feeding a particular level was not seen in coincidence with all transitions deexciting this state, its intensity was scaled up to include an unseen portion of this transition. For example, let's consider a transition with total intensity I_f that feeds a level, which is deexcited by four transitions with relative intensities I_1, I_2, I_3, and I_4, but it is observed in coincidence only with the two most intense transitions. The full intensity of transition f can be calculated as follows:

$$I_f = (I_{f,1} + I_{f,2}) \frac{I_1 + I_2 + I_3 + I_4}{I_1 + I_2}, \tag{4.4}$$

where $I_{f,1}$ and $I_{f,2}$ are intensities of the transition f determined from coincidences with transitions 1 and 2, respectively.

An important effect on transition intensities is the coincidence explained in Chapter 3.4.1. Note that a summing of γ rays with the 511 keV line from electron-positron annihilation, or platinum X rays can also occur since they are also in true coincidence with γ rays in ^{182}Pt. The correction was done in two ways. It is already performed for γ rays with intensity determined using γ-γ coincidences by the factor 0.75 in Eq. 4.2. This effectively adds one third of the detected counts to their intensity, since transitions in coincidence are detected in three detectors out of four in total. The same intensity was added to the gated γ ray and subtracted from the crossover transition if it existed. In the case of singles γ rays, the correction can be calculated in the following way

$$N_{sum} = \frac{1}{4} \varepsilon_1 S_2, \tag{4.5}$$

where ε_1 and S_2 are detection efficiency and detected counts in singles spectrum for the bottom and top γ ray in the cascade, respectively. The correction for the coincidence summing is the most important in cases of weak crossover transitions parallel to strong cascades. For example, the summing made up about 33% of the 1181-keV transition (1181 keV → 0 keV with parallel cascade of 155 keV and 1026 keV γ rays) and 46% of the 665-keV transition (1607 keV → 942 keV, where summing of the 155 keV γ ray with an annihilation quantum results in the same energy).

We observed differences in transition intensities obtained from the singles γ rays and γ-γ coincidences up to ~ 12%. This value was determined from intense transitions, where contamination by γ rays with similar energy was ruled out by γ-γ analysis. We attribute these differences to the γ-γ angular correlations. Angular distribution of γ rays depends on their multipolarities, which are unknown for most of the transitions in this work. Because of this, we added a systematic relative uncertainty of 12% in quadrature to all uncertainties of γ-ray intensities determined from coincidences.

4.2.2 Results of γ-ray analysis

We identified 147 excited levels and 386 transitions in ^{182}Pt based on coincidence data. The majority of them, 125 levels and 336 transitions, are new. A partial summary of deduced levels and observed transitions with their relative intensities is in Table 4.1. The full table is shown in Appendix C.

We confirm almost all γ-ray transitions and all levels reported in Ref. [Dav99]. The only exception is the tentatively assigned 644-keV transition previously placed between the 1419- and 775-keV (6^+_1) levels. Such a placement would require the coincidence of the 355-, 265- and 155-keV transitions with the 644-keV line, all with the same intensity when corrected for the internal conversion and γ-ray efficiency. As can be seen in Fig. 4.11, the 355-keV transition is missing, and the 265-keV peak is much weaker than the 155-keV one. Instead, lines at 513 and 668 keV are present, therefore, we place the 644-keV transition between the 1311- and the 668-keV levels in the level scheme, see Fig. 4.12. Transitions with energies 265 and 856 keV present in the spectrum do not fit this placement, however, they come from the admixture of the 646-keV line present in the gated region.

The lowest parts of the ^{182}Pt level scheme deduced in this Thesis are shown in Figs. 4.12 and 4.13. Figure 4.14 contains the highest-lying levels in ^{182}Pt assigned in this work. The whole level scheme is presented in Appendix B.

We note that most transitions, our values are 0.4-0.6 keV lower than the values

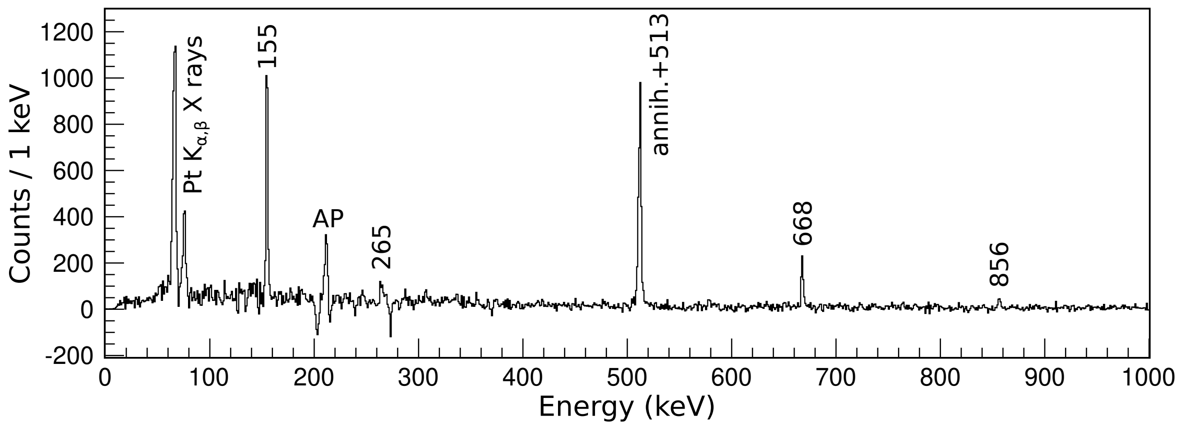

Figure 4.11: Background-subtracted γ-ray coincidence spectrum gated on the 643.5-keV transition. AP stands for the artificial peak caused by Compton scattering. Small peaks at 265 and 856 keV are caused by the presence of the 646-keV transition feeding the 856-keV level in the gated region.

published in Ref. [Dav99]. The highest difference is 1.0 keV for the 1386-keV transition deexciting the level at 1541 keV. We verified our calibration by comparing energy values for peaks from natural background or ^{182}Au daughter isotopes in Chapter 3.4.1. Based on these differences (see Table 3.2), we estimated the uncertainty of our calibration to be up to 0.2 keV and 0.3 keV for energies below and above 1600 keV, respectively.

We also found several transitions not reported in Ref. [Dav99] but observed in other studies. These are two tentatively assigned 1310.9- and 274.8-keV transitions deexciting the 1311- and 942-keV levels, respectively, from Ref. [Cai74]. Additionally, we placed five more transitions (296.4, 865.3, 900.4, 1054.4, and 1203.5 keV) in the level scheme, which were reported as unplaced in the same study. Three more γ rays with energies of 431.2, 1088.1 and 1444.0 keV coming from an in-beam spectroscopy study [Pop97] were also included in the level scheme. The first establishes the 5^- level at 1670.7 keV level, while the latter two deexcite the 6^+ 1863.4-keV level as shown in Figs. B.3 and B.4, respectively.

New transitions connecting excited states in ^{182}Pt directly to the g.s. were identified using coincidences with platinum X rays. Three of them with energies of 1181, 1568, and 1753 keV were placed in the decay scheme only tentatively (see Figs. 4.12, 4.13 and B.3). They were identified as doublets with transitions already placed in the level scheme based on the matching energy with established levels and large differences in intensity of corresponding peaks in the singles γ-ray and coincidence spectra. This difference was used for the determination of their intensity.

The analysis of observed transitions to levels of known spin allows us to assign spin values for certain levels. Since the observed γ-rays have prompt character, we only consider the $E1$, $M1$, $E2$, or $M2$ multipolarities, restricting the maximum change in angular momentum to 2. However, Weisskopf estimates predict half-lives of approximately 100 ns also for $E3$ transitions with energies above ~1300 keV, therefore, we consider $\Delta L \leq 3$ for transitions above this energy. This allows us to limit the range of possible spins to $I = (1,2)$ and $I = (2,3)$ for levels at 1722, 1753, 1966 keV and at 1568, 2006, 2077 keV, respectively, see Table C.1. Similarly, possible spin ranges for other levels were estimated based on the connecting transitions to levels with known I^π, as shown in Tables 4.1 and C.1.

The intensity of the 513-keV transition could not be determined directly from singles or coincidence spectra because of its vicinity to the annihilation peak at 511 keV. Instead, its intensity was obtained from transitions feeding the 668-keV level, see Fig. 4.15. These transitions can be seen in coincidence with the 668-keV and the 155-keV γ rays

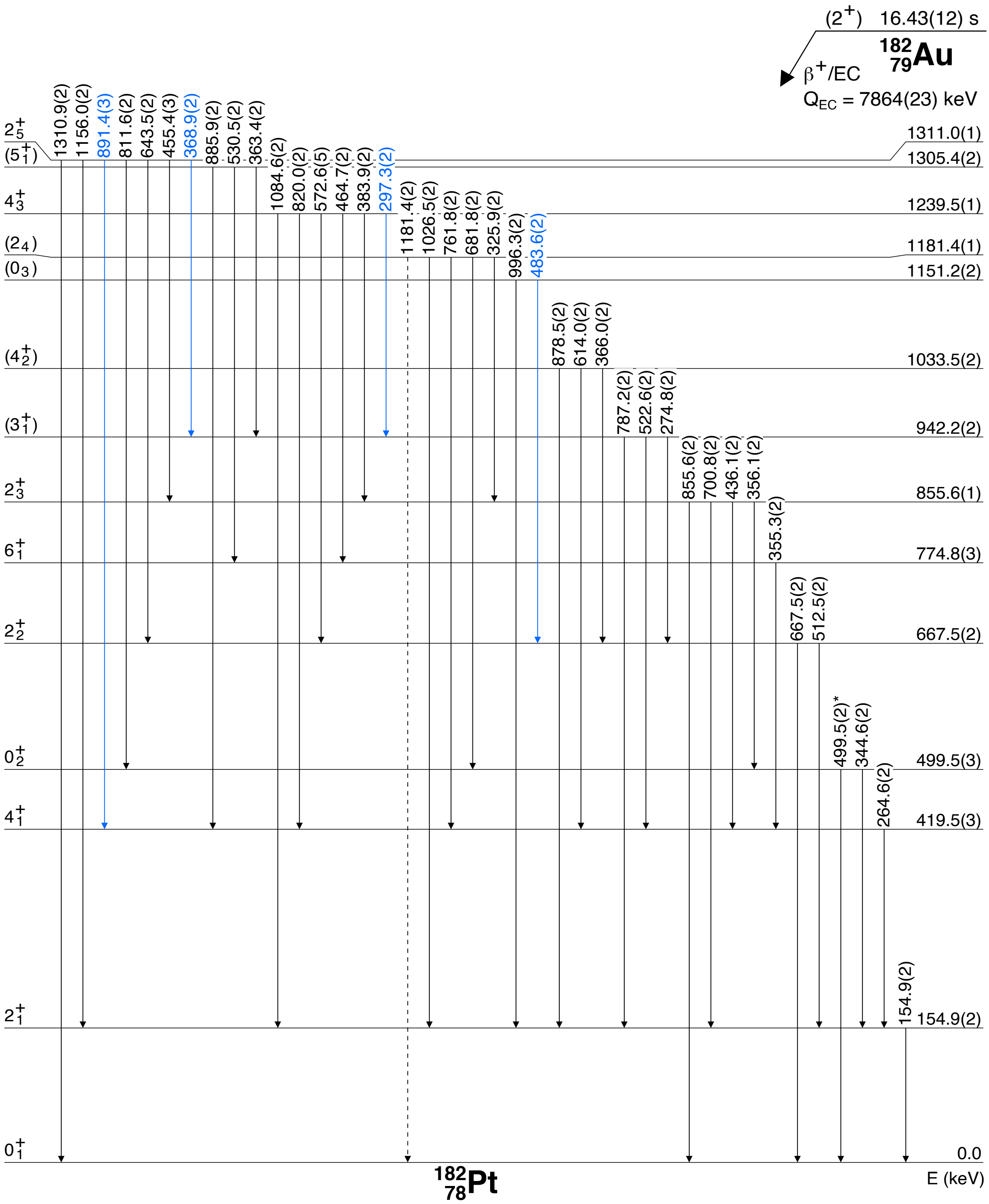

Figure 4.12: The first part of the level scheme of excited states in ^{182}Pt populated in EC/β^+ decay of ^{182}Au. The spin and parity values are taken from Ref. [Dav99]. Transitions and levels highlighted in blue are newly assigned in this study. Tentative transitions are plotted with dashed lines. Half-life, Q_{EC} and spin assignment for ^{182}Au g.s. are from our work, Ref. [Wan21] and Ref. [Har20], respectively.

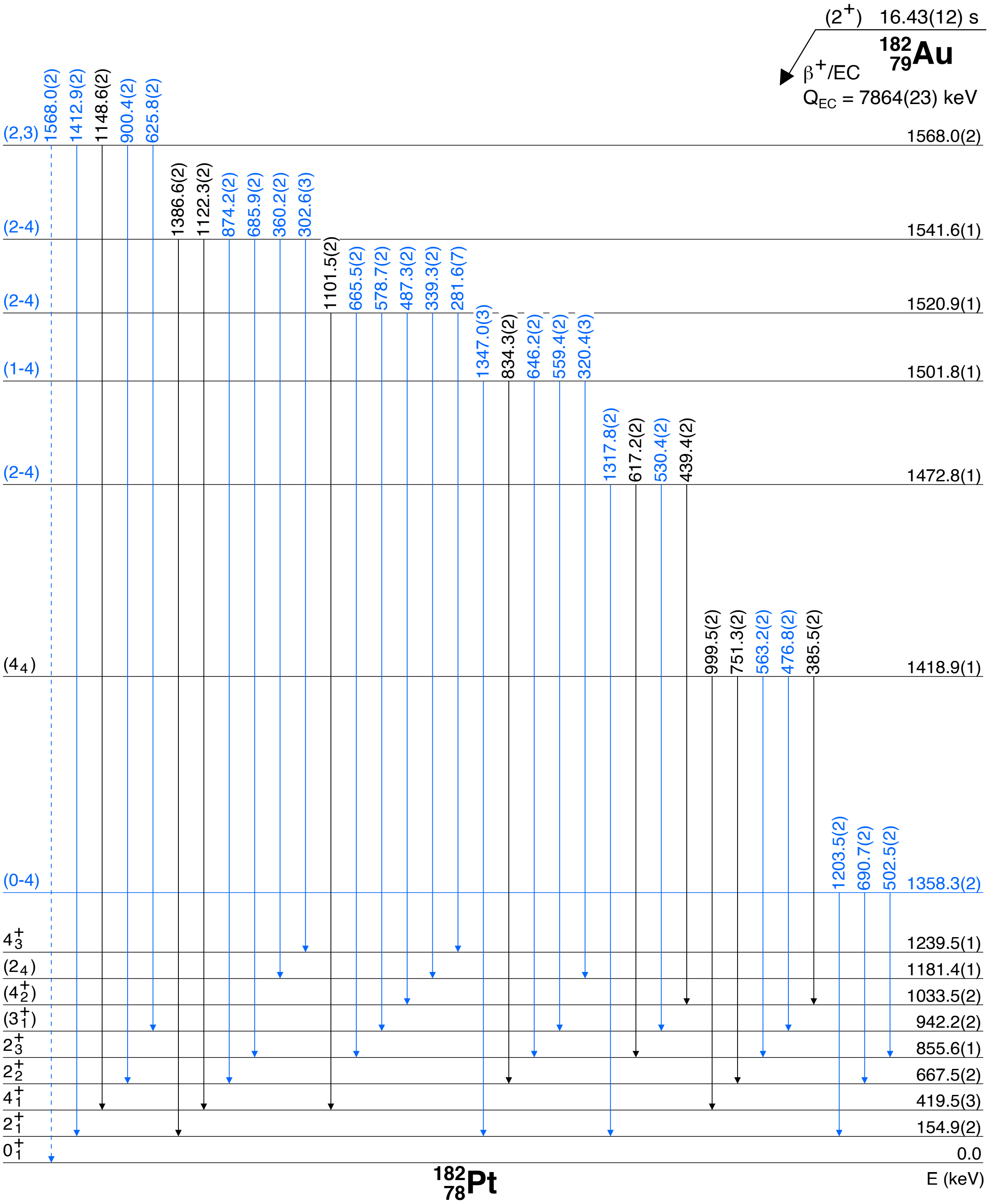

Figure 4.13: The second part of the level scheme of excited states in ^{182}Pt populated in EC/β^+ decay of ^{182}Au. The spin and parity values are taken from Ref. [Dav99] or deduced from the deexcitation paths. Transitions, levels and level spins highlighted in blue are newly assigned in this study. Tentative transition is plotted with a dashed line. Half-life, Q_{EC} and spin assignment for ^{182}Au g.s. are from our work, Ref. [Wan21] and Ref. [Har20], respectively.

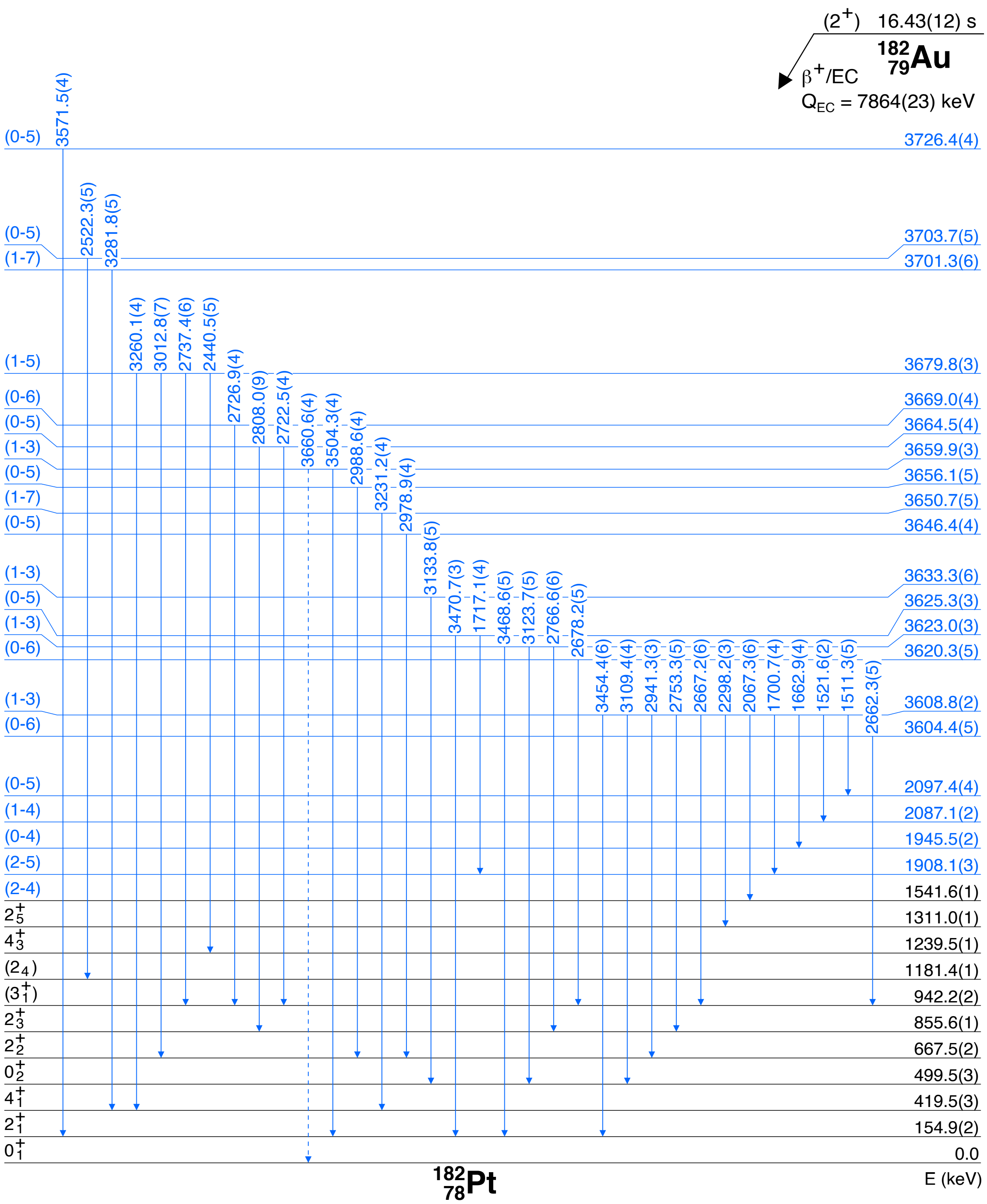

Figure 4.14: The final part of the level scheme of excited states in ^{182}Pt populated in EC/β^+ decay of ^{182}Au. The spin and parity values are taken from Ref. [Dav99] or deduced from the deexcitation paths. Transitions, levels and level spins highlighted in blue are newly assigned in this study. Tentative transition is plotted with a dashed line. Half-life, Q_{EC} and spin assignment for ^{182}Au g.s. are from our work, Ref. [Wan21] and Ref. [Har20], respectively.

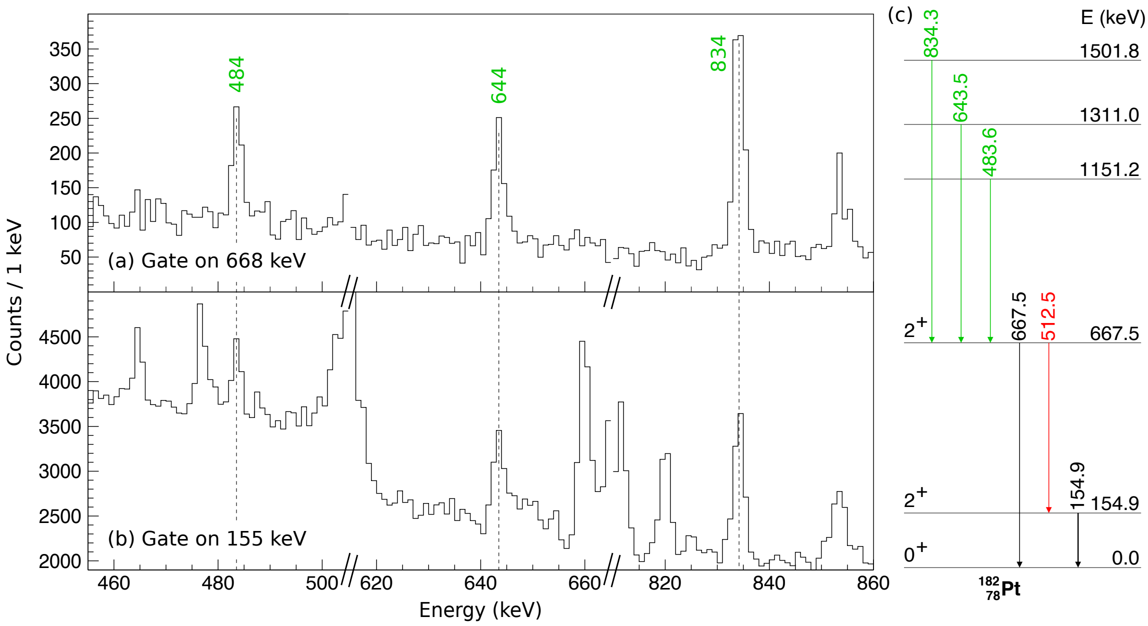

Figure 4.15: An example of γ-γ coincidences used to determine the intensity of the 513-keV γ ray (in red). It was calculated by comparing the intensity of several transitions (in green) feeding the 668-keV level, when gated on (a) the 668-keV and (b) the 155-keV transitions. (c) Partial level scheme of ^{182}Pt with relevant transitions and levels.

(the latter being in a cascade with the 513-keV transition, see Fig. 4.15), with intensities $I_{\gamma-668}$ and $I_{\gamma-155}$, respectively. By comparing these intensity values, we obtain an intensity ratio between the 513- and 668-keV γ rays. The intensity of the 513-keV transition can then be calculated in the following way:

$$I_{513} = I_{668} \frac{I_{\gamma-155}}{I_{\gamma-668}}, \tag{4.6}$$

where I_{668} is the intensity of the 668-keV transition determined from singles γ rays. The resulting value in Table C.1 was determined as the weighted average of values obtained from several of the most intense transitions feeding the 668-keV level.

Table 4.1: A partial list of levels and transitions following the EC/β^+ decay of ^{182}Au. E_i and E_f are the respective energies of the initial and final states of the γ-ray transition with the energy E_γ. Values of the initial and final spin and parity I_i^π, I_j^π are taken from Refs. [Dav99; Pop97], or deduced from the de-excitation paths. Tentative transitions and levels are written in italics. Relative γ-ray intensities I_γ are normalised to the intensity of the 155-keV transition. Values determined from coincidence γ-γ spectra are indicated with an asterisk. For the absolute intensity per 100 β decays, multiply by 0.438(9). The total transition intensities I_{tot} were calculated using internal conversion coefficients α_{tot} and are normalised to 100 units for the 155-keV γ-ray intensity. ICCs were taken from Ref. [Kib08] in the case of known multipolarity ([1], $E2$ in all cases), taken from the NNDC evaluation ([2]) [Sin10], evaluated in this work ([3]), or calculated as the average of the ICC for the $E1$ and $M2$ multipolarities ([4]), see Chapter 4.2.5 for details. The last column contains branching ratios b of transitions de-exciting each level, normalised to a sum of 100. The full table is shown in Appendix C.

E_i (keV)	I_i^π	E_f (keV)	I_f^π	E_γ (keV)	I_γ (%)	α_{tot}	I_{tot} (%)	b (%)
154.9(2)[d]	2_1^+	0	0_1^+	154.9(2)[d]	100	0.888(13) [1]	188.8(13)	100
419.5(3)[d]	4_1^+	154.9(2)	2_1^+	264.6(2)[d]	45.7(19)	0.1443(21)[1]	52.3(22)	100
499.5(3)[d]	0_2^+	154.9(2)	2_1^+	344.6(2)[d]	7.44(32)	0.0659(10)[1]	7.93(34)	68(3)
		0	0_1^+	499.5(3)[d]	-	-	3.82(43)	32(3)
667.5(2)[d]	2_2^+	154.9(2)	2_1^+	512.5(2)[d]	28.2(34)*	0.066(8)[3]	30.1(36)	76(2)
		0	0_1^+	667.5(2)[d]	9.64(41)	0.01268(18)[1]	9.76(42)	24(2)
774.8(3)[d]	6_1^+	419.5(3)	4_1^+	355.3(2)[d]	1.18(16)*	0.0605(9)[1]	1.25(17)	100
855.6(1)[d]	2_3^+	499.5(3)	0_2^+	356.1(2)[d]	1.63(23)*	0.0601(9)[1]	1.73(24)	7.1(10)
		419.5(3)	4_1^+	436.1(2)[d]	2.98(13)	0.0349(5)[1]	3.08(13)	12.6(6)
		154.9(2)	2_1^+	700.8(2)[d]	1.18(16)*	0.93(13)[3]	2.27(34)	9.2(13)
		0	0_1^+	855.6(2)[d]	17.20(73)	0.00749(11)[1]	17.33(74)	71.1(15)
942.2(2)[d]	(3_1^+)	667.5(2)	2_2^+	274.8(2)[a]	0.47(10)*	0.26(13)[2]	0.59(14)	3(7)
		419.5(3)	4_1^+	522.6(2)[d]	1.96(26)*	0.046(24)[2]	2.05(28)	10.5(13)
		154.9(2)	2_1^+	787.2(2)[d]	16.68(65)	0.0092(4)[2]	16.84(66)	86.4(14)
1033.5(2)[d]	(4_2^+)	667.5(2)	2_2^+	366.0(2)[d]	1.43(19)*	0.0557(8)[1]	1.51(20)	18(2)
		419.5(3)	4_1^+	614.0(2)[d]	5.72(24)	0.025(7)[2]	5.86(25)	71(2)
		154.9(2)	2_1^+	878.5(2)[d]	0.90(12)*	0.024(22)[4]	0.92(13)	11.1(14)
1151.2(2)[d]	(0_3)	667.5(2)	2_2^+	483.6(2)	0.48(8)*	0.13(12)[4]	0.55(11)	28(5)
		154.9(2)	2_1^+	996.3(2)[d]	1.38(19)*	0.00551(8)[1]	1.39(19)	72(5)
1181.4(1)[d]	(2_4)	855.6(1)	2_3^+	325.9(2)[d]	0.92(13)*	0.16(9)[2]	1.06(17)	10.5(15)
		499.5(3)	0_2^+	*681.8(2)*[d]	0.09(3)*	0.049(45)[4]	0.09(3)	0.9(3)
		419.5(3)	4_1^+	761.8(2)[d]	0.37(6)*	0.036(32)[4]	0.38(6)	3.7(6)
		154.9(2)	2_1^+	1026.5(2)[d]	8.08(34)	0.0102(19)[2]	8.16(35)	80.5(16)
		0	0_1^+	*1181.4(2)*	0.45(5)	0.011(10)[4]	0.45(5)	4.5(5)
1239.5(1)[d]	4_3^+	942.2(2)	(3_1^+)	297.3(2)	0.14(3)*	0.62(60)[4]	0.23(9)	3.5(14)
		855.6(1)	2_3^+	383.9(2)[d]	0.98(14)*	0.0489(7)[1]	1.03(14)	15.9(19)
		774.8(3)	6_1^+	464.7(2)[d]	0.37(6)*	0.0297(5)[1]	0.38(6)	5.8(9)

Table 4.1: (*Continued*)

E_i (keV)	I_i^π	E_f (keV)	I_f^π	E_γ (keV)	I_γ (%)	α_{tot}	I_{tot} (%)	b (%)
		667.5(2)	2_2^+	572.6(5)[d]	0.35(11)*	0.081(75)[4]	0.38(12)	5.8(18)
		419.5(3)	4_1^+	820.0(2)[d]	0.95(4)	0.20(7)[2]	1.14(8)	17.5(13)
		154.9(2)	2_1^+	1084.6(2)[d]	3.34(14)	0.00467(7)[1]	3.35(14)	52(2)
1305.4(2)[d]	(5_1^+)	942.2(2)	(3_1^+)	363.4(2)[d]	0.11(3)*	0.0568(8)[1]	0.12(3)	11(3)
		774.8(3)	6_1^+	530.5(2)[d]	0.13(2)*	0.10(9)[4]	0.14(3)	13(3)
		419.5(3)	4_1^+	885.9(2)[d]	0.79(11)*	0.024(21)[4]	0.81(11)	76(4)
1311.0(1)[d]	2_5^+	942.2(2)	(3_1^+)	368.9(2)	0.92(13)*	0.31(29)[4]	1.20(32)	17(4)
		855.6(1)	2_3^+	455.4(3)[d]	0.05(2)	17.3(75)[3]	0.97(11)	13.7(16)
		667.5(2)	2_2^+	643.5(2)	0.64(9)*	0.058(53)[4]	0.68(10)	9.6(15)
		499.5(3)	0_2^+	811.6(2)[d]	1.66(23)*	0.00835(12)[1]	1.67(24)	24(3)
		419.5(3)	4_1^+	891.4(3)	0.13(4)*	0.00689(10)[1]	0.13(4)	1.9(6)
		154.9(2)	2_1^+	1156.0(2)[d]	1.35(6)	0.012(10)[4]	1.37(6)	19.4(14)
		0	0_1^+	1310.9(2)[a]	1.05(5)	0.00326(5)[1]	1.05(5)	14.9(11)
1358.3(2)	(0-4)[f]	855.6(1)	2_3^+	502.5(2)	0.08(2)*	0.12(11)[4]	0.09(3)	9(3)
		667.5(2)	2_2^+	690.7(2)	0.19(7)*	0.047(43)[4]	0.19(7)	20(6)
		154.9(2)	2_1^+	1203.5(2)[b]	0.70(10)*	0.011(9)[4]	0.71(10)	72(6)
1418.9(1)[d]	(4_4)	1033.5(2)	(4_2^+)	385.5(2)[d]	0.10(3)*	0.10(6)[2]	0.11(4)	4.5(15)
		942.2(2)	(3_1^+)	476.8(2)	0.44(7)*	0.14(13)[4]	0.50(10)	20(4)
		855.6(1)	2_3^+	563.2(2)	0.15(3)*	0.09(8)[4]	0.16(3)	6.5(15)
		667.5(2)	2_2^+	751.3(2)[d]	1.03(17)*	0.00982(14)[1]	1.04(17)	42(5)
		419.5(3)	4_1^+	999.5(2)[d]	0.63(9)*	0.017(26)[4]	0.64(9)	26(4)
1472.8(1)[d]	(2-4)[f]	1033.5(2)	(4_2^+)	439.4(2)[d]	0.41(3)	0.180(13)[4]	0.49(8)	13(2)
		942.2(2)	(3_1^+)	530.4(2)	0.17(3)*	0.100(5)[4]	0.18(4)	5(10)
		855.6(1)	2_3^+	617.2(2)[d]	1.88(8)	0.070(54)[4]	2.00(14)	54(3)
		154.9(2)	2_1^+	1317.8(2)	1.02(15)*	0.0080(71)[4]	1.03(15)	28(3)

[a] Reported as a tentative transition in Ref. [Cai74].

[b] Reported as an unplaced transition in Ref. [Cai74].

[c] Known from in-beam spectroscopy study from Ref. [Pop97].

[d] Known from decay spectroscopy study from Ref. [Dav99].

[e] Observed only in the spectrum of conversion electrons.

[f] Value of spin deduced from the analysis of the deexcitation paths.

[1] Conversion coefficient taken from BrIcc [Kib08] considering an $E2$ multipolarity.

[2] Conversion coefficient taken from the NNDC evaluation [Sin10]

[3] Conversion coefficient evaluated in this work.

[4] Conversion coefficient calculated as the average of the ICC for the $E1$ and $M2$ multipolarities.

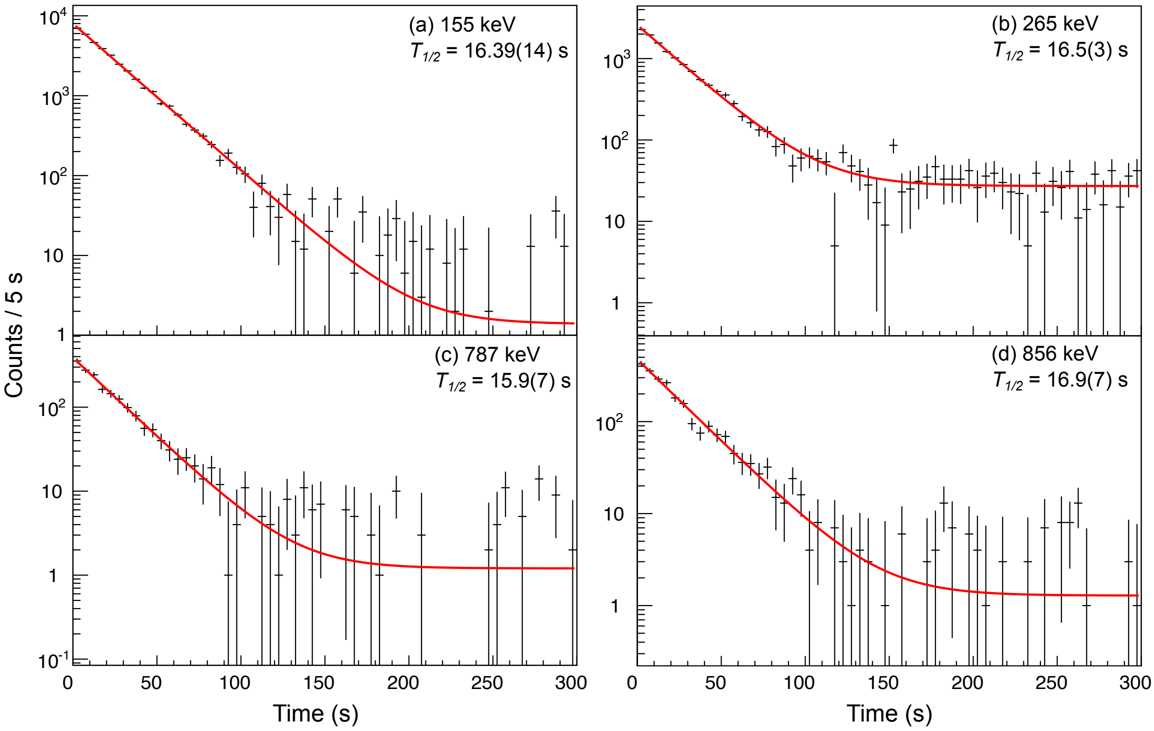

Figure 4.16: Time distributions of the (a) 155-keV, (b) 265-keV, (c) 787-keV and (d) 856-keV γ-ray transitions. The red line is the fit through experimental values using the exponential function with a constant background. Note that visual disagreement between the background regions of the time distributions and fitted functions comes from the choice of logarithmic scale, omitting negative bins, which lower the average background.

4.2.3 Half-life of ^{182}Au

To determine the ^{182}Au half-life, we used the decay curve from the end of the experimental measurement (see Fig. 4.4) when the beam gate was closed and the tape movement was stopped. Background subtraction for time distributions was performed in the same way as for the γ-γ coincidence spectra. Decay curves of several intense γ-ray transitions were fitted with an exponential function and a constant background. Fits of the time distributions for the 155-, 265-, 787- and 856-keV transitions are shown in Fig. 4.16. The list of all transitions used with the obtained values is in the Table 4.2. All values are compatible with each other within uncertainties. Their weighted average $T_{1/2}$ = 16.43(12) s agrees with the evaluated half-life of ^{182}Au $T_{1/2}$ = 15.5(4) s [Sin15] within 2σ.

Table 4.2: The values of ^{182}Au half-life obtained from time distributions gated on several different γ-ray transitions in ^{182}Pt.

E_γ [keV]	I_γ [%]	E_i [keV]	J_i^π	$T_{1/2}$ [s]
154.9	100	154.9	2_1^+	16.39(14)
264.6	45.7(19)	419.5	4_1^+	16.5(3)
344.6	7.4(3)	499.5	0_2^+	16.7(12)
614.0	5.7(2)	1033.5	(4_2^+)	17.2(16)
787.2	16.7(7)	942.2	(3_1^+)	15.9(7)
855.6	17.2(7)	855.6	2_3^+	16.9(7)
1026.5	8.1(3)	1181.4	(2_4)	16.8(14)
1084.6	3.3(1)	1239.5	4_3^+	18.5(31)
Weighted average				16.43(12)

4.2.4 Analysis of conversion electrons

Our analysis also focused on $I_i^\pi = I_f^\pi$ transitions proceeding via $E0$ transitions ($I = 0$) or transitions with an $E0$ component ($I \neq 0$). Such transitions are sensitive to band mixing and differences in mean-squared charge radii between the initial and final states [Kib22].

The singles energy spectrum of conversion electrons with marked peaks is shown in Fig. 4.17. As was mentioned in Chapter 3.4.2, we identified some of the known transitions in ^{182}Pt based on CE-γ coincidences. These coincidence spectra are shown in Fig. 4.18. Gamma rays gated on the 377-keV CEs, which correspond to the K conversion of the 455-keV $2_5^+ \rightarrow 2_3^+$ transition, are shown in Fig. 4.18(a). All of these γ rays come from the deexcitation of the populated 856-keV 2_3^+ level, confirming the assignment of the CEs as K CEs of the 455-keV transition. Figure 4.18(b) shows coincidences with the K CEs of the 500-keV $0_2^+ \rightarrow 0_1^+$ transition. All γ rays present in the spectrum were also observed in the coincidence spectrum gated on the 345-keV line, depopulating the 500-keV 0_2^+ level (see Fig. A.1). Two transitions marked with an asterisk (155 and 1027 keV) are not real peaks, because they consist of just one bin with the number of events above the background level. They were not fully subtracted because of the difference in the shape of these peaks in the background and the gated spectra. Coincidences with the 434-keV K CEs of the 513-keV $2_2^+ \rightarrow 2_1^+$ transition in Fig. 4.18(c) show the 155-keV line, which is in a cascade with the 513-keV

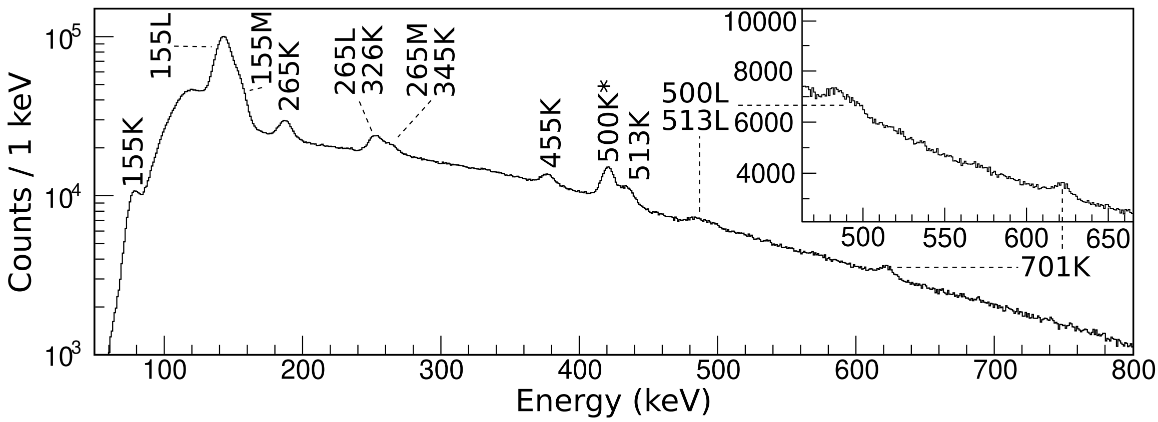

Figure 4.17: Energy spectrum of conversion electrons. Peaks are marked with internal transition energy and atomic orbital from which CE was emitted. The 500-keV transition (marked with an asterisk) was observed only in the spectrum of conversion electrons.

γ ray (see Fig. 4.12). Energies of K CEs from BrIcc [Kib08] for these three transitions (455, 500 and 513 keV, see Table 4.3) were used for energy calibration, allowing us to identify additional electrons originating from conversion of the 155-, 265, and 701-keV transitions. However, no new $E0$ transitions were observed, see Table 4.3.

Both the K and L CEs were observed for the known 500-keV $E0$ ($0_2^+ \rightarrow 0_1^+$) transition. The numbers of detected electrons were corrected for the detection efficiency of silicon detectors, giving the relative intensity $I_K(500) = 3.27(37)\%$ and $I_L(500) = 0.45(9)\%$. We did not observe CEs from higher shells, therefore, we used a theoretical fraction of K CEs for this transition of 0.8579 from BrIcc [Kib08] to obtain the total intensity of $I_{tot}(500) = 3.8(4)\%$.

The $E0/E2$ mixing ratio can be calculated for the $E0$ transition by reference to an $E2$ transition deexciting the same level (see Chapter 2.1.3). We used the 345-keV $E2$ $0_2^+ \rightarrow 2_1^+$ γ ray [Dav99] to calculate this mixing ratio for the 500-keV transition. Using $I_K(345) = \alpha_K(345) I_\gamma(345)$ in Eq. (2.58) we get:

$$q_K^2(E0/E2, 500) = \frac{I_K(500)}{I_\gamma(345)\alpha_K(345)} = 6.7(11). \tag{4.7}$$

Unfortunately, while several studies reported half-lives of yrast states in ^{182}Pt [Wal12; Gla12], the half-life of the 0_2^+ level is unknown. Therefore, we cannot determine the monopole transition strength $\rho^2(E0, 500)$. Instead, we used Eq. 2.60 to determine the $10^3 \cdot \rho^2(E0, 500) \cdot T_{1/2}(500) = 1.1(2)$ ns employing the branching ratio of the 345-keV

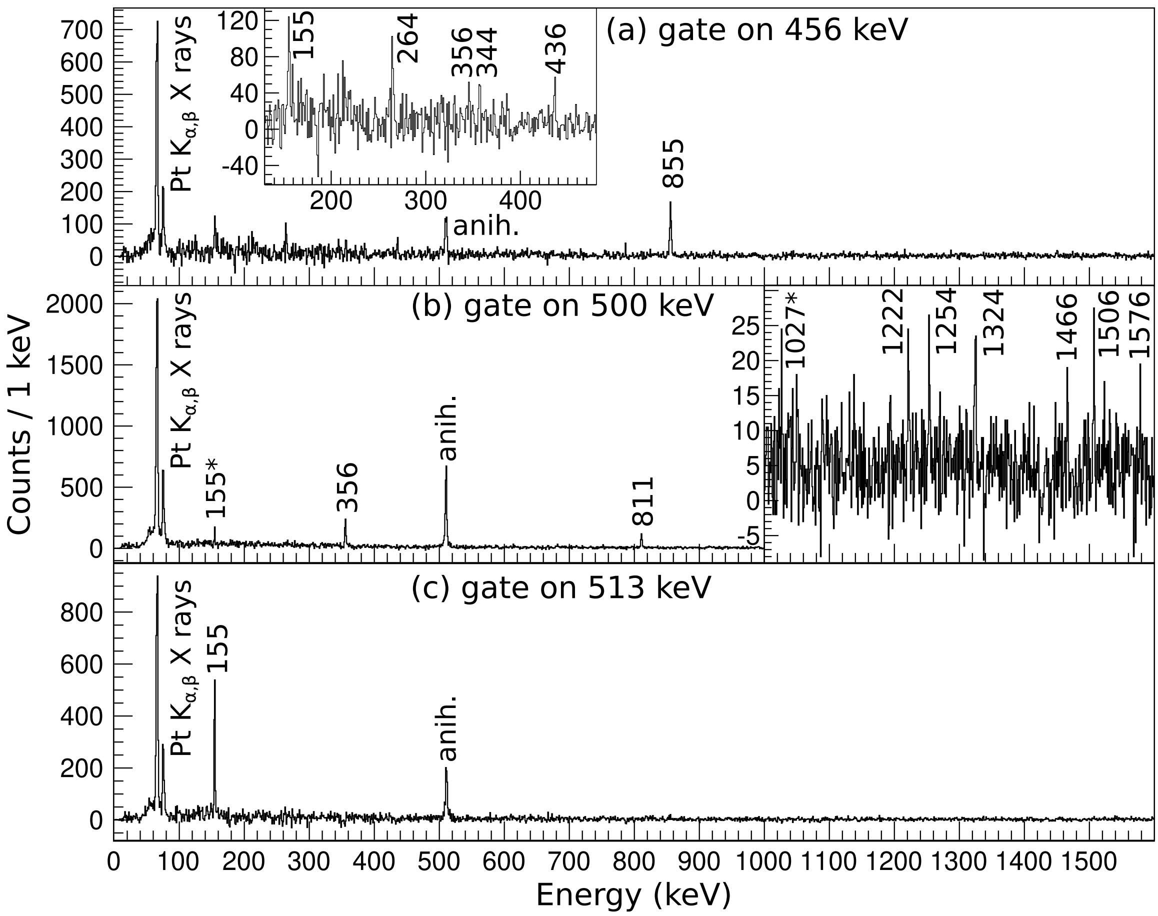

Figure 4.18: γ-ray coincidence spectra gated on the K CEs of the (a) 456-keV, (b) 500-keV and (c) 513-keV transitions, respectively. These CE transitions were identified based on γ-ray transitions in coincidence.

transition $b(E2, 345)$ (see Table 4.1) and electronic factor $\Omega_K(E0, 500)$ from BrIcc [Kib08; Dow20].

The second reported $E0$ transition is the 455-keV $2_5^+ \rightarrow 2_3^+$ transition. The $E0$ multipolarity was assumed for the 455-keV transition because no γ rays were observed in the previous studies [Cai74; Dav99], and only limits on conversion coefficients were given (see Table 4.4). However, γ-ray emission is allowed for such a transition, as opposed to the $0^+ \rightarrow 0^+$ case. We observed a weak γ-ray transition of the corresponding energy and K conversion electrons in γ-γ and γ-CE coincidences gated on the 856-keV transition, respectively, see Fig. 4.19. Because of this, we assign a mixed $E0 + M1 + E2$ multipolarity for the 455-keV transition. Comparison of intensity of CEs ($I_{CE,K}(456)$ = 0.78(9)%) and γ rays ($I_\gamma(456)$ = 0.05(2)%) yields the conversion coefficient $\alpha_K(456)$ =

Table 4.3: A list of transitions detected in the CE spectrum. The energy of emitted conversion electrons for a given transition and atomic shell was taken from BrIcc [Kib08].

Measured energy (keV)	Transition (keV)	Shell	CE energy [Kib08] (keV)
76.1(1)	154.9	K	76.5
142.5(1)	154.9	L	142.2
154.4(5)	154.9	M	152.0
186.9(2)	264.6	K	186.2
251.3(2)	264.6	L	251.7
	326.0	K	247.6
261.7(6)	264.6	M	261.6
	344.6	K	266.2
376.9(2)	455.4	K	377.0
420.8(1)	499.5	K	421.1
434.2(2)	512.5	K	434.1
485.7(8)	499.5	L	485.6
497.4(10)	512.5	L	498.8
622.4(3)	700.8	K	622.4

14.8(65). This value is much higher than the theoretical value for the $M1$ multipolarity, indicating a very strong $E0$ component. Because of such a high ICC, we estimated the contribution of other shells in the same way as for the 500-keV transition, using the theoretical fraction of K CEs of 0.8575 [Kib08], giving $I_{CE,tot}(456) = 0.91(11)\%$. A summary of internal conversion coefficients (ICCs) deduced for transitions in this Thesis is in the Table 4.4.

Only a limit on $\alpha_{K,ref}(513) > 0.165$ was given for the 513-keV $2_2^+ \rightarrow 2_1^+$ transition in Ref. [Cai74]. A smaller value of $\alpha_{K,ref}(513) = 0.044(6)$, incompatible with the previous limit, was determined in a later study [Dav99]. Because this value was smaller than the theoretical ICC for the $M1$ multipolarity (see Table 4.4), the existence of an $E0$ component for the 513-keV transition was questioned in Ref. [Dav99]. Our value $\alpha_K(513) = 0.055(7)$ agrees with the latter result. Additionally, we obtained a good agreement with $\alpha_{K,ref}(513) = 0.062(13)$ from the ENSDF evaluation [Sin10]. It was calculated using the CE intensity from Ref. [Cai74] and γ-ray intensity from

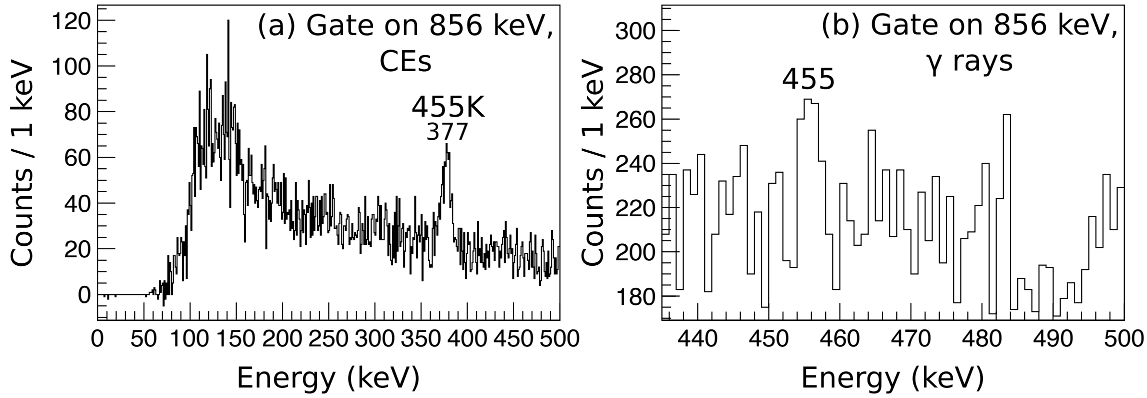

Figure 4.19: (a) Conversion electron and (b) γ-ray coincidence spectra gated on the 856-keV γ rays. K conversion electrons of the 455-keV transition with the energy of 377 keV are clearly visible in (a), and a weak γ-ray peak of the same energy is present in (b).

Table 4.4: Internal conversion coefficients α_{exp} of transitions in ^{182}Pt determined in this work compared with previously published values α_{ref} from Refs. [Cai74; Dav99] and theoretical values α_{th} from BrIcc [Kib08].

E (keV)	E_i (keV)	E_f (keV)	$J_i \to J_f$	Shell	α_{exp}	α_{ref} [Cai74]	α_{ref} [Dav99]	$\alpha_{th}(M1)$ [Kib08]
455.4(3)	1311.0(1)	855.6(1)	$2^+_5 \to 2^+_3$	K	14.8(65)	>1.7	>0.32	0.0824(12)
512.5(3)	667.5(3)	154.9(2)	$2^+_2 \to 2^+_1$	K	0.055(7)	>0.165	0.044(6)	0.0604(9)
				L	0.010(3)			0.00972(4)
700.8(2)	855.6(1)	154.9(2)	$2^+_3 \to 2^+_1$	K	0.78(13)	0.73(22)	>0.27	0.0269(4)

Ref. [Dav99]. We were also able to extract L conversion coefficient $\alpha_L(513) = 0.010(3)$. Both our values are comparable to the theoretical conversion coefficients for the $M1$ multipolarity, therefore, we cannot confirm the presence of the $E0$ component in this transition. We note, that similarly for the 486-keV $2^+_2 \to 2^+_1$ transition in neighbouring even-even isotope ^{184}Pt, no $E0$ component could be reliably assigned [Xu92].

For the 701-keV $2^+_3 \to 2^+_1$ transition, we obtained the K ICC of $\alpha_K(701) = 0.78(13)$. This ICC is in good agreement with the value $\alpha_{K,ref}(701) = 0.73(22)$ from Ref. [Cai74], and it is also compatible with the limit given in Ref. [Dav99]. Since the deduced α_K is much larger than the theoretical α_K for the $M1$ multipolarity, we can confirm the $E0$ component in this transition. Employing a mixing ratio $\delta(E2/M1) = 0.7^{+1.0}_{-0.3}$ for the 701-kev γ ray from Ref. [Dav99], we could determine the $q^2_K(E0/E2)$ mixing ratio using Eq. (2.56) with our conversion coefficient $\alpha_K^{exp}(701) = 0.78(13)$:

$$q_K^2(E0/E2, 701) = \frac{\alpha_K^{exp}(701)[1 + \delta^2(E2/M1)] - \alpha_K(M1, 701)}{\delta^2(E2/M1)\alpha_K(E2, 701)} - 1 = 258^{+458}_{-162}, \tag{4.8}$$

where $\alpha_K(M1, 701)$ and $\alpha_K(E2, 701)$ were ICCs for pure $M1$ and $E2$ multipolarities, respectively, taken from BrIcc [Kib08].

The Eq. (2.60) allows us to calculate the monopole strength for the 701-keV transition in a similar way as for the 500-keV γ ray. The half-life of the 856-keV 2_3^+ level is unknown, therefore, we calculated $10^3 \cdot \rho^2(E0, 701) \cdot T_{1/2}(856) = 0.8^{+1.4}_{-0.5}$ ns. However, the half-life of the 856-keV state can be estimated. It is a member of the rotational band built on top of the oblate 0_2^+ bandhead [Dav99]. Systematics of levels in platinum isotopes (see Fig 4.3) show that this band has a similar structure to g.s. bands in ^{188}Pt and heavier isotopes. Because of this, we can expect the 856-keV level to have a half-life similar to 2_1^+ states in ^{188,190,192,194}Pt (66(3) ps [Kon18], 62.3(31) ps [Sin20], 43.7(9) ps [Bag12] and 41.7(17) ps [Che21], respectively). Using the average of the smallest and the largest value with uncertainty covering the range of used values (53(13) ps), we obtained $10^3 \cdot \rho^2(E0, 701) = 14^{+26}_{-10}$. This value is similar to the monopole strengths of other $2_2^+ \to 2_1^+$ or $2_3^+ \to 2_1^+$ transitions connecting coexisting bands in nearby even-even isotopes (110(40), 90(30) and 49(23) in ^{182,184,186}Hg [Kib22], respectively, and 24(6) in ^{184}Pt [Ger20]).

4.2.5 β-decay feeding intensities and log ft values

Internal conversion is an alternative process to γ-ray emission, therefore, it needs to be accounted for to obtain total transition intensities. Depending on a specific case, we used ICCs determined in this work, calculated them using BrIcc for transitions with known multipolarity, took them from the NNDC evaluation [Sin10] in the case of mixed transitions, or estimated them in the case of unknown multipolarity. Considering the prompt character of the observed γ rays, we can limit their multipolarity to $E1$, $M1$, $E2$, $M2$, and, for higher energies ($E > 1300$ keV), also $E3$. We estimated their ICCs as the average value of ICCs for $E1$ and $M2$ multipolarities. These two values were chosen as the smallest and the largest among possible conversion coefficients. To cover the whole range of possible ICCs, we used the uncertainty of half of the difference between these two ICCs:

$$\alpha_{tot,est} = \frac{\alpha_{tot,E1} + \alpha_{tot,M2}}{2} \pm \frac{\alpha_{tot,E1} - \alpha_{tot,M2}}{2}. \tag{4.9}$$

The values of conversion coefficients and methods used to obtain them are listed in Table 4.1.

The apparent intensity of β-decay feeding I_β can be experimentally determined as a difference in intensity of transitions deexciting (I_d) and feeding (I_f) a level:

$$I_\beta = \sum I_d - \sum I_f. \tag{4.10}$$

We normalised relative feeding to the total number of ^{182}Au β decays. This was calculated as the sum of all transitions deexciting directly to the ground state. Their total intensity is 2.285 times larger than the γ-ray intensity of the 155-keV transition, giving a factor of 0.438(9) required for normalisation of transition intensities to 100 β decays. We also corrected these values for the β-decay branching ratio of ^{182}Au b_β = 99.879(11) % determined in this work in Chapter 4.3.2. Since we were measuring γ rays following β decay of ^{182}Au, we were not able to experimentally observe direct β-decay feeding into the $I^\pi = 0^+$ g.s. of ^{182}Pt. However, such β decay of the $I^\pi = (2^+)$ g.s. of ^{182}Au [Har20] would be the second forbidden non-unique β decay [Tur23], therefore, we consider this feeding to be negligible. Values of apparent β-decay feeding intensity are often influenced by the so-called pandemonium effect [Har77], as described in Chapter 2.1.4, and should be considered as upper limits. The apparent β-decay feeding intensities deduced in our work are listed in Tables 4.5 and C.2.

Table 4.5: A partial list of β-decay feeding intensity I_β into excited levels of ^{182}Pt and corresponding log ft values calculated using Fermi integrals for allowed and the first forbidden non-unique decay (log f_0t) and for the first forbidden unique decay (log f_1t). The values of spin and parity I^π are taken from Refs. [Dav99; Pop97] or from the analysis of de-excitation paths in this work as indicated by an asterisk. Column I_β^{ref} contains β-decay feeding intensity values calculated using the previous level scheme and transition intensities from Ref. [Dav99]. Internal conversion was accounted for in the same way as for our results. The full table is shown in Appendix C.

E (keV)	I^π	I_β^{ref} (%)	I_β (%)	log f_0t	log f_1t
154.9(2)	2_1^+	31(2)	10.9(21)	6.09(10)	8.18(10)
419.5(3)	4_1^+	11.4(8)	7.2(10)	6.20(7)	8.26(7)
499.5(3)	0_2^+	5.2(7)	1.58(30)	6.84(10)	8.89(10)
667.5(2)	2_2^+	10(2)	8.9(16)	6.04(9)	8.08(9)

Table 4.5: (*Continued)*

E (keV)	I^{π}	I_{β}^{ref} (%)	I_{β} (%)	log f_0t	log f_1t
774.8(3)	6_1^+	0.10(35)	0.22(8)	7.61(20)	9.64(20)
855.6(1)	2_3^+	7.1(8)	4.63(52)	6.27(6)	8.29(6)
942.2(2)	(3_1^+)	7.4(9)	4.21(40)	6.29(4)	8.30(4)
1033.5(2)	(4_2^+)	4.9(11)	2.03(20)	6.58(4)	8.58(4)
1151.2(2)	(0_3)	1.3(1)	0.61(10)	7.07(8)	9.06(8)
1181.4(1)	(2_4)	4.9(5)	3.06(26)	6.36(4)	8.35(4)
1239.5(1)	4_3^+	5.3(4)	1.80(15)	6.57(4)	8.56(4)
1305.4(2)	(5_1^+)	1.0(3)	0.37(6)	7.24(8)	9.22(8)
1311.0(1)	2_5^+	2.3(3)	2.88(20)	6.35(3)	8.32(3)
1358.3(2)	(0-4)*		0.25(7)	7.40(14)	9.37(14)
1418.9(1)	(4_4)	1.8(4)	0.97(10)	6.79(5)	8.75(5)
1472.8(1)	(2-4)*	1.5(4)	1.54(11)	6.57(3)	8.53(3)
1501.8(1)	(1-4)*	1.8(4)	1.13(11)	6.70(4)	8.65(4)
1520.9(1)	(2-4)*	0.75(24)	0.74(11)	6.87(7)	8.83(7)
1541.6(1)	(2-4)*	0.79(20)	1.31(14)	6.62(5)	8.57(5)
1568.0(2)	(2)*	0.37(14)	1.42(15)	6.58(5)	8.53(5)
1683.9(3)	(2-6)*	0.61(14)	0.45(6)	7.04(7)	8.98(7)
1888.7(2)	(2-4)*	0.47(14)	0.60(8)	6.85(7)	8.77(7)
2064.6(1)	(2-4)*		1.62(11)	6.37(3)	8.27(3)
3419.2(2)	(2-4)*		0.92(7)	6.17(3)	7.91(4)
3443.8(2)	(2-4)*		1.14(10)	6.07(4)	7.81(4)
3468.3(2)	(2-4)*		0.60(6)	6.34(5)	8.08(5)
3513.4(2)	(2-4)*		2.23(17)	5.75(3)	7.48(4)
3555.3(3)	(1,2)*		0.35(5)	6.54(7)	8.27(7)
3558.9(3)	(1,2)*		0.25(4)	6.70(8)	8.42(8)
3569.0(2)	(1,2)*		1.72(14)	5.85(4)	7.57(4)
3576.9(1)	(1,2)*		4.18(20)	5.46(2)	7.18(2)
3598.8(2)	(1,2)*		0.56(3)	6.33(3)	8.04(3)
3608.8(2)	(1,2)*		1.26(13)	5.97(5)	7.69(5)

Log ft values for the β decay of ^{182}Au can be calculated using the NNDC log ft

calculator [LOG]. We used values of β-decay feeding intensities and ^{182}Au half-life of $T_{1/2}$ = 16.43(12) s determined in this work, and the maximal energy of the decay Q_{EC}(^{182}Au) = 7864(23) keV from Ref. [Wan21]. Different decay types are described by different Fermi integrals, therefore, we calculated log f_0t values, as well as log f_1t values (see Table 4.5) to compare with systematics for the allowed and first forbidden non-unique decays, and for the first forbidden unique decays, respectively. Since the feeding intensities I_β are upper limits because of the pandemonium effect, the corresponding log ft values should be considered as lower limits.

As can be seen in Table 4.5 and Fig. 4.20, the highest amount of the observed feeding leads to the 2^+_1 level at 155 keV (I_β = 10.9(21)%), followed by the 2^+_2 state at 668 keV (I_β = 8.9(16)%). Strong feeding to other 2^+ states or the 942-keV (3^+_1) state is also present. This pattern is well expected since the β decay of the I^π = (2^+) g.s. in ^{182}Au [Har20] to these levels corresponds to an allowed β decay. Calculated log f_0t values for these states are in the range of 6.0 - 6.4, which are consistent with the typical values for the allowed or the first forbidden non-unique decays [Tur23].

However, the third strongest feeding is observed for the 4^+_1 level at 420 keV (I_β = 7.3(10)%). Feeding to other 4^+ states is also comparable to that of 2^+ states with similar excitation energy. Log f_0t values are approximately in the same range as for the 2^+ states (up to 6.6). Moreover, the largest log f_1t value for these levels is 8.56(4) (for the 4^+_2 1034-keV state), which is only slightly greater than the recommended lower limit for the first forbidden unique decay log $f_1t \geq 8.5$ [Tur23]. This is not consistent with the β decay of the I^π = 2^+ state to the 4^+ level, as it would be the second forbidden non-unique β decay with recommended lower limit of log $f_1t \gtrsim 11$ [Tur23] (see Chapter 2.1.2 and Fig. 2.2). Therefore, we should see several orders of magnitude lower β-decay feeding into these states, which would be below the detection limit. Feeding to 2^+, 4^+, and high-lying states will be further discussed in the following sections.

Feeding to the 2^+ states

Three band structures were identified in ^{182}Pt in the previous studies [Cai74; Pop97; Dav99]. The first one is the prolate yrast band with K = 0, the second band is built on top of the oblate 0^+_2 state (K = 0), and the third one is the γ band with K = 2 (see Fig. 4.20). Each of these bands contains a 2^+ state either as the first level above the bandhead (2^+_1 and 2^+_3 for the first two bands, respectively), or as the bandhead (2^+_2) in the case of the γ band. The g.s. of ^{182}Au is well-deformed with K = 2, therefore we could expect different degrees of hindrance in β decays to these states. A recent review showed

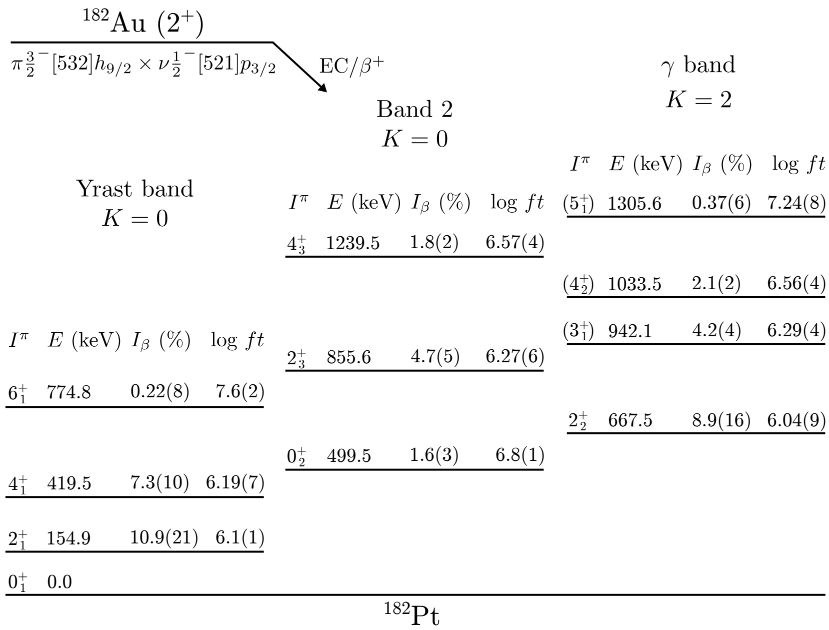

Figure 4.20: Simplified level scheme of ^{182}Pt. The band structure is taken from Ref. [Dav99]. Spin, parity and configuration of the ^{182}Au g.s. is taken from Ref. [Har20].

that $\Delta K = 2, \Delta J = 0$ decay, as in the case of decays to the 2_1^+ and 2_3^+ levels, can lead to log ft values in the range of 9-10 [Wal24]. It needs to be noted that only low Q_β cases without mixing of levels in the daughter isotopes were considered in the systematics in the review. The observed feeding intensity for the 2_3^+ level is slightly less than half of the feeding to the 2_1^+ state. However, these values can be considered comparable, since the resulting log ft values are approximately the same (6.09(10), 6.04(9) and 6.27(6) for the 2_{1-3}^+ levels, respectively). This indicates no K-hindrance in these β decays. We attribute the absence of K-hindrance to the mixing between the three bands, which was discussed in detail in Ref. [Dav99], and to the large effective Q values for β decays to these levels: $Q_{EC,eff} = Q_{EC} - E_f$, where $Q_{EC}(^{182}\text{Au}) = 7864(23)$ keV [Wan21] and E_f is the excitation energy of the populated state..

Feeding to the 4^+ states

Several possible explanations for substantial feeding into 4^+ states will be discussed. The first and natural explanation of the comparable β-decay feeding to the 2^+ and 4^+ levels would be the $I^\pi = 3^+$ assignment for the g.s. of ^{182}Au. This would correspond to the allowed β decay in both cases, which agrees with the calculated log ft values, see Table 4.5. As was mentioned in Chapter 4.1, initially the $I = 3$ value was assigned to ^{182}Au g.s., but later studies rejected this option and proposed $I^\pi = (2^+)$ [Ibr01; Har20;

Yan24]. Therefore, we exclude the $I^{\pi} = 3^{+}$ option as an explanation of large feeding into the 4^{+} states.

The second possible explanation is the presence of another β-decaying state in ^{182}Au, preferentially feeding the 4^{+} levels. We will consider only allowed and first forbidden non-unique β decays to the 4^{+} states since other types of β decay are usually highly suppressed [Tur23]. This limits the spin of a potential long-lived state in ^{182}Au to 3,4, and 5. The $M1$, $E1$, $E2$ or $M2$ transitions between the $I = 3, 4$ levels and the 2^{+} g.s. of ^{182}Au, respectively, would be prompt or have a very short lifetime. Thus, the only relevant value is $I = 5$. This would lead to a similar case as in ^{184}Au, where an isomeric 2^{+} state and a 5^{+} g.s. are present [Sau05]. It needs to be noted that an isomeric state in ^{182}Au has already been proposed because of the direct feeding of the 4^{+} and 5^{+} states evaluated based on γ-ray intensities from Ref. [Dav99] in the recent NUBASE evaluation [Kon21]. The spin and parity of this proposed state is $I^{\pi} = 5^{-}$, and its excitation energy $E^{*} = 120(40)$ keV and half-life of $T_{1/2} = 10$ s were estimated based on the trend in neighbouring nuclei.

Additionally, previously published results on ^{182}Au half-life seem to form two groups, which could be explained by a different admixture of the isomeric state in ^{182}Au in these studies. In the first group, there are values of 19(2) s [Han70], 22.1(13) s [Fin72] and 20(2) s [Hag79]. These half-lives were obtained from α or γ-ray spectroscopy at ISOLDE, where ^{182}Au was produced in the β decay of ^{182}Hg. The second group is formed by values of 15.6(4) s from nuclear orientation measurement at ISOLDE with production from ^{182}Hg β decay [Rom92], and 14.5(13) s and 15.3(10) s from α and γ-ray spectroscopy, respectively, at Oak Ridge [Bin95], where it was directly produced in a fusion-evaporation reaction. Different production methods could shift the ratio of the g.s. and isomeric state in the produced sample, changing the effective half-life. The highest values were determined with ^{182}Au produced in β decay, while the lowest values resulted from a study with the direct ^{182}Au production. However, one of the values in the second group (15.6(4) s [Rom92]) also comes from ^{182}Au produced in the β decay of ^{182}Hg. Therefore, no clear conclusion can be drawn based on the previous results.

The new 5^{+} isomeric state in ^{182}Au would preferentially feed different states in ^{182}Pt than the 2^{+} g.s. This would result in different half-lives obtained using γ rays deexciting levels with different spins. The analysis of ^{182}Au half-life using several γ transitions was performed in Chapter 4.2.3. The lowest and largest half-life values from our work (see Table 4.2) are 15.9(7) s and 18.5(31) s, which were obtained for the 787- (deexciting the (3_1^{+}) state) and 1085-keV (deexciting the 4_3^{+} state) transitions, respectively. These

γ-ray transitions deexcite levels with different spins, however, the difference in half-life is not statistically significant. Thus, our results are consistent with the decay of a single state in ^{182}Au.

The presence of an isomeric state in ^{182}Au was also investigated by theoretical configuration-constrained potential energy surface calculations [Jia24] (to be published in Ref. [Miš25]). These states are compared with the experimental levels known from the ^{182}Hg β-decay study [Ibr01; Sin15] in Fig. 4.21. Calculations reliably reproduced the spin of the g.s. ($I^{\pi} = 2^{+}$) with the same configuration as was deduced in Ref. [Har20]. The 5^{+} excited state in ^{182}Au is predicted at $E = 135$ keV with the same configuration ($\pi 3/2^{-}[532] \otimes \nu 7/2^{-}[514]$) as for the g.s. in ^{184}Au [Le 97]. Using Weisskopf estimates, see Eq. (2.47), and ICC from BrIcc [Kib08] we get an expected half-life of 0.7 s for an $M3$ transition between this level and the ^{182}Au g.s., making it an isomer. However, the theoretical calculations in Fig. 4.21 do not include rotational states. Energies of the g.s. band members in ^{182}Au are unknown, but we can estimate them since the deformation of ^{182}Au and ^{184}Au is very similar [Cub23b]. In ^{184}Au, rotational 6^{+} and 7^{+} states of the 5^{+} g.s. band lie at 84 and 187 keV, respectively [Zha05]. Equation (2.75) then gives us estimates of 41 and 101 keV for the rotational 3^{+} and 4^{+} states in ^{182}Au, respectively, placing them below the predicted 5^{+} level. Even with some degree of K hindrance [Kon15], the expected half-life of deexcitation via these rotational states would be much shorter. Thus, the predicted 5^{+} state would not create a β-decaying isomer with half-life comparable to the ^{182}Au g.s., which would not be distinguished in our half-life analysis in Chapter 4.2.3.

Moreover, we can expect the $I = 5$ isomer to also feed directly spin 5 and 6 states in ^{182}Pt. As can be seen in Table 4.5, we observed feeding to such states, but it is much lower compared to the feeding of the 4^{+} states (for example, 7.3(10)% and 0.22(8)% for the 4_1^{+} and 6_1^{+} levels, respectively). The highest observed β-decay feeding value for $I \geq 5$ states is $I_{\beta} = 0.37(6)\%$ for the 1305-keV (5_1^{+}) state, which is much smaller than for any 4^{+} level. Relative intensities of the $4_1^{+} \rightarrow 2_1^{+}$ (45.7(20)%) and $6_1^{+} \rightarrow 4_1^{+}$ (1.18(16)%) transitions in ^{182}Pt are also much lower, particularly in the $6_1^{+} \rightarrow 4_1^{+}$ case, compared to the same transitions in ^{184}Pt (90(9)% and 41(4)%, respectively) [Bag10]. While these relative intensities will depend on the isomer ratio in the given study, if the 4_1^{+} state in our data was indeed mostly fed by the β decay of the 5^{+} isomer, the ratio of intensities $I_{\gamma}(6_1^{+} \rightarrow 4_1^{+})/I_{\gamma}(4_1^{+} \rightarrow 2_1^{+})$ should be comparable in both studies. However, this ratio decreases from $\sim 1/2$ in ^{184}Pt to $\sim 1/40$ in ^{182}Pt, showing much stronger direct or indirect feeding from higher-spin states to the 6_1^{+} level in the case of β decay of the

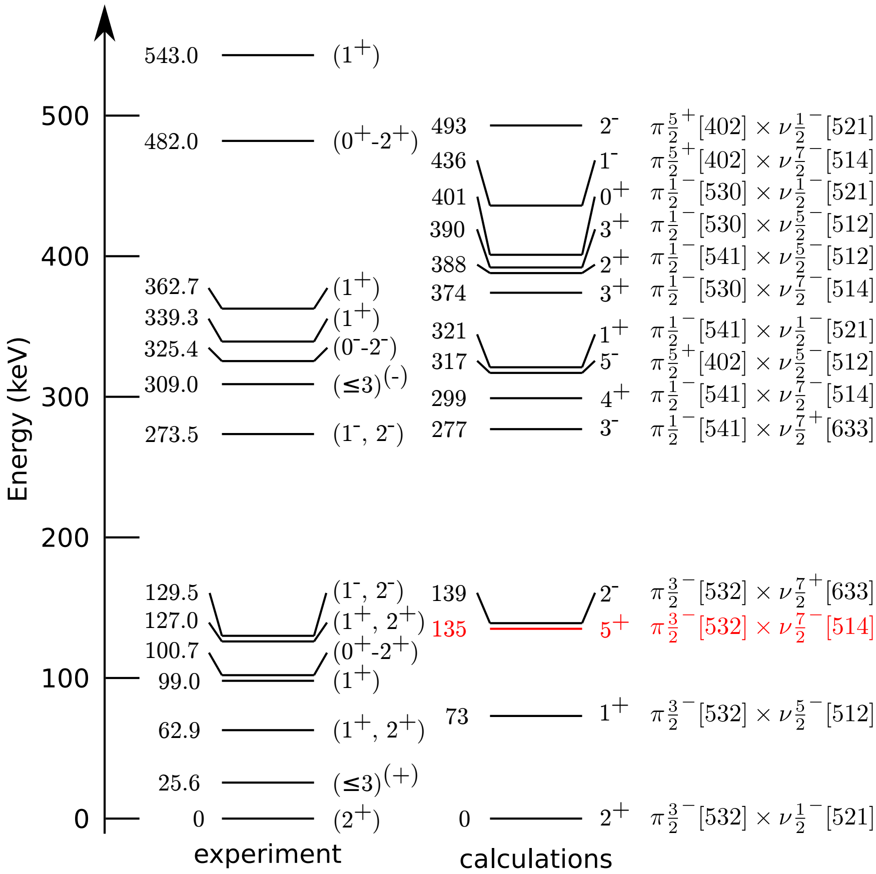

Figure 4.21: A comparison of experimental and theoretical excited levels in ^{182}Au. The predicted 5^+ state in ^{182}Au is highlighted in red. The figure was taken from Ref. [Miš25; Jia24].

5^+ g.s. in ^{184}Au.

Additionally, no hyperfine structure corresponding to another long-lived state in ^{182}Au besides its g.s. has been observed in the laser spectroscopy measurements scanning the 267.6-nm atomic transition in gold [Har20]. The published spectrum for ^{182}Au shows only a limited frequency range (see Fig. 4.22(a)), and therefore, additional components could be missed in the case of wider separation. However, an extra measurement using a broadband laser mode (broader laser linewidth) covering a wide frequency range was performed (see Fig. 4.22(b)), showing no signs of the second long-lived state. The only possible way for the isomeric state to be missed in such a measurement would be the overlapping of hyperfine components corresponding to the isomer with the hyperfine components of the g.s. This is unlikely, and additionally, it would lead to the distortion of the intensity ratio of hyperfine components of the g.s. Since the measured

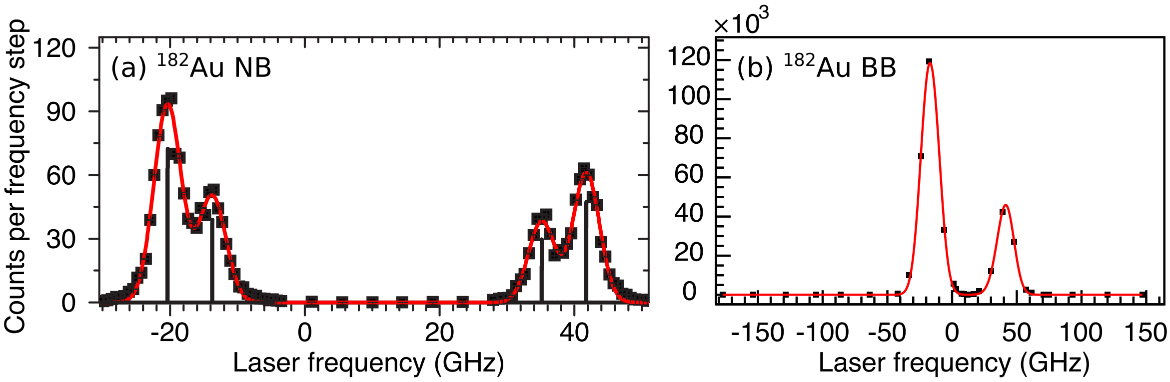

Figure 4.22: Hyperfine spectra of the 267.6-nm atomic transition in ^{182}Au measured using ion counting at the MR-ToF mass spectrometer. The zero frequency corresponds to the wave number of 37358.9 cm^{-1}. (a) Spectrum measured using the narrowband bandwidth laser, taken from Ref. [Har20]. (b) Unpublished results from the same experimental measurement using the broader bandwidth of the laser, showing a wider frequency range [Kre12].

ratio is in agreement with the hyperfine splitting caused by the $I = 2$ g.s., the contribution of the isomer would have to be small, and consequently, could not explain the large apparent β-decay feeding to the 4_1^+ state. Therefore, we conclude that there is no evidence for the β-decaying $I = 5$ isomeric state in ^{182}Au.

The third possible cause of the substantial apparent I_β to the 4^+ states is the unobserved feeding from higher-lying levels because of the pandemonium effect [Har77]. As was described in Chapter 2.1.4, pandemonium effect influences most of the high-resolution γ-ray spectroscopy measurements and the $I = 3$ assignment for the ^{182}Au g.s. and the presence of $I = 5$ isomeric state were both ruled out, therefore, we consider the pandemonium effect as the primary source of the large feeding to the 4^+ states in ^{182}Pt. However, this is unexpected for the 4^+ states, because the β decay of the (2^+) g.s. in ^{182}Au dominantly feeds the $I = 1 - 3$ states, which one could expect to deexcite mainly to the $I \leq 3$ levels. Although we expanded the level scheme of ^{182}Pt up to ~3.7 MeV (see Fig. 4.14) in comparison to 1.9 MeV from Ref. [Dav99], and were able to detect high-energy γ rays (see, for example Fig. 4.9), a substantial probability for the unobserved feeding still remains because of the high Q_{EC} value of 7864(23) keV [Wan21]. This explanation is supported by the total absorption spectroscopy measurement of ^{182}Au β decay, where direct β-decay feeding even up to 6 MeV in the excitation energy was observed (see Fig 4.23) [Hor75]. Moreover, no direct β-decay feeding into levels below 3 MeV was observed, which is a surprising result. However, the authors of the

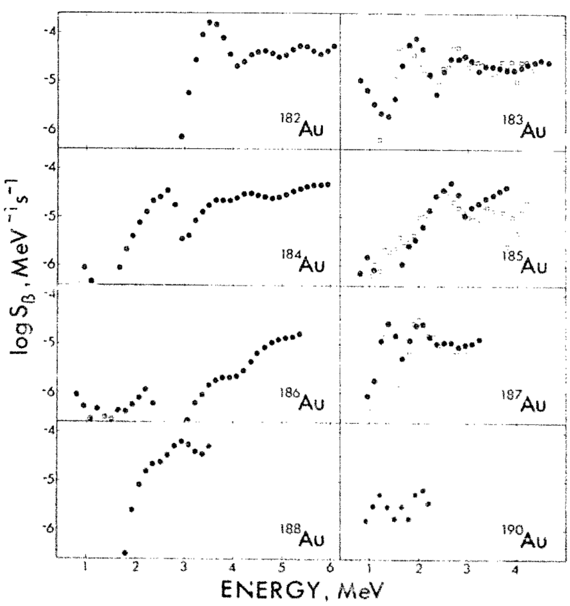

Figure 4.23: A plot of β-strength function S_β for ^{182}Au (top left panel) and other gold isotopes. β-strength function of an isotope is proportional to the distribution of β-decay feeding intensity into the daughter nucleus [Alg21]. The figure was taken from Ref. [Hor75].

study claim that the low-energy part of the spectrum should be regarded with caution. Therefore, we cannot draw any unambiguous conclusions based on this part of the spectrum.

No β-decay feeding intensities were reported in the previous study [Dav99], but they were calculated by the evaluators in Ref. [Sin15]. Since no details on the calculation were provided, we recalculated the reference feeding values I_β^{ref} considering the level scheme of ^{182}Pt and transition intensities from Ref. [Dav99], see Table 4.5. The internal conversion necessary for the calculation of the total transition intensities was included in the same way as for our data. A large decrease in apparent feeding can be seen for the 2_1^+ 155-keV state, which was reduced to about a third of that from Ref. [Dav99] (from 31(2)% to 10.9(21)%) after expanding the decay scheme in this Thesis. However, the feeding of the 4_1^+ 420-keV state decreased only slightly, from 11.4(8)% to 7.3(10)%. This indicates that levels indirectly feeding the 4_1^+ state are relatively high-lying, outside of the scope of our level scheme extension.

To estimate the effect of the ^{182}Pt level scheme extension on the observed pandemonium effect, we evaluated the β-decay feeding into newly assigned levels. Feeding to the previously known levels makes up approximately 55% of the apparent β-decay feeding intensity observed in our work. The remaining 45% lead to newly identified states, which were contributing to the pandemonium in the previous study [Dav99]. Therefore, a significant reduction of the pandemonium effect was achieved.

Feeding to the high-lying states

Besides the strongest apparent β-decay feeding intensity into the low-lying levels, we also observed strong feeding for some high-lying levels around ~3.5 MeV in the excitation energy. The highest value of $I_\beta = 4.18(20)\%$ is reached for the 3577-keV state, as shown in Table 4.5. Log f_1t values for many levels in the region (see Table C.2) are below the recommended lower limit for first forbidden unique decay of log $f_1t \geq 8.5$ [Tur23]. This limits the respective β decays to allowed, or first forbidden non-unique category with maximum change of spin of $\Delta I \leq 1$. Therefore, we could tentatively assign spins $I = (1-3)$ for such states, considering the β-decaying g.s. in ^{182}Au has $I^\pi = (2^+)$ [Har20]. However, as was mentioned earlier in this chapter, we observed a strong influence of the pandemonium effect on the apparent β-decay feeding intensity of the low-lying levels in ^{182}Pt. Although we can expect lower pandemonium for high-lying levels, it cannot be ruled out because of the large $Q_{EC} = 7864(23)$ keV [Wan21], therefore, log f_1t values were not used to limit spins given in tables and level schemes. These low log f_1t values are in contrast with the ~1.5 – 3 MeV region, where all log f_1t values (besides the one for the 2065-keV level) are above the aforementioned limit of 8.5, see Tables 4.5 and C.2. It is noteworthy that strong β decay feeding at ~3.5 MeV was also observed in the TAS measurement in Ref. [Hor75], where the β-strength function S_β for ^{182}Au reaches its maximum in the energy region around 3.5 MeV, see Fig. 4.23.

4.3 Results for α decay of ^{182}Au

4.3.1 α-γ analysis

All previously reported fine structure α decays of ^{182}Au (5403(5), 5352(5) and 5283(5) keV) from Ref. [Bin95] are visible in singles spectrum in Fig. 4.24(a). A peak originating from the α decay of ^{182}Pt and two peaks from ^{182}Hg are also present [Ach09]. The source of ^{182}Hg is the surface-ionised ^{182}Tl contamination in the implanted beam. The observed statistics for the 5871-keV α decay of ^{182}Hg is 830(30) α decays. It is in agreement with the expected amount of 880(160), which we calculated from the ^{182}Tl amount estimated in Chapter 4.2 using the $b_\beta(^{182}\text{Tl}) = 99.75(25)\%$, $b_\alpha(^{182}\text{Hg}) = 13.8(9)\%$ [Sin15]

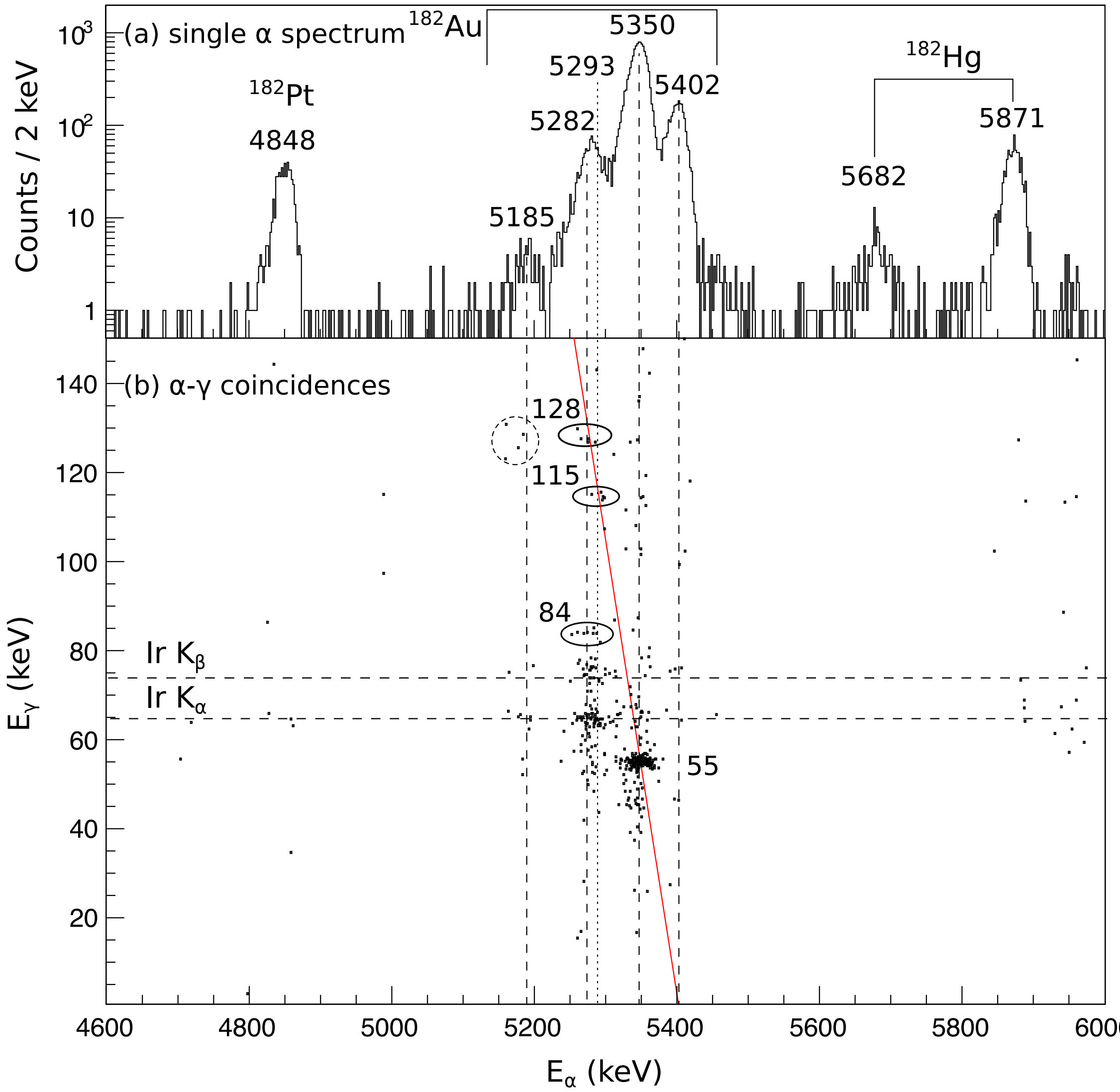

Figure 4.24: (a) α-decay spectrum of ^{182}Au. (b) α-γ coincidences for ^{182}Au α decay. The red line denotes $Q_{\alpha,tot} = Q_\alpha + E_\gamma = 5524\,\text{keV}$.

and detection efficiency $\varepsilon_\alpha = 3.8(4)\%$ determined in Chapter 3.4.2.

We constructed an α-γ coincidence matrix (Fig. 4.24(b)) using the same time window of 200 ns as for the γ-γ analysis. A summary of observed α-γ coincidences is shown in Table 4.6. The strongest visible group is the 5350-55 keV coincidence, which is the only α-γ coincidence reported in Refs. [Hag79; Bin95]. The $Q_{\alpha,tot}(5402\,\text{keV}) = 5524(5)$ keV value of the 5402-keV α transition, previously assigned feeding the g.s. of ^{178}Ir is indicated by the red line in Fig. 4.24(b). Two new coincidence groups lie along this line. The first one establishes a new 5293-keV fine structure α decay of ^{182}Au feeding the 115-keV level. The energy of this decay was determined as the average value

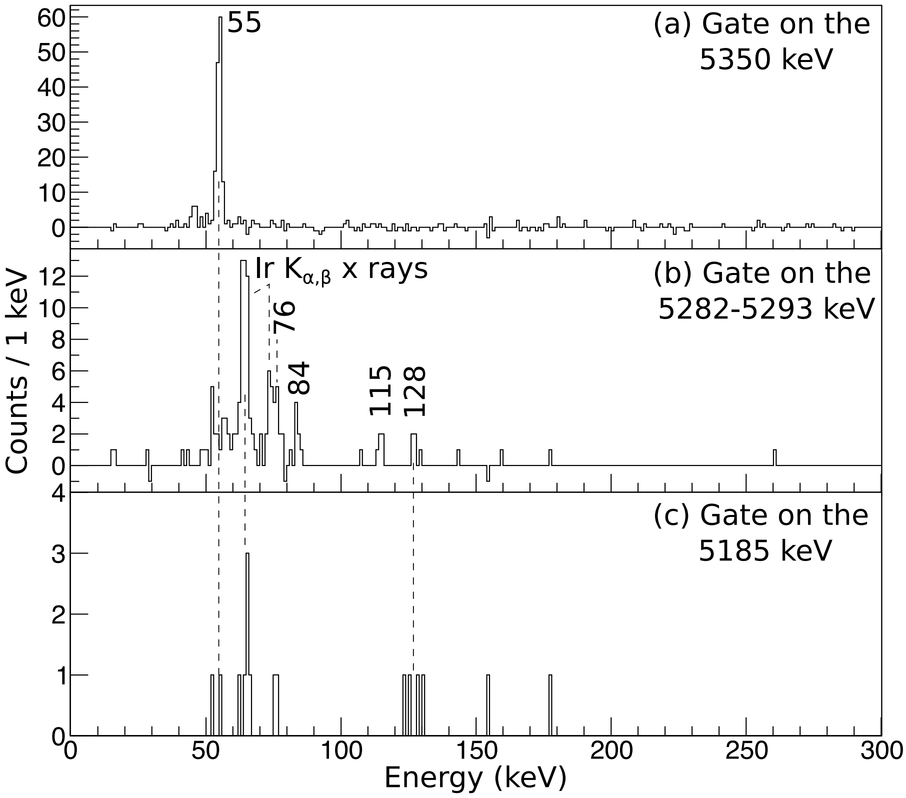

Figure 4.25: γ-ray coincidence spectra gated on (a) the 5350-keV, (b) the 5282- and 5293-keV and (c) the 5185-keV α decays.

of the 5 observed coincidence events. The second group lying on the $Q_{\alpha,tot}$ consists of the 5282-keV α decays and 128-keV γ rays, therefore, we can give a more precise energy value for the previously-known 123(7) keV state in ^{178}Ir, which is fed by this α decay. The 5282-keV α line is also in coincidence with the new 84-keV γ-ray transition. A γ ray with similar energy was reported in a β-decay study of ^{178}Pt [Mei93] but was not placed in the level scheme. The energy difference between this γ ray and the 128-keV level is 45 keV. A peak with similar energy is visible in γ-ray coincidence spectrum gated on the 5350-keV α line in Fig. 4.25(a)). However, the energy of this 45.7(4)-keV transition matches the energy of the Compton backscatter peak for the dominant 55-keV line:

$$E'_\gamma = \frac{E_\gamma}{1 + \frac{2E_\gamma}{m_e c^2}} = 45.3\,\text{keV}, \tag{4.11}$$

and we do not consider it to be a real transition. Thus, we cannot reliably place the 84-keV transition into the level scheme. Figure 4.26 shows the deduced α-decay scheme of ^{182}Au.

A spectrum of γ-rays in coincidence with the 5282- and 5293-keV α decays is shown in Fig. 4.25(b). All three γ-ray transitions visible in α-γ spectrum (at 128, 115 and 84 keV) are present together with iridium K_α and K_β X-rays. The measured energy of $E(K_\alpha, exp)$ = 64.5(4) keV matches the tabulated value of $E(K_\alpha, ref)$ = 64.3 keV [Fir96]. Since we cannot distinguish $K_{\alpha 1}$ and $K_{\alpha 2}$ in our measurement, we calculated this energy as the weighted average. In the case of K_β, the difference between the measured and expected energy is relatively large, 75.3(5) keV compared to $E(K_\beta, ref)$ = 73.8 keV, respectively. The width of this peak is also much larger (4.9 keV FWHM) compared to the K_α line (2.8 keV). We conclude that this peak is a doublet of $E(K_\beta, exp)$ = 73.7(6) keV and a new tentative 76.3(12)-keV transition. However, it could not be reliably placed into the decay scheme.

A 5185-keV α peak lies next to known ^{182}Au decays in singles spectrum in Fig. 4.24(a). A small peak of iridium K_α X-rays is present in its γ-ray coincidence spectrum in Fig. 4.25(c), therefore, we assign it as a new tentative fine structure decay of ^{182}Au. This establishes a tentative level in ^{178}Ir at 223 keV, which was determined from the difference between $Q_{\alpha,tot}$ and Q_α(5185). A group of four γ rays in the 123 − 130-keV region is visible, however, because of the low statistics and large spread of γ-ray energies, no γ transitions could be assigned as following the 5185-keV α decay.

Intensities of fine structure α decays were taken from the α-particle counts in the singles spectrum corrected for the detection efficiency of silicon detectors (see Table 4.6). This was not possible for the 5282- and 5293-keV decays, as we could not separate them. Instead, we determined their intensities based on α-γ coincidences shown in Fig. 4.25(b). We corrected the counts in the γ-ray peaks at 128, 84, and 76 keV (for the 5282-keV α decay) and 115 keV (for the 5293-keV α decay) for γ-ray detection efficiency and internal conversion. The correction for conversion was done similarly as for γ-rays from ^{182}Au β decay, where we took the average value of the smallest and largest ICCs using Eq. (4.9). The $M2$ transitions have a long half-life at low energies, therefore, they were not considered. Instead, $E2$ ICC for the 76-keV γ ray and the $M1$ ICCs for the remaining transitions were used as upper limits. Based on α-γ coincidences, we can expect 1156(722) and 105(79) counts for the 5282- and 5293-keV transitions, respectively. This is in agreement with the detected number of α particles 1197(49) (I_α = 8.1(3)%) in singles spectrum for the combined 5282-5293-keV peak. To not influence the intensity of other transitions, we divided the intensity of the combined peak based on the ratio of α-γ coincidence counts, resulting in I_α(5282) = 7.4(7)% and I_α(5293) = 0.7(6)%. All intensities are normalised to a sum of 100%. We also investi-

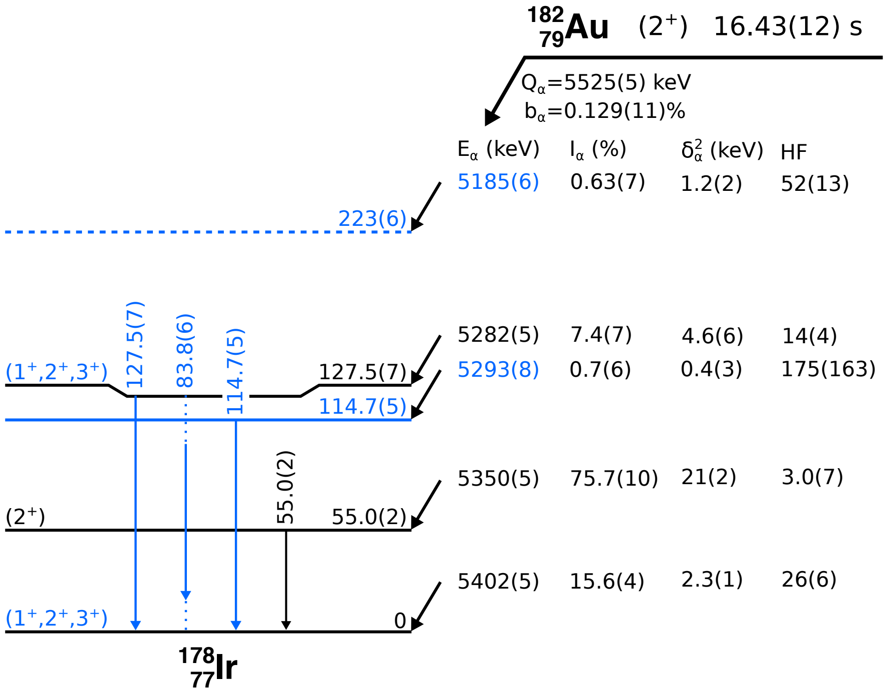

Figure 4.26: α-decay scheme of ^{182}Au. The tentative level at 223 keV is given with a dashed line. New levels and transitions are highlighted in blue.

gated the potential coincidence summing of α particles and CEs, which could influence extracted intensities, using a GEANT4 simulation and found it to be negligible.

Employing the deduced I_α, we calculated reduced α-decay widths δ^2_α using the Rasmussen method [Ras59], with the assumption of $\Delta L = 0$ decays. Values of half-life $T_{1/2}(^{182}\text{Au}) = 16.43(12)$ s and α-decay branching ratio $b_\alpha(^{182}\text{Au}) = 0.129(11)\%$ determined in this work (see Chapters 4.2.3 and 4.3.2) were employed. The calculation of hindrance factors using Eq. (2.25) requires a reference decay width for an unhindered transition. The $3/2^- \rightarrow 3/2^-$ α decay of ^{181}Au and the $5/2^- \rightarrow 5/2^-$ decay of ^{183}Au were chosen and we obtained reduced widths of $\delta^2_\alpha = 75(16)$ and $\delta^2_\alpha = 45(21)$, respectively, using the published data from Refs. [Bin95; Kon19; Bag09]. Hindrance factors shown in Table 4.6 were calculated using the weighted average of these values of $\delta^2_{\alpha,ref} = 64(13)$.

The low hindrance factor for the 5350-keV α decay HF = 3.0(7) suggested its unhindered character. It is in agreement with the previously deduced value HF = 3 from Ref. [Bin95], where the same spin and parity was proposed for the 55-keV state in ^{178}Ir as for the g.s. in ^{182}Au. No spin assignment for g.s. in ^{182}Au was known at the time of the study [Bin95], but currently, an $I^\pi = (2^+)$ assignment can be attributed to the 55-keV state.

Additional information can be deduced from the internal conversion coefficient for

Table 4.6: A summary of observed α-γ coincidences for the α decay of ^{182}Au. Tentative transitions are given in italics. Reduced α-decay widths δ_α were obtained using the Rasmussen approach [Ras59]. Hindrance factors HF were extracted relative to the average value of δ^2_α = 64(13) keV for the unhindered α decays in ^{181,183}Au [Bin95; Kon19; Bag09].

E_α (keV)	E_γ (keV)	$Q_{\alpha,tot}$ (keV)	I_α (%)	δ^2_α (keV)	HF
5402(5)	-	5524(5)	15.6(4)	2.4(2)	26(6)
5350(5)	55.0(2)	5525(5)	75.7(10)	21(2)	3.0(7)
5293(8)	114.7(5)	5527(9)	0.7(6)	0.4(3)	175(163)
5282(5)	127.5(7), 83.8(6), *76.3(12)*	5529(5)	7.4(7)	4.6(6)	14(4)
5185(6)	-	-	0.63(7)	1.2(2)	51(13)

the 55-keV transition deexciting this state. There are no other transitions present in the coincidence spectrum of the 5350-keV α decay, therefore, we can assume that all the missing α-γ intensity compared to the number of single α events is caused by internal conversion of the 55-keV transition. Thus, we can express its ICC in the following way:

$$\alpha_{tot}(55) = \frac{N_\alpha}{\varepsilon_\gamma N_{\alpha-\gamma}} - 1, \tag{4.12}$$

where $N_{\alpha-\gamma}$ is the number of coincidence events, ε_γ is the detection efficiency for the 55-keV γ ray and N_α is the number of 5350-keV α particles in the singles spectrum. The resulting value is $\alpha_{tot,exp}(55)$ = 11.7(12). This value lies between the theoretical conversion coefficients for the $M1$ and $E2$ multipolarities, $\alpha_{tot,th}(55, M1)$ = 6.16 and $\alpha_{tot,th}(55, E2)$ = 67.02, respectively [Kib08]. Therefore, we can assign it a mixed $M1 + E2$ multipolarity, fixing the maximum change in spin by the 55-keV transition to $\Delta L \leq 1$. This constrains I^π of the g.s. in ^{178}Ir to a range of $I^\pi = (1^+, 2^+, 3^+)$. Based on the deduced hindrance factor of HF = 26(6) for the 5402-keV α decay to the g.s., we can expect some degree of hindrance, making 1^+ and 3^+ options more probable. However, such a hindrance factor can also be explained by the decay to the 2^+ state, but with a largely different configuration compared to the (2^+) g.s. of ^{182}Au.

The second lowest hindrance factor from this work is for the 5282-keV line (HF = 14(4)). This is similar to the 5402-keV decay (HF = 26(6)), thus, we can expect this decay to connect levels with a similar structure. Because of this, we can give the same spin assignment for the 128-keV level in ^{178}Ir as for its g.s., $I^\pi = (1^+, 2^+, 3^+)$.

4.3.2 α-decay branching ratio

The α-decay branching ratio of ^{182}Au can be calculated in two ways. The first one compares the number of α and β decays of this isotope:

$$b_\alpha(^{182}\mathrm{Au}) = \frac{\frac{N_\alpha(^{182}\mathrm{Au})}{\varepsilon_\alpha}}{\frac{N_\alpha(^{182}\mathrm{Au})}{\varepsilon_\alpha} + N_\beta(^{182}\mathrm{Au})}, \tag{4.13}$$

where the number of alpha particles N_α was taken from singles α-particle spectrum and the number of β decays was determined from γ-spectroscopy analysis at the beginning of Chapter 4.2.1 as $N_\beta(^{182}\mathrm{Au})$=3.3(1)×10^8. Note that the same parts of the collected data were left out of the analysis when determining both the N_β and N_α as described in Chapter 4.2 (see Fig. 4.4). Using the α-particle detection efficiency ε_α = 3.8% (see Chapter 3.4.2) and N_α = 14 760(130), we obtained the value of $b_\alpha(^{182}\mathrm{Au})$ = 0.117(13)%. The number of β decays $N_\beta(^{182}\mathrm{Au})$ was calculated as a sum of the counts of all transitions feeding the g.s. corrected for the γ-ray detection efficiency. Any unobserved transitions to the g.s., because of the pandemonium effect, lower the estimated number of ^{182}Au β decays. Therefore, the resulting branching ratio should be considered as an upper limit.

The second method determines the number of β decays of ^{182}Au from the α-particle counts of β-decay daughter, ^{182}Pt, divided by its branching ratio $b_\alpha(^{182}\mathrm{Pt})$:

$$b_\alpha(^{182}\mathrm{Au}) = \frac{N_\alpha(^{182}\mathrm{Au})}{N_\alpha(^{182}\mathrm{Au}) + \frac{N_\alpha(^{182}\mathrm{Pt})}{b_\alpha(^{182}\mathrm{Pt})}}. \tag{4.14}$$

The second method compares only α-particle counts, therefore, it is independent of their detection efficiency. However, it requires that all platinum nuclei, created in the β decay of ^{182}Au, decay in the detection system. For the majority of the experiment duration, the implantation tape moved every ~30 seconds, which was much shorter than the ^{182}Pt half-life of 2.67(12) min [Sin15]. However, there were two parts of the measurement (see Fig. 4.27) when the tape movement was stopped for several minutes, allowing us to use this method. Only one 4843-keV α-decay transition of ^{182}Pt was observed in previous studies [Sii66; Bin95], however, a possible ~4715-keV transition was proposed in the evaluation [Ach09]. Therefore, when counting the number of ^{182}Pt α decays, we considered all events within the energy range of 4665-4900 keV.

The first interval in Fig. 4.27 without the tape movement was 27.6 min long, and gold nuclei were implanted several times during its duration. The last implantation occurred 606 s before the end of the interval. This is about 3.8 half-lives of ^{182}Pt, therefore, the decay of some platinum nuclei was not recorded. Additionally, the data

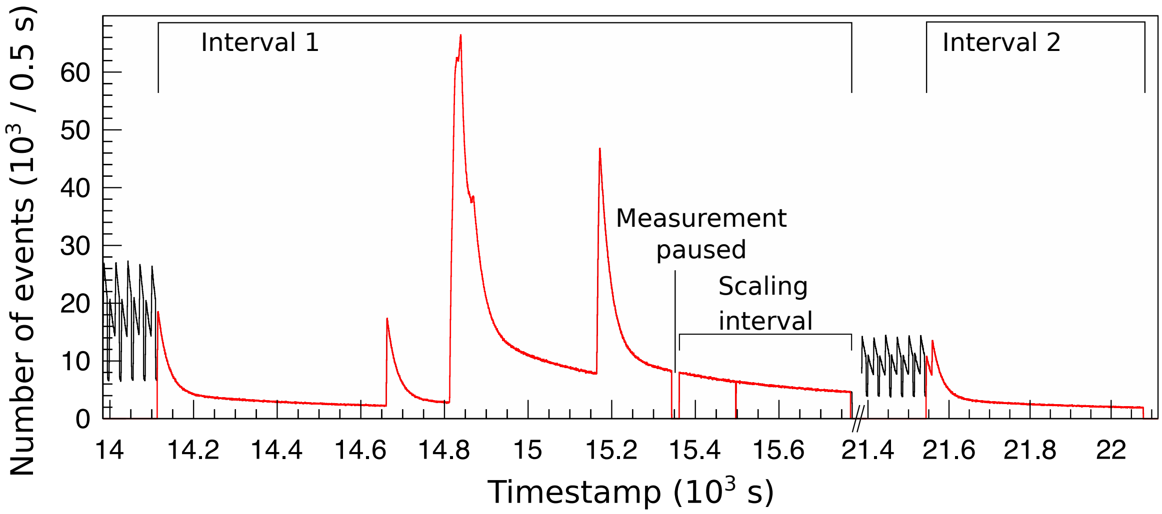

Figure 4.27: Time distribution of data used for the determination of $b_\alpha(^{182}\text{Au})$. Two parts of the measurement without tape movement, 27.6 and 8.9 min long, respectively, were used.

acquisition was stopped during the decay period after the last implantation for ≈ 18 s, starting 179 s after the last implantation. Thus, a correction needs to be made to account for the missing ^{182}Pt decays. To extrapolate the decay curve to the regions of interrupted data acquisition and stopped measurement, we chose the 409-s-long time interval (197-606 s) between these two regions, see Fig. 4.27. Since the chosen time period starts about twelve ^{182}Au half-lives after closing the beam gate, we can use a simple decay curve of ^{182}Pt in the missing regions. Equations (2.1) and (2.2) give us:

$$A_{\text{Pt}}(t) = \lambda_{Pt} N_0 e^{-\lambda_{\text{Pt}} t}, \tag{4.15}$$

where λ_{Pt} is the decay constant of ^{182}Pt calculated using Eq. (2.3) from $T_{1/2}(^{182}\text{Pt})$ = 2.67(12) min [Sin15]. We observed 47(7) α decays of ^{182}Pt during the chosen 409-s-long time interval, which we used to scale the decay curve of ^{182}Pt. This gives us 4.8(7) missed decays during the pause in measurement and 9.6(14) decays missed because the measurement time was not long enough.

The second interval without tape movement lasted for 8.9 min (see Fig. 4.27) and nuclei produced by two proton pulses (~ 15 s apart) were implanted into IDS at the beginning of this interval. We detected 11(3) α decays of ^{182}Pt during this part. In order to describe the decay curve of ^{182}Pt in this interval and to obtain a correction for missing decays, we cannot use the simple decay curve, since ^{182}Pt nuclei are created in the decay of ^{182}Au. Instead, we used the following function, which accounts for the gradual production of ^{182}Pt [Kra88]:

$$A_{\mathrm{Pt}}(t) = N_0 \frac{\lambda_{\mathrm{Pt}}\lambda_{\mathrm{Au}}}{\lambda_{\mathrm{Pt}} - \lambda_{\mathrm{Au}}}(e^{-\lambda_{\mathrm{Au}}t} - e^{-\lambda_{\mathrm{Pt}}t}), \tag{4.16}$$

where N_0 is the number of implanted ^{182}Au nuclei and λ_{Pt} and λ_{Au} are respective decay constants of ^{182}Pt and ^{182}Au. Since nuclei were implanted into the IDS twice during this period, we used a sum of two functions with equal N_0, assuming the same production of ^{182}Au during the two pulses. Time $t = 0$ for each of the distributions corresponds to the opening of the beam gate after the arrival of the first and second proton pulse, respectively. As was mentioned in Chapter 3.3, the beam gate was opened for 2 s after each pulse. Considering the relatively long half-life of ^{182}Au compared to this time, the effect of finite implantation time was neglected. Approximately 88.7% of created platinum nuclei decayed by the end of the interval. This gives us an estimate of 12.4(37) ^{182}Pt α decays. A summary of detected α particles in both measurement periods is given in Table 4.7.

This method needs α-decay branching ratio of ^{182}Pt (see Eq. (4.14)). Two values were reported in previous studies, $b_\alpha(^{182}\mathrm{Pt}) = 0.023^{+0.023}_{-0.012}\%$ [Sii66] and $b_\alpha(^{182}\mathrm{Pt}) = 0.038(2)\%$ [Bin95]. We used the latter, more precise value to obtain $b_\alpha(^{182}\mathrm{Au}) = 0.129(11)\%$, which will be a subject of our discussion. For completeness, the result using the older value is $b_\alpha(^{182}\mathrm{Pt}) = 0.079^{+0.079}_{-0.041}\%$. It needs to be noted that both the previous value $b_{\alpha,ref}(^{182}\mathrm{Au}) = 0.13(5)\%$ and $b_\alpha(^{182}\mathrm{Pt}) = 0.038(2)\%$ used in our calculation come from the same study [Bin95]. However, $b_{\alpha,ref}(^{182}\mathrm{Au})$ in Ref. [Bin95] study was not calculated using $b_\alpha(^{182}\mathrm{Pt})$. Both of these values were calculated independently from each other from the number of β decays of ^{182}Au and ^{182}Pt, respectively (method 1). Therefore, we can use $b_\alpha(^{182}\mathrm{Pt})$ to update the branching ratio of ^{182}Au in this Thesis.

Both obtained values of ^{182}Au α-decay branching ratio are consistent with each other within the uncertainty. A good agreement is also reached with the previously known value $b_{\alpha,ref}(^{182}\mathrm{Au}) = 0.13(5)\%$ [Bin95]. The first value calculated from the number of ^{182}Au β decays ($b_\alpha(^{182}\mathrm{Au}) = 0.117(13)\%$) can be affected by the pandemonium effect, therefore, we used the second value $b_\alpha(^{182}\mathrm{Au}){=}0.129(11)\%$ (respectively its complementary value $b_\beta(^{182}\mathrm{Au}) = 99.871(11)\%$) to calculate β-decay feeding intensities into excited levels in ^{182}Pt.

As was already mentioned, a possible ~4715-keV fine structure α decay of ^{182}Pt feeding the 132-keV 2^+ level in ^{178}Os with relative intensity of up to $I_\alpha = 17\%$ was included in the evaluation [Ach09]. We did not observe this decay in our work as

Table 4.7: Detected α-particle counts of ^{182}Au and ^{182}Pt used for the calculation of $b_\alpha(^{182}\mathrm{Au})$. A correction accounting for missing ^{182}Pt α decays was performed, see the text for details.

Isotope	Counts in Interval 1	Counts in Interval 2	Total counts
^{182}Au	967(31)	35(6)	1002(32)
^{182}Pt	265(16)	11(3)	276(16)
^{182}Pt corrected	279(16)	12.4(37)	292(17)

shown in Fig. 4.24. There were only 10(3) events in the relevant energy range of 4665-4765 keV. The expected background of 4(1) counts in the 4665-4765 keV interval was estimated based on the number of events (26(5)) in the 4000 − 4665 keV region. The resulting upper limit on the intensity of the α decay to the 132-keV 2^+ state of $I_\alpha < 1.8\%$ is significantly lower than the estimate from the evaluation.

Summary

In this Thesis, we presented the results of the decay spectroscopy of the neutron-deficient isotope ^{182}Au, where we focused on both the β and α decay of this nucleus. Our goal was the study of decay properties of ^{182}Au and the structure of its daughter isotopes ^{182}Pt and ^{178}Ir. Therefore, we aimed for the extension of the ^{182}Pt level scheme, calculation of log ft values, a search for isomeric states and new information on shape coexistence in ^{182}Pt. In the case of ^{178}Ir, we focused on the study of ^{182}Au fine-structure α decays and the calculation of the corresponding hindrance factors.

The isotope of interest was produced in the proton-induced spallation of a uranium target at ISOLDE facility [Kug00; Bor17b] in CERN during the IS665 experiment. An isotopically pure ion beam of ^{182}Au was created using element-selective resonance laser ionisation by RILIS [Fed17] and mass separation by the General Purpose Separator. Decay measurement of ^{182}Au took place at a permanent detection setup IDS (ISOLDE Decay Station) [IDS]. Four HPGe Clover detectors with four crystals each were employed to detect γ quanta and X-rays following the decay of ^{182}Au. Additionally, an array of seven silicon PIN diodes for the detection of charged particles and two plastic scintillators for the β-particle detection were used.

We performed the energy and efficiency calibration of HPGe detectors of IDS using radioactive sources of known activities. Because of the shift of calibration during the measurement, energy calibration was corrected using already known γ rays following the β decay of ^{182}Au and its daughter products. The α-particle detection efficiency of silicon detectors was determined from the ^{181}Au α-decay data measured during the same experiment. Energy dependence of the detection efficiency for conversion electrons was obtained using the GEANT4 [Ago03] simulation.

The first part of the Thesis focused on the study of EC/β^+ decay of ^{182}Au. The method of prompt γ-γ coincidences was employed in this analysis. We confirmed all transitions and levels assigned in the previous study [Dav99], except for one transition. Additionally, thanks to the large collected statistics, we identified 336 new γ rays and

125 levels. As a result, the level scheme of ^{182}Pt was considerably extended up to ~3.7 MeV in excitation energy. The intensities of transitions were determined either from singles γ ray or γ-γ coincidence spectra. We performed correction for coincidence summing and calculated total transition intensities accounting for internal conversion.

Based on decay characteristics of different γ-ray transitions following the β decay obtained in the last part of the measurement, we determined the half-life of ^{182}Au. All deduced values are consistent with each other. Their weighted average is $T_{1/2}(^{182}\mathrm{Au}) = 16.43(12)$ s and is consistent with the previously-known evaluated half-life of ^{182}Au.

Our analysis included the investigation of the $E0$ transitions via detected conversion electrons. We confirmed the 500-keV $E0$ $0^+_2 \to 0^+_1$ transition and determined its intensity and $q^2_K(E0/E2)$ mixing ratio. Besides conversion electrons, corresponding γ rays were observed for the first time for the 455-keV $2^+_5 \to 2^+_3$ transition previously observed only via conversion electrons [Dav99] and assigned it the mixed $E0 + M1 + E2$ character. Internal conversion coefficients were determined for two additional transitions. Both K and L ICCs for the 513-keV $2^+_2 \to 2^+_1$ transition are comparable to theoretical values for $M1$ multipolarity, which is in disagreement with the previously assumed presence of the $E0$ component [Cai74]. On the other hand, the $E0$ component was confirmed for the 701-keV $2^+_3 \to 2^+_1$ transition. We calculated its monopole strength using the estimated half-life of the 2^+_3 level. The obtained value of $10^3 \cdot \rho^2(E0, 701) = 14^{+26}_{-10}$ is similar to that of equivalent transitions in nearby nuclei connecting two coexisting bands.

The intensity of β-decay feeding to each level was determined as the difference in intensity of incoming and outgoing transitions. From these feedings, log ft values for each level were calculated [LOG]. Log ft values for previously assigned 2^+ and 3^+ states in ^{182}Pt fall within the range of allowed decay, which is expected for the decay of $I^\pi = (2^+)$ g.s. in ^{182}Au. However, β-decay feeding of comparable magnitude was observed for 4^+ states. The following three explanations were considered.

Feeding of the 2^+ and 4^+ could be easily explained by the 3^+ g.s. of ^{182}Au. While the initial study [Rom92] suggested such an assignment, later experiments [Ibr01; Har20] convincingly assigned $I = (2^+)$ for the g.s. of ^{182}Au. The second considered explanation was a new, β-decaying isomeric state in ^{182}Au with spin $I = 5$. Such an isomer was proposed in a recent NUBASE evaluation [Kon21]. Theoretical calculations also predict a 5^+ excited state in ^{182}Au, but not as an isomer. Unlike for β decay of ^{184}Au, where two 5^+ and 2^+ long-lived states are present [Le 97], much lower feeding to the 6^+_1 level was observed for β decay of ^{182}Au. Additionally, the laser-spectroscopy study [Har20] did not observe any hyperfine structure corresponding to a new isomeric state. Moreover, our values of ^{182}Au half-life obtained from several transitions are consistent with the decay of a single state, therefore, the scenario involving an isomer was also rejected. The third, and the most probable explanation, is the pandemonium effect [Har77], which influences γ-ray spectroscopy studies using high-resolution detectors, such as HPGe detectors employed during the experiment. The detection efficiency of these detectors rapidly decreases for high-energy γ rays. As a consequence, low-intensity and high-energy transitions may remain unobserved by the HPGe detectors. Because of this, β-decay feeding intensities determined from the intensity balance at each level may be overestimated. We extended the ^{182}Pt level scheme by a large amount, up to 3.7 MeV, and reduced the influence of the pandemonium effect, as approximately 45% of all observed apparent β-decay feeding led to new states. However, because of the large Q_{EC} = 7864(23) keV [Wan21], there is still a high possibility of unobserved feeding to higher-lying states.

The second part of the Thesis focused on the α decay of ^{182}Au. We observed all previously reported fine-structure α decays [Bin95]. Four groups of α-γ coincidence events were detected, of which three were new. This allowed us to give a more precise energy of 127.5(7) keV for the previously known 123(7)-keV level in ^{178}Ir and assign a new 5293-keV α decay feeding the 115-keV level. Additionally, the fifth tentative fine-structure α decay with the energy of 5185 keV was suggested.

Relative intensities of all ^{182}Au α decays determined from singles spectrum or α-γ coincidences were used to calculate reduced α-decay widths. We calculated the corresponding hindrance factors relative to unhindered α decays of neighbouring ^{181,183}Au. Low hindrance factor of the most intense 5350-keV α decay HF = 3.0(7) agrees with the previous $I^\pi = (2^+)$ assignment of the 55-keV state in ^{178}Ir. A mixed $M1 + E2$ character of the 55-keV transition de-exciting this level was deduced based on its internal conversion, resulting in the $I^\pi = (1^+, 2^+, 3^+)$ assignment for the g.s. of ^{178}Ir.

The α-decay branching ratio of ^{182}Au was determined employing two different methods. Direct comparison of α and β decays of ^{182}Au resulted in $b_\alpha(^{182}\mathrm{Au}) = 0.117(13)\%$. Indirect comparison using the number of ^{182}Pt α decays and its branching ratio yielded the value $b_\alpha(^{182}\mathrm{Au}) = 0.129(11)\%$. Both results were in agreement with each other and with the previously known value $b_\alpha(^{182}\mathrm{Au}) = 0.13(5)\%$.

Future studies of ^{182}Au and ^{182}Pt would benefit from the recent improvements to the IDS setup [Cub23a], which now offers higher γ-ray efficiency with an increased number of mountable detectors. The employment of $LaBr_3$(Ce) detectors for fast-timing measurements would provide lifetime data on levels in the second rotational band in ^{182}Pt, which remain unknown. These half-lives would allow us to extract the monopole strengths for the 500- and 701-keV transitions ($0^+_2 \rightarrow 0^+_1$ and $2^+_3 \rightarrow 0^+_1$, respectively), which we were unable to determine in this Thesis. In particular, the former could be used to extract the difference in mean-squared charge radii of the 0^+_1 and 0^+_2 coexisting states. Additionally, a set of two coexisting bands with $K = 2$ connected by transitions with strong $E0$ components was observed in ^{184}Pt alongside the well-established $K = 0$ bands [Xu92]. No such structures were identified in our study, which could be caused by the insufficient experimental sensitivity to conversion electrons. A follow-up measurement at IDS with improved detection efficiency for conversion electrons, for example, using the SPEDE spectrometer successfully employed to study neutron-deficient mercury isotopes in Ref. [Str23], would be able to search for these transitions. Verifying the presence of coexisting $K = 2$ bands in ^{182}Pt would enhance the systematics of shape coexistence in this mass region.

Appendix

Appendix A

Coincidence spectra

The following Figs. A.1-A.6 show γ-ray coincidences gated on several of the most intense transitions in ^{182}Pt. New transitions are highlighted in blue. AP stands for artificial peak from Compton scattering. Transitions marked with an asterisk are caused by a summation of denoted γ or X rays. Transitions marked with a circle $\circ$ are not true coincidences with the gated transition, but with other transitions present in the gated energy range.

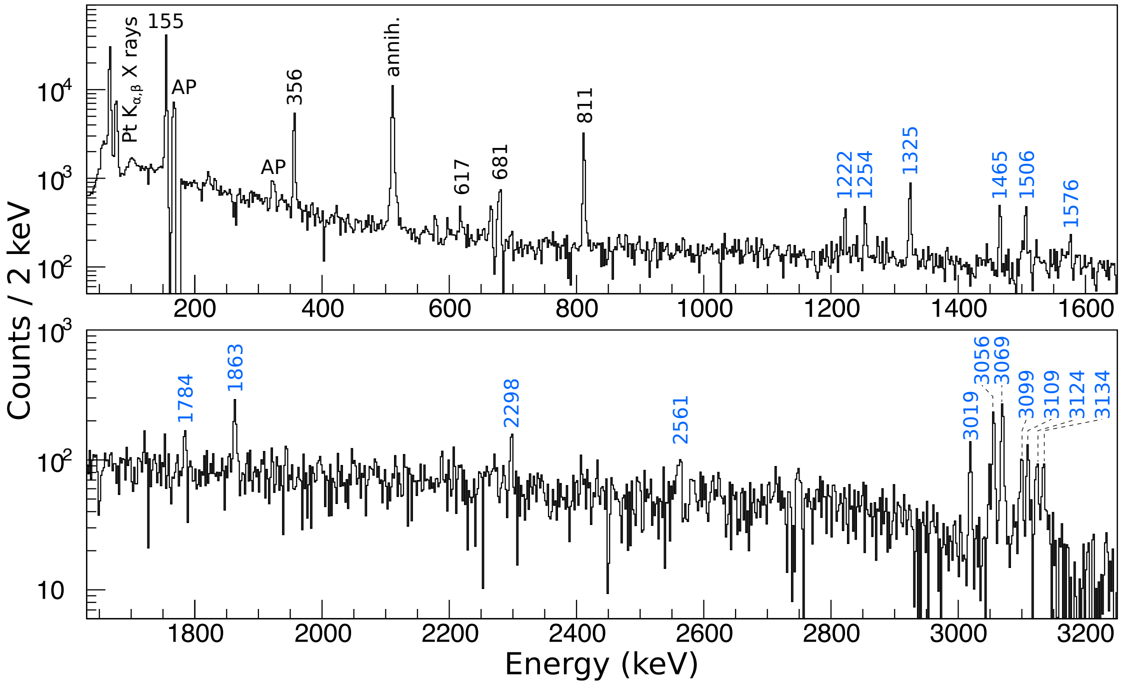

Figure A.1: γ-ray coincidences gated on the 345-keV $0_2^+ \rightarrow 2_1^+$ transition.

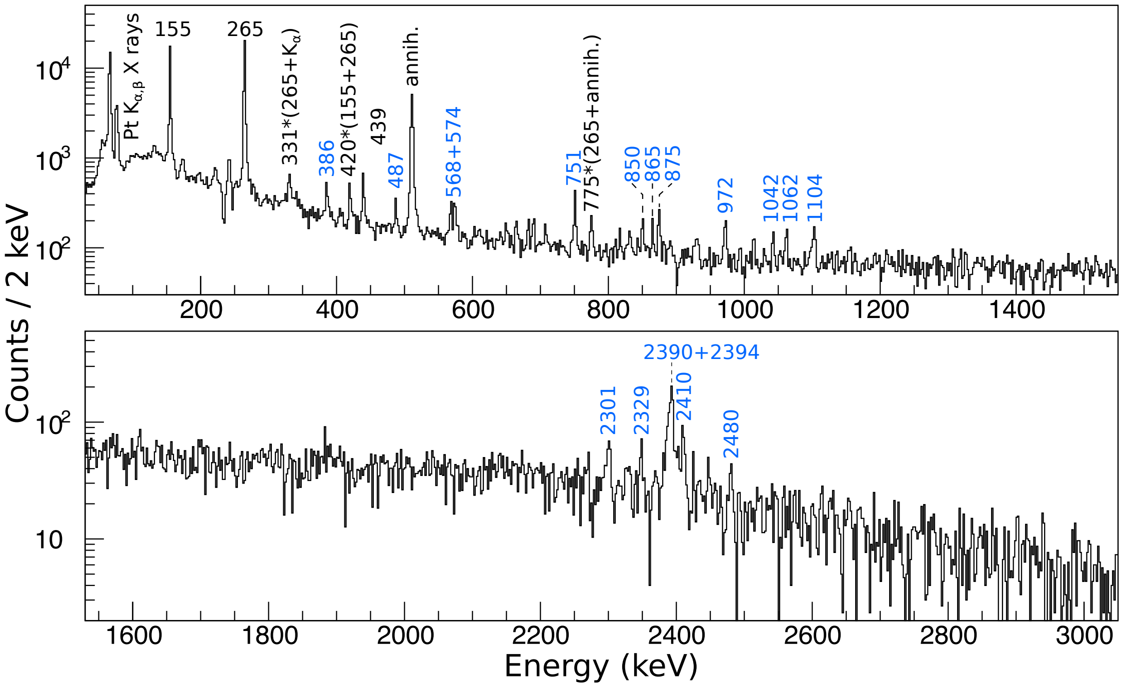

Figure A.2: γ-ray coincidences gated on the 614-keV $4_2^+ \rightarrow 4_1^+$ transition.

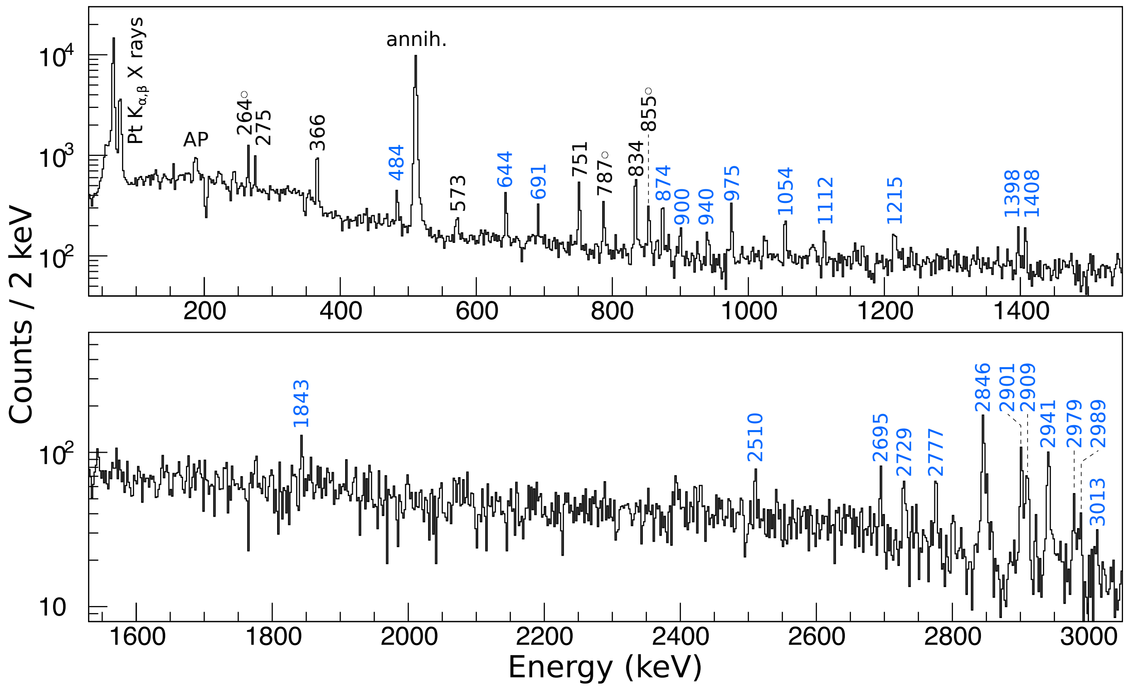

Figure A.3: γ-ray coincidences gated on the 668-keV $2_2^+ \rightarrow 0_1^+$ transition. Peaks marked with circles are in coincidence with the 665- and 666-keV transitions.

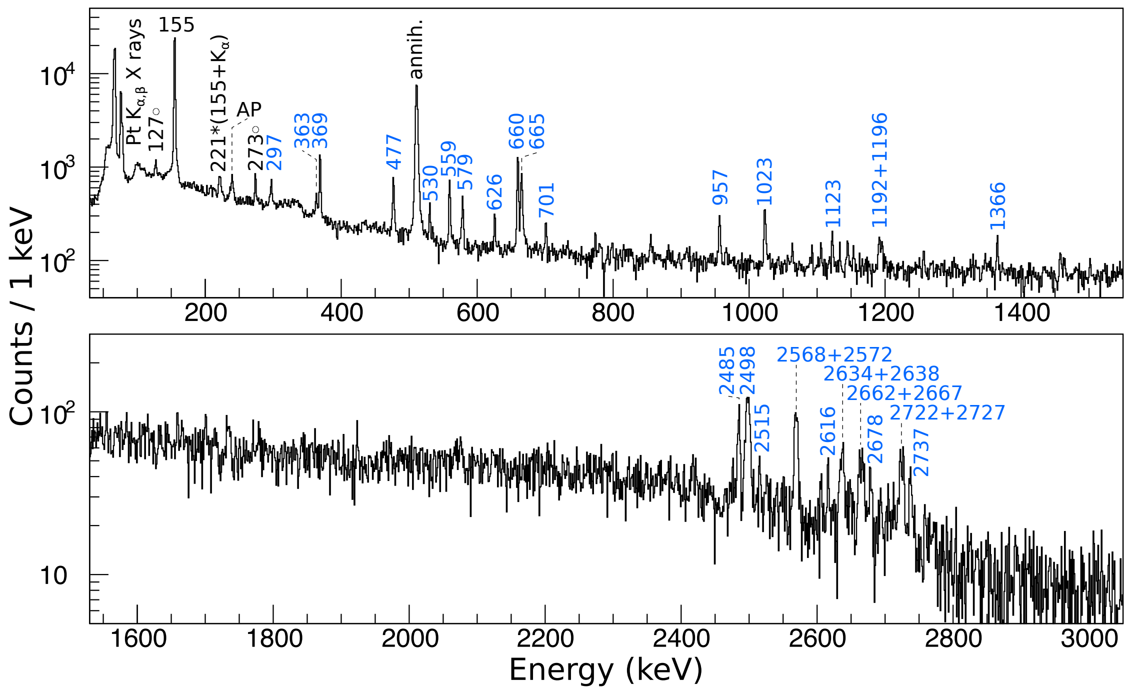

Figure A.4: γ-ray coincidences gated on the 787-keV $(3_1^+) \rightarrow 2_1^+$ transition. Peaks marked with circles are in coincidence with the 790-keV transition (β decay of ^{182}Ir).

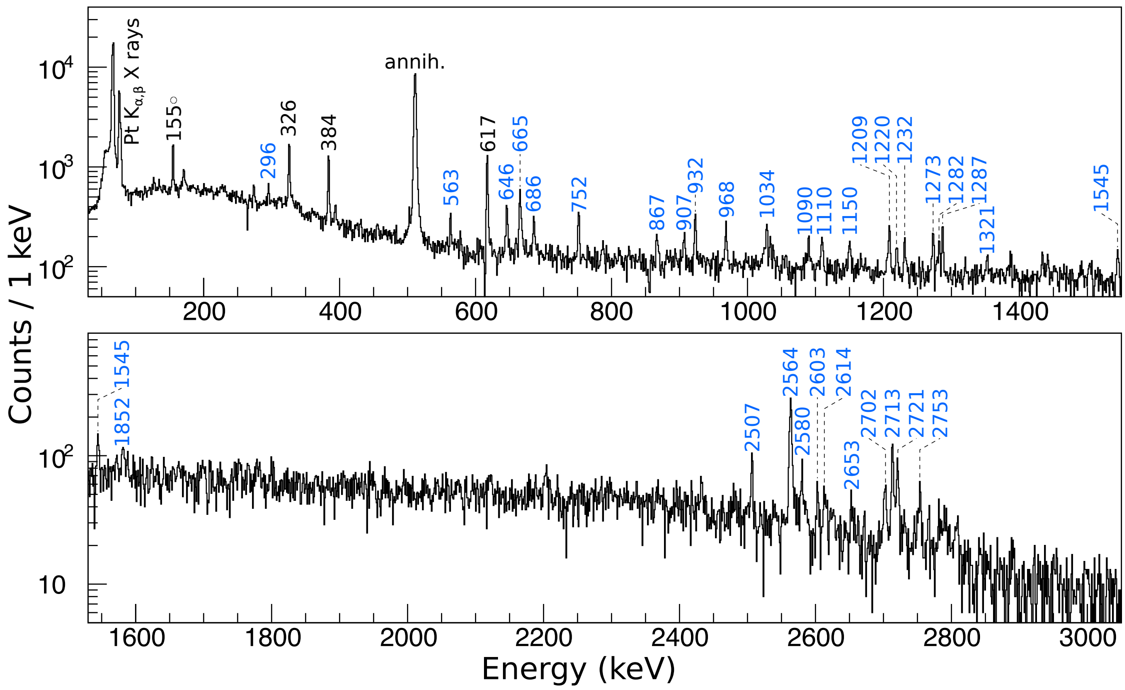

Figure A.5: γ-ray coincidences gated on the 856-keV $2_3^+ \to 0_1^+$ transition. Peak marked with a circle is in coincidence with the 853-keV (787 keV+K_α summing) transitions.

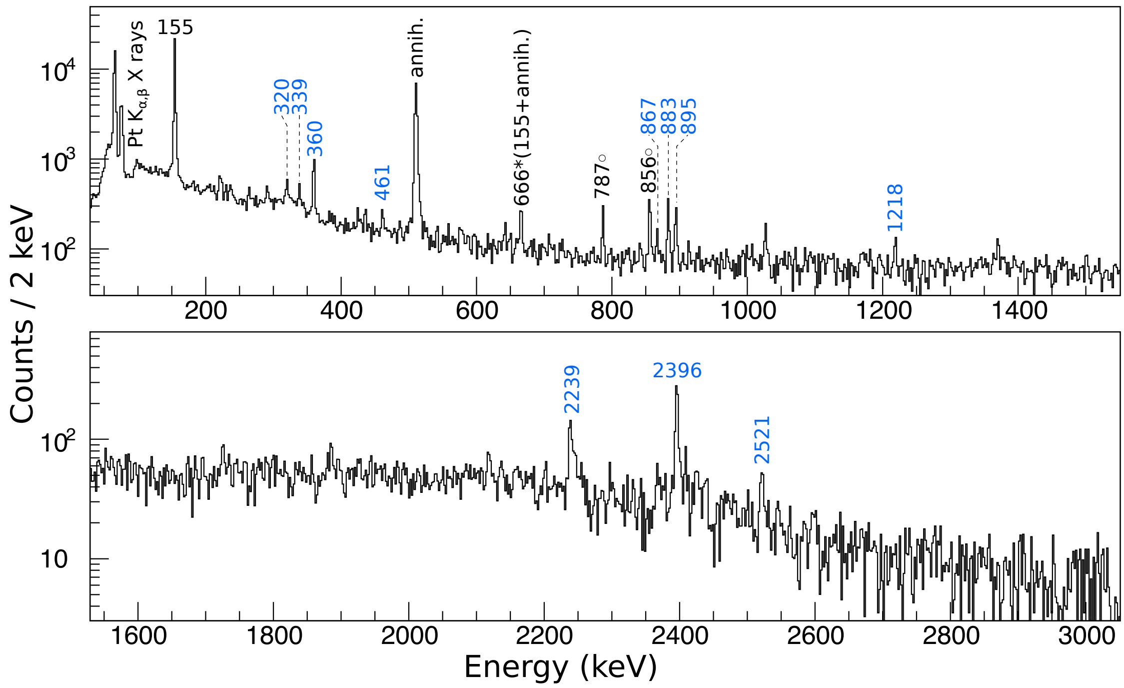

Figure A.6: γ-ray coincidences gated on the 1027-keV $(2_4) \to 2_1^+$ transition. Peaks marked with circles are in coincidence with the 1023- and 1028-keV transitions.

Appendix B

Level scheme of ^{182}Pt

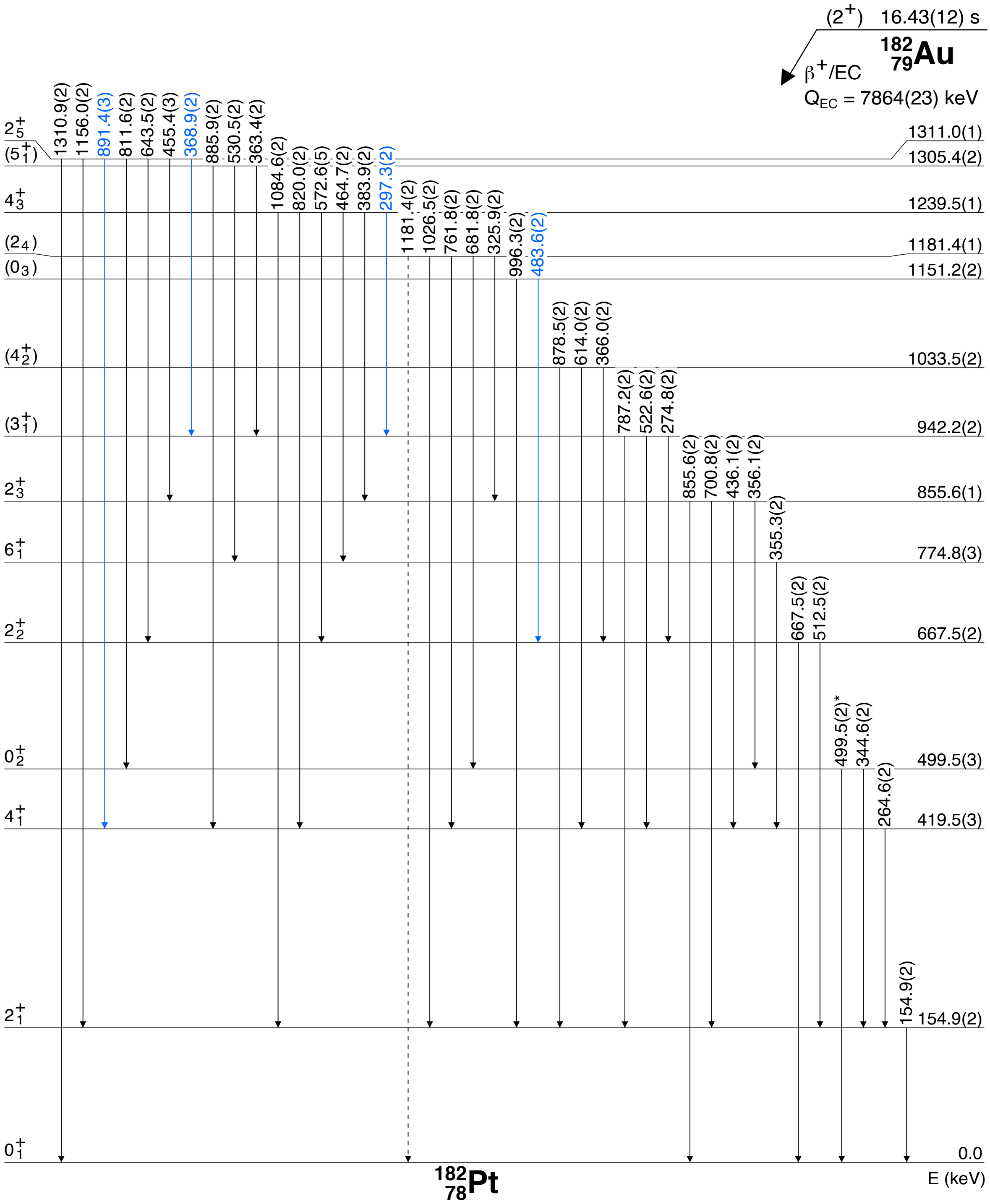

Figure B.1: Part 1 of the level scheme of excited states in ^{182}Pt populated in EC/β^{+} decay of ^{182}Au. The spin and parity values are taken from Ref. [Dav99]. Transitions and levels highlighted in blue are newly observed in this study. Tentative transition is given in a dashed line. Half-life, Q_{EC} and spin assignment for ^{182}Au g.s. are from our work, Ref. [Wan21] and Ref. [Har20], respectively.

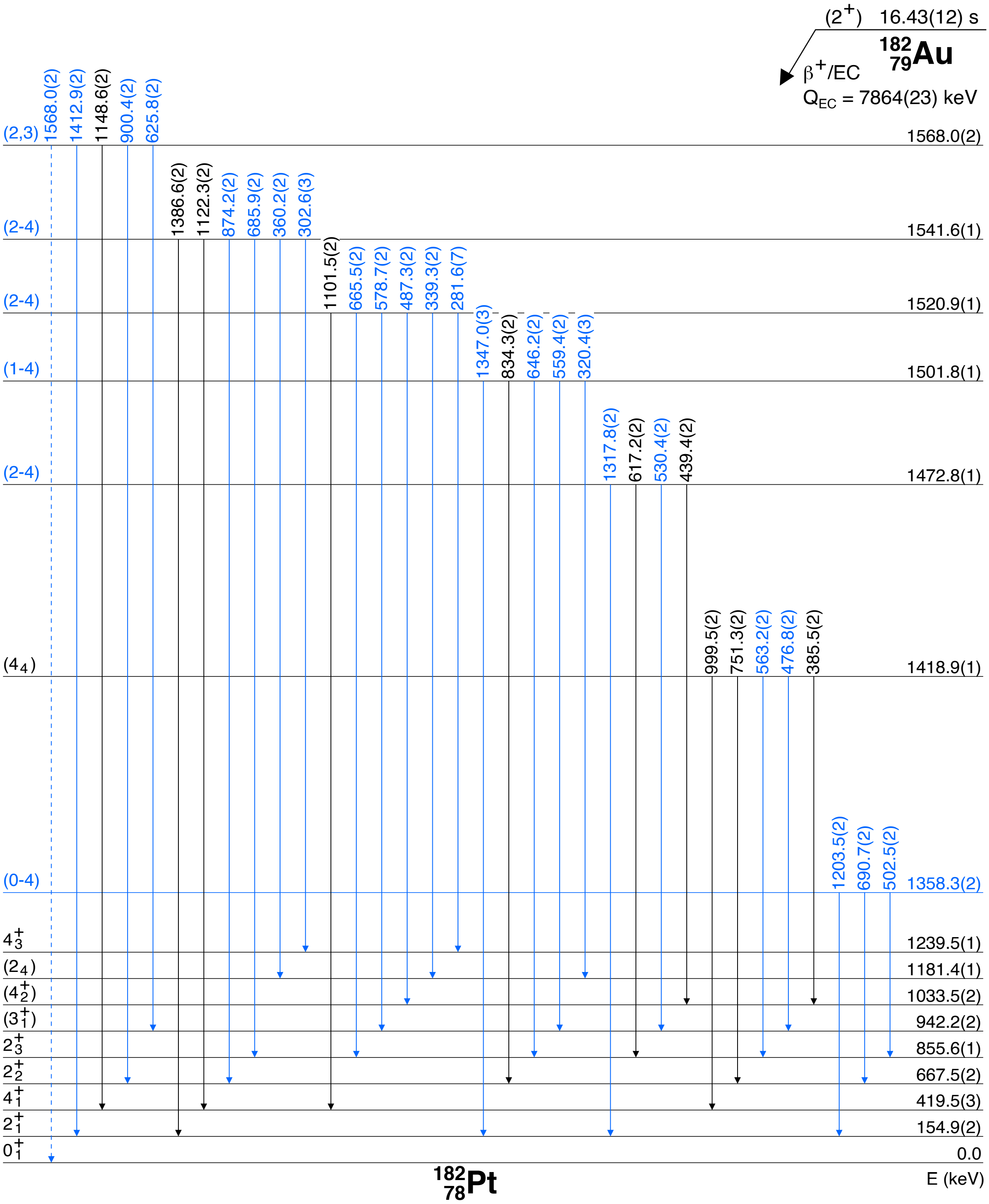

Figure B.2: Part 2 of the level scheme of excited states in ^{182}Pt populated in EC/β^+ decay of ^{182}Au. The spin and parity values are taken from Ref. [Dav99] or deduced from the de-excitation paths. Transitions, levels and level spins highlighted in blue are newly assigned in this study. Tentative transition is given in a dashed line. Half-life, Q_{EC} and spin assignment for ^{182}Au g.s. are from our work, Ref. [Wan21] and Ref. [Har20], respectively.

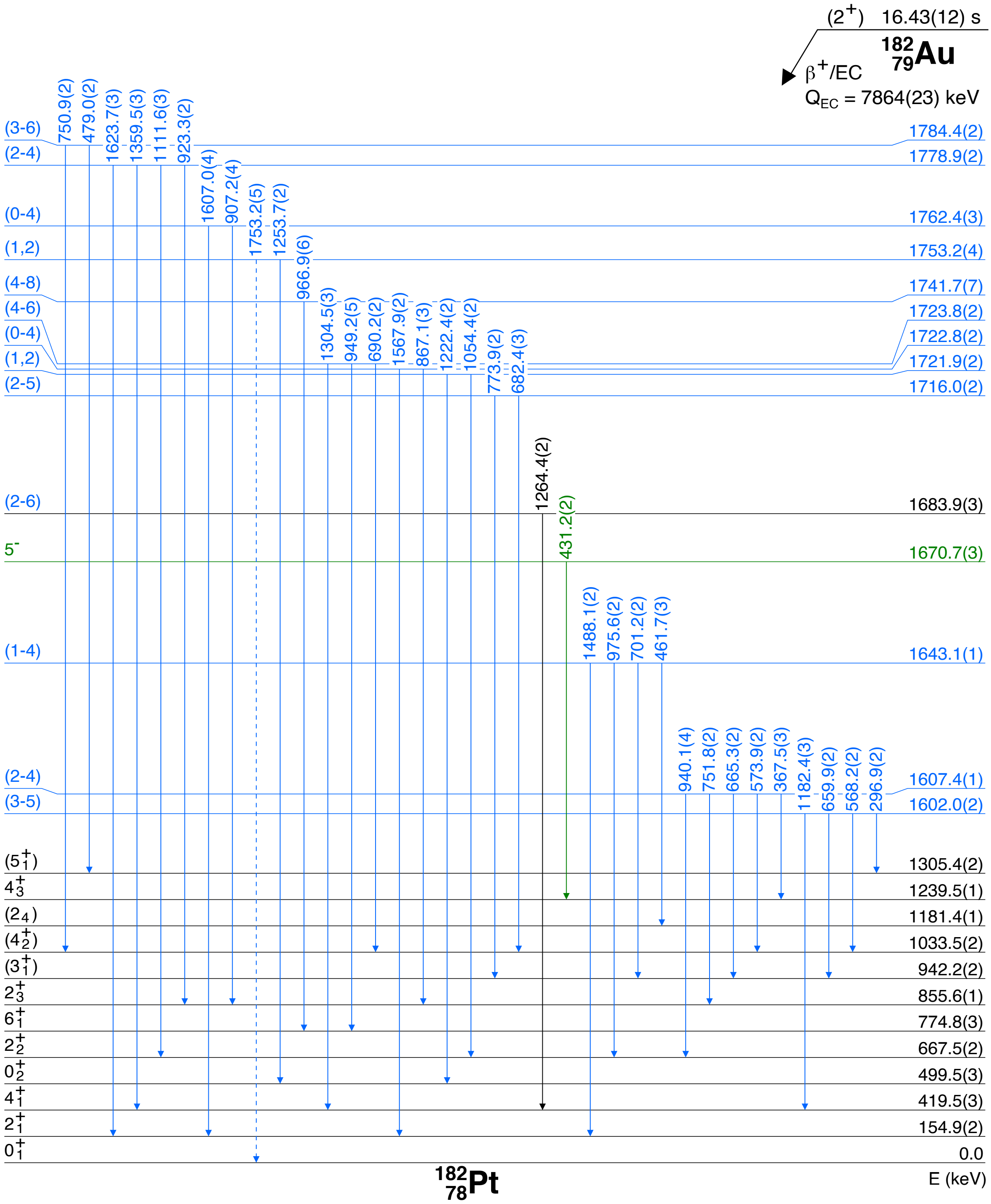

Figure B.3: Part 3 of the level scheme of excited states in ^{182}Pt populated in EC/β^+ decay of ^{182}Au. The spin and parity values are taken from Refs. [Dav99; Pop97] or deduced from the de-excitation paths. Transitions, levels and level spins highlighted in blue are newly assigned in this study. Transitions and levels in green are known from the in-beam study [Pop97]. Tentative transition is given in a dashed line. Half-life, Q_{EC} and spin assignment for ^{182}Au g.s. are from our work, Ref. [Wan21] and Ref. [Har20], respectively.

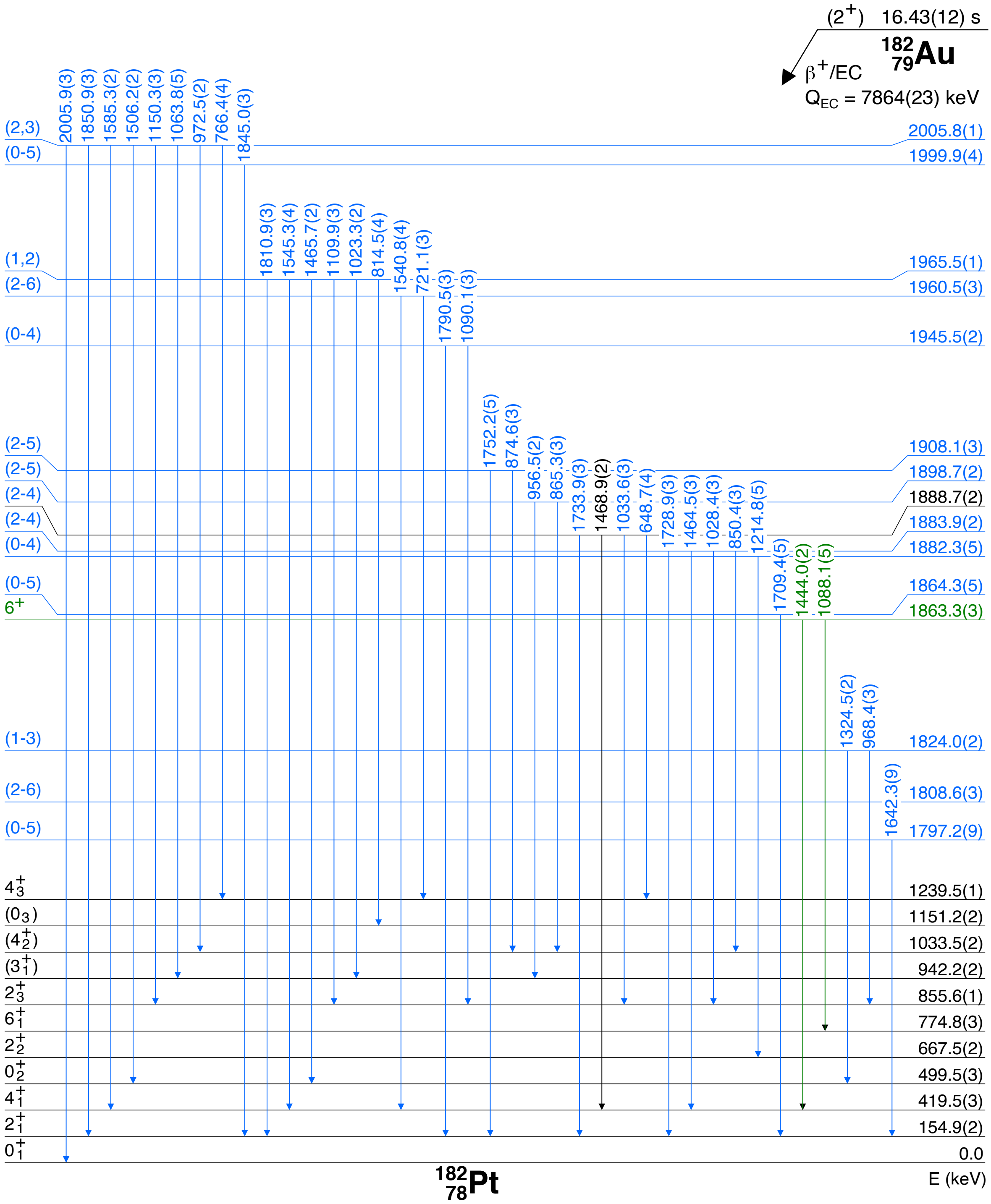

Figure B.4: Part 4 of the level scheme of excited states in ^{182}Pt populated in EC/β^{+} decay of ^{182}Au. The spin and parity values are taken from Refs. [Dav99; Pop97] or deduced from the de-excitation paths. Transitions, levels and level spins highlighted in blue are newly assigned in this study. Transitions and levels in green are known from the in-beam study [Pop97]. Half-life, Q_{EC} and spin assignment for ^{182}Au g.s. are from our work, Ref. [Wan21] and Ref. [Har20], respectively.

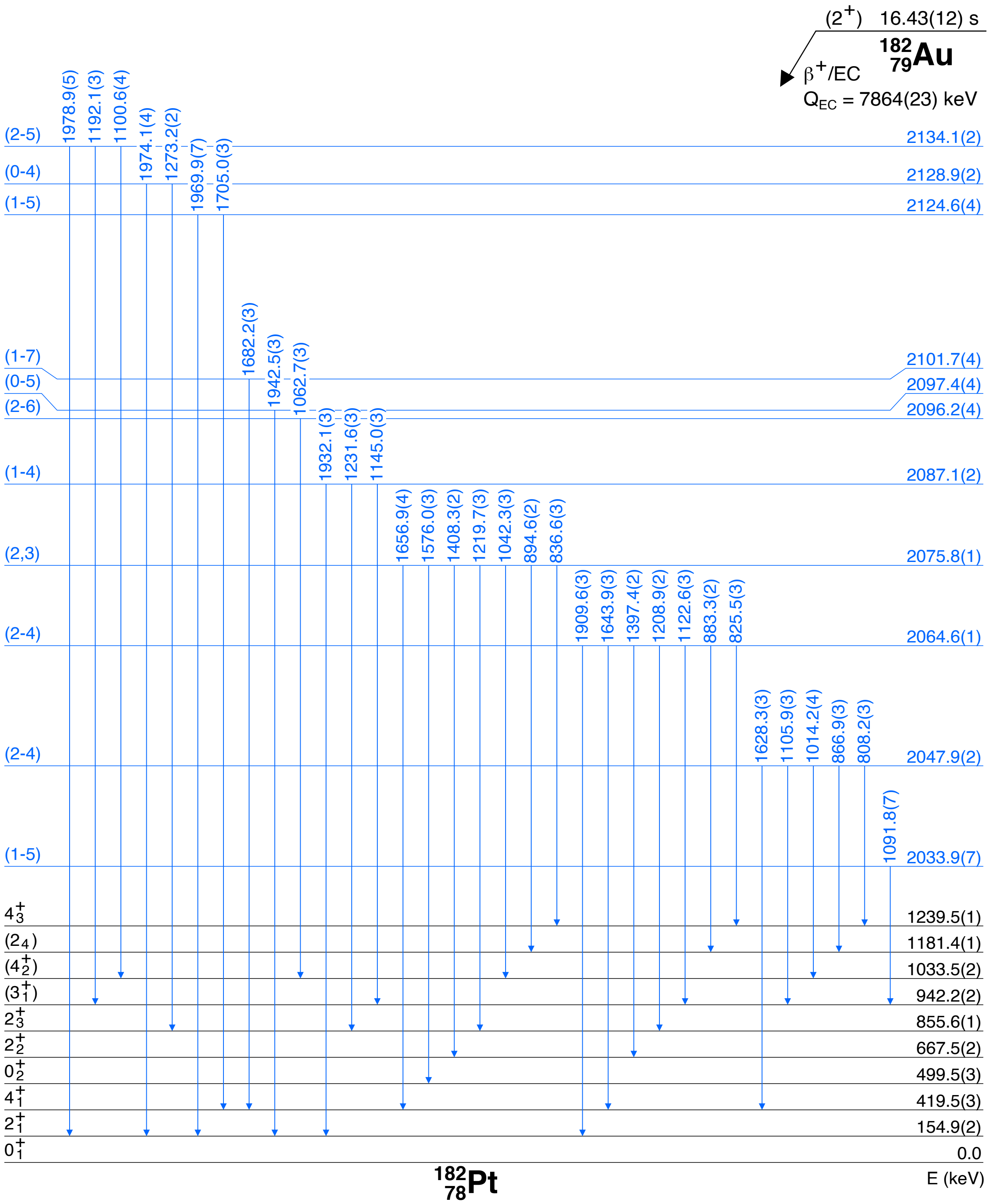

Figure B.5: Part 5 of the level scheme of excited states in ^{182}Pt populated in EC/β^+ decay of ^{182}Au. The spin and parity values are taken from Ref. [Dav99] or deduced from the de-excitation paths. Transitions, levels and level spins highlighted in blue are newly assigned in this study. Half-life, Q_{EC} and spin assignment for ^{182}Au g.s. are from our work, Ref. [Wan21] and Ref. [Har20], respectively.

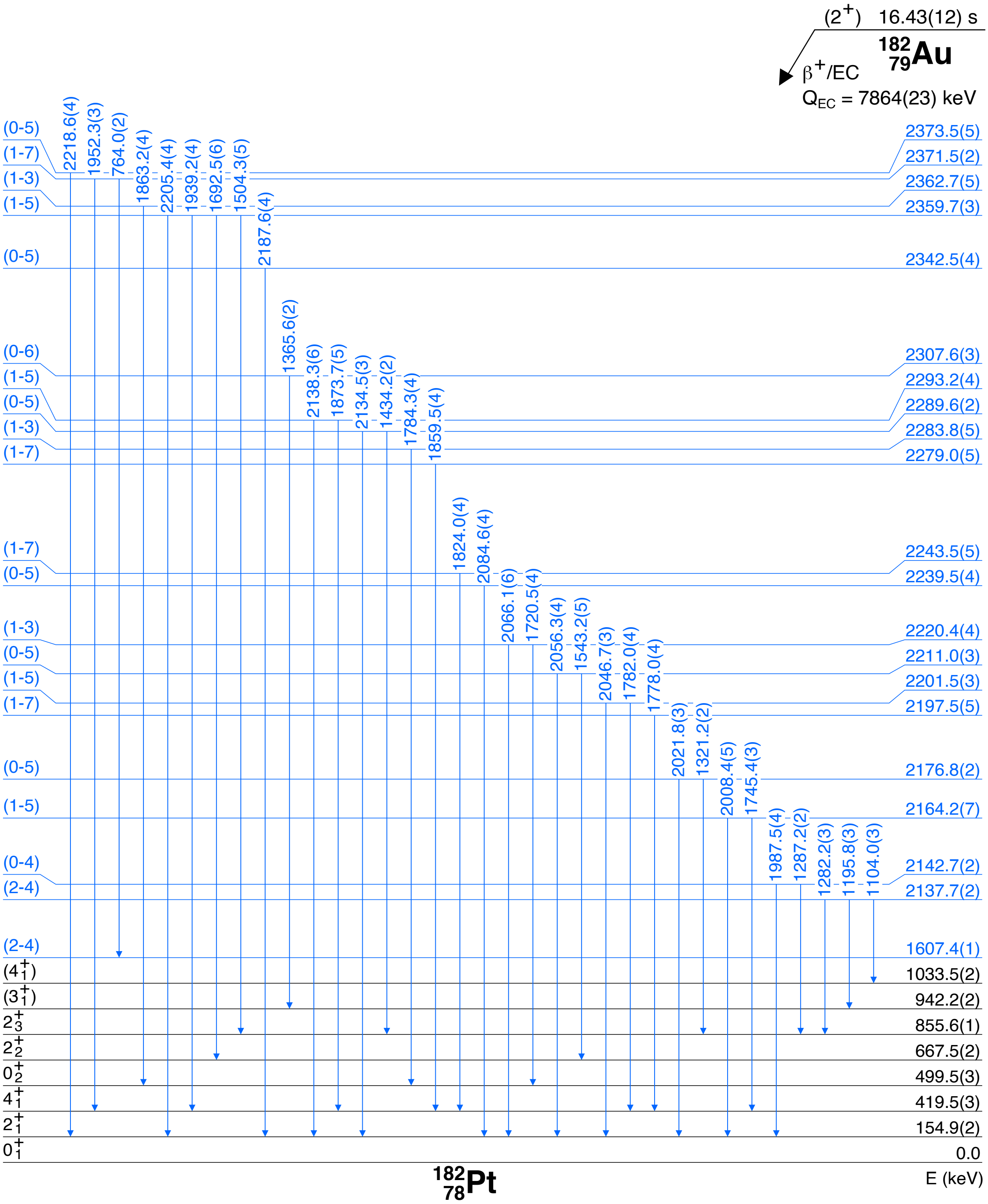

Figure B.6: Part 6 of the level scheme of excited states in ^{182}Pt populated in EC/β^+ decay of ^{182}Au. The spin and parity values are taken from Ref. [Dav99] or deduced from the de-excitation paths. Transitions, levels and level spins highlighted in blue are newly assigned in this study. Half-life, Q_{EC} and spin assignment for ^{182}Au g.s. are from our work, Ref. [Wan21] and Ref. [Har20], respectively.

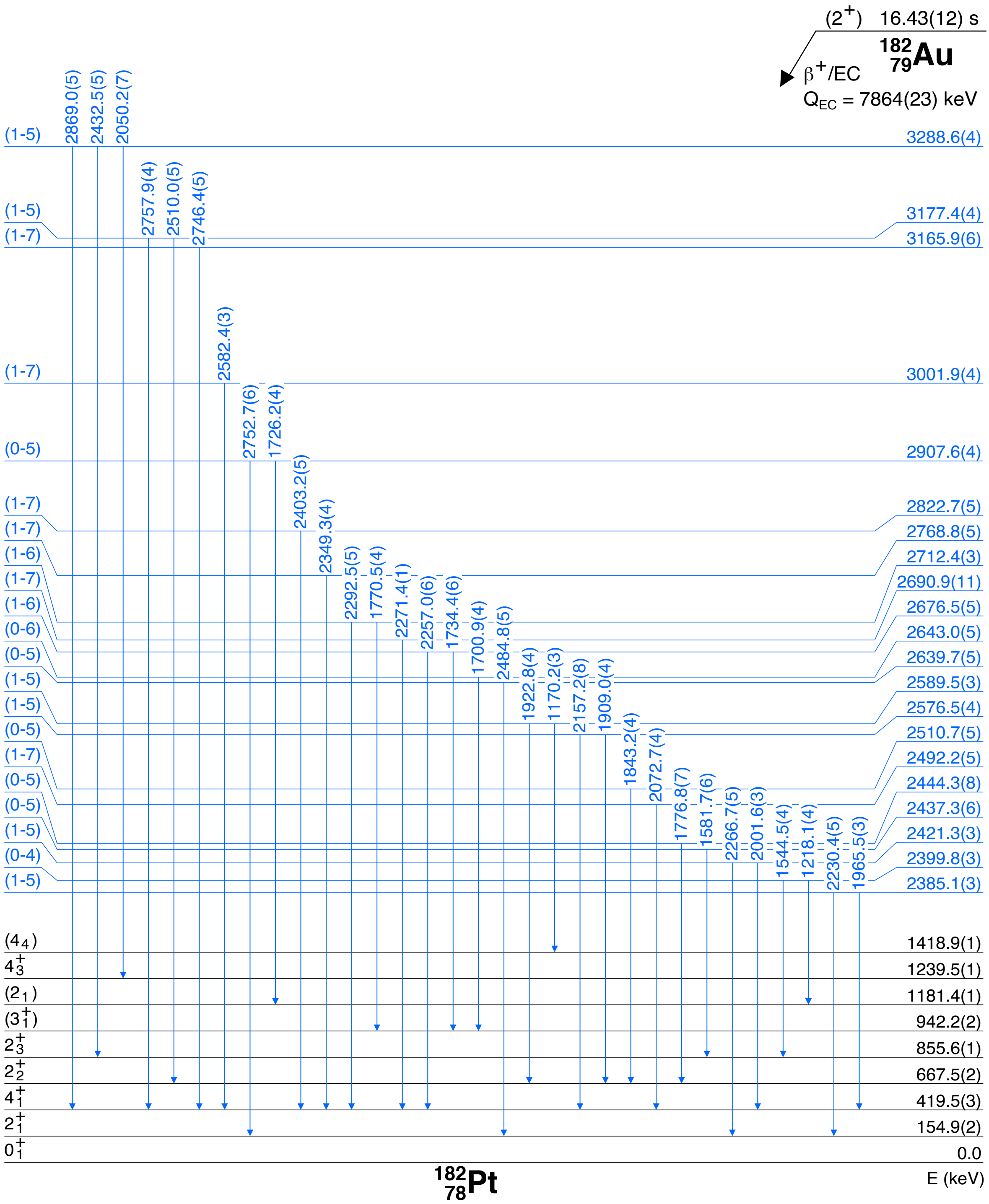

Figure B.7: Part 7 of the level scheme of excited states in ^{182}Pt populated in EC/β^+ decay of ^{182}Au. The spin and parity values are taken from Ref. [Dav99] or deduced from the de-excitation paths. Transitions, levels and level spins highlighted in blue are newly assigned in this study. Half-life, Q_{EC} and spin assignment for ^{182}Au g.s. are from our work, Ref. [Wan21] and Ref. [Har20], respectively.

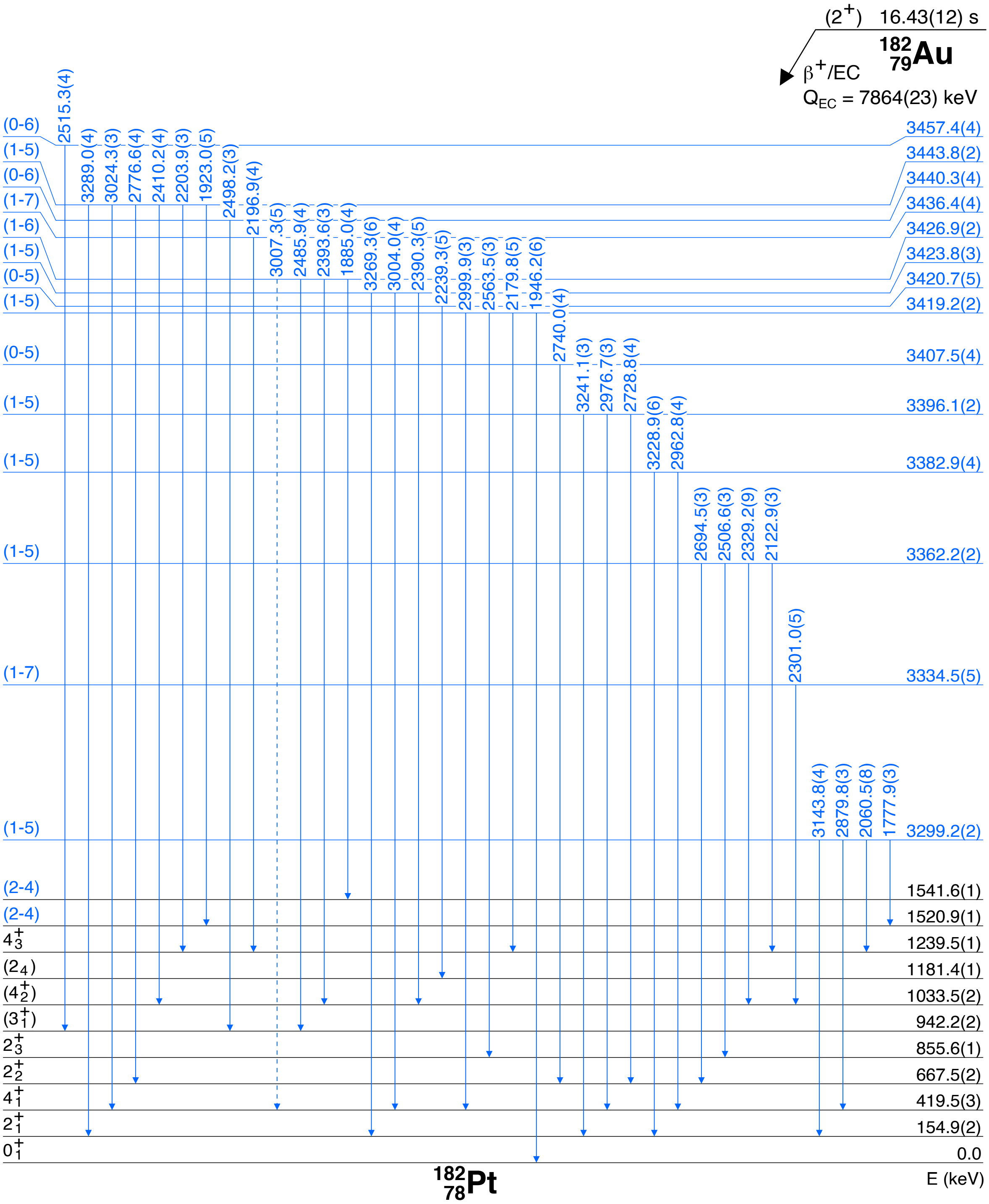

Figure B.8: Part 8 of the level scheme of excited states in ^{182}Pt populated in EC/β^+ decay of ^{182}Au. The spin and parity values are taken from Ref. [Dav99] or deduced from the de-excitation paths. Transitions, levels and level spins highlighted in blue are newly assigned in this study. Tentative transition is given in a dashed line. Half-life, Q_{EC} and spin assignment for ^{182}Au g.s. are from our work, Ref. [Wan21] and Ref. [Har20], respectively.

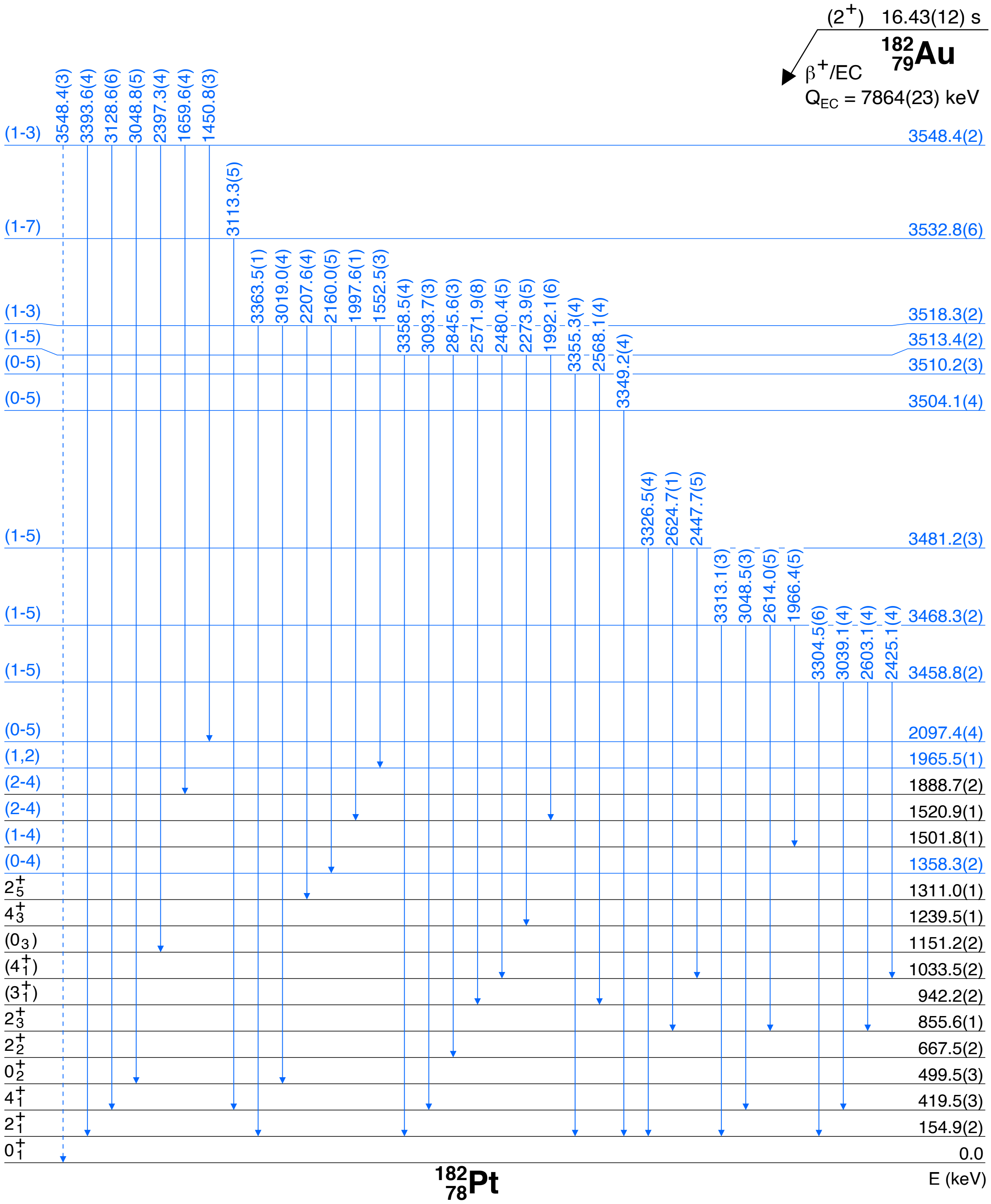

Figure B.9: Part 9 of the level scheme of excited states in ^{182}Pt populated in EC/β^+ decay of ^{182}Au. The spin and parity values are taken from Ref. [Dav99] or deduced from the de-excitation paths. Transitions, levels and level spins highlighted in blue are newly assigned in this study. Tentative transition is given in a dashed line. Half-life, Q_{EC} and spin assignment for ^{182}Au g.s. are from our work, Ref. [Wan21] and Ref. [Har20], respectively.

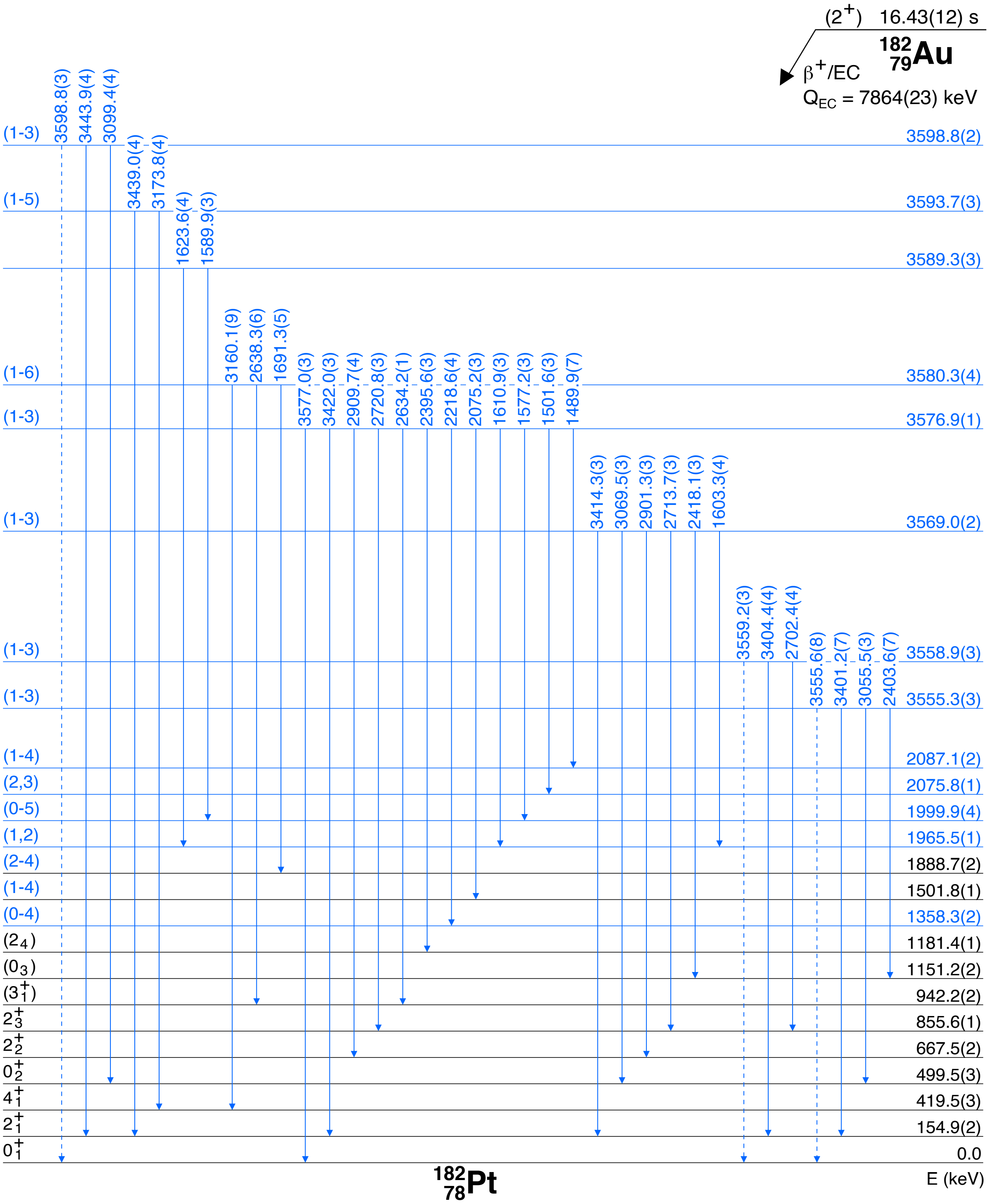

Figure B.10: Part 10 of the level scheme of excited states in ^{182}Pt populated in EC/β^+ decay of ^{182}Au. The spin and parity values are taken from Ref. [Dav99] or deduced from the de-excitation paths. Transitions, levels and level spins highlighted in blue are newly assigned in this study. Tentative transitions are given in dashed lines. Half-life, Q_{EC} and spin assignment for ^{182}Au g.s. are from our work, Ref. [Wan21] and Ref. [Har20], respectively.

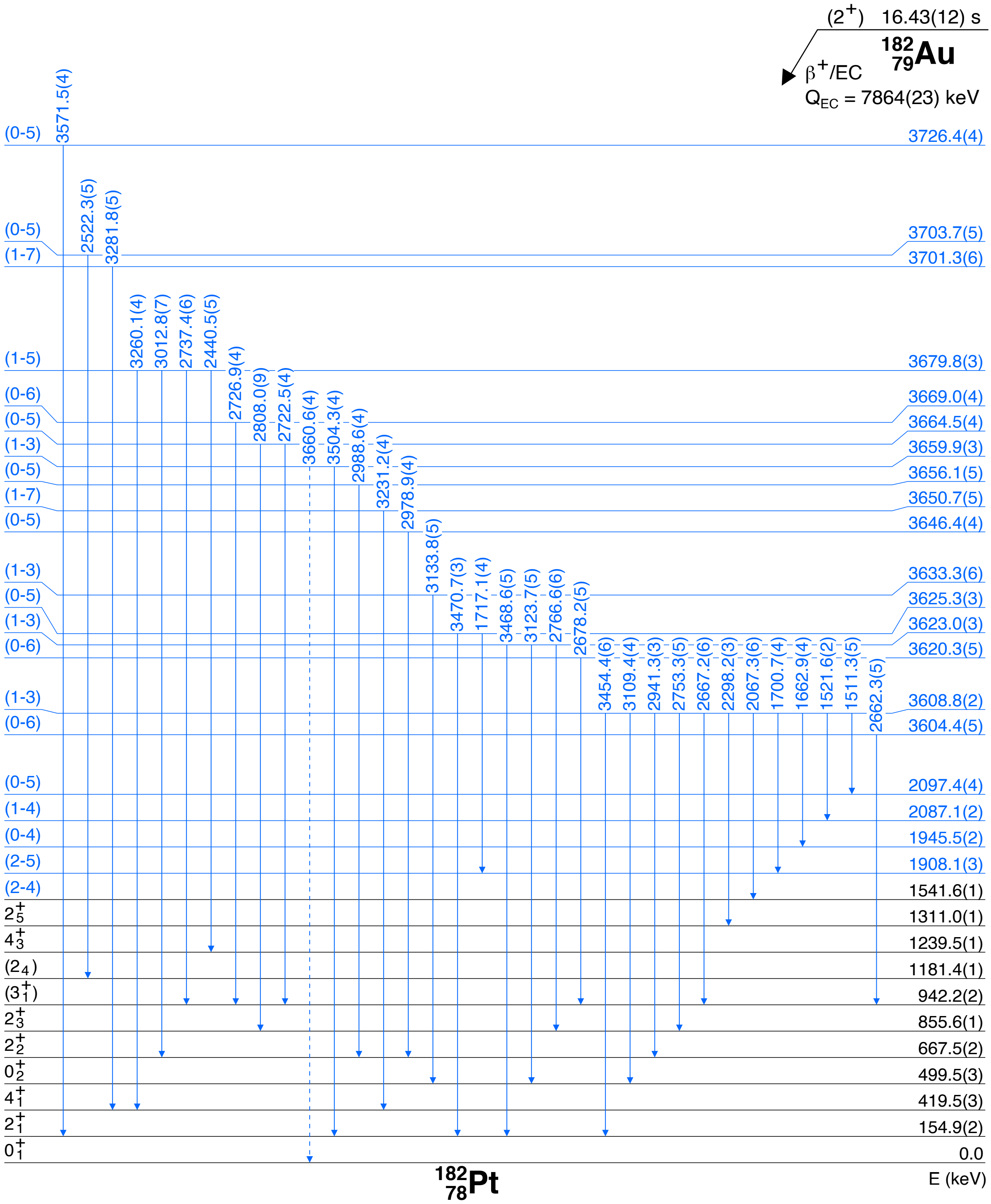

Figure B.11: Part 11 of the level scheme of excited states in ^{182}Pt populated in EC/β^{+} decay of ^{182}Au. The spin and parity values are taken from Ref. [Dav99] or deduced from the de-excitation paths. Transitions, levels and level spins highlighted in blue are newly assigned in this study. Tentative transition is given in a dashed line. Half-life, Q_{EC} and spin assignment for ^{182}Au g.s. are from our work, Ref. [Wan21] and Ref. [Har20], respectively.

Appendix C

Transitions and levels in ^{182}Pt

Table C.1: A list of levels and transitions following the EC/β^+ decay of ^{182}Au. E_i and E_f are the respective energies of the initial and final states of the γ-ray transition with the energy E_γ. Values of the initial and final spin and parity I_i^π, I_j^π are taken from Refs. [Dav99; Pop97], or deduced from the de-excitation paths. Tentative transitions and levels are written in italics. Relative γ-ray intensities I_γ are normalised to the intensity of the 155-keV transition. Values determined from coincidence γ-γ spectra are indicated with an asterisk. For the absolute intensity per 100 β decays, multiply by 0.438(9). The total transition intensities I_{tot} were calculated using internal conversion coefficients α_{tot} and are normalised to 100 units for the 155-keV γ-ray intensity. ICCs were taken from Ref. [Kib08] in the case of known multipolarity ([1], $E2$ in all cases), taken from the NNDC evaluation ([2]) [Sin10], evaluated in this work ([3]), or calculated as the average of the ICC for the $E1$ and $M2$ multipolarities ([4]), see Chapter 4.2.5 for details. The last column contains branching ratios b of transitions de-exciting each level, normalised to a sum of 100.

E_i (keV)	I_i^π	E_f (keV)	I_f^π	E_γ (keV)	I_γ (%)	α_{tot}	I_{tot}	b (%)
154.9(2)[d]	2_1^+	0	0_1^+	154.9(2)[d]	100	0.888(13) [1]	188.8(13)	100
419.5(3)[d]	4_1^+	154.9(2)	2_1^+	264.6(2)[d]	45.7(19)	0.1443(21)[1]	52.3(22)	100
499.5(3)[d]	0_2^+	154.9(2)	2_1^+	344.6(2)[d]	7.44(32)	0.0659(10)[1]	7.93(34)	68(3)
		0	0_1^+	499.5(3)[d]	-	-	3.82(43)	32(3)
667.5(2)[d]	2_2^+	154.9(2)	2_1^+	512.5(2)[d]	28.2(34)*	0.066(8)[3]	30.1(36)	76(2)
		0	0_1^+	667.5(2)[d]	9.64(41)	0.01268(18)[1]	9.76(42)	24(2)
774.8(3)[d]	6_1^+	419.5(3)	4_1^+	355.3(2)[d]	1.18(16)*	0.0605(9)[1]	1.25(17)	100
855.6(1)[d]	2_3^+	499.5(3)	0_2^+	356.1(2)[d]	1.63(23)*	0.0601(9)[1]	1.73(24)	7.1(10)
		419.5(3)	4_1^+	436.1(2)[d]	2.98(13)	0.0349(5)[1]	3.08(13)	12.6(6)
		154.9(2)	2_1^+	700.8(2)[d]	1.18(16)*	0.93(13)[3]	2.27(34)	9.2(13)
		0	0_1^+	855.6(2)[d]	17.20(73)	0.00749(11)[1]	17.33(74)	71.1(15)
942.2(2)[d]	(3_1^+)	667.5(2)	2_2^+	274.8(2)[a]	0.47(10)*	0.26(13)[2]	0.59(14)	3(7)
		419.5(3)	4_1^+	522.6(2)[d]	1.96(26)*	0.046(24)[2]	2.05(28)	10.5(13)

Table C.1: (*Continued*)

E_i (keV)	I_i^π	E_f (keV)	I_f^π	E_γ (keV)	I_γ (%)	α_{tot}	I_{tot}	b (%)
		154.9(2)	2_1^+	787.2(2)[d]	16.68(65)	0.0092(4)[2]	16.84(66)	86.4(14)
1033.5(2)[d]	(4_2^+)	667.5(2)	2_2^+	366.0(2)[d]	1.43(19)*	0.0557(8)[1]	1.51(20)	18(2)
		419.5(3)	4_1^+	614.0(2)[d]	5.72(24)	0.025(7)[2]	5.86(25)	71(2)
		154.9(2)	2_1^+	878.5(2)[d]	0.90(12)*	0.024(22)[4]	0.92(13)	11.1(14)
1151.2(2)[d]	(0_3)	667.5(2)	2_2^+	483.6(2)	0.48(8)*	0.13(12)[4]	0.55(11)	28(5)
		154.9(2)	2_1^+	996.3(2)[d]	1.38(19)*	0.00551(8)[1]	1.39(19)	72(5)
1181.4(1)[d]	(2_4)	855.6(1)	2_3^+	325.9(2)[d]	0.92(13)*	0.16(9)[2]	1.06(17)	10.5(15)
		499.5(3)	0_2^+	*681.8(2)*[d]	0.09(3)*	0.049(45)[4]	0.09(3)	0.9(3)
		419.5(3)	4_1^+	761.8(2)[d]	0.37(6)*	0.036(32)[4]	0.38(6)	3.7(6)
		154.9(2)	2_1^+	1026.5(2)[d]	8.08(34)	0.0102(19)[2]	8.16(35)	80.5(16)
		0	0_1^+	*1181.4(2)*	0.45(5)	0.011(10)[4]	0.45(5)	4.5(5)
1239.5(1)[d]	4_3^+	942.2(2)	(3_1^+)	297.3(2)	0.14(3)*	0.62(60)[4]	0.23(9)	3.5(14)
		855.6(1)	2_3^+	383.9(2)[d]	0.98(14)*	0.0489(7)[1]	1.03(14)	15.9(19)
		774.8(3)	6_1^+	464.7(2)[d]	0.37(6)*	0.0297(5)[1]	0.38(6)	5.8(9)
		667.5(2)	2_2^+	572.6(5)[d]	0.35(11)*	0.081(75)[4]	0.38(12)	5.8(18)
		419.5(3)	4_1^+	820.0(2)[d]	0.95(4)	0.20(7)[2]	1.14(8)	17.5(13)
		154.9(2)	2_1^+	1084.6(2)[d]	3.34(14)	0.00467(7)[1]	3.35(14)	52(2)
1305.4(2)[d]	(5_1^+)	942.2(2)	(3_1^+)	363.4(2)[d]	0.11(3)*	0.0568(8)[1]	0.12(3)	11(3)
		774.8(3)	6_1^+	530.5(2)[d]	0.13(2)*	0.10(9)[4]	0.14(3)	13(3)
		419.5(3)	4_1^+	885.9(2)[d]	0.79(11)*	0.024(21)[4]	0.81(11)	76(4)
1311.0(1)[d]	2_5^+	942.2(2)	(3_1^+)	368.9(2)	0.92(13)*	0.31(29)[4]	1.20(32)	17(4)
		855.6(1)	2_3^+	455.4(3)[d]	0.05(2)	17.3(75)[3]	0.97(11)	13.7(16)
		667.5(2)	2_2^+	643.5(2)	0.64(9)*	0.058(53)[4]	0.68(10)	9.6(15)
		499.5(3)	0_2^+	811.6(2)[d]	1.66(23)*	0.00835(12)[1]	1.67(24)	24(3)
		419.5(3)	4_1^+	891.4(3)	0.13(4)*	0.00689(10)[1]	0.13(4)	1.9(6)
		154.9(2)	2_1^+	1156.0(2)[d]	1.35(6)	0.012(10)[4]	1.37(6)	19.4(14)
		0	0_1^+	1310.9(2)[a]	1.05(5)	0.00326(5)[1]	1.05(5)	14.9(11)
1358.3(2)	(0-4)[f]	855.6(1)	2_3^+	502.5(2)	0.08(2)*	0.12(11)[4]	0.09(3)	9(3)
		667.5(2)	2_2^+	690.7(2)	0.19(7)*	0.047(43)[4]	0.19(7)	20(6)
		154.9(2)	2_1^+	1203.5(2)[b]	0.70(10)*	0.011(9)[4]	0.71(10)	72(6)
1418.9(1)[d]	(4_4)	1033.5(2)	(4_2^+)	385.5(2)[d]	0.10(3)*	0.10(6)[2]	0.11(4)	4.5(15)
		942.2(2)	(3_1^+)	476.8(2)	0.44(7)*	0.14(13)[4]	0.50(10)	20(4)
		855.6(1)	2_3^+	563.2(2)	0.15(3)*	0.09(8)[4]	0.16(3)	6.5(15)
		667.5(2)	2_2^+	751.3(2)[d]	1.03(17)*	0.00982(14)[1]	1.04(17)	42(5)
		419.5(3)	4_1^+	999.5(2)[d]	0.63(9)*	0.017(26)[4]	0.64(9)	26(4)
1472.8(1)[d]	(2-4)[f]	1033.5(2)	(4_2^+)	439.4(2)[d]	0.41(3)	0.180(13)[4]	0.49(8)	13(2)
		942.2(2)	(3_1^+)	530.4(2)	0.17(3)*	0.100(5)[4]	0.18(4)	5(10)
		855.6(1)	2_3^+	617.2(2)[d]	1.88(8)	0.070(54)[4]	2.00(14)	54(3)

Table C.1: (*Continued*)

E_i (keV)	I_i^π	E_f (keV)	I_f^π	E_γ (keV)	I_γ (%)	α_{tot}	I_{tot}	b (%)
		154.9(2)	2_1^+	1317.8(2)	1.02(15)*	$0.0080(71)^4$	1.03(15)	28(3)
1501.8(1)^{d}	(1-4)^{f}	1181.4(1)	(2_4)	320.4(3)	0.07(3)*	$0.490(3)^4$	0.11(5)	3.5(17)
		942.2(2)	(3_1^+)	559.4(2)	0.65(3)	$0.090(23)^4$	0.71(6)	23(2)
		855.6(1)	2_3^+	646.2(2)	0.38(6)*	$0.060(13)^4$	0.40(7)	13(2)
		667.5(2)	2_2^+	834.3(2)^{d}	1.47(19)*	$0.028(49)^4$	1.51(20)	49(4)
		154.9(2)	2_1^+	1347.0(3)	0.32(7)*	$0.0080(67)^4$	0.33(7)	11(2)
1520.9(1)^{d}	(2-4)^{f}	1239.5(1)	4_3^+	281.6(7)	0.08(5)*	$0.740(6)^4$	0.14(11)	6(4)
		1181.4(1)	(2_4)	339.3(2)	0.36(18)*	$0.400(22)^4$	0.51(29)	22(10)
		1033.5(2)	(4_2^+)	487.3(2)	0.09(3)*	$0.130(4)^4$	0.10(4)	4.2(16)
		942.2(2)	(3_1^+)	578.7(2)	0.32(6)*	$0.080(15)^4$	0.35(7)	15(3)
		855.6(1)	2_3^+	665.5(2)	0.17(6)*	$0.053(8)^4$	0.18(7)	8(3)
		419.5(3)	4_1^+	1101.5(2)^{d}	1.01(14)*	$0.013(45)^4$	1.03(14)	45(7)
1541.6(1)^{d}	(2-4)^{f}	1239.5(1)	4_3^+	302.6(3)	0.10(2)*	$0.590(5)^4$	0.16(7)	5(2)
		1181.4(1)	(2_4)	360.2(2)	0.46(11)*	$0.330(18)^4$	0.61(21)	18(5)
		855.6(1)	2_3^+	685.9(2)	0.20(4)*	$0.048(6)^4$	0.20(4)	6.1(13)
		667.5(2)	2_2^+	874.2(2)	0.61(10)*	$0.025(19)^4$	0.63(10)	19(3)
		419.5(3)	4_1^+	1122.3(2)^{d}	0.65(10)*	$0.013(20)^4$	0.66(10)	20(3)
		154.9(2)	2_1^+	1386.6(2)^{d}	1.10(15)*	$0.0070(62)^4$	1.10(15)	33(4)
1568.0(2)^{d}	(2,3)^{f}	942.2(2)	(3_1^+)	625.8(2)	0.12(3)*	$0.060(4)^4$	0.13(3)	4.1(9)
		667.5(2)	2_2^+	900.4(2)^{b}	0.42(8)*	$0.023(13)^4$	0.43(9)	13(3)
		419.5(3)	4_1^+	1148.6(2)^{d}	0.68(3)	$0.012(21)^4$	0.69(3)	21(2)
		154.9(2)	2_1^+	1412.9(2)	0.65(10)*	$0.0070(59)^4$	0.66(10)	20(3)
		0	0_1^+	*1568.0(2)*	1.33(29)	$0.0056(44)^4$	1.34(29)	41(6)
1602.0(2)	(3-5)^{f}	1305.4(2)	(5_1^+)	296.9(2)^{b}	0.07(2)*	$0.620(7)^4$	0.11(5)	7(3)
		1033.5(2)	(4_2^+)	568.2(2)	0.10(3)*	$0.080(6)^4$	0.11(4)	6(2)
		942.2(2)	(3_1^+)	659.9(2)	1.24(16)*	$0.054(80)^4$	1.31(18)	80(4)
		419.5(3)	4_1^+	1182.4(3)	0.11(3)*	$0.0110(95)^4$	0.11(3)	6.9(18)
1607.4(1)	(2-4)^{f}	1239.5(1)	4_3^+	367.5(3)	0.07(2)*	$0.310(7)^4$	0.09(3)	7(3)
		1033.5(2)	(4_2^+)	573.9(2)	0.14(4)*	$0.080(12)^4$	0.15(5)	12(4)
		942.2(2)	(3_1^+)	665.3(2)	0.45(8)*	$0.053(39)^4$	0.47(9)	39(6)
		855.6(1)	2_3^+	751.8(2)	0.31(5)*	$0.037(26)^4$	0.32(5)	26(4)
		667.5(2)	2_2^+	940.1(4)	0.19(8)*	$0.020(16)^4$	0.20(8)	16(6)
1643.1(1)	(1-4)^{f}	1181.4(1)	(2_4)	461.7(3)	0.08(2)*	$0.150(7)^4$	0.09(3)	7(2)
		942.2(2)	(3_1^+)	701.2(2)	0.12(3)*	$0.045(10)^4$	0.13(3)	10(2)
		667.5(2)	2_2^+	975.6(2)	0.57(9)*	$0.018(44)^4$	0.58(9)	44(5)
		154.9(2)	2_1^+	1488.1(2)	0.51(8)*	$0.0060(51)^4$	0.51(8)	39(5)
1670.7(3)	5^-	1239.5(1)	4_3^+	431.2(2)^{c}	0.11(2)*	$0.19(0)^4$	0.13(3)	100
1683.9(3)^{d}	(2-6)^{f}	419.5(3)	4_1^+	1264.4(2)^{d}	1.02(14)*	$0.0090(79)^4$	1.03(14)	100

Table C.1: (*Continued*)

E_i (keV)	I_i^π	E_f (keV)	I_f^π	E_γ (keV)	I_γ (%)	α_{tot}	I_{tot}	b (%)
1716.0(2)	(2-5)^f	1033.5(2)	(4_2^+)	682.4(3)	0.09(3)*	0.049(44)^4	0.09(4)	44(13)
		942.2(2)	(3_1^+)	773.9(2)	0.11(4)*	0.034(56)^4	0.11(4)	56(13)
1721.9(2)	(1,2)^f	667.5(2)	2_2^+	1054.4(2)^b	0.80(11)*	0.015(77)^4	0.81(12)	77(4)
		499.5(3)	0_2^+	1222.4(2)	0.24(4)*	0.0100(87)^4	0.25(4)	23(4)
1722.8(2)	(0-4)^f	855.6(1)	2_3^+	867.1(3)	0.20(5)*	0.025(10)^4	0.20(5)	10(2)
		154.9(2)	2_1^+	1567.9(2)	1.90(26)*	0.0056(44)^4	1.91(26)	90(2)
1723.8(2)	(4-6)^f	1033.5(2)	(4_2^+)	690.2(2)	0.12(5)*	0.047(22)^4	0.12(5)	22(7)
		774.8(3)	6_1^+	949.2(5)	0.08(2)*	0.020(14)^4	0.08(2)	14(4)
		419.5(3)	4_1^+	1304.5(3)	0.35(7)*	0.0090(73)^4	0.35(7)	64(8)
1741.7(7)	(4-8)^f	774.8(3)	6_1^+	966.9(6)	0.10(4)*	0.02(0)^4	0.10(4)	100
1753.2(4)	(1,2)^f	499.5(3)	0_2^+	1253.7(2)	0.28(5)*	0.0100(81)^4	0.28(5)	30(5)
		0	0_1^+	*1753.2(4)*	0.66(11)	0.0044(32)^4	0.66(11)	70(5)
1762.4(3)	(0-4)^f	855.6(1)	2_3^+	907.2(4)	0.13(3)*	0.022(17)^4	0.14(3)	17(5)
		154.9(2)	2_1^+	1607.0(4)	0.66(13)*	0.0053(41)^4	0.67(13)	83(5)
1778.9(2)	(1-4)^f	855.6(1)	2_3^+	923.3(2)	0.33(6)*	0.021(18)^4	0.34(6)	18(4)
		667.5(2)	2_2^+	1111.6(3)	0.32(7)*	0.013(17)^4	0.32(7)	17(4)
		419.5(3)	4_1^+	1359.5(3)	0.16(4)*	0.0080(65)^4	0.16(4)	8(2)
		154.9(2)	2_1^+	1623.7(3)	1.06(29)	0.0052(40)^4	1.07(29)	57(7)
1784.4(2)	(3-6)^f	1305.4(2)	(5_1^+)	479.0(2)	0.09(2)*	0.140(30)^4	0.10(3)	30(9)
		1033.5(2)	(4_2^+)	750.9(2)	0.23(8)*	0.037(70)^4	0.24(8)	70(9)
1797.2(9)	(0-5)^f	154.9(2)	2_1^+	1642.3(9)	0.68(33)*	0.0051(39)^4	0.69(33)	100
1824.0(2)	(1-3)^f	855.6(1)	2_3^+	968.4(3)	0.28(6)*	0.019(32)^4	0.29(6)	32(6)
		499.5(3)	0_2^+	1324.5(2)	0.61(9)*	0.0080(70)^4	0.62(9)	68(6)
1863.3(3)	6^+	774.8(3)	6_1^+	1088.1(5)^c	0.04(2)*	0.014(8)^4	0.04(2)	8(4)
		419.5(3)	4_1^+	1444.0(2)^c	0.50(8)*	0.0070(55)^4	0.50(8)	92(4)
1864.3(5)	(0-5)^f	154.9(2)	2_1^+	1709.4(5)	0.06(3)*	0.0046(35)^4	0.06(3)	100
1882.3(5)	(0-4)^f	667.5(2)	2_2^+	1214.8(5)	0.55(18)*	0.0100(89)^4	0.56(19)	52(10)
1883.9(2)	(2-4)^f	1033.5(2)	(4_2^+)	850.4(2)	0.08(3)*	0.027(24)^4	0.09(3)	9(3)
		855.6(1)	2_3^+	1028.4(2)	0.24(5)*	0.016(14)^4	0.24(5)	24(5)
		264.6(3)	4_1^+	1464.5(2)	0.15(4)*	0.0066(53)^4	0.15(4)	15(4)
		154.9(2)	2_1^+	1728.9(3)	0.51(10)*	0.0045(34)^4	0.51(10)	52(6)
1888.7(2)^d	(2-4)^f	1239.5(1)	4_3^+	648.7(4)	0.12(3)*	0.060(7)^4	0.12(3)	7.2(19)
		855.6(1)	2_3^+	1033.6(3)	0.09(3)*	0.016(6)^4	0.09(3)	5.6(16)
		419.5(3)	4_1^+	1468.9(2)^d	0.75(11)*	0.0070(53)^4	0.75(11)	44(5)
		154.9(2)	2_1^+	1733.9(3)	0.72(12)*	0.0045(33)^4	0.73(12)	43(5)
1898.7(2)	(2-5)^f	1033.5(2)	(4_2^+)	865.3(3)^b	0.07(3)*	0.025(19)^4	0.07(3)	19(7)
		942.2(2)	(3_1^+)	956.5(2)	0.29(6)*	0.019(81)^4	0.30(6)	81(7)
1908.1(3)	(2-5)^f	1033.5(2)	(4_2^+)	874.6(3)	0.07(3)*	0.025(17)^4	0.07(3)	17(7)

Table C.1: (*Continued*)

E_i (keV)	I_i^π	E_f (keV)	I_f^π	E_γ (keV)	I_γ (%)	α_{tot}	I_{tot}	b (%)
		154.9(2)	2_1^+	1752.2(5)	0.34(10)*	$0.0036(12)^4$	0.34(10)	83(7)
1945.5(2)	(0-4)$^{\mathrm{f}}$	855.6(1)	2_3^+	1090.1(3)	0.15(4)*	$0.014(10)^4$	0.15(4)	10(3)
		154.9(2)	2_1^+	1790.5(3)	1.40(19)*	$0.0042(31)^4$	1.40(19)	90(3)
1960.5(3)	(2-6)$^{\mathrm{f}}$	1239.5(1)	4_3^+	721.1(3)	0.09(3)*	$0.042(26)^4$	0.09(3)	26(8)
		419.5(3)	4_1^+	1540.8(4)	0.25(7)*	$0.0058(46)^4$	0.25(7)	74(8)
1965.5(1)	(1,2)$^{\mathrm{f}}$	1151.2(2)	(0_3)	814.5(4)	0.09(3)*	$0.030(3)^4$	0.09(3)	3(10)
		942.2(2)	(3_1^+)	1023.3(2)	0.43(7)*	$0.016(14)^4$	0.44(7)	14(2)
		855.6(1)	2_3^+	1109.9(3)	0.19(4)*	$0.013(6)^4$	0.20(4)	6.4(14)
		499.5(3)	0_2^+	1465.7(2)	0.62(14)*	$0.0070(53)^4$	0.62(14)	20(4)
		419.5(3)	4_1^+	1545.3(4)	0.27(7)*	$0.0058(46)^4$	0.28(7)	9(2)
		154.9(2)	2_1^+	1810.9(3)	1.45(6)	$0.0041(30)^4$	1.46(6)	47(3)
1999.9(4)	(0-5)$^{\mathrm{f}}$	154.9(2)	2_1^+	1845.0(3)	1.57(21)*	$0.0040(28)^4$	1.58(21)	100
2005.8(1)	(2,3)$^{\mathrm{f}}$	1239.5(1)	4_3^+	766.4(4)	0.08(3)*	$0.035(4)^4$	0.08(3)	4(15)
		1033.5(2)	(4_2^+)	972.5(2)	0.14(5)*	$0.019(7)^4$	0.14(5)	7(2)
		942.2(2)	(3_1^+)	1063.8(5)	0.08(3)*	$0.015(4)^4$	0.09(3)	4(16)
		855.6(1)	2_3^+	1150.3(3)	0.16(4)*	$0.012(8)^4$	0.16(4)	7.7(18)
		499.5(3)	0_2^+	1506.2(2)	0.31(5)*	$0.0061(49)^4$	0.32(5)	15(2)
		419.5(3)	4_1^+	1585.3(2)	0.28(8)*	$0.0055(43)^4$	0.28(8)	13(3)
		154.9(2)	2_1^+	1850.9(3)	0.45(7)*	$0.0039(28)^4$	0.46(8)	21(3)
		0	0_1^+	2005.9(3)	0.60(4)	$0.0034(22)^4$	0.61(4)	28(3)
2033.9(7)	(1-5)$^{\mathrm{f}}$	942.2(2)	(3_1^+)	1091.8(7)	0.13(6)*	$0.014(12)^4$	0.14(6)	100
2047.9(2)	(2-4)$^{\mathrm{f}}$	1239.5(1)	4_3^+	808.2(3)	0.09(2)*	$0.031(15)^4$	0.09(2)	15(4)
		1181.4(1)	(2_4)	866.9(3)	0.07(2)*	$0.025(11)^4$	0.07(3)	11(4)
		1033.5(2)	(4_2^+)	1014.2(4)	0.07(3)*	$0.017(11)^4$	0.07(3)	11(4)
		942.2(2)	(3_1^+)	1105.9(3)	0.06(2)*	$0.013(10)^4$	0.06(2)	10(3)
		419.5(3)	4_1^+	1628.3(3)	0.32(5)*	$0.0052(40)^4$	0.32(5)	52(6)
2064.6(1)	(2-4)$^{\mathrm{f}}$	1239.5(1)	4_3^+	825.5(3)	0.15(3)*	$0.029(4)^4$	0.16(3)	4.3(9)
		1181.4(1)	(2_4)	883.3(2)	0.23(6)*	$0.024(6)^4$	0.24(6)	6.4(16)
		942.2(2)	(3_1^+)	1122.6(3)	0.12(4)*	$0.013(3)^4$	0.12(4)	3.3(11)
		855.6(1)	2_3^+	1208.9(2)	0.34(6)*	$0.0100(90)^4$	0.35(6)	9.3(16)
		667.5(2)	2_2^+	1397.4(2)	0.48(9)*	$0.0070(60)^4$	0.48(9)	13(2)
		419.5(3)	4_1^+	1643.9(3)	1.03(15)*	$0.0050(39)^4$	1.04(15)	28(3)
		154.9(2)	2_1^+	1909.6(3)	1.31(10)	$0.0037(25)^4$	1.31(10)	36(3)
2075.8(1)	(2,3)$^{\mathrm{f}}$	1239.5(1)	4_3^+	836.6(3)	0.06(2)*	$0.028(4)^4$	0.06(2)	3.6(12)
		1181.4(1)	(2_4)	894.6(2)	0.21(6)*	$0.023(13)^4$	0.22(6)	13(4)
		1033.5(2)	(4_2^+)	1042.3(3)	0.11(4)*	$0.015(7)^4$	0.11(4)	7(3)
		855.6(1)	2_3^+	1219.7(3)	0.16(4)*	$0.0100(88)^4$	0.16(4)	10(3)
		667.5(2)	2_2^+	1408.3(2)	0.40(7)*	$0.0070(59)^4$	0.40(7)	25(5)

Table C.1: (*Continued*)

E_i (keV)	I_i^π	E_f (keV)	I_f^π	E_γ (keV)	I_γ (%)	α_{tot}	I_{tot}	b (%)
		499.5(3)	0_2^+	1576.0(3)	0.11(3)*	0.0055(44)^4	0.11(3)	6.9(19)
		419.5(3)	4_1^+	1656.9(4)	0.56(22)*	0.0050(38)^4	0.56(22)	35(9)
2087.1(2)	(1-4)^f	942.2(2)	(3_1^+)	1145.0(3)	0.10(3)*	0.012(9)^4	0.11(3)	9(3)
		855.6(1)	2_3^+	1231.6(3)	0.22(4)*	0.0100(85)^4	0.22(4)	19(4)
		154.9(2)	2_1^+	1932.1(3)	0.82(13)*	0.0036(25)^4	0.82(13)	72(5)
2096.2(4)	(2-6)^f	1033.5(2)	(4_2^+)	1062.7(3)	0.08(3)*	0.015(13)^4	0.09(3)	100
2097.4(4)	(0-5)^f	154.9(2)	2_1^+	1942.5(3)	1.06(17)*	0.0036(24)^4	1.06(17)	100
2101.7(4)	(1-7)^f	419.5(3)	4_1^+	1682.2(3)	0.22(4)*	0.0048(36)^4	0.23(4)	100
2124.6(4)	(1-5)^f	419.5(3)	4_1^+	1705.0(3)	0.26(5)*	0.0047(35)^4	0.26(5)	22(7)
		154.9(2)	2_1^+	1969.9(7)	0.93(33)*	0.0035(23)^4	0.93(33)	78(7)
2128.9(2)	(0-4)^f	855.6(1)	2_3^+	1273.2(2)	0.23(4)*	0.0090(78)^4	0.23(4)	32(11)
		154.9(2)	2_1^+	1974.1(4)	0.50(23)*	0.0035(23)^4	0.50(23)	68(11)
2134.1(2)	(2-5)^f	1033.5(2)	(4_2^+)	1100.6(4)	0.06(3)*	0.013(9)^4	0.06(3)	9(4)
		942.2(2)	(3_1^+)	1192.1(3)	0.14(3)*	0.0110(93)^4	0.14(3)	21(6)
		154.9(2)	2_1^+	1978.9(5)	0.47(15)*	0.0035(23)^4	0.47(15)	70(8)
2137.7(2)	(2-4)^f	1033.5(2)	(4_2^+)	1104.0(3)	0.07(3)*	0.013(21)^4	0.07(3)	21(8)
		942.2(2)	(3_1^+)	1195.8(3)	0.08(3)*	0.0110(92)^4	0.08(3)	24(7)
		855.6(1)	2_3^+	1282.2(3)	0.17(4)*	0.0090(76)^4	0.17(4)	55(9)
2142.7(2)	(0-4)^f	855.6(1)	2_3^+	1287.2(2)	0.30(5)*	0.0090(76)^4	0.30(5)	69(7)
		154.9(2)	2_1^+	1987.5(4)	0.13(4)*	0.0034(23)^4	0.13(4)	31(7)
2164.2(7)	(1-5)^f	419.5(3)	4_1^+	1745.4(3)	0.31(8)*	0.0044(33)^4	0.32(8)	60(9)
		154.9(2)	2_1^+	2008.4(5)	0.21(6)*	0.0034(22)^4	0.21(6)	40(9)
2176.8(2)	(0-5)^f	855.6(1)	2_3^+	1321.2(2)	0.35(8)*	0.0080(70)^4	0.35(8)	27(6)
		154.9(2)	2_1^+	2021.8(3)	0.98(17)*	0.0033(22)^4	0.98(17)	73(6)
2197.5(5)	(1-7)^f	419.5(3)	4_1^+	1778.0(4)	0.09(5)*	0.0043(31)^4	0.09(5)	100
2201.5(3)	(1-5)^f	419.5(3)	4_1^+	1782.0(4)	0.31(5)*	0.0043(31)^4	0.31(5)	44(6)
		154.9(2)	2_1^+	2046.7(3)	0.39(7)*	0.0033(21)^4	0.39(7)	56(6)
2211.0(3)	(0-5)^f	667.5(2)	2_2^+	1543.2(5)	0.19(8)*	0.0058(46)^4	0.19(8)	34(11)
		154.9(2)	2_1^+	2056.3(4)	0.36(8)*	0.0032(20)^4	0.36(8)	66(11)
2220.4(4)	(1-3)^f	499.5(3)	0_2^+	1720.5(4)	0.06(2)*	0.0046(34)^4	0.06(2)	9(4)
		154.9(2)	2_1^+	2066.1(6)	0.57(12)*	0.0032(20)^4	0.58(12)	91(4)
2239.5(4)	(0-5)^f	154.9(2)	2_1^+	2084.6(4)	0.78(14)*	0.0032(20)^4	0.78(14)	100
2243.5(5)	(1-7)^f	419.5(3)	4_1^+	1824.0(4)	0.20(4)*	0.0041(29)^4	0.20(4)	100
2279.0(5)	(1-7)^f	419.5(3)	4_1^+	1859.5(4)	0.23(5)*	0.0039(27)^4	0.23(5)	100
2283.8(5)	(1-3)^f	499.5(3)	0_2^+	1784.3(4)	0.11(3)*	0.0042(31)^4	0.11(3)	100
2289.6(2)	(0-5)^f	855.6(1)	2_3^+	1434.2(2)	0.10(3)*	0.0070(56)^4	0.10(3)	21(6)
		154.9(2)	2_1^+	2134.5(3)	0.38(9)*	0.0030(18)^4	0.38(9)	79(6)
2293.2(4)	(1-5)^f	419.5(3)	4_1^+	1873.7(5)	0.18(6)*	0.0038(27)^4	0.18(6)	44(11)

Table C.1: (*Continued*)

E_i (keV)	I_i^π	E_f (keV)	I_f^π	E_γ (keV)	I_γ (%)	α_{tot}	I_{tot}	b (%)
		154.9(2)	2_1^+	2138.3(6)	0.23(7)*	$0.0030(18)^4$	0.23(7)	56(11)
2307.6(3)	$(0\text{-}6)^f$	942.2(2)	(3_1^+)	1365.6(2)	0.18(4)*	$0.0080(64)^4$	0.18(4)	100
2342.5(4)	$(0\text{-}5)^f$	154.9(2)	2_1^+	2187.6(4)	0.47(9)*	$0.0029(17)^4$	0.47(9)	100
2359.7(3)	$(1\text{-}5)^f$	855.6(1)	2_3^+	1504.3(5)	0.15(5)*	$0.0062(49)^4$	0.15(5)	13(4)
		667.5(2)	2_2^+	1692.5(6)	0.37(11)*	$0.0047(36)^4$	0.38(11)	34(8)
		419.5(3)	4_1^+	1939.2(4)	0.17(4)*	$0.0036(24)^4$	0.17(4)	15(4)
		154.9(2)	2_1^+	2205.4(4)	0.42(14)*	$0.0029(17)^4$	0.43(14)	38(9)
2362.7(5)	$(1\text{-}3)^f$	499.5(3)	0_2^+	1863.2(4)	0.26(5)*	$0.0039(27)^4$	0.27(5)	100
2371.5(2)	$(1\text{-}7)^f$	1607.4(1)		764.0(2)	0.13(2)*	$0.036(36)^4$	0.13(2)	36(6)
		419.5(3)	4_1^+	1952.3(3)	0.24(5)*	$0.0036(24)^4$	0.24(5)	64(6)
2373.5(5)	$(0\text{-}5)^f$	154.9(2)	2_1^+	2218.6(4)	0.62(13)*	$0.0029(16)^4$	0.62(14)	100
2385.1(3)	$(1\text{-}5)^f$	419.5(3)	4_1^+	1965.5(3)	0.22(5)*	$0.0035(23)^4$	0.22(5)	49(10)
		154.9(2)	2_1^+	2230.4(5)	0.23(8)*	$0.0028(16)^4$	0.23(8)	51(10)
2399.8(3)	$(0\text{-}4)^f$	1181.4(1)	(2_4)	1218.1(4)	0.13(4)*	$0.0100(88)^4$	0.13(4)	40(10)
		855.6(1)	2_3^+	1544.5(4)	0.20(5)*	$0.0058(46)^4$	0.20(5)	60(10)
2421.3(3)	$(1\text{-}5)^f$	419.5(3)	4_1^+	2001.6(3)	0.27(5)*	$0.0034(22)^4$	0.27(5)	34(7)
		154.9(2)	2_1^+	2266.7(5)	0.54(13)*	$0.0028(15)^4$	0.54(14)	66(7)
2437.3(6)	$(0\text{-}5)^f$	855.6(1)	2_3^+	1581.7(6)	0.15(5)*	$0.0055(43)^4$	0.15(5)	100
2444.3(8)	$(0\text{-}5)^f$	667.5(2)	2_2^+	1776.8(7)	0.46(17)*	$0.0043(31)^4$	0.46(17)	100
2492.2(5)	$(1\text{-}7)^f$	419.5(3)	4_1^+	2072.7(4)	0.32(7)*	$0.0032(20)^4$	0.32(7)	100
2510.7(5)	$(0\text{-}5)^f$	667.5(2)	2_2^+	1843.2(4)	0.44(11)*	$0.0040(28)^4$	0.45(11)	100
2576.5(4)	$(1\text{-}5)^f$	667.5(2)	2_2^+	1909.0(4)	0.22(7)*	$0.0037(25)^4$	0.22(7)	61(11)
		419.5(3)	4_1^+	2157.2(8)	0.14(5)*	$0.0030(18)^4$	0.14(5)	39(11)
2589.5(3)	$(0\text{-}5)^f$	1418.9(1)	(4_4)	1170.2(3)	0.22(6)*	$0.0110(98)^4$	0.23(6)	40(10)
		667.5(2)	2_2^+	1922.8(4)	0.34(10)*	$0.0037(25)^4$	0.34(10)	60(10)
2639.7(5)	$(0\text{-}5)^f$	154.9(2)	2_1^+	2484.8(5)	0.29(8)*	$0.0025(11)^4$	0.29(8)	100
2643.0(5)	$(0\text{-}6)^f$	942.2(2)	(3_1^+)	1700.9(4)	0.08(2)*	$0.0047(35)^4$	0.08(2)	100
2676.5(5)	$(1\text{-}6)^f$	942.2(2)	(3_1^+)	1734.4(6)	0.17(5)*	$0.0045(33)^4$	0.17(5)	48(10)
		419.5(3)	4_1^+	2257.0(6)	0.19(5)*	$0.0028(15)^4$	0.19(5)	52(10)
2690.9(11)	$(1\text{-}7)^f$	419.5(3)	4_1^+	2271.4(10)	0.27(9)*	$0.0028(15)^4$	0.27(9)	100
2712.4(3)	$(1\text{-}6)^f$	942.2(2)	(3_1^+)	1770.5(4)	0.05(2)*	$0.0043(31)^4$	0.05(2)	36(11)
		419.5(3)	4_1^+	2292.5(5)	0.09(3)*	$0.0027(15)^4$	0.09(3)	64(11)
2768.8(5)	$(1\text{-}7)^f$	419.5(3)	4_1^+	2349.3(4)	0.12(4)*	$0.0026(14)^4$	0.12(4)	100
2822.7(5)	$(1\text{-}7)^f$	419.5(3)	4_1^+	2403.2(5)	0.09(3)*	$0.0026(13)^4$	0.09(3)	100
2907.6(4)	$(0\text{-}5)^f$	1181.4(1)	(2_4)	1726.2(4)	0.07(3)*	$0.0045(34)^4$	0.07(3)	37(13)
		154.9(2)	2_1^+	2752.7(6)	0.13(5)*	$0.0022(8)^4$	0.13(5)	63(13)
3001.9(4)	$(1\text{-}7)^f$	419.5(3)	4_1^+	2582.4(3)	0.45(7)*	$0.0024(10)^4$	0.45(7)	100
3165.9(6)	$(1\text{-}7)^f$	419.5(3)	4_1^+	2746.4(5)	0.13(3)*	$0.0022(8)^4$	0.13(3)	100

Table C.1: (*Continued)*

E_i (keV)	I_i^π	E_f (keV)	I_f^π	E_γ (keV)	I_γ (%)	α_{tot}	I_{tot}	b (%)
3177.4(4)	(1-5)^f	667.5(2)	2_2^+	2510.0(5)	0.22(7)*	0.0024(11)^4	0.22(7)	56(10)
		419.5(3)	4_1^+	2757.9(4)	0.18(4)*	0.0022(8)^4	0.18(4)	44(10)
3288.6(4)	(1-5)^f	1239.5(1)	4_3^+	2050.2(7)	0.03(2)*	0.0033(21)^4	0.03(2)	13(7)
		855.6(1)	2_3^+	2432.5(5)	0.11(4)*	0.0025(12)^4	0.11(4)	43(10)
		419.5(3)	4_1^+	2869.0(5)	0.11(3)*	0.0021(7)^4	0.11(3)	44(9)
3299.2(2)	(1-5)^f	1520.9(1)		1777.9(3)	0.21(5)*	0.0043(31)^4	0.21(5)	100
		1239.5(1)	4_3^+	2060.5(8)	0.05(3)*	0.0032(20)^4	0.05(3)	100
		419.5(3)	4_1^+	2879.8(3)	0.13(3)*	0.0021(7)^4	0.13(3)	41(10)
		154.9(2)	2_1^+	3143.8(4)	0.19(5)*	0.0020(5)^4	0.19(5)	59(10)
3334.5(5)	(1-7)^f	1033.5(2)	(4_2^+)	2301.0(5)	0.13(5)*	0.0027(15)^4	0.14(5)	100
3362.2(2)	(1-5)^f	1239.5(1)	4_3^+	2122.9(3)	0.39(7)*	0.0031(19)^4	0.39(7)	41(6)
		1033.5(2)	(4_2^+)	2329.2(9)	0.08(4)*	0.0027(14)^4	0.08(4)	8(4)
		855.6(1)	2_3^+	2506.6(3)	0.21(4)*	0.0024(11)^4	0.21(4)	22(4)
		667.5(2)	2_2^+	2694.5(3)	0.27(5)*	0.0023(9)^4	0.27(5)	28(5)
3382.9(4)	(1-5)^f	419.5(3)	4_1^+	2962.8(4)	0.18(4)*	0.0021(6)^4	0.18(4)	40(8)
		154.9(2)	2_1^+	3228.9(6)	0.26(7)*	0.0020(4)^4	0.26(7)	60(8)
3396.1(2)	(1-5)^f	667.5(2)	2_2^+	2728.8(4)	0.53(15)*	0.0022(8)^4	0.54(15)	29(6)
		419.5(3)	4_1^+	2976.7(3)	0.45(2)	0.0021(6)^4	0.45(2)	25(3)
		154.9(2)	2_1^+	3241.1(3)	0.84(4)	0.0020(4)^4	0.84(4)	46(4)
3407.5(4)	(0-5)^f	667.5(2)	2_2^+	2740.0(4)	0.18(6)*	0.0022(8)^4	0.18(6)	100
3419.2(2)	(1-5)^f	1472.8(1)		1946.2(6)	0.18(5)*	0.0036(24)^4	0.18(5)	9(2)
		1239.5(1)	4_3^+	2179.8(5)	0.09(3)*	0.0029(17)^4	0.09(3)	4(13)
		855.6(1)	2_3^+	2563.5(3)	1.10(5)	0.0024(10)^4	1.10(5)	52(4)
		419.5(3)	4_1^+	2999.9(3)	0.74(12)*	0.0021(6)^4	0.74(12)	35(4)
3420.7(5)	(0-5)^f	1181.4(1)	(2_4)	2239.3(5)	0.33(9)*	0.0028(16)^4	0.34(9)	100
3423.8(3)	(1-5)^f	1033.5(2)	(4_2^+)	2390.3(5)	0.47(16)*	0.0026(13)^4	0.47(16)	37(9)
		419.5(3)	4_1^+	3004.0(4)	0.31(10)*	0.0021(6)^4	0.32(10)	24(7)
		154.9(2)	2_1^+	3269.3(6)	0.50(14)*	0.0020(4)^4	0.50(15)	39(9)
3426.9(2)	(1-6)^f	1541.6(1)		1885.0(4)	0.14(3)*	0.0038(26)^4	0.14(3)	18(4)
		1033.5(2)	(4_2^+)	2393.6(3)	0.32(7)*	0.0026(13)^4	0.32(7)	41(7)
		942.2(2)	(3_1^+)	2485.9(4)	0.26(5)*	0.0025(11)^4	0.26(5)	33(6)
		419.5(3)	4_1^+	3007.3(5)	0.06(4)*	0.0021(6)^4	0.06(4)	8(4)
3436.4(4)	(1-7)^f	1239.5(1)	4_3^+	2196.9(4)	0.13(3)*	0.0029(17)^4	0.13(3)	100
3440.3(4)	(0-6)^f	942.2(2)	(3_1^+)	2498.2(3)	0.66(10)*	0.0024(11)^4	0.67(10)	100
3443.8(2)	(1-5)^f	1520.9(1)		1923.0(5)	0.18(5)*	0.0037(25)^4	0.18(5)	6.7(18)
		1239.5(1)	4_3^+	2203.9(3)	0.37(7)*	0.0029(17)^4	0.37(7)	14(3)
		1033.5(2)	(4_2^+)	2410.2(4)	0.15(5)*	0.0026(13)^4	0.15(5)	6(2)
		667.5(2)	2_2^+	2776.6(4)	0.46(10)*	0.0022(8)^4	0.46(10)	18(4)

Table C.1: (*Continued*)

E_i (keV)	I_i^π	E_f (keV)	I_f^π	E_γ (keV)	I_γ (%)	α_{tot}	I_{tot}	b (%)
		419.5(3)	4_1^+	3024.3(3)	0.95(13)*	$0.0021(6)^4$	0.95(13)	36(4)
		154.9(2)	2_1^+	3289.0(4)	0.51(9)*	$0.0020(4)^4$	0.51(9)	19(3)
3457.4(4)	(0-6)^f	942.2(2)	(3_1^+)	2515.3(4)	0.07(2)*	$0.0024(11)^4$	0.07(2)	100
3458.8(2)	(1-5)^f	1033.5(2)	(4_2^+)	2425.1(4)	0.05(2)*	$0.0025(12)^4$	0.05(2)	8(4)
		855.6(1)	2_3^+	2603.1(4)	0.14(3)*	$0.0023(10)^4$	0.14(3)	25(6)
		419.5(3)	4_1^+	3039.1(4)	0.21(5)*	$0.0021(6)^4$	0.21(5)	37(7)
		154.9(2)	2_1^+	3304.5(6)	0.17(6)*	$0.0020(4)^4$	0.17(6)	30(8)
3468.3(2)	(1-5)^f	1501.8(1)		1966.4(5)	0.11(3)*	$0.0035(23)^4$	0.11(3)	8(2)
		855.6(1)	2_3^+	2614.0(5)	0.18(5)*	$0.0023(10)^4$	0.19(5)	14(3)
		419.5(3)	4_1^+	3048.5(3)	0.52(8)*	$0.0021(5)^4$	0.52(8)	38(5)
		154.9(2)	2_1^+	3313.1(3)	0.55(9)*	$0.0020(4)^4$	0.55(9)	40(5)
3481.2(3)	(1-5)^f	1033.5(2)	(4_2^+)	2447.7(5)	0.06(3)*	$0.0025(12)^4$	0.06(3)	12(6)
		855.6(1)	2_3^+	2624.7(10)	0.12(6)*	$0.0023(10)^4$	0.12(6)	25(10)
		154.9(2)	2_1^+	3326.5(4)	0.30(5)*	$0.0020(4)^4$	0.30(6)	63(10)
3504.1(4)	(0-5)^f	154.9(2)	2_1^+	3349.2(4)	0.39(8)*	$0.0020(4)^4$	0.39(8)	100
3510.2(3)	(0-5)^f	942.2(2)	(3_1^+)	2568.1(4)	0.27(6)*	$0.0024(10)^4$	0.27(6)	25(6)
		154.9(2)	2_1^+	3355.3(4)	0.81(14)*	$0.0020(4)^4$	0.81(14)	75(6)
3513.4(2)	(1-5)^f	1520.9(1)		1992.1(6)	0.13(4)*	$0.0034(22)^4$	0.13(4)	2.6(9)
		1239.5(1)	4_3^+	2273.9(5)	0.13(4)*	$0.0028(15)^4$	0.13(4)	2.6(7)
		1033.5(2)	(4_2^+)	2480.4(5)	0.07(3)*	$0.0025(11)^4$	0.07(3)	1.3(6)
		942.2(2)	(3_1^+)	2571.9(8)	0.24(6)*	$0.0024(10)^4$	0.24(6)	4.7(12)
		667.5(2)	2_2^+	2845.6(3)	1.42(31)*	$0.0022(7)^4$	1.42(31)	28(5)
		419.5(3)	4_1^+	3093.7(3)	2.84(12)	$0.0020(5)^4$	2.85(12)	56(4)
		154.9(2)	2_1^+	3358.5(4)	0.26(7)*	$0.0020(4)^4$	0.26(7)	5.1(13)
3518.3(2)	(1-3)^f	1965.5(1)		1552.5(3)	0.14(11)*	$0.0057(45)^4$	0.15(11)	18(12)
		1520.9(1)		1997.6(13)	0.09(6)*	$0.0034(22)^4$	0.09(6)	12(7)
		1358.3(2)		2160.0(5)	0.10(3)*	$0.0030(18)^4$	0.10(3)	12(4)
		1311.0(1)	2_5^+	2207.6(4)	0.09(3)*	$0.0029(17)^4$	0.09(3)	11(4)
		499.5(3)	0_2^+	3019.0(4)	0.23(4)*	$0.0021(6)^4$	0.23(4)	28(7)
		154.9(2)	2_1^+	3363.5(10)	0.15(12)*	$0.0020(4)^4$	0.15(12)	19(12)
3532.8(6)	(1-7)^f	419.5(3)	4_1^+	3113.3(5)	0.06(2)*	$0.0020(5)^4$	0.06(2)	100
3548.4(2)	(1-3)^f	2097.4(4)		1450.8(3)	0.14(3)*	$0.0070(55)^4$	0.15(3)	12(2)
		1888.7(2)		1659.6(4)	0.16(4)*	$0.0049(38)^4$	0.17(4)	14(3)
		1151.2(2)	(0_3)	2397.3(4)	0.10(3)*	$0.0026(13)^4$	0.10(3)	9(2)
		499.5(3)	0_2^+	3048.8(5)	0.09(3)*	$0.0021(5)^4$	0.09(3)	8(2)
		419.5(3)	4_1^+	3128.6(6)	0.10(3)*	$0.0020(5)^4$	0.10(3)	9(2)
		154.9(2)	2_1^+	3393.6(4)	0.26(7)*	$0.0020(3)^4$	0.26(7)	22(5)
		0	0_1^+	*3548.4(3)*	0.33(2)	$0.0020(3)^4$	0.33(2)	28(3)

Table C.1: (*Continued*)

E_i (keV)	I_i^π	E_f (keV)	I_f^π	E_γ (keV)	I_γ (%)	α_{tot}	I_{tot}	b (%)
3555.3(3)	(1-3)^f	1151.2(2)	(0_3)	2403.6(7)	0.08(3)*	0.0026(13)^4	0.08(3)	10(3)
		499.5(3)	0_2^+	3055.5(3)	0.43(7)*	0.0021(5)^4	0.43(7)	54(7)
		154.9(2)	2_1^+	3401.2(7)	0.09(5)*	0.0020(3)^4	0.09(5)	11(5)
		0	0_1^+	*3555.6(8)*	0.20(7)	0.0020(3)^4	0.20(7)	25(7)
3558.9(3)	(1-3)^f	855.6(1)	2_3^+	2702.4(4)	0.18(4)*	0.0023(9)^4	0.18(4)	33(7)
		154.9(2)	2_1^+	3404.4(4)	0.11(4)*	0.0020(3)^4	0.11(4)	20(7)
		0	0_1^+	*3559.2(3)*	0.26(7)	0.0020(3)^4	0.26(7)	47(8)
3569.0(2)	(1-3)^f	1965.5(1)		1603.3(4)	0.30(22)*	0.0053(42)^4	0.30(23)	8(5)
		1151.2(2)	(0_3)	2418.1(3)	0.26(5)*	0.0025(12)^4	0.26(5)	6.5(13)
		855.6(1)	2_3^+	2713.7(3)	0.65(3)	0.0022(8)^4	0.66(3)	16.7(15)
		667.5(2)	2_2^+	2901.3(3)	0.80(13)*	0.0021(7)^4	0.80(14)	20(3)
		499.5(3)	0_2^+	3069.5(3)	0.51(8)*	0.0021(5)^4	0.52(8)	13(2)
		154.9(2)	2_1^+	3414.3(3)	1.40(6)	0.0020(3)^4	1.40(6)	36(3)
3576.9(1)	(1-3)^f	2087.1(2)		1489.9(7)	0.06(5)*	0.0060(51)^4	0.06(5)	0.6(5)
		2075.8(1)		1501.6(3)	0.10(3)*	0.0062(50)^4	0.10(3)	1(3)
		1999.9(4)		1577.2(3)	0.06(5)*	0.0055(43)^4	0.06(5)	0.6(5)
		1965.5(1)		1610.9(3)	0.63(17)*	0.0053(41)^4	0.64(17)	6.7(17)
		1501.8(1)		2075.2(3)	0.34(6)*	0.0032(20)^4	0.34(6)	3.6(6)
		1358.3(2)		2218.6(4)	0.33(7)*	0.0029(16)^4	0.33(7)	3.5(7)
		1181.4(1)	(2_4)	2395.6(3)	0.62(16)*	0.0026(13)^4	0.62(16)	6.5(16)
		942.2(2)	(3_1^+)	2634.2(10)	0.08(5)*	0.0023(9)^4	0.08(5)	0.9(5)
		855.6(1)	2_3^+	2720.8(3)	0.29(5)*	0.0022(8)^4	0.29(5)	3.1(6)
		667.5(2)	2_2^+	2909.7(4)	1.19(6)	0.0021(7)^4	1.19(6)	12.5(9)
		154.9(2)	2_1^+	3422.0(3)	2.81(12)	0.0020(3)^4	2.81(12)	29.5(17)
		0	0_1^+	3577.0(3)	3.01(13)	0.0020(3)^4	3.02(13)	32(2)
3580.3(4)	(1-6)^f	1888.7(2)		1691.3(5)	0.15(4)*	0.0047(36)^4	0.15(4)	38(9)
		942.2(2)	(3_1^+)	2638.3(6)	0.15(4)*	0.0023(9)^4	0.15(4)	37(9)
		419.5(3)	4_1^+	3160.1(9)	0.10(5)*	0.0020(5)^4	0.10(5)	25(10)
3589.3(3)		1999.9(4)		1589.9(3)	0.14(10)*	0.0054(42)^4	0.14(11)	27(21)
		1965.5(1)		1623.6(4)	0.38(28)*	0.0052(40)^4	0.38(28)	73(21)
3593.7(3)	(1-5)^f	419.5(3)	4_1^+	3173.8(4)	0.08(2)*	0.0020(5)^4	0.08(2)	12(4)
		154.9(2)	2_1^+	3439.0(4)	0.56(10)*	0.0020(3)^4	0.57(10)	88(4)
3598.8(2)	(1-3)^f	499.5(3)	0_2^+	3099.4(4)	0.16(4)*	0.0020(5)^4	0.16(4)	13(3)
		154.9(2)	2_1^+	3443.9(4)	0.46(3)	0.0020(3)^4	0.46(3)	36(2)
		0	0_1^+	3598.8(3)	0.65(3)	0.0020(2)^4	0.66(3)	51(3)
3604.4(5)	(0-6)^f	942.2(2)	(3_1^+)	2662.3(5)	0.11(3)*	0.0023(9)^4	0.11(3)	100
3608.8(2)	(1-3)^f	2097.4(4)		1511.3(5)	0.11(4)*	0.0061(49)^4	0.11(4)	14.4(12)
		2087.1(2)		1521.6(2)	0.22(15)*	0.0060(48)^4	0.22(16)	29(5)

Table C.1: (*Continued*)

E_i (keV)	I_i^π	E_f (keV)	I_f^π	E_γ (keV)	I_γ (%)	α_{tot}	I_{tot}	b (%)
		1945.5(2)		1662.9(4)	0.15(11)*	0.0049(38)^4	0.15(11)	20(4)
		1908.1(3)		1700.7(4)	0.07(2)*	0.0047(35)^4	0.07(2)	8.8(6)
		1541.6(1)		2067.3(6)	0.21(5)*	0.0032(20)^4	0.21(5)	28.3(18)
		1311.0(1)	2_5^+	2298.2(3)	0.40(6)*	0.0027(15)^4	0.40(6)	17(2)
		942.2(2)	(3_1^+)	2667.2(6)	0.14(4)*	0.0023(9)^4	0.14(4)	6.1(14)
		855.6(1)	2_3^+	2753.3(5)	0.20(5)*	0.0022(8)^4	0.20(5)	8.6(17)
		667.5(2)	2_2^+	2941.3(3)	0.91(4)	0.0021(6)^4	0.91(4)	39(3)
		499.5(3)	0_2^+	3109.4(4)	0.22(4)*	0.0020(5)^4	0.22(4)	9.4(15)
		154.9(2)	2_1^+	3454.4(6)	0.26(2)	0.0020(3)^4	0.26(2)	11.2(10)
3620.3(5)	(0-6)^f	942.2(2)	(3_1^+)	2678.2(5)	0.11(3)*	0.0023(9)^4	0.11(3)	100
3623.0(3)	(1-3)^f	855.6(1)	2_3^+	2766.6(6)	0.06(2)*	0.0022(8)^4	0.06(2)	7(3)
		499.5(3)	0_2^+	3123.7(5)	0.18(4)*	0.0020(5)^4	0.18(4)	22(5)
		154.9(2)	2_1^+	3468.6(5)	0.58(12)*	0.0020(3)^4	0.58(12)	70(6)
3625.3(3)	(0-5)^f	1908.1(3)		1717.1(4)	0.03(1)*	0.0046(34)^4	0.03(1)	20(8)
		154.9(2)	2_1^+	3470.7(3)	0.13(4)*	0.0020(3)^4	0.13(4)	80(8)
3633.3(6)	(1-3)^f	499.5(3)	0_2^+	3133.8(5)	0.17(4)*	0.0020(5)^4	0.17(4)	100
3646.4(4)	(0-5)^f	667.5(2)	2_2^+	2978.9(4)	0.36(9)*	0.0021(6)^4	0.36(9)	100
3650.7(5)	(1-7)^f	419.5(3)	4_1^+	3231.2(4)	0.28(6)*	0.0020(4)^4	0.28(6)	100
3656.1(5)	(0-5)^f	667.5(2)	2_2^+	2988.6(4)	0.17(5)*	0.0021(6)^4	0.17(5)	100
3659.9(3)	(1-3)^f	154.9(2)	2_1^+	3504.3(4)	0.28(6)*	0.0020(3)^4	0.28(6)	53(7)
		0	0_1^+	3660.6(4)	0.24(4)	0.0020(2)^4	0.24(4)	47(7)
3664.5(4)	(0-5)^f	942.2(2)	(3_1^+)	2722.5(4)	0.13(3)*	0.0022(8)^4	0.13(3)	63(12)
		855.6(1)	2_3^+	2808.0(9)	0.07(3)*	0.0022(8)^4	0.07(3)	37(12)
3669.0(4)	(0-6)^f	942.2(2)	(3_1^+)	2726.9(4)	0.11(3)*	0.0022(8)^4	0.11(3)	100
3679.8(3)	(1-5)^f	1239.5(1)	4_3^+	2440.5(5)	0.07(2)*	0.0025(12)^4	0.07(2)	10(3)
		942.2(2)	(3_1^+)	2737.4(6)	0.12(4)*	0.0022(9)^4	0.12(4)	17(6)
		667.5(2)	2_2^+	3012.8(7)	0.16(8)*	0.0021(6)^4	0.16(8)	23(9)
		419.5(3)	4_1^+	3260.1(4)	0.37(9)*	0.0020(4)^4	0.37(9)	51(9)
3701.3(6)	(1-7)^f	419.5(3)	4_1^+	3281.8(5)	0.18(8)*	0.0020(4)^4	0.18(8)	100
3703.7(5)	(0-5)^f	1181.4(1)	(2_4)	2522.3(5)	0.14(4)*	0.0024(11)^4	0.14(4)	100
3726.4(4)	(0-5)^f	154.9(2)	2_1^+	3571.5(4)	0.12(3)*	0.0020(3)^4	0.12(3)	100

[a] Reported as a tentative transition in Ref. [Cai74].

[b] Reported as an unplaced transition in Ref. [Cai74].

[c] Known from in-beam spectroscopy study from Ref. [Pop97].

[d] Known from decay spectroscopy study from Ref. [Dav99].

[e] Observed only in the spectrum of conversion electrons.

[f] Value of spin deduced from the analysis of the deexcitation paths.

[1] Conversion coefficient taken from BrIcc [Kib08] considering an $E2$ multipolarity.
[2] Conversion coefficient taken from the NNDC evaluation [Sin10]
[3] Conversion coefficient evaluated in this work.
[4] Conversion coefficient calculated as the average of the ICC for the $E1$ and $M2$ multipolarities.

Table C.2: Values of β-decay feeding intensity I_β into excited levels of ^{182}Pt and corresponding log ft values calculated using Fermi integrals for allowed and the first forbidden non-unique decay (log f_0t) and for the first forbidden unique decay (log f_1t). The values of spin and parity I^π are taken from Refs. [Dav99; Pop97] or from the analysis of de-excitation paths in this work as indicated by an asterisk. Column I_β^{ref} contains β-decay feeding intensity values calculated using the previous level scheme and transition intensities from Ref. [Dav99]. Internal conversion was accounted for in the same way as for our results.

E (keV)	I^π	I_β^{ref} (%)	I_β (%)	log f_0t	log f_1t
154.9(2)	2_1^+	31(2)	10.9(21)	6.09(10)	8.18(10)
419.5(3)	4_1^+	11.4(8)	7.2(10)	6.20(7)	8.26(7)
499.5(3)	0_2^+	5.2(7)	1.58(30)	6.84(10)	8.89(10)
667.5(2)	2_2^+	10(2)	8.9(16)	6.04(9)	8.08(9)
774.8(3)	6_1^+	0.10(35)	0.22(8)	7.61(20)	9.64(20)
855.6(1)	2_3^+	7.1(8)	4.63(52)	6.27(6)	8.29(6)
942.2(2)	(3_1^+)	7.4(9)	4.21(40)	6.29(4)	8.30(4)
1033.5(2)	(4_2^+)	4.9(11)	2.03(20)	6.58(4)	8.58(4)
1151.2(2)	(0_3)	1.3(1)	0.61(10)	7.07(8)	9.06(8)
1181.4(1)	(2_4)	4.9(5)	3.06(26)	6.36(4)	8.35(4)
1239.5(1)	4_3^+	5.3(4)	1.80(15)	6.57(4)	8.56(4)
1305.4(2)	(5_1^+)	1.0(3)	0.37(6)	7.24(8)	9.22(8)
1311.0(1)	2_5^+	2.3(3)	2.88(20)	6.35(3)	8.32(3)
1358.3(2)	(0-4)*		0.25(7)	7.40(14)	9.37(14)
1418.9(1)	(4_4)	1.8(4)	0.97(10)	6.79(5)	8.75(5)
1472.8(1)	(2-4)*	1.5(4)	1.54(11)	6.57(3)	8.53(3)
1501.8(1)	(1-4)*	1.8(4)	1.13(11)	6.70(4)	8.65(4)
1520.9(1)	(2-4)*	0.75(24)	0.74(11)	6.88(7)	8.83(8)
1541.6(1)	(2-4)*	0.79(20)	1.31(14)	6.62(5)	8.57(5)
1568.0(2)	(2,3)*	0.37(14)	1.42(15)	6.58(5)	8.53(5)
1602.0(2)	(3-5)*		0.72(9)	6.86(6)	8.81(6)
1607.4(1)	(2-4)*		0.48(7)	7.04(7)	8.99(7)

Table C.2: (*Continued*)

E (keV)	I^{π}	I_{β}^{ref} (%)	I_{β} (%)	log f_0t	log f_1t
1643.1(1)	(1-4)*		0.57(6)	6.95(4)	8.89(4)
1670.7(3)	5^-		0.06(1)	7.94(13)	9.88(13)
1683.9(3)	(2-6)*	0.61(14)	0.45(6)	7.04(7)	8.98(7)
1716.0(2)	(2-5)*		0.09(2)	7.74(13)	9.67(13)
1721.9(2)	(1,2)*		0.46(6)	7.02(6)	8.95(6)
1722.8(2)	(0-4)*		0.92(12)	6.72(7)	8.66(7)
1723.8(2)	(4-6)*		0.24(4)	7.30(8)	9.24(8)
1741.7(7)	(4-8)*		0.04(2)	8.02(24)	9.96(24)
1753.2(4)	(1,2)*		0.41(6)	7.06(7)	8.99(7)
1762.4(3)	(0-4)*		0.35(6)	7.13(9)	9.06(9)
1778.9(2)	(1-4)*		0.82(14)	6.75(9)	8.68(9)
1784.4(2)	(3-6)*		0.15(4)	7.49(13)	9.41(13)
1797.2(9)	(0-5)*		0.30(14)	7.18(28)	9.11(28)
1824.0(2)	(1-3)*		0.40(5)	7.06(6)	8.98(6)
1863.3(3)	6^+		0.24(3)	7.27(7)	9.19(7)
1864.3(5)	(0-5)*		0.03(1)	8.21(29)	10.13(29)
1882.3(5)	(0-4)*		0.25(8)	7.25(18)	9.16(18)
1883.9(2)	(2-4)*		0.43(6)	7.00(6)	8.91(7)
1888.7(2)	(2-4)*	0.47(14)	0.60(8)	6.85(7)	8.77(7)
1898.7(2)	(2-5)*		0.16(3)	7.43(10)	9.35(10)
1908.1(3)	(2-5)*		0.13(5)	7.50(19)	9.41(19)
1945.5(2)	(0-4)*		0.61(10)	6.83(8)	8.74(8)
1960.5(3)	(2-6)*		0.15(3)	7.44(11)	9.35(11)
1965.5(1)	(1,2)*		0.71(20)	6.76(15)	8.67(15)
1999.9(4)	(0-5)*		0.60(11)	6.82(9)	8.73(9)
2005.8(1)	(2,3)*		0.93(7)	6.63(3)	8.53(4)
2033.9(7)	(1-5)*		0.06(3)	7.82(26)	9.72(26)
2047.9(2)	(2-4)*		0.27(3)	7.15(6)	9.05(6)
2064.6(1)	(2-4)*		1.62(11)	6.37(3)	8.27(3)
2075.8(1)	(2,3)*		0.67(11)	6.75(8)	8.65(8)
2087.1(2)	(1-4)*		0.38(9)	6.99(13)	8.89(13)
2096.2(4)	(2-6)*		0.04(2)	7.99(22)	9.89(22)
2097.4(4)	(0-5)*		0.35(8)	7.02(11)	8.92(11)

Table C.2: (*Continued)*

E (keV)	I^{π}	I_{β}^{ref} (%)	I_{β} (%)	log f_0t	log f_1t
2101.7(4)	(1-7)*		0.10(2)	7.58(9)	9.47(9)
2124.6(4)	(1-5)*		0.52(15)	6.84(15)	8.74(15)
2128.9(2)	(0-4)*		0.32(10)	7.05(17)	8.95(17)
2134.1(2)	(2-5)*		0.30(7)	7.08(12)	8.98(12)
2137.7(2)	(2-4)*		0.14(2)	7.42(9)	9.31(9)
2142.7(2)	(0-4)*		0.19(3)	7.28(8)	9.17(8)
2164.2(7)	(1-5)*		0.23(5)	7.18(10)	9.07(10)
2176.8(2)	(0-5)*		0.58(9)	6.78(7)	8.67(7)
2197.5(5)	(1-7)*		0.04(2)	7.92(34)	9.81(34)
2201.5(3)	(1-5)*		0.30(4)	7.05(7)	8.94(7)
2211.0(3)	(0-5)*		0.24(5)	7.16(11)	9.04(11)
2220.4(4)	(1-3)*		0.28(6)	7.09(10)	8.97(10)
2239.5(4)	(0-5)*		0.34(6)	6.99(9)	8.87(9)
2243.5(5)	(1-7)*		0.09(2)	7.58(12)	9.46(12)
2279.0(5)	(1-7)*		0.10(2)	7.52(12)	9.39(12)
2283.8(5)	(1-3)*		0.05(1)	7.85(15)	9.72(15)
2289.6(2)	(0-5)*		0.21(4)	7.18(10)	9.06(10)
2293.2(4)	(1-5)*		0.18(4)	7.25(12)	9.13(12)
2307.6(3)	(0-6)*		0.08(2)	7.59(10)	9.47(10)
2342.5(4)	(0-5)*		0.21(4)	7.17(10)	9.05(10)
2359.7(3)	(1-5)*		0.49(9)	6.80(9)	8.66(9)
2362.7(5)	(1-3)*		0.12(2)	7.42(10)	9.29(10)
2371.5(2)	(1-7)*		0.17(2)	7.26(7)	9.13(7)
2373.5(5)	(0-5)*		0.27(6)	7.05(11)	8.92(11)
2385.1(3)	(1-5)*		0.20(4)	7.19(11)	9.05(11)
2399.8(3)	(0-4)*		0.15(3)	7.31(10)	9.18(10)
2421.3(3)	(1-5)*		0.35(6)	6.92(9)	8.78(9)
2437.3(6)	(0-5)*		0.06(2)	7.65(20)	9.51(20)
2444.3(8)	(0-5)*		0.20(8)	7.15(21)	9.01(21)
2492.2(5)	(1-7)*		0.14(3)	7.29(11)	9.14(11)
2510.7(5)	(0-5)*		0.19(5)	7.15(13)	9.00(13)
2576.5(4)	(1-5)*		0.16(4)	7.22(12)	9.06(12)
2589.5(3)	(1-5)*		0.25(5)	7.02(11)	8.86(11)

Table C.2: (*Continued*)

E (keV)	I^{π}	I_{β}^{ref} (%)	I_{β} (%)	log $f_0 t$	log $f_1 t$
2639.7(5)	(0-5)*		0.13(4)	7.30(15)	9.14(15)
2643.0(5)	(0-6)*		0.03(1)	7.88(18)	9.71(18)
2676.5(5)	(1-6)*		0.16(3)	7.19(10)	9.02(10)
2690.9(11)	(1-7)*		0.12(4)	7.30(18)	9.13(18)
2712.4(3)	(1-6)*		0.06(1)	7.58(13)	9.41(13)
2768.8(5)	(1-7)*		0.05(2)	7.64(18)	9.46(18)
2822.7(5)	(1-7)*		0.04(1)	7.72(17)	9.54(17)
2907.6(4)	(0-5)*		0.09(2)	7.36(15)	9.17(15)
3001.9(4)	(1-7)*		0.20(3)	6.98(9)	8.78(9)
3165.9(6)	(1-7)*		0.06(2)	7.48(14)	9.26(14)
3177.4(4)	(1-5)*		0.17(4)	6.97(11)	8.75(11)
3288.6(4)	(1-5)*		0.11(2)	7.13(10)	8.89(10)
3299.2(2)	(1-5)*		0.25(4)	6.77(7)	8.53(7)
3334.5(5)	(1-7)*		0.06(2)	7.39(21)	9.15(21)
3362.2(2)	(1-5)*		0.42(5)	6.53(6)	8.28(6)
3382.9(4)	(1-5)*		0.19(4)	6.86(9)	8.61(9)
3396.1(2)	(1-5)*		0.80(7)	6.24(4)	7.99(4)
3407.5(4)	(0-5)*		0.08(3)	7.23(19)	8.98(19)
3419.2(2)	(1-5)*		0.92(7)	6.17(3)	7.91(4)
3420.7(5)	(0-5)*		0.15(4)	6.97(14)	8.71(14)
3423.8(3)	(1-5)*		0.56(10)	6.38(9)	8.13(9)
3426.9(2)	(1-6)*		0.34(4)	6.60(7)	8.34(7)
3436.4(4)	(1-7)*		0.06(1)	7.37(13)	9.11(13)
3440.3(4)	(0-6)*		0.29(5)	6.66(8)	8.40(8)
3443.8(2)	(1-5)*		1.14(10)	6.07(4)	7.81(4)
3457.4(4)	(0-6)*		0.03(1)	7.66(17)	9.40(17)
3458.8(2)	(1-5)*		0.25(4)	6.73(8)	8.47(8)
3468.3(2)	(1-5)*		0.60(6)	6.34(5)	8.08(5)
3481.2(3)	(1-5)*		0.21(4)	6.80(9)	8.53(9)
3504.1(4)	(0-5)*		0.17(4)	6.87(11)	8.61(11)
3510.2(3)	(0-5)*		0.47(7)	6.43(8)	8.16(8)
3513.4(2)	(1-5)*		2.23(17)	5.75(3)	7.48(4)
3518.3(2)	(1-3)*		0.35(8)	6.56(12)	8.29(12)

Table C.2: (*Continued*)

E (keV)	I^{π}	I_{β}^{ref} (%)	I_{β} (%)	log f_0t	log f_1t
3532.8(6)	(1-7)*		0.02(1)	7.71(21)	9.44(21)
3548.4(2)	(1-3)*		0.52(5)	6.37(4)	8.10(4)
3555.3(3)	(1-3)*		0.35(5)	6.55(7)	8.27(7)
3558.9(3)	(1-3)*		0.25(4)	6.70(8)	8.42(8)
3569.0(2)	(1-3)*		1.72(14)	5.85(4)	7.57(4)
3576.9(1)	(1-3)*		4.18(20)	5.46(2)	7.18(2)
3580.3(4)	(1-6)*		0.18(3)	6.84(10)	8.56(10)
3589.3(3)			0.23(13)	6.70(40)	8.40(40)
3593.7(3)	(1-5)*		0.28(5)	6.62(8)	8.34(8)
3598.8(2)	(1-3)*		0.56(3)	6.33(3)	8.05(3)
3604.4(5)	(0-6)*		0.05(2)	7.37(16)	9.09(16)
3608.8(2)	(1-3)*		1.26(13)	5.97(5)	7.69(5)
3620.3(5)	(0-6)*		0.05(1)	7.39(17)	9.11(17)
3623.0(3)	(1-3)*		0.36(6)	6.50(8)	8.22(8)
3625.3(3)	(0-5)*		0.07(2)	7.22(15)	8.94(15)
3633.3(6)	(1-3)*		0.08(2)	7.18(13)	8.89(13)
3646.4(4)	(0-5)*		0.16(4)	6.86(13)	8.57(13)
3650.7(5)	(1-7)*		0.12(3)	6.96(10)	8.68(10)
3656.1(5)	(0-5)*		0.07(2)	7.18(18)	8.89(18)
3659.9(3)	(1-3)*		0.23(3)	6.70(7)	8.41(7)
3664.5(4)	(0-5)*		0.09(2)	7.10(12)	8.81(12)
3669.0(4)	(0-6)*		0.05(1)	7.38(14)	9.09(14)
3679.8(3)	(1-5)*		0.31(6)	6.55(9)	8.25(9)
3701.3(6)	(1-7)*		0.08(4)	7.13(26)	8.84(26)
3703.7(5)	(0-5)*		0.06(2)	7.26(16)	8.96(16)
3726.4(4)	(0-5)*		0.05(2)	7.31(16)	9.01(16)

Bibliography

[Abu14] K. Abusaleem. In: *Nucl. Data Sheets* 116 (2014), p. 163.
DOI: 10.1016/j.nds.2014.01.002.

[Ago03] S. Agostinelli et al. In: *Nucl. Instrum. Methods A* 506. (2003), p. 250.
DOI: 10.1016/S0168-9002(03)01368-8.

[Ach09] E. Achterberg, O. Capurro, and G. Marti. In: *Nucl. Data Sheets* 110. (2009), p. 1473.
DOI: 10.1016/j.nds.2009.05.002.

[Alg18] A. Algora, B. Rubio, and J. L. T. and. In: *Nuclear Physics News* 28. (2018), p. 12.
DOI: 10.1080/10619127.2018.1427933.

[Alg21] A. Algora, J. Tain, and B. Rubio. In: *Eur. Phys. J. A* 57 (2021), p. 85.
DOI: 10.1140/epja/s10050-020-00316-4.

[Amo11] S. Amos, J. Gross, and M. Thoennessen. In: *At. Data Nucl. Data Tables* 97. (2011), p. 383.
DOI: 10.1016/j.adt.2011.03.001.

[And00] A. N. Andreyev et al. In: *Nature* 405. (2000), p. 430.
DOI: 10.1038/35013012.

[And10] A. N. Andreyev et al. In: *Phys. Rev. Lett.* 105 (2010), p. 252502.
DOI: 10.1103/PhysRevLett.105.252502.

[And13] A. N. Andreyev, M. Huyse, and P. Van Duppen. In: *Rev. Mod. Phys.* 85 (2013), p. 1541.
DOI: 10.1103/RevModPhys.85.1541.

[And18] A. N. Andreyev, K. Nishio, and K.-H. Schmidt. In: *Rep. Prog. Phys.* 81. (2018), p. 016301.
DOI: 10.1088/1361-6633/aa82eb.

[And20a] B. Andel et al. Laser assisted studies of β-delayed fission in ^{178,176}Au and of the structure of ^{175}Au. 2020.
URL: https://cds.cern.ch/record/2717952/files/INTC-P-558.pdf.

[And20b] B. Andel et al. In: *Phys. Rev. C* 102 (2020), p. 014319.
DOI: 10.1103/PhysRevC.102.014319.

[And24] B. Andel et al. In: *Phys. Rev. C* 109 (2024), p. 064321.
DOI: 10.1103/PhysRevC.109.064321.

[Bag09] C. M. Baglin. In: *Nucl. Data Sheets* 110 (2009), p. 265.
DOI: 10.1016/j.nds.2009.01.001.

[Bag10] C. M. Baglin. In: *Nucl. Data Sheets* 111. (2010), p. 275.
DOI: 10.1016/j.nds.2010.01.001.

[Bag12] C. M. Baglin. In: *Nucl. Data Sheets* 113. (2012), p. 1871.
DOI: 10.1016/j.nds.2012.08.001.

[Bal22] M. Balogh et al. In: *Phys. Rev. C* 106 (2022), p. 064324.
DOI: 10.1103/PhysRevC.106.064324.

[Bas06] M. S. Basunia. In: *Nucl. Data Sheets* 107. (2006), p. 2323.
DOI: 10.1016/j.nds.2006.07.001.

[Ben87] R. Bengtsson et al. In: *Phys. Lett. B* 183. (1987), p. 1.
DOI: 10.1016/0370-2693(87)91406-7.

[Ber20] T. A. Berry et al. In: *Phys. Rev. C* 101 (2020), p. 054311.
DOI: 10.1103/PhysRevC.101.054311.

[Bin95] C. R. Bingham et al. In: *Phys. Rev. C* 51 (1995), p. 125.
DOI: 10.1103/PhysRevC.51.125.

[Bor17a] M. J. G. Borge and B. Jonson. In: *J. Phys. G* 44. (2017), p. 044011.
DOI: 10.1088/1361-6471/aa5f03.

[Bor17b] M. J. G. Borge and K. Blaum. In: *J. Phys. G* 45 (2017), p. 010301.
DOI: 10.1088/1361-6471/aa990f.

[Bro07] E. Browne and J. Tuli. In: *Nucl. Data Sheets* 111 (2007), p. 2173.
DOI: 10.1016/j.nds.2007.09.002.

[Bro13] E. Browne and J. Tuli. In: *Nucl. Data Sheets* 114. (2013), p. 1849.
DOI: 10.1016/j.nds.2013.11.002.

[Bru97] R. Brun and F. Rademakers. In: *Nucl. Instrum. Methods A* 389. (1997), p. 81.
DOI: 10.1016/S0168-9002(97)00048-X.

[Cai74] M. Cailliau et al. In: *J. Physique Lett.* 35. (1974), p. 233.
DOI: 10.1051/jphyslet:019740035012023300.

[Cam16] P. Campbell, I. Moore, and M. Pearson. In: *Prog. Part. Nucl. Phys.* 86 (2016), p. 127.
DOI: 10.1016/j.ppnp.2015.09.003.

[Car90] M. Carpenter et al. In: *Nucl. Phys. A* 513. (1990), p. 125.
DOI: 10.1016/0375-9474(90)90346-N.

[Cas90] R. F. Casten. “Nuclear structure from a simple perspective”. New York: Oxford University Press, 1990. ISBN: 0-19-504599-8.

[Cat17] R. Catherall et al. In: *J. Phys. G* 44. (2017), p. 094002.
DOI: 10.1088/1361-6471/aa7eba.

[Clé05] E. Clément et al. In: *AIP Conference Proceedings* 764. (2005), p. 55.
DOI: 10.1063/1.1905291.

[CRI] Collinear Resonance Ionization Spectroscopy experiment website.
URL: https://isolde-cris.web.cern.ch.

[Cub18] J. G. Cubiss et al. In: *Phys. Lett. B* 786 (2018), p. 355.
DOI: 10.1016/j.physletb.2018.10.005.

[Cub20] J. G. Cubiss et al. In: *Phys. Rev. C* 102 (2020), p. 044332.
DOI: 10.1103/PhysRevC.102.044332.

[Cub22] J. G. Cubiss. In: *ISOLDE Newsletter*. 2022, p. 34.
URL: https://isolde.cern/isolde-newsletter-2022-0.

[Cub23a] J. G. Cubiss. In: *ISOLDE Newsletter*. 2023, p. 66.
URL: https://isolde.web.cern.ch/isolde-newsletter-2023.

[Cub23b] J. G. Cubiss et al. In: *Phys. Rev. Lett.* 131 (2023), p. 202501.
DOI: 10.1103/PhysRevLett.131.202501.

[Cub24] J. G. Cubiss. *Private communication*. 2024.

[Dav99] P. M. Davidson et al. In: *Nucl. Phys. A* 657. (1999), p. 219.
DOI: 10.1016/S0375-9474(99)00340-1.

[De 90] M. De Voigt et al. In: *Nucl. Phys. A* 507. (1990), p. 472.
DOI: 10.1016/0375-9474(90)90304-5.

[Dow20] J. Dowie et al. In: *At. Data Nucl. Data Tables* 131 (2020), p. 101283.
DOI: 10.1016/j.adt.2019.06.002.

[Eis70] J. M. Eisenberg and W. Greiner. "Nuclear Theory, Vol. 1: Nuclear Models-Collective and Single Particle Phenomena". North-Holland Pub. Co., 1970.
ISBN: 0-7204-0158-5.

[Els11] J. Elseviers et al. In: *Phys. Rev. C* 84 (2011), p. 034307.
DOI: 10.1103/PhysRevC.84.034307.

[Els13] J. Elseviers et al. In: *Phys. Rev. C* 88 (2013), p. 044321.
DOI: 10.1103/PhysRevC.88.044321.

[Fed03] V. Fedosseev et al. In: *Nucl. Instrum. Methods Phys. Res. Sect. B Beam Interact. Mater. Atoms* 204 (2003). 14th International Conference on Electromagnetic Isotope Separators and Techniques Related to their Applications, p. 353.
DOI: 10.1016/S0168-583X(02)01959-6.

[Fed17] V. Fedosseev et al. In: *J. Phys. G* 44. (2017), p. 084006.
DOI: 10.1088/1361-6471/aa78e0.

[Fin72] M. Finger et al. In: *Nucl. Phys. A* 188. (1972), p. 369.
DOI: 10.1016/0375-9474(72)90064-4.

[Fir96] R. B. Firestone et al. "Table of Isotopes, eight edition". CD-ROM Edition. New York: John Wiley & Sons, 1996.

[Fra17] L. M. Fraile. In: *J. Phys. G* 44. (2017), p. 094004.
DOI: 10.1088/1361-6471/aa8217.

[Fyn17] H. Fynbo, O. S. Kirseboom, and O. Tengblad. In: *J. Phys. G* 44. (2017), p. 094005.
DOI: 10.1088/1361-6471/aa5e09.

[Gam28] G. Gamow. In: *Z. Phys.* 51. (1928), p. 204.
DOI: 10.1007/BF01343196.

[Gar22] P. E. Garrett, M. Zielińska, and E. Clément. In: *Prog. Part. Nucl. Phys.* 124 (2022), p. 103931.
DOI: 10.1016/j.ppnp.2021.103931.

[Gar23] S. Garg et al. In: *At. Data Nucl. Data Tables* 150 (2023), p. 101546.
DOI: 10.1016/j.adt.2022.101546.

[Gei11] H. Geiger and J. Nuttall. In: *The London, Edinburgh, and Dublin Philosophical Magazine and Journal of Science* 22. (1911), p. 613.
DOI: 10.1080/14786441008637156.

[Ger20] M. S. M. Gerathy. "Investigating nuclear structure through γ-ray and electron spectroscopy with Solenogam". PhD thesis. The Australian National University, 2020.
URL: https://openresearch-repository.anu.edu.au/server/api/core/bitstreams/c73d00c9-7c67-438a-83d1-d2a8920034f5/content.

[Gla12] K. Gladnishki et al. In: *Nucl. Phys. A* 877 (2012), p. 19.
DOI: 10.1016/j.nuclphysa.2012.01.001.

[Got16] A. Gottberg. In: *Nucl. Instrum. Methods Phys. Res. Sect. B Beam Interact. Mater. Atoms* 376 (2016), p. 8.
DOI: 10.1016/j.nimb.2016.01.020.

[Gra63] S. Graeffe. In: *Ann. Acad. Sci. Fennicae, Ser. A* VI. (1963), p. 1.

[Gur28] R. W. Gurney and E. U. Condon. In: *Nature* 122. (1928), p. 439.
DOI: 10.1038/122439a0.

[Hag79] E. Hagberg et al. In: *Nucl. Phys. A* 318. (1979), p. 29.
DOI: 10.1016/0375-9474(79)90467-6.

[Hal92] H. L. Hall and D. C. Hoffman. In: *Annu. Rev. Nucl. Part. Sci.* 42. (1992), p. 147.
DOI: 10.1146/annurev.ns.42.120192.001051.

[Hama] Hamamatsu Photonics. Si PIN photodiode S3204-09.
URL: https://www.hamamatsu.com/eu/en/product/optical-sensors/photodiodes/si-photodiodes/S3204-09.html.

[Hamb] Hamamatsu Photonics. Si PIN photodiode S3590-09.
URL: https://www.hamamatsu.com/eu/en/product/optical-sensors/photodiodes/si-photodiodes/S3590-09.html.

[Han70] P. Hansen et al. In: *Nucl. Phys. A* 148. (1970), p. 249.
DOI: 10.1016/0375-9474(70)90622-6.

[Har20] R. D. Harding et al. In: *Phys. Rev. C* 102 (2020), p. 024312.
DOI: 10.1103/PhysRevC.102.024312.

[Har21] R. D. Harding et al. In: *Phys. Rev. C* 104 (2021), p. 024326.
DOI: 10.1103/PhysRevC.104.024326.

[Har77] J. Hardy et al. In: *Phys. Lett. B* 71. (1977), p. 307.
DOI: 10.1016/0370-2693(77)90223-4.

[Hax49] O. Haxel, J. H. D. Jensen, and H. E. Suess. In: *Phys. Rev.* 75 (1949), p. 1766.
DOI: 10.1103/PhysRev.75.1766.2.

[Heb90] G. Hebbinghaus et al. In: *Nucl. Phys. A* 514. (1990), p. 225.
DOI: https://doi.org/10.1016/0375-9474(90)90068-W.

[Hey00] K. Heyde et al. In: *Hyperfine Interact.* 127 (2000), p. 65.
DOI: 10.1023/A:1012698224101.

[Hey11] K. Heyde and J. L. Wood. In: *Rev. Mod. Phys.* 83 (2011), p. 1467.
DOI: 10.1103/RevModPhys.83.1467.

[Hod97] P. E. Hodgson, E. Gadioli, and E. G. Erba. "Introductory nuclear physics". New York: Oxford University Press Inc., 1997. ISBN: 0-19-851897-8.

[Hor75] P. Hornshøj et al. In: *Nucl. Phys. A* 239. (1975), p. 15.
DOI: 10.1016/0375-9474(75)91130-6.

[Hul14] M. Hult et al. In: *Appl. Radiat. Isot.* 87 (2014), p. 112.
DOI: 10.1016/j.apradiso.2013.11.071.

[Hus76] J. P. Husson et al. In: *Proc.Int.Conf.Nuclei Far from Stability, Cargese, Corsica* A85 (1976), p. 460.
DOI: 10.5170/CERN-1976-013.460.

[Che21] J. Chen and B. Singh. In: *Nucl. Data Sheets* 177 (2021), p. 1.
DOI: 10.1016/j.nds.2021.09.001.

[Chu58] E. L. Church, M. E. Rose, and J. Weneser. In: *Phys. Rev.* 109 (1958), p. 1299.
DOI: 10.1103/PhysRev.109.1299.

[Ibr01] F. Ibrahim et al. In: *Eur. Phys. J. A* 10 (2001), p. 139.
DOI: 10.1007/s100500170125.

[IDS] ISOLDE Decay Station web site.
URL: https://isolde-ids.web.cern.ch/.

[IDSa] A photo of ISOLDE Decay Station.
URL: https://cernbox.cern.ch/index.php/s/i69D4VL3ae4uD7U.

[Isa11] P. V. Isacker. In: *J. Phys. Conf. Series* 322. (2011), p. 012003.
DOI: 10.1088/1742-6596/322/1/012003.

[ISO] The ISOLDE facility web site.
URL: https://isolde.web.cern.ch/.

[Jai21] A. K. Jain, B. Maheshwari, and A. Goel. "Nuclear Isomers: A Primer". Springer Nature, 2021. ISBN: 978-3-030-78675-5.
DOI: 10.1007/978-3-030-78675-5.

[Jia24] C. F. Jiao, R. Y. Dong, and Z. Liu. *Private communication.* 2024.

[Jul01] R. Julin, K. Helariutta, and M. Muikku. In: *J. Phys. G* 27. (2001), p. R109.
DOI: 10.1088/0954-3899/27/7/201.

[Kib08] T. Kibédi et al. In: *Nucl. Instrum. Methods, A* 589. (2008), p. 202.
DOI: 10.1016/j.nima.2008.02.051.

[Kib22] T. Kibédi, A. Garnsworthy, and J. Wood. In: *Prog. Part. Nucl. Phys.* 123 (2022), p. 103930.
DOI: 10.1016/j.ppnp.2021.103930.

[Kon00] F. G. Kondev et al. In: *Phys. Rev. C* 61 (Mar. 2000), p. 044323.
DOI: 10.1103/PhysRevC.61.044323.

[Kon15] F. Kondev, G. Dracoulis, and T. Kibédi. In: *At. Data Nucl. Data Tables* 103-104 (2015), p. 50.
DOI: 10.1016/j.adt.2015.01.001.

[Kon18] F. Kondev, S. Juutinen, and D. Hartley. In: *Nucl. Data Sheets* 150 (2018), p. 1.
DOI: 10.1016/j.nds.2018.05.001.

[Kon19] F. Kondev. In: *Nucl. Data Sheets* 159 (2019), p. 1.
DOI: 10.1016/j.nds.2019.100514.

[Kon21] F. Kondev et al. In: *Chin. Phys. C* 45. (2021), p. 030001.
DOI: 10.1088/1674-1137/abddae.

[Kra88] K. S. Krane. "Introductory nuclear physics". Hoboken: John Wiley & Sons, 1988. ISBN: 0-471-80553-X.

[Kre12] S. Kreim, A. Barzakh, and ISOLTRAP Collaboration. *Private communication*. 2012.

[Krö88] U. Krönert et al. In: *Z. Phys. A* 331. (1988), p. 521.
DOI: 10.1007/BF01291911.

[Kug00] E. Kugler. In: *Hyperfine Interact.* 129. (2000), p. 23.
DOI: 10.1023/A:1012603025802.

[Lan82] J. Lange, K. Kumar, and J. H. Hamilton. In: *Rev. Mod. Phys.* 54 (1982), p. 119.
DOI: 10.1103/RevModPhys.54.119.

[Le 97] F. Le Blanc et al. In: *Phys. Rev. Lett.* 79 (1997), p. 2213.
DOI: 10.1103/PhysRevLett.79.2213.

[Leh17] B. Lehnert et al. In: *Phys. Rev. C* 95 (2017), p. 044306.
DOI: 10.1103/PhysRevC.95.044306.

[Lib13] V. Liberati et al. In: *Phys. Rev. C* 88 (2013), p. 044322.
DOI: 10.1103/PhysRevC.88.044322.

[Lic] R. Lică et al. XIA DGF Pixie-16 .ldf data file converter into ROOT and GASPware format for IDS.
URL: https://github.com/rlica/xia4ids.

[Lil01] J. S. Lilley. "Nuclear Physics: Principles and Applications". Chichester: John Wiley & Sons, 2001. ISBN: 0-471-97936-8.

[Lin04] M. Lindroos. In: *Proceedings of EPAC*. 2004, p. 45.
URL: https://accelconf.web.cern.ch/e04/papers/tuxch01.pdf.

[LOG] LOGFT. NNDC log ft calculator. Accessed: 7/11/2022.
URL: https://www.nndc.bnl.gov/logft/.

[Lov06] W. D. Loveland, D. J. Morrissey, and G. T. Seaborg. "Modern Nuclear Chemistry". Hoboken: John Wiley & Sons, 2006. ISBN: 0-471-11532-0.

[Mar06] B. A. Marsh et al. In: *Hyperfine Interact.* 171. (2006), p. 109.
DOI: 10.1007/s10751-006-9498-8.

[Mar07] M. J. Martin. In: *Nucl. Data Sheets* 108. (2007), p. 1583.
DOI: 10.1016/j.nds.2007.07.001.

[Mar13] M. J. Martin. In: *Nucl. Data Sheets* 114. (2013), p. 1497.
DOI: 10.1016/j.nds.2013.11.001.

[May48] M. G. Mayer. In: *Phys. Rev.* 74 (1948), p. 235.
DOI: 10.1103/PhysRev.74.235.

[May49] M. G. Mayer. In: *Phys. Rev.* 75 (1949), p. 1969.
DOI: 10.1103/PhysRev.75.1969.

[May79] T. Mayer-Kuckuk. "Fyzika atomového jádra". Praha: SNTL - Nakladatelství technické literatury, 1979.

[Mei93] F. Meissner et al. In: *Phys. Rev. C* 48 (1993), p. 2089.
DOI: 10.1103/PhysRevC.48.2089.

[Mir] Mirion Technologies. Clover™ Detectors Four Coaxial Germanium Detectors.
URL: https://www.mirion.com/products/technologies/spectroscopy-scientific-analysis/research-education-and-industrial-solutions/special-hpge-sili-detectors/clover-detectors-four-coaxial-germanium-detectors.

[Miš24] J. Mišt. In: *Acta Phys. Pol. B Proc. Sup.* 17 (2024), p. A8.
DOI: 10.5506/APhysPolBSupp.17.3-A8.

[Miš25] J. Mišt et al. In: *Submitted to Phys. Rev. C* (2025).

[Möl09] P. Möller et al. In: *Phys. Rev. Lett.* 103 (2009), p. 212501.
DOI: 10.1103/PhysRevLett.103.212501.

[Mue99] W. F. Mueller et al. In: *Phys. Rev. C* 59 (1999), p. 2009.
DOI: 10.1103/PhysRevC.59.2009.

[Nil55] S. G. Nilsson. In: *Dan. Mat. Fys. Medd.* 29 (1955), p. 1.
URL: https://cds.cern.ch/record/212345/files/p1.pdf.

[Oja22] J. Ojala et al. In: *Communications Physics* 5 (2022), p. 213.
DOI: 10.1038/s42005-022-00990-4.

[Pet16] W. A. Peters et al. In: *Nucl. Instrum. Methods, A* 836 (2016), p. 122.
DOI: 10.1016/j.nima.2016.08.054.

[Pix] Pixie-16 data acquisition system. XIA.
URL: https://xia.com/support/pixie-16/.

[Pop97] D. G. Popescu et al. In: *Phys. Rev. C* 55 (1997), p. 1175.
DOI: 10.1103/PhysRevC.55.1175.

[Ram73] S. Raman and N. B. Gove. In: *Phys. Rev. C* 7 (1973), p. 1995.
DOI: 10.1103/PhysRevC.7.1995.

[Rap17] E. Rapisarda et al. In: *J. Phys. G* 44. (2017), p. 074001.
DOI: 10.1088/1361-6471/aa6bb6.

[Ras59] J. O. Rasmussen. In: *Phys. Rev.* 113 (1959), p. 1593.
DOI: 10.1103/PhysRev.113.1593.

[Rin80] P. Ring and P. Schuck. "The Nuclear Many-Body Problem". Berlin, Heidelberg: Springer, 1980. ISBN: 0-387-09820-8.

[Rom92] I. Romanski et al. In: *Hyperfine Interact.* 75 (1992), p. 457.
DOI: 10.1007/BF02399003.

[Rot13] S. Rothe et al. In: *Nat. Commun.* 4 (2013).
DOI: 10.1038/ncomms2819.

[Rub09] B. Rubio and W. Gelletly. In: *The Euroschool Lectures on Physics with Exotic Beams, Vol. III.* Ed. by J. Al-Khalili and E. Roeckl. Berlin, Heidelberg: Springer Berlin Heidelberg, 2009, p. 99. ISBN: 978-3-540-85839-3.
DOI: 10.1007/978-3-540-85839-3_4.

[Rut11] E. Rutherford. In: *The London, Edinburgh, and Dublin Philosophical Magazine and Journal of Science* 21. (1911), p. 669.
DOI: 10.1080/14786440508637080.

[Sau05] J. Sauvage et al. In: *Eur. Phys. J. A* 25 (2005), p. 5.
DOI: 10.1140/epja/i2004-10236-0.

[Sed20] M. Sedlák et al. In: *Eur. Phys. J. A* 56 (2020), p. 161.
DOI: 10.1140/epja/s10050-020-00174-0.

[Sii66] A. Siivola. In: *Nucl. Phys.* 84 (1966), p. 385.
DOI: 10.1016/0029-5582(66)90377-4.

[Sin10] B. Singh and J. C. Roediger. In: *Nucl. Data Sheets* 111. (2010), p. 2081.
DOI: 10.1016/j.nds.2010.08.001.

[Sin15] B. Singh. In: *Nucl. Data Sheets* 130 (2015), p. 21.
DOI: 10.1016/j.nds.2015.11.002.

[Sin20] B. Singh and J. Chen. In: *Nucl. Data Sheets* 169 (2020), p. 1.
DOI: 10.1016/j.nds.2020.10.001.

[Sin98] B. Singh et al. In: *Nucl. Data Sheets* 84. (1998), p. 487. DOI: 10.1006/ndsh.1998.0015.

[Str18] M. Stryjczyk et al. In: *Phys. Rev. C* 98 (2018), p. 064326. DOI: 10.1103/PhysRevC.98.064326.

[Str20] M. Stryjczyk et al. In: *Phys. Rev. C* 102 (2020), p. 024322. DOI: 10.1103/PhysRevC.102.024322.

[Str21] M. Stryjczyk. *Private communication.* 2021.

[Str23] M. Stryjczyk et al. In: *Phys. Rev. C* 108 (2023), p. 014308. DOI: 10.1103/PhysRevC.108.014308.

[Suh07] J. Suhonen. "From Nucleons to Nucleus". Berlin: Springer-Verlag Berlin Heidelberg, 2007. ISBN: 978-3-540-48861-3. DOI: 10.1007/978-3-540-48861-3.

[Tip08] P. A. Tipler and R. A. Llewellyn. "Modern Physics". New York: W.H. Freeman and Company, 2008. ISBN: 978-0-7167-7550-8.

[Tur23] S. Turkat et al. In: *At. Data. Nucl. Data Tables* 152 (2023), p. 101584. DOI: 10.1016/j.adt.2023.101584.

[Van06] P. Van Duppen. In: *The Euroschool Lectures on Physics with Exotic Beams, Vol. II.* Ed. by J. Al-Khalili and E. Roeckl. Berlin, Heidelberg: Springer Berlin Heidelberg, 2006, p. 37. ISBN: 978-3-540-33787-4. DOI: 10.1007/3-540-33787-3_2.

[Van18] P. Van Duppen and A. N. Andreyev. In: *The Euroschool on Exotic Beams - Vol. 5.* Ed. by C. Scheidenberger and M. Pfützner. Cham: Springer International Publishing, 2018, p. 65. ISBN: 978-3-319-74878-8. DOI: 10.1007/978-3-319-74878-8_3.

[Ven17] M. Venhart et al. In: *J. Phys. G* 44. (2017), p. 074003. DOI: 10.1088/1361-6471/aa7297.

[Ven20] M. Venhart et al. In: *Phys. Lett. B* 806 (2020), p. 135488. DOI: 10.1016/j.physletb.2020.135488.

[Ven22] M. Venhart et al. In: *Phys. Rev. C* 105 (2022), p. 034338. DOI: 10.1103/PhysRevC.105.034338.

[Wal12] J. C. Walpe et al. In: *Phys. Rev. C* 85 (2012), p. 057302. DOI: 10.1103/PhysRevC.85.057302.

[Wal20] P. Walker and Z. Podolyák. In: *Physica Scripta* 95. (2020), p. 044004. DOI: 10.1088/1402-4896/ab635d.

[Wal24] P. Walker and F. Kondev. In: *Eur. Phys. J. Spec. Top.* 233 (2024), p. 983. DOI: 10.1140/epjs/s11734-024-01096-4.

[Wal87] K. Wallmeroth et al. In: *Phys. Rev. Lett.* 58 (1987), p. 1516. DOI: 10.1103/PhysRevLett.58.1516.

[Wal89] K. Wallmeroth et al. In: *Nucl. Phys. A* 493. (1989), p. 224. DOI: 10.1016/0375-9474(89)90396-5.

[Wal99] P. Walker and G. Dracoulis. In: *Nature* 399 (1999), p. 35. DOI: 10.1038/19911.

[Wan21] M. Wang et al. In: *Chin. Phys. C* 45 (2021), p. 030003. DOI: 10.1088/1674-1137/abddaf.

[Wei35] C. F. Weizsäcker. In: *Z. Physik* 96 (1935), p. 431. DOI: 10.1007/BF01337700.

[Wei51] V. F. Weisskopf. In: *Phys. Rev.* 83 (1951), p. 1073. DOI: 10.1103/PhysRev.83.1073.

[Woo54] R. D. Woods and D. S. Saxon. In: *Phys. Rev.* 95 (1954), p. 577. DOI: 10.1103/PhysRev.95.577.

[Woo92] J. Wood et al. In: *Phys. Rep.* 215. (1992), p. 101. DOI: 10.1016/0370-1573(92)90095-H.

[Woo99] J. Wood et al. In: *Nucl. Phys. A* 651 (1999), p. 323. DOI: 10.1016/S0375-9474(99)00143-8.

[Wu05] S.-C. Wu. In: *Nucl. Data Sheets* 106. (2005), p. 367. DOI: 10.1016/j.nds.2005.11.001.

[Xu92] Y. Xu et al. In: *Phys. Rev. Lett.* 68 (1992), p. 3853. DOI: 10.1103/PhysRevLett.68.3853.

[Yan24] X. Yang. *Private communication.* 2024.

[Zha05] Y. H. Zhang et al. In: *J. Phys. G* 31. (2005), p. S1545. DOI: 10.1088/0954-3899/31/10/029.

[Zhu21] S. Zhu and E. McCutchan. In: *Nucl. Data Sheets* 175 (2021), p. 1. DOI: 10.1016/j.nds.2021.06.001.

List of Publications

Publications in current contents

- *Beta- and alpha-decay spectroscopy of ^{182}Au*
  J.Mišt, B. Andel, A. N. Andreyev, A. E. Barzakh, J. G. Cubiss, A. Algora, S. Antalic, M. Athanasakis-Kaklamanakis, M. Au, S. Bara, R. A. Bark, M. J. G. Borge, A. Camaiani, K. Chrysalidis, T. E. Cocolios, C. Costache, H. De Witte, R. Y. Dong, D. V. Fedorov, V. N. Fedosseev, L. M. Fraile, H. O. U. Fynbo, R. Grzywacz, R. Heinke, C. F. Jiao, J. Johnson, P. M. Jones, D. S. Judson, D. T. Kattikat Melcom, M. M. Khan, J. Klimo, A. Korgul, M. Labiche, R. Lică, Z. Liu, M. Madurga, N. Marginean, P. Marini, B. A. Marsh, C. Mihai, P. L. Molkanov, E. Nácher, C. Neacsu, J. N. Orce, R. D. Page, J. Pakarinen, P. Papadakis, S. Pascu, A. Perea, M. Piersa-Silkowska, Zs. Podolyák, M. D. Seliverstov, A. Sitarčík, E. Stamati, A. Stoica, A. Stott, M. Stryjczyk, O. Tengblad, I. Tsekhanovich, A. Turturica, J. M. Udías, P. Van Duppen, N. Warr, and A. Youssef
  Submitted to Phys. Rev. C (2025)

- *New upper limits for beta-delayed fission probabilities of $^{230,232}Fr$ and $^{230,232,234}Ac$*
  S. Bara, A. Algora, B. Andel, A. N. Andreyev, S. Antalic, R. A. Bark, M. J. G. Borge, A. Camaiani, T. E. Cocolios, J. G. Cubiss, H. De Witte, C. M. Fajardo-Zambrano, Z. Favier, L. M. Fraile, H. O. U. Fynbo, S. Goriely, R. Grzywacz, M. Heines, F. Ivandikov, J. D. Johnson, P. M. Jones, D. S. Judson, J. Klimo, A. Korgul, M. Labiche, R. Lica, M. Madurga, N. Marginean, C. Mihai, **J. Mišt**, E. Nácher, C. Neacsu, J. N. Orce, C. Page, R. D. Page, J. Pakarinen, P. Papadakis, A. Perea, M. Piersa-Silkowska, Zs. Podolyák, R. Raabe, W. Ryssens, A. Sánchez-Fernández, A. Sitarčík, O. Tengblad, J. M. Udías, V. Van Den Bergh, P. Van Duppen, N. Warr, A. Youssef, and Z. Yue
  Accepted for publication in Phys. Rev. C (2025)
  DOI: 10.1103/c19c-8bjd

Other publications

- *High-statistics decay spectroscopy of $^{178,182}Au$ at IDS*
  J. Mišt, C. Page
  Submitted to ISOLDE Newsletter 2025 (2025)

- *Evaluation of β-decay feeding intensity in ^{182}Au EC/β^{+} decay ^{182}Au*
  J. Mišt on behalf of the IS665 experiment and the IDS Collaboration
  Acta Phys. Pol. B Proc. Suppl. 17, 3-A8, (2024)
  DOI: 10.5506/APhysPolBSupp.17.3-A8

- *Fast-timing investigation of A = 128 isobars populated in the β-decay of ^{128}Cd*
  M. Llanos-Expósito, L. M. Fraile, J. Benito, J. Acosta, A. Algora, B. Andel, A. N. Andreyev, S. Antalic, R.A. Bark, C. Bernerd, N. Bernier, B. Bhengu, D. Bittner, M. J. G. Borge, J. A. Briz, K. Chrysalidis, T. E. Cocolios, C. Costache, J.G. Cubiss, H. De Witte, N. Encina, A. Esmaylzadeh, Z. Favier, D. Fernández, C. Ferrera, H. O. U. Fynbo, V. García-Távora, G. Georgiev, M. Górska, R. Heinke, J. L. Herraiz, A. Illana, P. Jones, D. S. Judson, A. Jungclaus, M. Karny, A. Korgul, U. Köster, Th. Kröll, M. Labiche, S. Lalkovski, B. Lesch, M. Ley, R. Lică, M. Madurga, N. Mărginean, B. A. Marsh, K. Miernik, C. Mihai, M. Mikolajczuk, **J. Mišt**, J.R. Murias, E. Nácher, C. Neacsu, V. M. Nouvilas, S. Ntshangase, B. Olaizola, J. N. Orce, C. Page, J. Pakarinen, P. Papadakis, A. Perea, M. Piersa-Siłkowska, Zs. Podolyak, J. Rog, S. Rothe, B. Rozwoda, V. Sánchez-Tembleque, K. Solak, S. Stegemann, M. Stepaniuk, A. Stoica, M. Stryjczyk, O. Tengblad, A. Turturica, G. Turturica, J. M. Udías, S. Ujeniuc, P. Van Duppen, M. von Tresckow, Ir. B. Vasilev, N. Warr, Z. Yue and S. Zajda
  Acta Phys. Pol. B Proc. Suppl. 17, 3-A7, (2024)
  DOI: 10.5506/APhysPolBSupp.17.3-A7

- *Study of isotopes using the β-γ measurements*
  J. Mišt
  27$^{\text{th}}$ Conference of Slovak Physicists Proceedings, (2024), p. 29-30
  ISBN: 978-80-89855-26-1

- *Pandemonium effect in the β decay of ^{182}Au*
  J. Mišt
  Proceedings of the Student Science Conference 2024, (2024), p. 316
  ISBN: 978-80-8147-151-3

- *Investigation of ^{182}Au β decay*
  J. Mišt
  Proceedings of the Student Science Conference 2023, (2023), p. 262
  ISBN: 978-80-8147-136-0

- *Study of ^{182}Pt via β decay of ^{182}Au*
  J. Mišt
  Proceedings of the Student Science Conference 2022, (2022), p. 274
  ISBN: 978-80-8147-127-8

- *Účinné prierezy pre produkciu izotopov seaborgia vo fúzno-výparných reakciách*
  J. Mišt
  Proceedings of the Student Science Conference 2021, (2021), p. 75-86
  ISBN: 978-80-8147-107-0

Conferences

- *Structure of ^{182}Pt investigated via β decay of ^{182}Au*
  J. Mišt
  Mazurian Lakes Conference on Physics, 3-9 September 2023, Piaski, Poland

- *Investigation of ^{182}Pt via β decay of ^{182}Au*
  J. Mišt
  IDS Collaboration Meeting, 28 November 2023, Geneva, Switzerland

- *Investigation of ^{182}Pt via β decay of ^{182}Au*
  J. Mišt
  ISOLDE Workshop and Users Meeting 2023, 29 November - 1 December 2023, Geneva, Switzerland

- *Investigation of ^{182}Pt via EC/β decay of ^{182}Au*
  J. Mišt
  Zakopane Conference on Nuclear Physics, 25 August - 1 September 2024, Zakopane, Poland

- *Study of ^{182}Pt via β decay of ^{182}Au*
  J. Mišt
  27$^{\text{th}}$ Conference of Slovak Physicists, 2-5 September 2024, Žilina, Slovakia